Engineering

Studia Universitatis Babeş-Bolyai ENGINEERING

The Journal of the Faculty of Engineering at Reşiţa

Babeş-Bolyai University from Cluj-Napoca

Leveraging smart contracts for enhanced traceability and security in bank transactions on a blockchain platform

Obamehinti Adeolu Seun* ⒾⒹ, Adekunle Eludire ⒾⒹ, Araoluwa Simileolu Filani ⒾⒹ

Abstract. *Traceability of transaction have been an issue facing the financial institution for a long time. The banks are the actors who have overall responsibility for financial transaction, thus placing them in a position of responsibility for realizing the traceability demands. The bank has the coordinating role in financial transfers as well as performing tasks during transaction. Due to lack of traceability, a lot of fraudulent activities go on without being detected one of which is the issue of fake alert system, where money could assume to be transferred to a recipient account and yet not reflect in the account balance. It needs to be established that financial traceability is a problem that requires solution. In other to address these, blockchain technology which is a noble disruptive technology that is tamperproof, secure and transparent and store hash value of data is the most viable way of addressing the challenge of traceability of financial transactions.*

Keywords*: traceability, smart contract, blockchain, proof of work.*

1. Introduction

Financial traceability is the process by which a transaction is properly traced to its destination, that is, the recipient of the transaction and where the transaction emanated from. Traceability has experienced an increased importance for bank practices in recent years [1].states that bank sector sees it as a high priority on the management agenda today. Financial Traceability is often understood from environmental aspects, but it also includes the social and economic aspects of the corporation [2]. Traceability is becoming a customer requirement, pressuring corporations to further consider it. It has, however, a positive effect on the profit as well since it often becomes more efficient

in its use of resources [4]. Thus, practicing Corporate Social Responsibility (CSR) can make companies improve the traceability of transactions in within the sector. The financial sector is experiencing an increasing traceability awareness within their projects. This includes both materials that have less impact on the environment which are fairly produced, as well as financial conditions and other social aspects during actual transaction [3]. The main financial institutions or banks are the actors who have overall responsibility for financial transactions, thus placing them in a position of responsibility for realizing the traceability demands. The bank has the coordinating role in financial transfers as well performing tasks during transactions. Financial traceability has it challenges over the years due to lack of a secured network system to properly manage the transparency of transaction that goes in and out of an account [7]. First, unlike blockchain technologies, bank transactions are not only centralized, but they are also backed up using third-party institutions (Bracci, 2021). Second, cryptocurrency payments are new technologies that will potentially disrupt the traditional way of bank operations especially in its level of transaction security and traceability [8]. Third, since their inception, most banks in Nigeria have their information dispersed in a wat that transaction histories are often lost [5]. Fourth, banks owners associate blockchain technology with complexity and cost concerns[6].Embracing blockchain technology is one of the most viable ways of helping financial institutions reach such milestones especially by ensuring the traceability of their assets and operations. Blockchain technology, is an innovative technology renowned for high traceability, transparency, confidentiality, irreversibility, accuracy, and delivery [10]. When it comes to traceability, blockchain technology, leverage the use of smart contracts which is an executable code that serves as policy guide in the blockchain network will ensure that every user can track the history of trusteeship and journey of an asset in real-time. As defined by the United Nations Global Compact, "Traceability is the ability to identify and trace the history, distribution, location and application of products, parts and materials, to ensure the reliability of sustainability claims, in the areas of human rights, labour (including health and safety), the environment and anti-corruption [3]. Even with favourable opportunity for fin4ancial institutions to adopt blockchain technology [11] found that existing research is yet to show the extent to which blockchain technology has the potential to promote traceability of bank activities in Nigeria. Since bank transactions over the year have had issues of accurate traceability of their activities, [12] calls for the implementation of traceability systems that can provide transparency in their operations by arguing that it is both a social and economic challenge.

Traceability has been acknowledged as an effective tool for achieving sustainability objectives in a number of businesses. This is caused by the constantly increasing demand from consumers for responsibly sourced and produced products together with the obligations by regulatory framework to improve transparency and tracking

in supply chain [13]. Although other sectors, industries, countries, and regions have already started implementing traceability, bank sector are yet to tap into it despite their massive numbers and assimilation in the global economy. The traceability system of blockchain technology also facilitates the detection of fraud and secures the integrity of the supply chain globally [4]. In the context of blockchain technology, this study seeks to understand the traceability of bank transactions in other to prevent the menace of fake alert. Using Nigeria as a case study based on existing information technology-based systems and leverage on blockchain technology to provide a traceable transaction system in the bank sector. This research looks into what various sectors used different technologies for traceability, and its limitations and the need to adopt blockchain technology for traceability of transactions. Blockchain smart contract will serve as the driving force in the area of policy guidance in the transaction network. Smart contract is an executable code which helps to secure every transaction, that is carried out in the blockchain network system. The agricultural sector has already proposed a number of blockchain-based solutions to livestock data management [13] along with food traceability and safety [14]. However, this research mainly delves into how banks can implement blockchain technology-based traceability in their business context by identifying and exploring key factors that are crucial to the effective application of the systems in the traceability of transactions

2. Literature review

The review of literature discusses the existing practices with which banks uses to trace transaction. It also discusses a brief description of blockchain technology, layers of blockchain technology, existing systems and sectors where blockchain technology have been applied and used to solve various challenges in bank and related sectors. According to [14] blockchain technology presents unique opportunities as regards its traceability capabilities it explored the critical success factors for adopting blockchain technology to promote traceability in the supply chain of Small and Medium Enterprises (SMEs). [12] identified that blockchain technology can be used in the real estate sector, for the purpose of tenant and landlord rent. It discusses how smart contract is written as executable rule for the purpose of the real estate sector so as to provide solution to the rental challenges and a secured platform for the said transaction. Blockchain was introduced to give override to primitive business process, where trusted parties are needed for transaction verification and it also run a centralized architecture. With blockchain technology, sectors can now run a decentralized system of transaction and no need for third part interference, with credible transactions. The unique characteristics of blockchain technology has provided security, tamper proof, transparent, database for proper public record keeping

according to [11]. Blockchain is regarded as a public ledger of database for public repository. According to [13] stated that blockchain can be used in banking sectors, where banks use same blockchain for customers transaction thereby providing transparency off transaction. Blockchain is also seen to be used for auditing of transactions there it was proposed by [12] for company to put resources together and invest in blockchain technology to used it to build a decentralized architecture thereby minimizing transaction cost as the technology also proffer safe, fast and transparent system

Furthermore, [10] identified that blockchain is considered beyond crypto currency, with smart contract playing a pivotal role. Also, according to [11] indicated that smart contract was considered the next level of blockchain used as executable code for transaction policy. It can therefore be said that smart contracts within the context of blockchain as embedded code run in a decentralized way used in the blockchain without the need of a centralized authority to operate the blockchain, according to [8]. Blockchain system [4] states the importance of smart contract in order to accommodate complex transaction and interaction within the limitless application. This in a way has indicated another relevance of blockchain technology. In addition, according to the research findings of [7] 33% of C-suite executives has shown interest in considering rather actively engages in blockchain.

Furthermore [11] pointed out that developers are beginning to see the effectiveness and capabilities of blockchain technology and need to explore various application depending on sectors to adopt the technology. Also, according [9] based on the audience there are three distinguished generations of blockchain which are: blockchain 1.0 this is the cryptocurrency digital transaction while Blockchain 2.0 includes smart contract, which provides a system beyond cryptocurrency and blockchain 3.0 involves science, internet of things, government and health sector. [7] states that blockchain has not covered its full capabilities. Another research was carried out by [4] on how blockchain and decentralized system can be used for internet of things and how it can also manage big data in a decentralized way this is according to [15] found that blockchain technology can be used in the real estate sector, for the purpose of tenant and landlord rent. It was clearly discussed in the research how smart contract is written as executable rule for the purpose of the real estate sector so as to provide solution to the rental challenges and a secured platform for the said transaction. According to [9] Blockchain technology can not only process currency transactions but can also ensure that transactions comply with programmable rules in the form of "smart contracts". All these transactions could be validated between parties who fully trust each other without relying on a trusted middleman". Honduras government has set up all land records on the Blockchain. Whenever there is a change of ownership of a property, it gets recorded openly [9]. The tamper proof and straightforward of the Blockchain technology make it fit for records, create

transaction and keep record of such transactions. Presently, the majority of the establishments, such as firms, have received Blockchain innovations to keep up discreet and secure databases. Blockchain can be utilized as a legal official administration to make it simple and modest by connecting some required information with the record of transaction. [14] noted that" There are different type of consensus mechanism, the most outstanding is the Proof-of-Work (PoW). it requires solving the problem of a computational procedure, like discovering hashes with explicit examples, for example a main number of zeroes [4] found to guarantee verification and undeniable nature". In the case of power of stake, it is not determined by their mining power, Proof-of-Stake (PoS) conventions split stake block according to the present abundance of miners [13] Thus, the determination is more pleasant and keeps the wealthiest member from overwhelming the system. Numerous blockchain, for example, [5] found that ethereum are bit by bit moving to Proof of Stake (PoS) which usually requires miners to use high computational power and because of the noteworthy reduction in power utilization and improved adaptability [1]. An extra layer, the compute interface, permits blockchain to offer greater usefulness. For all intents and purposes, a blockchain stores a state which comprises for example of the considerable number of exchanges that have been made by the clients, in this way permitting the count of every client's equalization. Notwithstanding, for further developed applications we have to store complex states which are refreshed powerfully utilizing disseminated figuring, for example states that move starting with one then onto the next once explicit criteria are met. A unified blockchain is a cross breed mix of public and private Blockchain [11]. In spite of the fact that it has comparable versatility and security assurance level with private blockchain, their difference is that it has a set of hubs, named pioneer hubs, is chosen rather than a solitary element to check the transaction record. This empowers a mostly decentralized plan where pioneer hubs can allow authorizations to different clients. [12] found that on the grounds that, notwithstanding established highlights, for example, the proprietorship and the executives of the data shared in the blockchain, we consider highlights, for example, transaction endorsement time, or security perspectives, for example, obscurity. The blockchain innovation is highly secured and autonomous and also keep record of the unique finger prints of a computerized resource without putting away the advanced resource [4] "highlights all banks are currently engaged in developing a vision of what this technology means for their business". [2] discussed that in research and practice that the main parameters for Blockchain implementations such as security, data privacy. [12] discusses proof-of-work approaches that require high levels of energy but guarantee relatively high levels of consistency and protection against forgery by any actor in the network for example, in bitcoin, compete against less costly ones. Such alternative approaches require a portion of a trust in some elements of the network, such as actors based on the resources they put at risk during validation for example, the proof-of stake or in

the manufacturers of devices that are used to validate transactions for example, proof-of-elapsed time in hyper-ledger saw-tooth lake. For the design and deployment of blockchain implementations [14] found that there are different selection criteria or parameters that are required to be considered while designing and deploying the implemented blockchain

3. Research methodology

This chapter discusses the methodology used. It explains the method approach and algorithm framework to be adopted in this research. The method and algorithms are explained in the subtopics. Steps Approach to the methodology adopted as it is shown in the figure 1.1 is stated below;

i. **The registration phase:** The registration phase allows intending participant to register with their identity, after the registration the user can login with its private key where the intending users gives is details such as name, national identification number and bank verification number. The miners, mine block using the proof-of-concept algorithm.

ii. **The Proof of work concept:** Under the proof of work data administration is taken into the ledger of the blockchain system, where the block miners are required to mine a block for the user. Upon mining this block, a user is expected to generate a private key which is for validation by the owner of the transaction. Another key which is generated is the public key which is available to every participant in the blockchain in order to verify the transaction actually belongs to the owner. Once this is done a smart contract policy is written to serve as policy guide in the blockchain system.

iii. **Smart contract policy:** The smart contract will serve as the policy guide in the blockchain system. This uses its policy which is written in solidity language to set rules in the blockchain network. After the smart contract is written then the chaotic map/ elliptic curve is used for encryption and decryption.

iv. **Transaction hash value:** This is where the transactions are saved. Every transaction in the blockchain is saved in the hash pull of data and can be recalled or generated when needed. It further provides durability of transactions. Meta-mask. This is a test-net platform where the application will be evaluated.
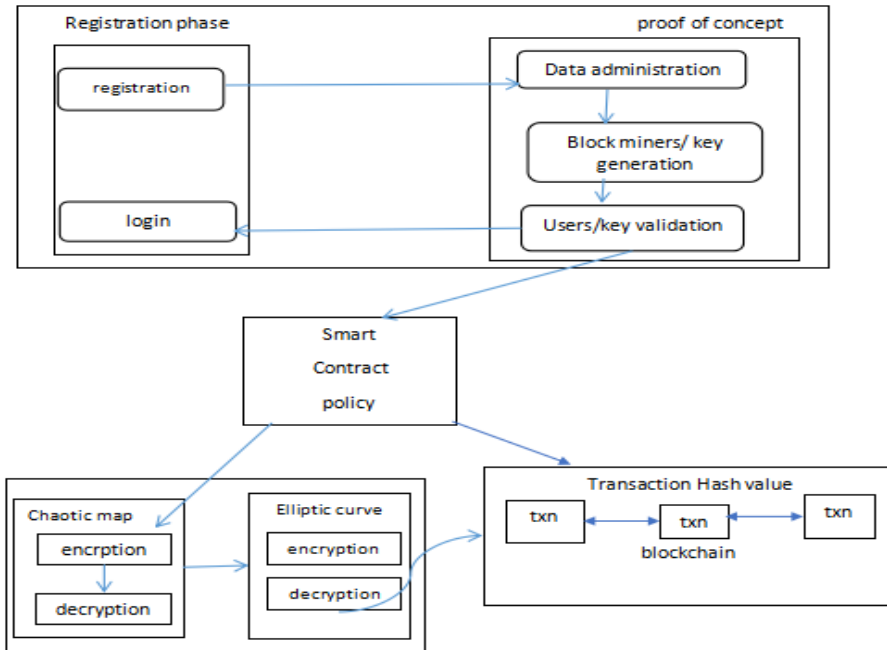
Figure 1. Architecture of the proposed system adopted from [9]

3.1. Proof of Work Concept

The first step to achieve the desired research is to use the proof of work concept of algorithm which requires all miners on the network to solve a cryptographic puzzle by applying the brute force formula. Take for example if the ethereum blockchain has a new transaction which are tentatively committed and they are based on Proof of Work (PoW) output, a selected block created by the winning node is broadcasted to all the nodes, at specific synchronization interval. Once the block is transmitted using a peer-to-peer network to other nodes the same is included in the blockchain and any other tentative transaction are rolled back (According to (Zhao, 2018) by rule of probability the consensus is achieved by 51% if power of work in the algorithm rather than 51% people count). The proof of work concept is used in this study because compared to other algorithm it is considered secure as it is almost impossible for the concept to be attacked unless a miner acquires 51% of computing power which is made impossible by the blockchain structure. This is indicated in figure 1 architecture frame work of the proposed system.

Proof of work concept steps;

Proof of work with sha 256^2

Ethereum uses $\{0, 1\}2^{64}$ $\{0, 1\}$ ^256▼

X   sha 256 (sha 256(x)) e $\{0, 1\}$ ^256▼

Given a 'target' T.E $\{0, 256\}$

To 'mine' block – data until hash<t

Nonce=next nonce

Hash= h (block – data/nonce)

There is no better way than guessing probability of success for on nonce $t/2^{256}$ T is adjusted every 2016 blocks to keep producing block every 10 minutes.

3.2. Smart Contract

The smart contract is the executable code which verifies the value of the transaction and checks if it meets all the rules embedded in the contract before it can proceed to send a message through individual addresses to others. The principal parts of the smart contract are a lot of executable capacities and state factors. Every exchange has input parameters which are required a capacity in the agreement. Amid the execution of a capacity, the status of the state factors is changed relying upon the rationale usage. The smart contract code is written in abnormal state dialects, for example, Solidity and Python for Ethereum applications. The code is aggregated into bytecode utilizing compilers as Solidity or Serpent.

The agreement code will be transferred into the blockchain once the compiler is executed with no mistakes. Each agreement will be allotted a one-of-a-kind location by the blockchain system. Ethereum is one of the favored advances for the improvement of the keen contracts. The fundamental segments for the exchanges depend on state machine and capacities. The state machine is a turing-complete contract handling and execution stage based on a Blockchain decentralized shared record. The plan and the usage of the ethereum are absolutely autonomously from the digital money bitcoin. An abnormal state programming language called Solidity is utilized to compose brilliant contracts and Decentralized Applications (DApp). The software engineer can make their exchanges groups, state changes and occasions capacities, and guidelines for proprietorship. The product code is executed on a virtual machine alluded to as the Ethereum Virtual Machine (EVM).

3.3. Hash value veneration using Blockchain technology

Blockchain technology verifies the user's authentication process and the hash value function generated using the transaction between the user and the banking server. The transactions performed by the user are stored in the hyper-ledger technology which is a distributed enterprise grade that provides a high level of security.

Transactions define an electronic coin as a chain of digital signatures. Each owner transfers the coin to the next by digitally signing a hash of the previous transaction and the public key of the next owner and adding these to the end of the coin. A payee can verify the signatures to verify the chain of ownership.
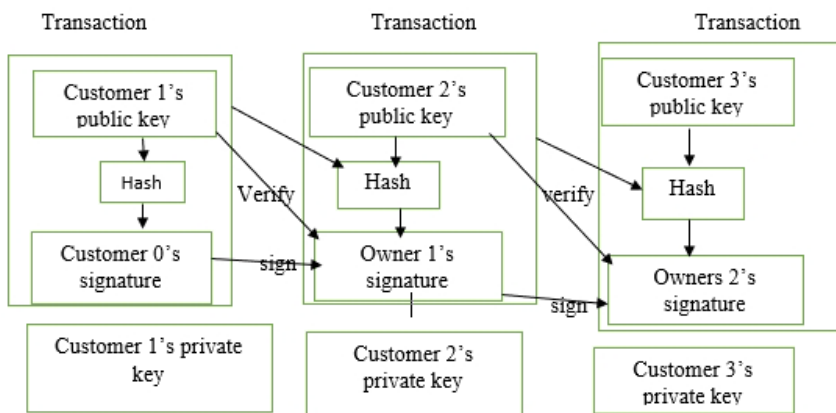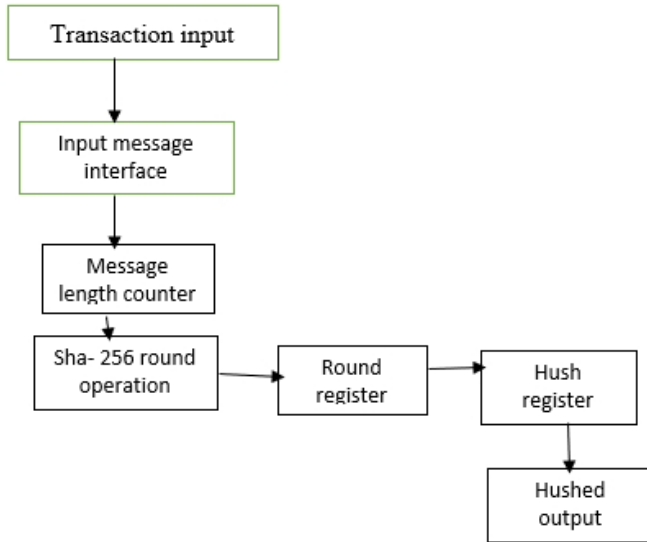

Figure 2. Transaction Hash Algorithm [6]

The chain of blocks is composed of multiple transactions which are composed of transaction id, previous transaction id, user's public key, the owners 0's, 1's, 2's 3's are various owners of transaction that is being stored in the hash value. The owner's signature is a private key that is used by every transaction owner in the blockchain to verify transactions before it can go through. All pf these transactions are saved in the hash which serve as data repository in the blockchain system. Low entropy password, chain code function, functional parameters, as depicted in Figure 2.

The Figure 3 depicts the components involved in the generation of 0 hash function for the Series of blocks created in the blockchain technology. The blockchain is composed of series of blocks and each block is bounded with hash value, transactions performed between the user (U_i) and the Banking Server (BS_i), iterations, time stamp and the hash value of the previous block. Once the transaction is inputed, the message is interfaced with the message length counter and padding unit which in turns check the validity of the message and sends it to the message register. The sha 256 operation relate the message to the round register and hash register which finally sends it to the hashed output.

i) The chain of blocks has been created based on the hash value generated by incorporating Secure Hash Algorithm (SHA-256) as Depicted in Figure 3.

ii) The incoming message digest from the user UID is performed with Secure Hash Function (SHA-256). The new hash function is generated whenever-the comparison of existing hash value is not matched but with matching credentials.

Figure 3. Hash Algorithm [4]

4. Conclusion

Traceability of bank transaction is an important factor that gives customers the desired satisfaction of the willingness to continue using a particular bank. With the aid of blockchain technology, every transaction that will be cared out within the banking system will be properly traced in other to prevent fake alert transfer.

All authors have read and agreed to the published version of the manuscript.

Conflicts of Interest: The authors declare no conflict of interest.

References

1. M.W. Agungi, *The business blockchain promise traceability: practice, and application of the next Internet Technology*, John Wiley & Sons, Inc., 128 (2), 2022, pp. 1-16.
2. S.A. Anderson, The traceability of fees payment through banks by student to various institutions, *International Journal of Information Science*, 275 (1), 2017, pp. 1-12.
3. M. Atzori, *Blockchain bad architectures for the internet of things*, Springer, 2016.
4. O.S. Azubuike, Banking sector a critical sector addressing the bottle necks. *International of Advanced Trends in Computer Science and Engineering*, 4(9), 2019.
5. M.E. Bracci, Smart contracts: terminology, technical limitations and real-world complexity, *Law, International Journal of Innovation and Technology*, 269(3), 2021, pp. 1-14.
6. V. Buterin, Public and private blockchain, *Ethereum blog*. 45(2), 2015.
7. J.S. Chen, PayPal transactions effectives towards payment to various sectors, *International Journal of Information and Computing*, 189(3), 2020.
8. Das Mankatail, Blockchain use cases for food traceability and control, *Journal of Natural Science*, 45(2), 2018, pp. 1-13. https://www.sklkommentus.se/globalassets/kommentus/bilder/publication
9. E. Das, Privacy and security challenges in internet of things. *Journal of Distributed Computing Internet Technology,* 78(2), 2018.
10. European (2020). Effect of customer feedback on traceability.
11. P. Glaser, Towards a more democratic mining in bitcoin, 2019.
12. M. Gupta, *Blockchain for Dummies*, IBM Limited Edition. [E-book]. 2017 Available online: https://www-01.ibm.com/common/ssi/cgi-bin/ssialias?htmlfid=XIM12354USEN
13. S.M. Jason, *The blockchain and kudos: distributed system for educational record, reputation and reward*, Proceedings of 11th European Conference on Technology 4(2), 2019, pp. 1-12.
14. K.D. Jude, PayPal transactions effectives towards payment to various sectors, *International Journal of Information Science and Computing*, 2(21) 2020, pp. 1-13.
15. I.P. Karamitsos, Design of the blockchain smart contract; A use case for real estate. *International Journal of Management Information Technology and Engineering*, 8(4), 2018, pp. 1-6.

Addresses:

- Obamehinti Adeolu Seun, Joseph Ayo Babalola University, Nigeria,
  lebiobamehinti@gmail.com
  (*corresponding author*)
- Adekunle Eludire, Joseph Ayo Babalola University, Nigeria,
  aaeludire@jabu.edu.ng
- Araoluwa Simileolu Filani, Joseph Ayo Babalola University, Nigeria,
  asfilani@jabu.edu.ng

Computational algorithm for evaluating gravitational and inertial loads acting on an industrial robot for palletizing operations

Roxana-Mariana Nechita* , Cozmin Cristoiu , Mihai Mărgăritescu

Abstract. *This paper introduces a computational algorithm designed to calculate the gravitational and inertial loads affecting a four-axis numerically controlled (NC) industrial robot (IR) used in palletizing operations. The methodology includes the development of precise calculation models that account for the dynamic interactions between the robot's mechanical components and its operational environment. These models enable the accurate determination of load distributions and stresses on each axis, which are critical for optimizing the robot's performance and ensuring reliable operation under various loading conditions. The algorithm can be applied to the optimization and refinement of existing robotic systems, as well as to the design of new robots tailored for specific industrial applications.*

***Keywords****: industrial robot, optimal structure, calculus algorithm, palletizing, unfavorable position.*

1. Introduction

Palletizing is the process of arranging objects into uniform horizontal layers and multiple vertical layers on standardized transport supports known as pallets. This process involves handling various types of objects, either individually or in groups, by industrial robots or automated palletizing machines. The application underpinning this study (Figure 1) is a robotic cell designed for palletizing prismatic objects, featuring a single entry and exit point, integrating an IR with a four-axis NC articulated arm. Within this cell, a pallet is introduced from a stack into the cell via a roller conveyor. After the pallet is evacuated from the cell, another pallet is brought in to continue the palletizing process. On the input conveyor, products to be handled are transported. These products consist of prismatic cardboard boxes, each containing six 750 ml bottles of wine. During transport, the products are inspected by two measurement sensors positioned above the conveyor to identify any defects. If defective products are identified, they are removed

from the flow through a system that marks the end of the objects' path on the roller conveyor-defective items are allowed to fall into a container located at the end of the conveyor. Conforming products are then brought into the workspace of the IR. The IR picks up the boxes that have reached the end of the conveyor and positions them optimally on the pallet according to a predefined algorithm. When the pallet, along with the accumulated load, reaches the maximum allowable height, it is evacuated from the cell via the conveyor. The loaded pallet is then taken by a human operator using a forklift to proceed to the next stage of the logistic process.
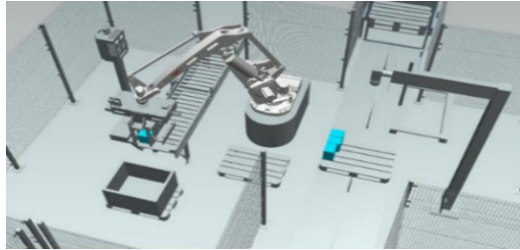
Figure 1. Robotic palletizing cell

1.1. Robot equivalence

Palletizing operations can be performed using robots with articulated arm or gantry architecture, which are commonly equipped with 5 or 6 degrees of freedom. In the case of IR with articulated arms, there is an option to use dedicated robots specifically tailored for palletizing operations. These dedicated articulated-arm robots typically feature 5 rotational degrees of freedom but are NC through only 4 axes. The distinctive feature of these dedicated robots lies in a specially designed mechanical system that enables pitch orientation movement [1]. This system ensures the permanent vertical alignment of the roll axis, regardless of the angular positions of the articulated arm segments. Implementing such a system involves the use of two closed-loop kinematic chain subsystems and a unique coupling design that facilitates pitch orientation movements [2].

The ABB IRB 660=180/3.15 [3] is an articulated arm robot with a closed kinematic chain designed for palletizing. Its workspace is spherically articulated with a radius of 3150 mm. These structural and functional parameters justify the capabilities of the robot in the following aspects:

- Bearing load capacity:

The weight of a single product (a crate containing 6 bottles of 0.75l of wine with cardboard separators) is :

$$0.6 \, kg \, (cardboard) + 4.5 \, kg \, (wine) + 2.622 \, kg \, (glass) \\ + 0.012 \, kg \, (cork) = 7.7 kg \tag{1}$$

The unfavorable position (Figure 2) of the IR in the application captures the handling of 3 boxes, weighing 23.1kg. The robot can handle heavy loads in palletizing applications. In an unfavorable situation, it can handle up to 93.541 kg, including a 70.441 kg prism object handling effector.
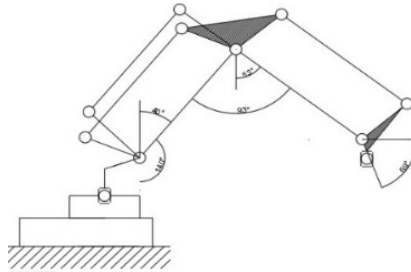
Figure 2. The structural kinematic diagram of the robot
in the unfavorable position.

The maximum length required to move in the unfavorable position is 1859.69 mm. The robot has an articulated spherical workspace with a radius of 3150 mm, which is compatible with the cell requirements shown in Figure 1.

The robot shall be accurate and repeatable in its operations. This includes the volumetrically orderly arrangement in the horizontal and vertical plane (layers with homogeneous heights) and the accurate handling of prismatic bodies for pallet assembly. Technical specifications of ABB IRB 660=180/3.15 [3] are: maximum payload: 180 kg; nc axis number: 4; controller type: irc5 single/dual; cabinet maximum reach: 3.15 m and robot weight: 1650 kg. Thus, the ABB IRB 660=180/3.15 robot is optimized for palletizing tasks due to its robust structure, generous workspace and ability to handle heavy loads in a precise and repeatable manner.

2. Sequence of calculation stages

Concerning the order of the major computational steps for the design of the overall IR assembly, in addition to the aspects mentioned above, it is crucial to follow the following fundamental principles to perform the necessary computations for the overall IR's assembly [4]. In the preliminary stages of calculation, it is essential to establish the input data taking into account the specificity of the application in which the IR will be integrated and the functional characteristics of the previously selected reference IR model. These inputs include the IR-specific design parameters and the maximum limits of velocities and motions on the numerically controlled axes of the IR. In order to start the design of a rotational axis in a robot with n degrees of freedom (DOF), all constructive elements for each partial assembly corresponding to the NC axes (k + 1 to n) must be determined based on the

previous design and calculation steps [5]. Next, it is essential to correctly identify and locate the loads in the design scheme, including specific forces and moments.

In order to carefully follow these issues, the main computational steps for the overall IR assembly design are realized in the following sequences: development of the computational scheme for the design of the IR; identifying the location of mass in each major partial assembly of the RI;identification of the general distribution of gravitational and inertial loads applied on the overall robot structure, using the most appropriate configuration; determine the calculation for each IR's partial assembly; distribution of spatial loads on the computational centers over the entire robot structure; calculation of the results of reduced forces and moments (F, M); distribution of the forces and moments (F, M) previously applied on each IR joint, applied on the bearings or guides of the movable elements and components included in the kinematic/driving chain responsible for the rotational/linear motion of each IR movable element. The computational steps for obtaining the final usable results, including the final selection of the standardized IR's part assemblies, include: preliminary dimensioning, choosing, and ultimate validation of mechanical components; preliminary assessment, choice, and validation of servomotors and position/speed sensors employed across each NC axis; final verification of the selected servomotors and encoder systems used for continuous adjustment of the servomotor parameters on each NC axis; evaluating the performance of each individual sub-assembly within the robot; assessing the overall performance of the complete robot assembly. These steps provide a detailed methodology for the complete design and evaluation of the IR, ensuring compliance with specific design and functionality requirements in various industrial applications.

### 3. Determination of distribution for gravitational and inertial loads

In this calculation stage, using the established calculation scheme and the optimal configuration for designing partial assemblies, the following key aspects are determined:

• The gravitational loads (Gi) specific to each structural element of the IR and each partial subsystem, along with their spatial distribution across the entire IR assembly (Figure 3).

a.   **b.**
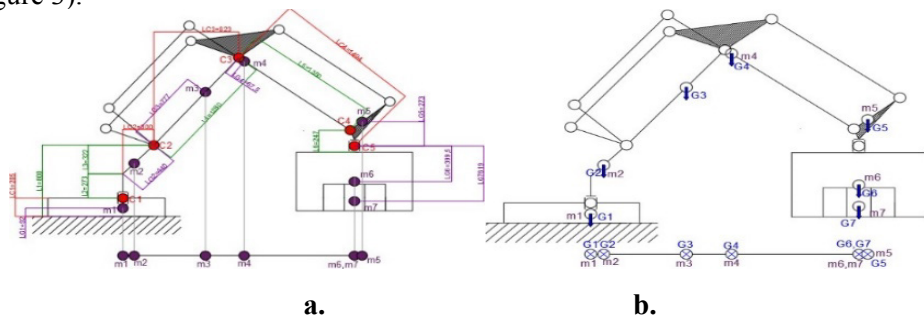
Figure 3. a. Locating calculation centers and mass centers on the kinematic diagram; **b.** Representation of gravitational forces on the kinematic diagram.

18

• The inertial forces generated by the mass of the IR's mobile elements and their manner of distribution in the rotational joints (Figure 4).

a.

b.

c.
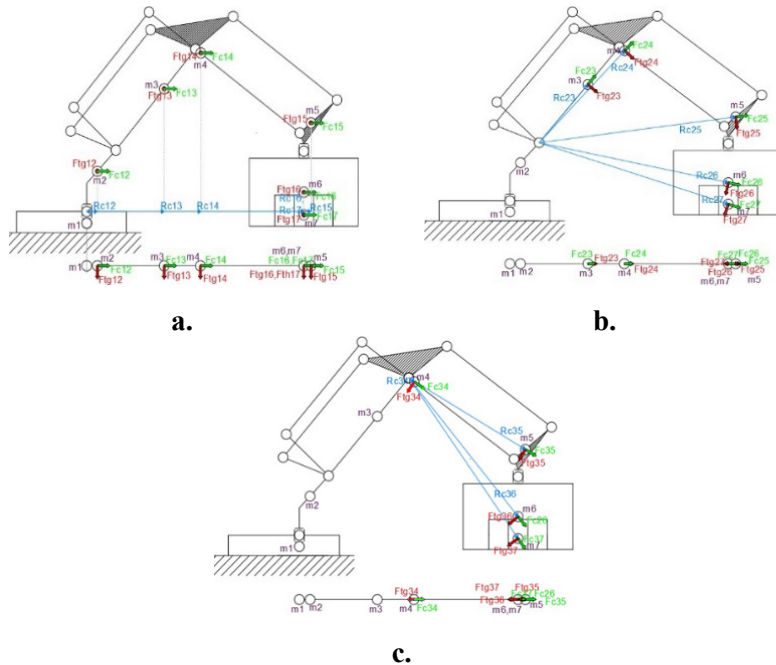
Figure 4.a. Representation of centrifugal forces, tangential forces, and kinematic radii on the kinematic calculation scheme for the possibility of motion in coupling 1; **b.** Representation of centrifugal forces, tangential forces, and kinematic radii on the kinematic calculation scheme for the possibility of motion in coupling 2; **c.** Representation of centrifugal forces, tangential forces, and kinematic radii on the kinematic calculation scheme for the possibility of motion in coupling 3.

• The principal moments of inertia of the structural elements/partial assemblies of the IR caused by rotational movements in each major/active joint.

To determine the spatial distribution of the gravitational and inertial loads considered in the design of the IR's NC axes, numerical evaluation and detailed graphical representation are employed on the previously developed calculation scheme: gravitational forces and inertial forces acting at characteristic mass centers of the IR's structural elements. In graphical representation on the calculation scheme, gravitational and inertial force loads are applied only at their respective centers, while inertial moments are applied around the rotation axes that generate them. Additionally, for each type of inertial force/moment of inertia, the specific direction and mode of action are determined, taking into account the movements of the elements and the timing of the inertial load [6].

The known input data for determining the specific radii and angles are presented in Table 1.

Table 1. Input data.

LC_n[mm]	LG_n[mm]	$L_n = 800$ [mm]
$LC_1 = 205$	$LG_1 = 92$	$L_1 = 800$
$LC_2 = 300$	$LG_2 = 161$	$L_2 = 273$
$LC_3 = 823$	$LG_3 = 777$	$L_3 = 322$
$LC_4 = 1494$	$LG_4 = 67.5$	$L_4 = 1280$
	$LG_5 = 273$	$L_5 = 1350$
	$LG_6 = 399.5$	
	$LG_7 = 619$	

For couple 1, the radii will be determined as follows:
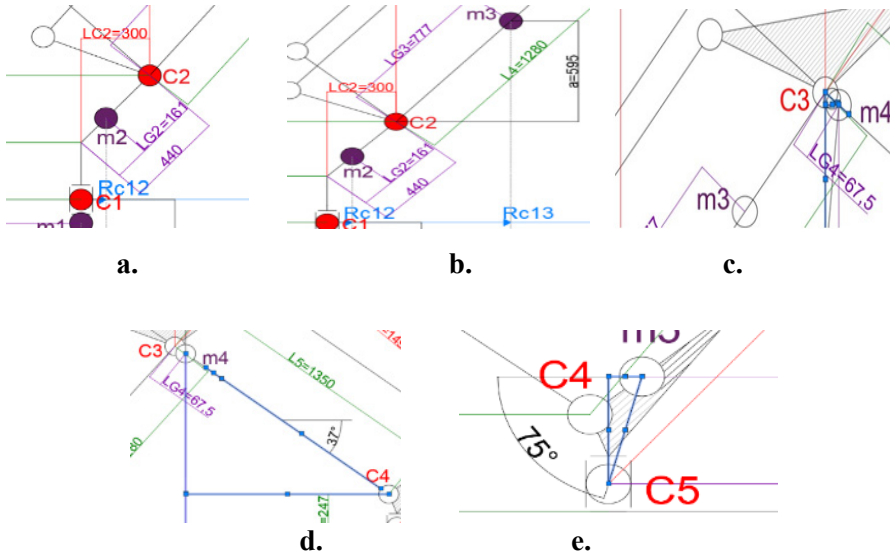
Figure 5. Sketches used to determine Rc_{1n}: **a.** triangle for Rc_{13}; **b.** triangle for Rc_{14}; **c.** Triangle for Rc_{15}; **d.** Triangle for Rc_{16}; **e.** triangle for Rc_{17}.

To determine Rc_{12}, we will use the similarity of triangles, using the triangle (Figure 5) a with sides: $LC_2 = 300 \ mm$, $L_3 = 322 \ mm$ and $LG_2 = 161 \ mm$.

$$\frac{a}{L_3} = \frac{LG_2}{b} = \frac{Rc_{12}}{LC_2} \tag{2}$$

$$Rc_{12} = \frac{LG_2 \cdot LC_2}{b} \tag{3}$$

To determine Rc$_{13}$, we will use the triangle (Figure 5.a) with sides $LG_3 + LG_2$, Zm_3, and Rc_{13}-Rc_{12}:

$$Zm_3 - 800 \; mm = 595 \; mm \tag{4}$$
$$Rc_{13} = \sqrt{(LG_3 + 440)^2 - (a + L_3)^2} \tag{5}$$

We will construct the following right triangle (Figure 5.b) to find Rc_{14} using the Law of Sines.

$$\frac{67.5 \; mm}{sin \, (90°)} = 67.5 \; mm \tag{6}$$
$$67.5 \; mm = 2R \tag{7}$$
$$2R \cdot sin(53°) = 53.91 \; mm \tag{8}$$
$$Rc_{14} = 53.91 \; mm + LC_3 + LC_3 \tag{9}$$

Use the right triangle in Figure 5.c. to find the projection of m_4-C_4, using the Sine Theorem:

$$\frac{L5 - LG4}{sin \, (90°)} = \frac{1350 - 67.5}{sin \, (90°)} \tag{10}$$
$$Rc_{14} = 53.91 \; mm + 823 \; mm + 300 \; mm \tag{11}$$
$$Rc_{15} = Rc_{14} + 1024.25 \; mm + 115{,}58 \; mm \tag{12}$$

Use the following right triangle (Figure 5.e) to deduce $Rc_{16} = Rc_{17}$, using the Sine Theorem:

$$\frac{LG_5}{sin \, (75°)} = \frac{247}{sin \, (75°)} \tag{13}$$
$$\frac{C_{4\_}m_5}{sin \, (15°)} = 283.26 \; mm \tag{14}$$
$$Rc_{16} = Rc_{17} \tag{15}$$
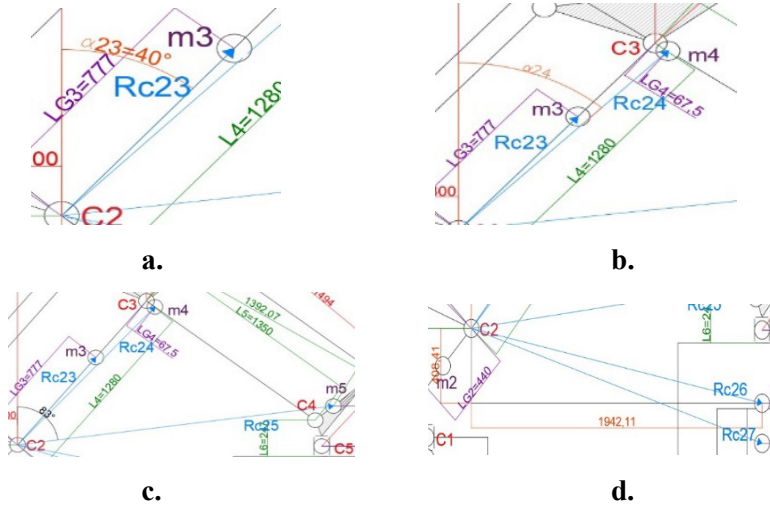$$Rc_{16} = Rc_{15} - 74.4 \; mm \tag{16}$$

Thus, Rc_{1n} are known (Table 2).

Table 2. The values of $Rc_{1n}[mm]$

Rc_{12}	Rc_{13}	Rc_{14}	Rc_{15}	Rc_{16}	Rc_{17}
109.05	799.45	1176.68	2316.51	2242.11	2242.11

For couple 2, the radii will be determined as follows:

Figure 6. Sketches used to determine the Rc_{2n}: **a.** The triangle used to determine Rc_{23}, α_{23}; **b.** The triangle used to determine Rc_{24}, α_{24}; **c.** The triangle used to determine Rc_{25}, α_{25}; **d.** The triangle used to determine $Rc_{26}, \alpha_{26}, Rc_{27}, \alpha_{27}$.

Rc_{23} corresponds to LG_3 (Figure 6.a).

α_{23} corresponds to the angle of the unfavorable position.

To determine Rc_{24}, we will use the triangle (Figure 6.b) with sides Rc_{24}, L_4, and LG_4, applying the Cosine Theorem as follows:

$$Rc_{24} = \sqrt{(LG_4{}^2 + LG_4{}^2 - 2 \cdot LG_4 \cdot L_4 \cdot cos\ (93°)} mm \tag{17}$$

To determine the angle α_{24}, the angle formed between Rc_{23} and Rc_{24} will be used, which will be found by applying the Sine Theorem in the triangle (Figure 6.b) with sides Rc_{24}, L_4, and LG_4.

$$\frac{Rc_{24}}{\sin\ (93°)} = \frac{LG_4}{\sin\ b} \tag{18}$$

$$sin^{-1}\ (0.05) = \ 3° \tag{19}$$

$$\alpha_{24} = \alpha_{23} + 3° \tag{20}$$

To determine Rc_{25}, the Sine Theorem will be applied (Figure 6.c):

$$Rc_{25} = \sqrt{(1392.07^2 + 1280^2 - 2 \cdot 1392.07 \cdot 1280 \cdot cos\ (99°)} mm \tag{21}$$

22

To determine , α_{25}, the Sine Theorem will be applied (Figure 6.c):

$$\frac{Rc_{25}}{\sin(99°)} = \frac{2033.77\ mm}{\sin(99°)} \tag{22}$$

$$\frac{1392.07\ mm}{\sin a} = 2059.36\ mm \tag{23}$$

$$\sin a = \frac{1392.07}{2059.36}\ mm \tag{24}$$

$$\alpha_{25} = (43 + Rc_{23})° \tag{25}$$

To determine Rc26, the Pythagorean Theorem will be applied (Figure 6.d):

$$Rc_{26} = \sqrt{1942.11^2 + 408.41^2}\ mm \tag{26}$$

$$Rc_{27} = \sqrt{1942.11^2 + 627.91^2}\ mm \tag{27}$$

$$\frac{1984.59}{\sin(90°)} = \frac{1942.11\ mm}{\sin b} \tag{28}$$

$$\sin b = \frac{1942.11}{1984.59}\ mm \tag{29}$$

$$\frac{2041.1}{\sin(90°)} = \frac{1942.11}{\sin c} \tag{30}$$

$$\alpha_{27} = 180° - 72° \tag{31}$$

Thus, Rc_{2n} (Table 3) and α_{2n} (Table 4) are known.

Table 3. The values of $Rc_{2n}[mm]$

Rc_{23}	Rc_{24}	Rc_{25}	Rc_{26}	Rc_{27}
777	1285.3	2033.77	1984.59	2041.1

Table 4. The values of α_{2n}

α_{2n}	α_{2n}	α_{2n}	α_{2n}	α_{2n}
40°	43°	83°	102°	108°

For coupling 3, the radii will be determined as follows:

a.

b.

c.
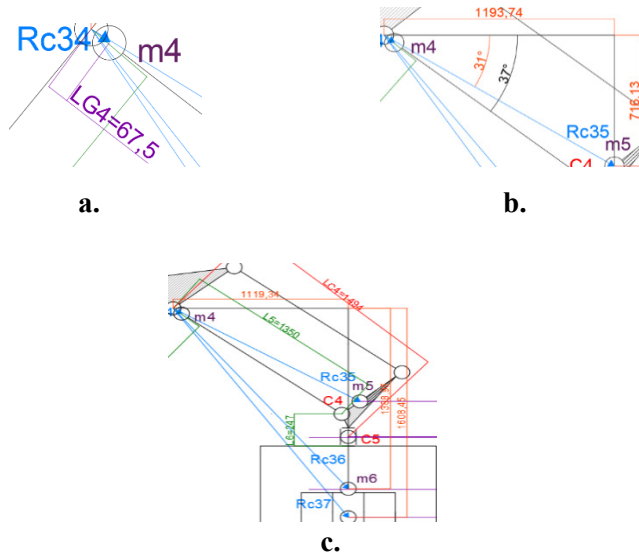
Figure 7. Sketches used to determine the Rc_{3n} triangles:
a. The triangle used to determine Rc_{34}, α_{34}; **b.** The triangle used to determine Rc_{36}, α_{36}, Rc_{37}, α_{37}; **c.** The triangle used to determine Rc_{35}, α_{35}

In the case of Rc_{34}, the procedure will be as follows:

$$Rc_{34} \text{ corresponds to } LG_4 = Rc_{34} \tag{32}$$

$$Rc_{34} = 67.5 \; mm \tag{33}$$

α34 corresponds to the angle of the unfavorable position (Figure 7.a)

To determine R35, the Pythagorean Theorem will be used (Figure 7.b) as follows:

$$Rc_{15} - Rc_{14} + 53.91 = 1193.74 \; mm \tag{34}$$

$$Rc_{35} = \sqrt{(1193.74^2 + 716.13^2} \; mm \tag{35}$$

The Sine Theorem will be applied (Figure 7.c) to find the value of the angle α_{35}:

$$\frac{Rc_{35}}{sin\,(90)} = \frac{1392.07 \; mm}{sin\,(90°)} \tag{36}$$

$$sin\,\alpha_{35} = \frac{716.13}{1392.07} mm \tag{37}$$

To determine Rc_{36} and Rc_{37}, the Pythagorean theorem will be used first (Figure 7.b), followed by applying the Sine theorem to find the angles α_{36} and α_{37}.

$$Rc_{36} = \sqrt{(1119.34^2 + 1388.95^2} \; mm \qquad (38)$$

$$Rc_{37} = \sqrt{(1119.34^2 + 1608.45^2} \qquad (39)$$

$$\frac{Rc_{36}}{\sin(90)} = \frac{1783.85 \; mm}{\sin(90°)} \qquad (40)$$

$$\frac{1388.95 \; mm}{\sin \alpha_{36}} = 1783.85 \; mm \qquad (41)$$

$$\frac{Rc_{37}}{\sin(90)} = \frac{1959.6 \; mm}{\sin(90°)} \qquad (42)$$

Thus, Rc_{2n} (Table 5) and α_{2n} (Table 6) are known.

Table 5. The values of $Rc_{2n}[mm]$

Rc_{34}	Rc_{35}	Rc_{36}	Rc_{37}
67.5	1303.07	1783.85	1959.6

Table 6. The values of α_{2n}

α_{2n}	α_{2n}	α_{2n}	α_{2n}
37°	31°	51°	55°

To determine the values of the gravitational forces acting on the robot in the actuation of couplings 1, 2 and 3 the following formula will be used: $G_n = m_n * g$ [N], where $g = 9.81 \frac{m}{s^2}$ (Table 7).

Table 7. The values of $G_n[N]$

G_1	G_2	G_3	G_4	G_5	G_6	G_7
3979.12	5979.24	3040.29	2330.89	873.95	686.7	226.61

The angular velocities ω_n of axes 1, 2 and 3 are as follows:

$$\omega_1 = 130°/s = 2.2689 \; rad/s \qquad (43)$$
$$\omega_2 = 130°/s = 2.2689 \; rad/s \qquad (44)$$
$$\omega_3 = 130°/s = 2.2689 \; rad/s \qquad (45)$$

Angular accelerations ε_n, will be determined (Table 8), knowing that $t_{acc/fr} = 0.5s$:

$$\varepsilon_n = \frac{\omega_n}{t_{acc/fr}} \qquad (46)$$

Table 8. The values of $\varepsilon_n[rad/s^2]$

ε_1	ε_2	ε_3
4.5378	4.5378	4.5378

The angular accelerations, centrifugal forces, and tangential forces caused by the motion in couple n are as follows:

$$atg_{n,n+a} = \varepsilon_n \cdot Rc_{n,n+a} \cdot 10^{-3} \tag{47}$$
$$Fcf_{n,n+a} = m_{n+a} \cdot Rc_{12} \cdot 10^{-3} \tag{48}$$
$$Ftg_{n,n+a} = m_2 \cdot atg_{n,n+a} \tag{49}$$

The following were thus determined: $atg_{n,n+a}, Fcf_{n,n+a}, Ftg_{n,n+a}$ (Table 9).

Table 9. The values of $atg_{n,n+a}, Fcf_{n,n+a}, Ftg_{n,n+a}$

$atg_{n,n+a}[m/s^2]$	$Fcf_{n,n+a}[N]$	$Ftg_{n,n+a}[N]$
$atg_{12} = 0.49$	$Fcf_{12} = 66.63$	$Ftg_{12} = 302.35$
$atg_{13} = 3.62$	$Fcf_{13} = 247.76$	$Ftg_{13} = 1124.76$
$atg_{14} = 5.33$	$Fcf_{14} = 279.58$	$Ftg_{14} = 1268.69$
$atg_{15} = 10.51$	$Fcf_{15} = 206.37$	$Ftg_{15} = 936.48$
$atg_{16} = 10.17$	$Fcf_{16} = 156.94$	$Ftg_{16} = 712.19$
$atg_{17} = 10.17$	$Fcf_{17} = 51.791$	$Ftg_{17} = 235.025$

Determine the values of the following force projections on the axes:
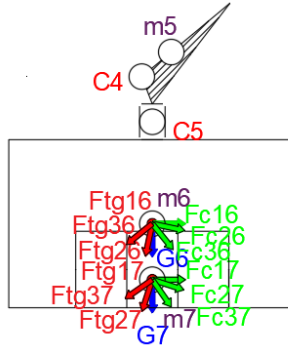
Figure 8. Representation of forces acting on the effector and the manipulated object.

•The projections of the forces acting on the effector (Figure 8) on the X-axis:

$$Fcf_{26}^x = Fcf_{26} \cdot cos(\alpha_{26} - 90°) \tag{50}$$
$$Fcf_{36}^x = Fcf_{36} \cdot cos(\alpha_{36}) \tag{51}$$
$$Ftg_{26}^x = Ftg_{26} \cdot cos(180° - \alpha_{26}) \tag{52}$$
$$Ftg_{36}^x = Ftg_{36} \cdot cos(180° - (90° + \alpha_{36})) \tag{53}$$
$$F_6^x = Fcf_{26}^x + Fcf_{36}^x + Ftg_{26}^x + Ftg_{36}^x + Fcf_{16}^x \tag{54}$$

•The projections of the forces acting on the manipulated object (Figure 8) on the X-axis:

$$Fcf_{27}^x = Fcf_{27} \cdot cos(\alpha_{27} - 90°) \tag{55}$$
$$Fcf_{37}^x = Fcf_{37} \cdot cos(\alpha_{37}) \tag{56}$$
$$Ftg_{27}^x = Ftg_{27} \cdot cos(180° - \alpha_{27}) \tag{57}$$
$$Ftg_{37}^x = Ftg_{37} \cdot cos(180° - (90° + \alpha_{37})) \tag{58}$$
$$F_7^x = Fcf_{27}^x + Fcf_{37}^x + Ftg_{27}^x + Ftg_{37}^x + Fcf_{17}^x \tag{59}$$
$$F_{RED}^X = F_6^x + F_7^x \tag{60}$$

•The projections of the forces acting on the effector (Figure 8) on the Z-axis:

$$Fcf_{26}^z = Fcf_{26} \cdot cos(\alpha_{26}) \tag{61}$$
$$Fcf_{36}^z = Fcf_{36} \cdot cos(90° - \alpha_{36}) \tag{62}$$
$$Ftg_{26}^z = Ftg_{26} \cdot cos(90° - \alpha_{26}) \tag{63}$$
$$Ftg_{36}^z = Ftg_{36} \cdot cos(\alpha_{36}) \tag{64}$$
$$F_6^z = Fcf_{26}^z - Fcf_{36}^z - Ftg_{26}^z - Ftg_{36}^z - G_6 \tag{65}$$
$$Fcf_{27}^z = Fcf_{27} \cdot cos(\alpha_{26}) \tag{66}$$
$$Fcf_{37}^z = Fcf_{37} \cdot cos(90° - \alpha_{36}) \tag{67}$$
$$Ftg_{27}^z = Ftg_{27} \cdot cos(90° - \alpha_{26}) \tag{68}$$
$$Ftg_{37}^z = Ftg_{37} \cdot cos(\alpha_{36}) \tag{69}$$
$$F_7^z = Fcf_{27}^z - Fcf_{37}^z - Ftg_{27}^z - Ftg_{37}^z - G_7 \tag{70}$$
$$F_{RED}^z = F_6^z + F_7^z \tag{71}$$

•The projections of the forces acting on the effector and on the manipulated object (Figure 8) on the Y-axis:

$$F_6^y = -Ftg_{16} \tag{72}$$
$$F_7^y = -Ftg_{17} \tag{73}$$
$$F_{RED}^y = F_6^y + F_7^y \tag{74}$$

Thus the forces acting on the effector and on the manipulated object were determined (Table 10).

Table 10. The values of forces actiong on the effector / manipulated object

Forces acting on X[N]	Forces acting on Z[N]	Forces acting on Y[N]
$Fcf_{26}^{x} = 135,88$	$Fcf_{26}^{z} = -28.88$	$F_{6}^{y} = -712.19$
$Fcf_{36}^{x} = 78.58$	$Fcf_{36}^{z} = 97.04$	$F_{7}^{zy} = -235.025$
$Ftg_{26}^{x} = 131.06$	$Ftg_{26}^{z} = 616.62$	$F_{RED}^{y} = -947.22$
$Ftg_{36}^{x} = 440.35$	$Ftg_{36}^{z} = 356.59$	
$F_{6}^{x} = 942.83$	$F_{6}^{z} = -1785.84$	
$Fcf_{27}^{x} = 44.84$	$Fcf_{27}^{z} = -9.806$	
$Fcf_{37}^{x} = 25.96$	$Fcf_{37}^{z} = 35.17$	
$Ftg_{27}^{x} = 66.11$	$Ftg_{27}^{z} = 209.27$	
$Ftg_{37}^{x} = 168.26$	$Ftg_{37}^{z} = 129.26$	
$F_{7}^{x} = 356.97$	$F_{7}^{z} = -610.14$	
$F_{RED}^{X} = 1299.81$	$F_{RED}^{Z} = -2395.98$	

Thus the axial (F_A) and radial (F_R) forces are:

$$F_A = F_{RED}^{z} \tag{75}$$

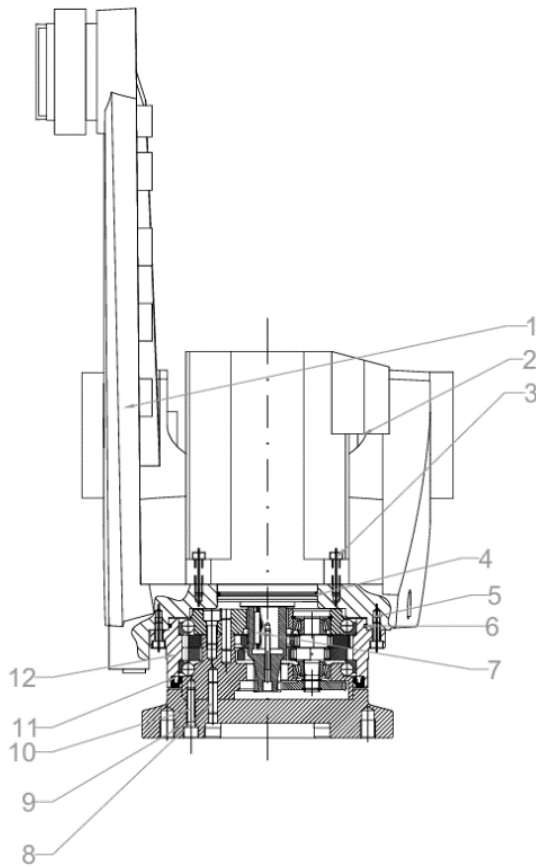$$F_R = \sqrt{{F_{RED}^{X}}^{2} + {F_{RED}^{Y}}^{2}} \tag{76}$$

The resulting moments resulting from the rotations in the pairs are:

$$M_{RED}^{X} = F_{7}^{Y} \cdot LG_7 \cdot 10^{-3} + F_{6}^{Y} \cdot LG_6 \cdot 10^{-3} \tag{77}$$
$$M_{RED}^{Y} = F_{7}^{X} \cdot LG_7 \cdot 10^{-3} + F_{6}^{X} \cdot LG_6 \cdot 10^{-3} \tag{78}$$
$$M_{REDUS} = 843.98 \, N \tag{79}$$

Following these calculations, the RV-40E gearbox from Nabtesco's catalog and the 9C1.1.60 actuator servomotor model, from ABB's catalog for numerically controlled axis 4 were chosen (Figure 9).

Figure 9. Sectional view of numerically controlled axis 4 where: 1 — ACN 4 housing; 2 — ACN 4 motor; 3— M6x30 screw; 4 — O-ring; 5— M6x20 screw; 6 — O-ring, 7 — Keyway; 8 — Threaded pin M8x20; 9 — Flange; 10 — M8x25 Screw; 11 — Shaft seal; 12 — RV-40E -105 Gearbox

Meanwhile, the calculus algorithm can also be employed for the same purpose in other IR models that have a similarly designed end-effector orientation subsystem.

4. Conclusion

This paper addresses two current approaches in the development of new pallet cells: the use of a prefabricated pallet cell and the design of a customized pallet cell optimized for the management of gravitational and inertial forces. It also lays the foundations for an improved model of a custom-designed palletizing cell tailored to optimize the kinematics of the structure **[7]**.

The second part of the paper focuses on a specialized algorithm developed for optimal motor selection in industrial robots used in palletizing applications. The detailed computational procedure presented in the paper is applied to various models of industrial robots, ensuring optimal motor selection, taking into account the gravitational and inertial forces inherent to palletizing operations. In addition, the applicability of the algorithm extends to similar robot models with comparable end-effector orientation subsystem designs. Rigorous testing of the proposed algorithm validated its effectiveness on several industrial robot models analyzed in this study.

References

1. G. Gamazeliuc, O. Ulerich, E. Rolea, M. Mărgăritescu, *Implementation of Human-Robot Interaction Through Hand Gesture Recognition Algorithms*, International Conference on Reliable Systems Engineering (ICoRSE) - 2023, D.D. Cioboată, Ed., Cham: Springer Nature Switzerland, 2023, pp. 147–154. doi: 10.1007/978-3-031-40628-7_12.
2. B.M. Verdete, C. Pupăză, G. Alexandru, Reduced order model for evaluating the temperature gradients of the surfacing weld process, *RRIA*, 33(1), pp. 7–20, Mar. 2023, doi: 10.33436/v33i1y202301.
3. IRB 660, M2004, Product specification. Accessed: Jul. 16, 2024. [Online]. Available: https://search.abb.com/library/Download.aspx?DocumentID=3HAC023932-001&LanguageCode=en&DocumentPartId=&Action=Launch
4. M.-A. Stamate, A.-F. Nicolescu, C. Pupază, Mathematical model of a multi-rotor drone prototype and calculation algorithm for motor selection, *Proceedings in Manufacturing Systems*, 12(3), 2017, pp. 119–128.

5. C.G. Coman, A.F. Nicolescu, C.A. Cristoiu, Calculus algorithm for evaluation of gravitational and inertial loads acting on a 6 dof articulated arm type industrial robot, *Proceedings in Manufacturing Systems*, 12(4), 2017, pp.187-194.
6. C. Dumitrașcu, F.A. Nicolescu, C.A. Cristoiu, Optimized overall design of a robotic arc welding cell and calculation procedures for optimal selection of ir motors, *Proceedings in Manufacturing Systems,* 16(2), 2021, pp. 75-88.
7. A.M. Ivan, A.F. Nicolescu, G.C. Avram, L Stan, Robotic deburring cell virtual prototyping, *Proceedings in Manufacturing Systems,*10(4), 2015, pp. 183-188.

Addresses:

- Roxana-Mariana Nechita, National Institute of Research and Development in Mechatronics and Measurement Technique, Bucharest, Romania roxana.nechita2000@gmail.com
  (*corresponding author*)
- Cozmin Cristoiu, National University of Science and Technology Politehnica Bucharest, Faculty of Industrial Engineering and Robotics, Bucharest, Romania, Cozzy Technologies SRL Pitesti, Romania cozmin.cristoiu@upb.ro
- Mihai Mărgăritescu, National Institute of Research and Development in Mechatronics and Measurement Technique, Bucharest, Romania, mihai.margaritescu@gmail.com

Predictive control of an induction machine drive system for field-weakening regime

Elena Selim* ⓘD, Ion Voncilă ⓘD

Abstract. *In this paper is studied the model predictive control (MPC) of an induction machine (IM) drive for wakening applications. The control structure is implemented in Matlab software. The predictive control law is based on finite set combinations imposed by the two-level inverter topology. The study developed for field-wakening regime shows that the speed tracking objective remains stable despite stator resistance variation. Also, the load torque disturbance rejection is efficiently done to evaluate un unrated parameter. Thus, the operation of the IM drive with MPC law is robust on the sensitivity of parameters of the model.*

Keywords*: induction machine (IM), model predictive control (MPC), Matlab software, speed response, load torque rejection.*

1. Introduction

In recent years, induction machine (IM) has become the most popular solution for medium and high power fields applications. Having a simple, robustness, and cheap structure, IM is largely used in industrial and residential applications for a large variety of electrical drives: electrical traction, motion system, electrical propulsion, special applications.

The IM drives powered directly from electrical grid, have a limited area of applications, usually in pumps, mils and some domestic areas that does not require high performances. More advanced features aroused once with IM drives supplied by power invertors [1] together with field oriented control (FOC). Thus, the magnitude and frequency of voltage are independently controlled which make the possibility to obtain new benefits on IM drive operation [2]: large range of speed and torque, field-weakening, constant torque mode operation, constant torque regime and constant power mode.

Although the classical PI linear controllers become a certainty in the IM industrial application, there are also several limitations [1-3]: non-optimal control law, difficulties in constraints imposing and low robustness on the variation of plant parameters.

To overcome the above-mentioned drawbacks, a high-performance strategy based on IM model is developed. The model predictive control (MPC) has the ability to improve the classical results. There are two types of MPC methods, with continuous set control (CSC) and finite set control (FSC). The MPC – CSC starting for large industrial plant [4-5] and requires advanced mathematical algorithm and wide amount of hardware resources. In the recent years, the increasing of the computational effort make possible the MPC – CSC control law implementation of the IM drive [6-7]. However, the MPC – CSC strategy requires a frequency modulator for command synthesis. A last iteration is the MPC strategy with finite set control (FSC) which gives an optimal control obtained by an optimal switching states combinations of the electronic power inverter of the IM drive system [8-9]. In the rest of the paper, the MPC strategy discussed is MPC – FSC, being simply replaced by MPC.

In the paper is proposed a MPC control of an IM drive for field-weakening applications. For this aim, when the mechanical speed exceeds the base speed, the magnetic flux reference will decrease. The MPC control used for controlling flux and speed has a multivariable structure being developed for state-space representation. A case study developed in Matlab software will illustrate the effectives of the presented study.

The rest of the paper is organized as follows. In the second section is presented the IM model in a stationary system reference frame. The MPC strategy for IM cascade structure is developed in the third section. A case study approached in Matlab software simulation environment is discussed in section four. Finally, in section fourth are summarized the main benefits of the study of the paper.

2. IM mathematical modelling

The IM control model represented in a fixed system reference frame (α, β) is obtained by starting from stator and rotor voltages equations, respectively, as follows [8]:

$$u_{s\alpha} = R_s i_{s\alpha} + \frac{d\psi_{s\alpha}}{dt},$$

(1)

$$u_{s\beta} = R_s i_{s\beta} + \frac{d\psi_{s\beta}}{dt},$$

(2)

$$0 = R_r i_{r\alpha} + \frac{d\psi_{r\alpha}}{dt} + p_b \omega \psi_{s\beta},$$

(3)

$$0 = R_r i_{r\beta} + \frac{d\psi_{r\beta}}{dt} - p_b \omega \psi_{s\alpha} \; , \tag{4}$$

where the involved magnetic flux is:

$$\psi_{s\alpha} = L_s i_{s\alpha} + L_m L_{r\alpha} \; , \tag{5}$$

$$\psi_{s\beta} = L_s i_{s\beta} + L_m L_{r\beta} \; , \tag{6}$$

$$\psi_{r\alpha} = L_r i_{r\alpha} + L_m L_{r\alpha} \; , \tag{7}$$

$$\psi_{r\beta} = L_r i_{r\beta} + L_m L_{r\beta} \; . \tag{8}$$

The motion equation is described by:

$$\tau - \tau_1 = J \frac{d\omega}{dt} \; , \tag{9}$$

with the electromagnetic torque relationship:

$$\tau = \frac{3}{2} p_b (\psi_{s\alpha} i_{s\beta} - \psi_{s\beta} i_{s\alpha}) \; . \tag{10}$$

In Eq. (1) – (10), the quantities involved has the next significance: $(u \, / \, i \, / \, \psi)_{\alpha / \beta}$ are the stator/rotor components of voltage, current and magnetic flux space vectors, (R_s, R_r) denotes the stator and rotor resistances, (L_s, L_r, L_m) are stator, rotor and magnetizing inductance, respectively, ω is the rotor speed, τ_1 represents the load torque, J is the rotor inertia, p_b is the number of magnetic stator pairs of poles.

Some important remarks may be done about this model.

By using the forward Euler discretization method, a first-order linear approximation method is obtained for a generic quantity x(t) as follows:

$$\left. \frac{dx(t)}{dt} \right|_{x=x[k+1]} = \frac{x[k+1] - x[k]}{T_e} \; , \tag{11}$$

where T_e is the sampling time period.

Taking into account the approximation (11) of the first derivative, from (1) – (8) are obtained the discrete flux equations:

$$\begin{bmatrix} \hat{\psi}_{s\alpha}(k) \\ \hat{\psi}_{s\beta}(k) \end{bmatrix} = \begin{bmatrix} \hat{\psi}_{s\alpha}(k-1) \\ \hat{\psi}_{s\beta}(k-1) \end{bmatrix} + T_e \begin{bmatrix} u_{s\alpha}(k) \\ u_{s\beta}(k) \end{bmatrix} - R_s T_e \begin{bmatrix} i_{s\alpha}(k) \\ i_{s\beta}(k) \end{bmatrix} \; , \tag{12}$$

$$\begin{bmatrix} \hat{\psi}_{r\alpha}(k) \\ \hat{\psi}_{r\beta}(k) \end{bmatrix} = \frac{L_r}{L_m} \begin{bmatrix} \hat{\psi}_{s\alpha}(k-1) \\ \hat{\psi}_{s\beta}(k-1) \end{bmatrix} + \begin{bmatrix} i_{s\alpha}(k) \\ i_{s\beta}(k) \end{bmatrix} + \left(L_m - \frac{L_s L_r}{L_m} \right) \; , \tag{13}$$

that were used for magnetic flux estimation.

Further, by applying (11) to (1) – (8) there are obtained the flux and current predictions in the discrete state-space representation:

$$\begin{bmatrix} \psi_{s\alpha}^{p}(k+1) \\ \psi_{s\beta}^{p}(k+1) \end{bmatrix} = \begin{bmatrix} \hat{\psi}_{s\alpha}(k) \\ \hat{\psi}_{s\beta}(k) \end{bmatrix} + T_e \begin{bmatrix} u_{s\alpha}(k) \\ u_{s\beta}(k) \end{bmatrix} - R_s T_e \begin{bmatrix} i_{s\alpha}(k) \\ i_{s\beta}(k) \end{bmatrix},$$ (14)

$$\begin{bmatrix} i_{s\alpha}^{p}(k+1) \\ i_{s\beta}^{p}(k+1) \end{bmatrix} = \left(1 + \frac{T_s}{T_t}\right) \begin{bmatrix} i_{s\alpha}(k) \\ i_{s\beta}(k) \end{bmatrix} + \frac{T_s}{T_t + T_s} \left\{ \frac{1}{R_t} \begin{bmatrix} \frac{k_r}{T_r} \begin{bmatrix} \hat{\psi}_{s\alpha}(k) \\ \hat{\psi}_{s\beta}(k) \end{bmatrix} \\ + k_r \omega \begin{bmatrix} \hat{\psi}_{s\alpha}(k) \\ -\hat{\psi}_{s\beta}(k) \end{bmatrix} + \begin{bmatrix} u_{s\alpha}(k) \\ u_{s\beta}(k) \end{bmatrix} \end{bmatrix} \right\},$$ (15)

where the used group of constants are:

$$T_s = \frac{L_s}{R_s}; T_r = \frac{L_r}{R_r}; k_s = \frac{L_m}{L_s}; k_r = \frac{L_m}{L_r}$$

$$T_t = \left(1 - \frac{L_s}{L_r}\right) \frac{L_s}{R_t}; R_t = R_s + R_r k_r^2$$ (16)

Finally, based on previous flux and current prediction (15) – (16), there is obtained the one-step-ahead prediction of electromagnetic torque:

$$\tau^{p}(k+1) = \frac{3}{2} p_b (\psi_{s\alpha}^{p} i_{s\beta}^{p} - \psi_{s\beta}^{p} i_{s\alpha}^{p})$$ (17)

3. Predictive control of IM

In the operation of IM drive, the power electronic inverter has an important role, ensuring the derived voltages required for meeting the high performances.

A typical power inverter structure with two voltage levels is depicted in Fig. 1. The command on the same leg of inverter is negated through an inverter.

The scope of the MPC algorithm is to find a direct command, without a frequency modulator, which is included in the finite set of all possible combinations of the switching states of the power inverter.

A common method using power inverter modeling is based on switching functions, that are associated to each phase and leg of the inverter:

$$\mathbf{S}_a = \begin{cases} 1, & if \quad S_1 \equiv on \quad and \quad S_4 \equiv off \\ 0, & if \quad S_1 \equiv off \quad and \quad S_4 \equiv on \end{cases},$$ (18)

$$\mathbf{S}_b = \begin{cases} 1, & if \quad S_2 \equiv on \quad and \quad S_5 \equiv off \\ 0, & if \quad S_2 \equiv off \quad and \quad S_5 \equiv on \end{cases}, \tag{19}$$

$$\mathbf{S}_c = \begin{cases} 1, & if \quad S_3 \equiv on \quad and \quad S_6 \equiv off \\ 0, & if \quad S_3 \equiv off \quad and \quad S_6 \equiv onf \end{cases}, \tag{20}$$

where $\{\mathbf{S}_a, \mathbf{S}_b, \mathbf{S}_c\}$ are the set switching state corresponding to each phase, while $S_i, i = 1, 6$ is the state corresponding to each electronic device of power electronic inverter.
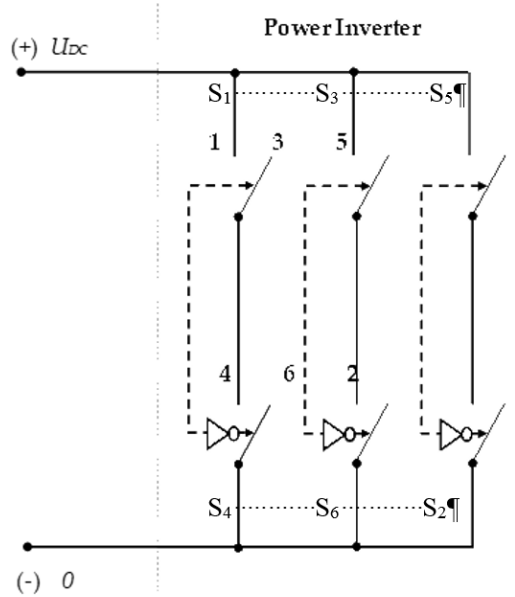
Figure 1. The two-level power inverter topology.

Based on the switching function of legs of the inverter, a space vector switching function may be defined:

$$\mathbf{S} = \frac{2}{3}(S_a + \mathbf{a}S_b + \mathbf{a}^2 S_c), \tag{21}$$

where $\mathbf{a} = -1/2 + j\sqrt{3}/2$ is the rotational operator used for the three-phase coordinate representation.

The output voltage of the power inverter results as a function of DC link voltage U_{DC}:

$$u_{s,anc} = U_{DS}\mathbf{S}, \tag{22}$$

where U_{DS} is the Direct Current link voltage.

The MPC control law is formulated as an optimization problem which found the best switching function combination [8]:
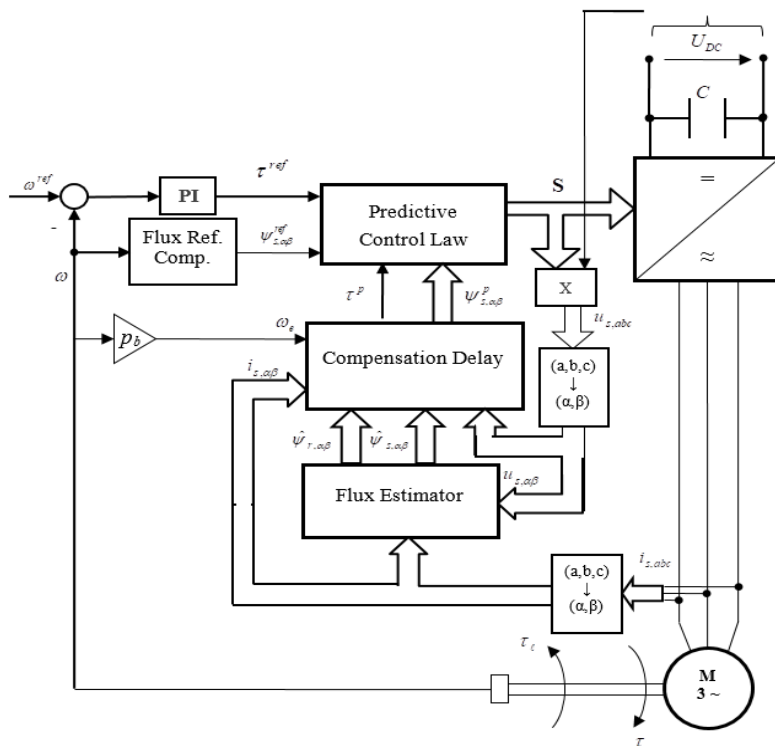
$$\min_{\mathbf{S}} g(\mathbf{S})$$

$$s.t.: \quad g = \left\| \tau^{ref} - \tau^p(k+1) \right\| + \delta_\psi \left\| \psi_s^{ref} - \psi_{s,\alpha\beta}^p(k+1) \right\|, \tag{23}$$

where δ_ψ is the flux weight factor.

The stator magnetic flux reference is selected to have a constant value or to decreasing, depending on the mechanical speed range:

$$\psi_s^{ref} = \begin{cases} \psi_{sN}, & \|\omega\| \le \omega_n \\ \psi_{sN} \dfrac{\omega_n}{\|\omega\|}, & \|\omega\| > \omega_n \end{cases} \tag{24}$$

The block scheme of the IM cascade MPC structure is depicted in Fig. 2. The IM is supplied by a power electronic inverter from Fig. 1.

Figure 2. The two-level power inverter topology.

37

The inner loop of the cascade structure is designed for controlling both magnetic flux and electromagnetic torque by a MPC space-state multivariable controller according to (23).

To obtain a fast speed response, the outer loop is designed via a classical PI controller by classical pole placement method [3].

The structure is developed in the coordinates (α, β), and for ensuring the compatibility of $\alpha\beta$ model with the natural abc model, there are used coordinates transformations as it is shown in Fig. 2.

At last, the MPC law requires the knowledge of DC-link voltage U_{DC} of the power inverter that is considered constant on the entire operation domain.

4. Simulation results

In the previous section has been established the IM control law for a cascade structure. To prove the performances above mentioned in MPC IM control structure, it is considered a case study for an IM with the parameters given by Table 1.

Table 1. IM model parameters

| No.	Quantity	Symbol	Value	Unit
1.	Stator resistance	R_s	1.2	Ω
2.	Rotor resistance	R_r	1	Ω
3.	Stator inductance	L_s	175e-3	H
4.	Rotor inductance	L_r	175e-3	H
5.	Magnetizing inductance	L_r	175e-3	H
6.	Rotor inertia	J	0.063	kg·m^2

The discretizing process of the MPC algorithm is accomplished with the time sampling period $T_s = 4e-5$.

A speed stairs-steps profile of speed reference is adopted, with operation, at starting for 1 second in no-weakening regime, and then for 1 second in weakening regime, and finally return for 1 second in no-weakening, as depicted in Fig. 3. The study considers the results obtained for the rated value of stator resistance R_s and for a stator resistance value equal to R_s·1.2 which can often appear in practice. It can be easily observed from Fig. 3 that, for rated conditions, the MPC control presents acceptable speed response. In the case of stator resistance variation, the setting time of speed is increased and, supplementary appear unwanted variations. For the IM

drive, it is applied a step load torque $\tau_1 = 2Nm$. Compared with electromagnetic torque obtained in rated conditions, in case of stator resistance variation, the electromagnetic torque presents a slow fluctuation and an unwanted dynamic component, as illustrated in Fig. 4. Overall, we can appreciate that MPC control law remains robust on speed response despite unwanted electromagnetic torque variations. However, the rejection of the load torque disturbance is efficiently done.
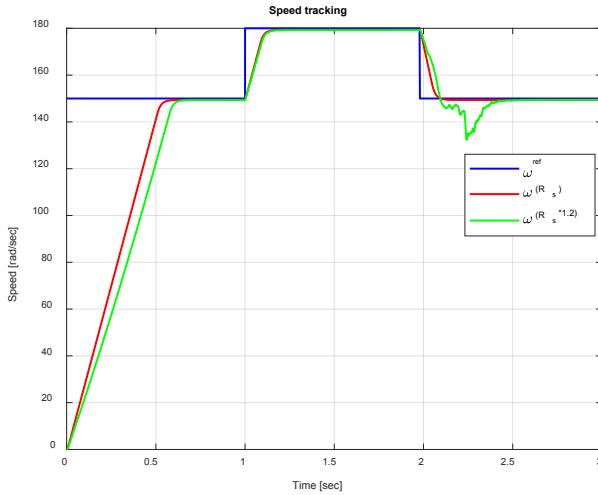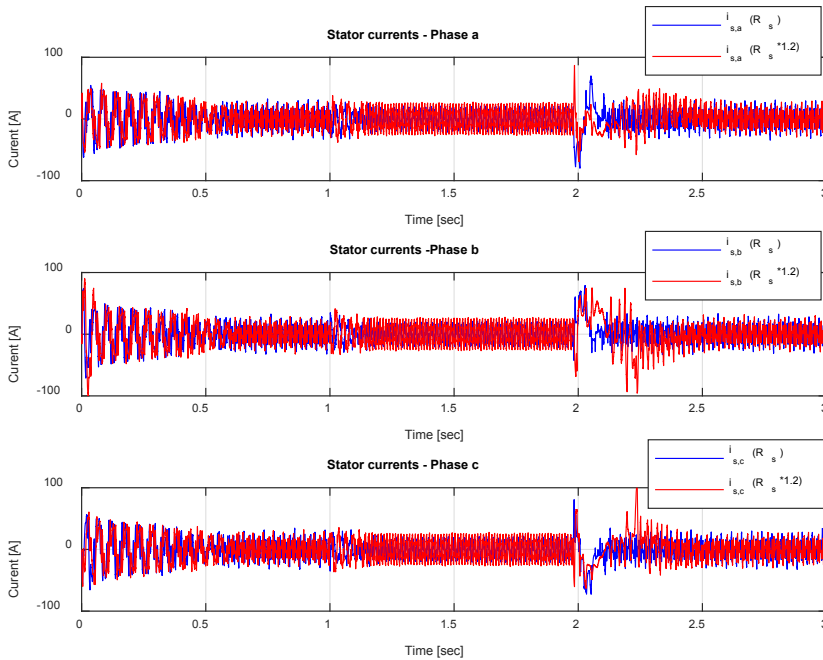

Figure 3. Speed responses of IM drive.
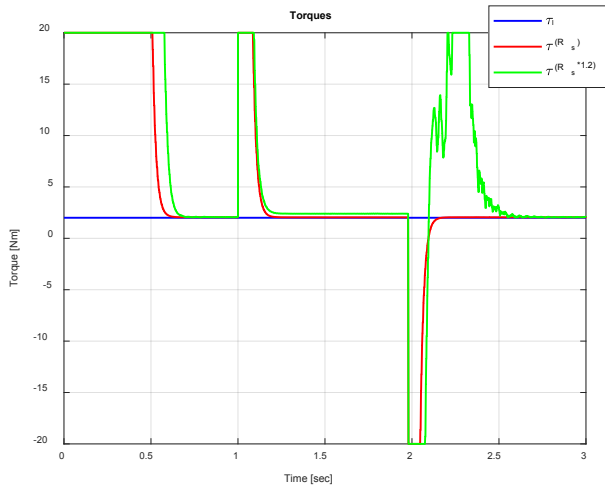
Figure 4. Load and electromagnetic torques.

The stator phase currents are depicted in Fig. 5. It is clearly that, in steady-state regime, they are insignificant. In dynamic regime there are increased peak values as a consequence of stator resistance modifications.

Figure 5. Stator phase currents.

5. Conclusions

The MPC control strategy is a high-performance control law that ensures reliable results for advanced IM drives. Compared with the classical linear controller PI, the MPC law presents an optimal law implemented without modulator of frequency, the power electronic inverter being taking into account for designing the optimal control law.

High speed tracking results and load torque disturbance rejection of IM has been proven by simulation in both field-wakening regime and up to rated speed situations.

A robust feature of the MPC law has been also shown at stator resistance variation, and it is important to highlight that the operation remains stable in this case that occurs in practical situation. The speed and phase currents present acceptable differences, which show the robust feature of the MPC advance control strategy.

References

1. I. Boldea, S.A. Nasar, *The Induction Machine Design Handbook*, Second Edition, CRC Press Publishing House, 2009.
2. I. Boldea, S.A. Nasar, *Electric Drives,* Second Edition, CRC Press Publishing House, 2005.
3. K.J. Astrom, B. Wittenmark, *Computer-Controlled Systems: Theory and Design*, 3rd ed., Prentice Hall, 1997.
4. D.W. Clarke, C. Mohtadi, P.S. Tuffs, Generalized Predictive Control. Part I*, Automatica,* 23(2), 1987, pp. 137–148.
5. D.W. Clarke, C. Mohtadi, P.S. Tuffs, Generalized Predictive Control. Part II. Extensions and Interpretations, *Automatica*, 23(2), 1987, pp. 149–160.
6. M. Costin, C. Lazar, *Predictive dq Current Control of an Induction Motor,* 2021 25th International Conference on System Theory, Control and Computing (ICSTCC), Oct. 20-23, 2021, Sinaia, Romania, pp. 637- 642.
7. M. Costin, C. Lazar, Induction Motor Improved Vector Control using Predictive and Model-Free Algorithms together with Homotopy-Based Feedback Linearization, *Energies*, 17, 875, 2024.
8. J. Rodriguez, P. Cortes, *Predictive Control of Power Converters and Electrical Drives*, Wiley Publishing House, 2012.
9. M. Costin, Implementation Issues for One-Step-Ahead Predictive Control of an Induction Machine, 2020, *Bul. Inst. Polit. Iaşi,* 66(70), 1, 2020, pp. 73-87.

Addresses:

- Lect. Dr. Eng. Elena Selim, „Dunărea de Jos "University of Galați, Faculty of Automation, Computers, Electrical and Electronics Engineering, Str. Științei, nr. 2, 800146, Galați, România elena.selim@ugal.ro
  (*corresponding author*)
- Conf. Dr. Eng. Ion Voncilă, „Dunărea de Jos "University of Galați, Faculty of Automation, Computers, Electrical and Electronics Engineering, Str. Științei, nr. 2, 800146, Galați, România
  ion.voncila@ugal.ro

Performance of 32kb/s ADPCM for data transmission

Muhanned AL-Rawi ⓘ

Abstract. *This study introduces a brand-new modified QAM modem that transmits data at a rate of 14.4 kbps over a 32 kbps Adaptive Differential Pulse Code Modulation (ADPCM) channel. This modified QAM modem's goal is to lessen the nonlinear distortion that ADPCM introduces. The effectiveness of ADPCM is investigated using modified and regular QAM modems with various constellations. The simulation findings demonstrate that ADPCM performs better when using a customized QAM modem than when using a normal QAM modem. Additionally, a circular constellation performs better than a rectangular one.*

Keywords*: Data transmission, QAM modem, 32 kbps ADPCM.*

1. Introduction

Different sorts of extremely effective speech coding techniques have been developed in response to the growing demand for efficient use of digital communication channels. Adaptive Differential Pulse Code Modulation (ADPCM) is one of these coding techniques that was standardized by the International Telecommunication Union (ITU; formerly known as the International Telephone & Telegraph Consultative Committee (CCITT)) as recommendation G726 [1]. The main reasons for choosing ADPCM over alternative bandwidth reduction approaches were its superior performance, economics, and application flexibility.

ADPCM's standard makes a wide range of applications in telecommunication networks possible. Three groups can be made of these applications: ones for telephone companies, ones for end users, and ones for brand-new services. The most recent ADPCM applications [2–5], which are explained briefly below.

A packet loss concealing scheme using an ADPCM codec and a packet loss compensation (PLC) circuit is presented in [2]. The method establishes a predetermined transition period between the correct signal and a replacement signal, and the difference

between the replacement signal and a computed prediction signal is combined with a dequantized prediction error to produce a dequantized combined prediction error that is added to a predicted signal to produce a combined transition signal as the basis for an output signal throughout the predetermined transition period for adjusting all decoder parameters. According to one implementation, the error combiner circuit has an analysis filterbank at one input for downsampling the replacement signal received from the PLC circuit into subband signals and an adaptive dequantization unit at another input.quantization unit for the prediction error that the ADPCM decoder receives after being quantized, downsampled, and encoded. One of the two outputs of an adaptive prediction unit is connected to a subtractor, which receives the subband substitution signal from the analysis filterbank, while the other output is connected to an adder. The output of the adder has a feedback loop to the adaptive prediction unit and leads to a synthesis filterbank for recombining the combined subband substitute signals to gain an output signal. A concealment prediction error shaper is connected to the output of the adaptive dequantization unit between the subtractor and the adder. A weighted sum of the dequantized prediction error and the prediction error of the concealment prediction error shaper is created in a predetermined way.

A method for coordinating an encoder and a decoder in a wireless communication system using discontinuous transmission was developed in [3]. The method involves giving the encoder and the decoder a syncless reset command to put them in stable and compatible states. The syncless reset command can be executed by either performing a conventional reset command followed by the encoding or decoding of a predefined number of predetermined sample values, or by setting the variables of the encoder and decoder into prepared values. In a communication system that uses discontinuous transmission, one aspect of the disclosure relates to a method for coordinating an ADPCM-based encoder in the transmitting unit and an ADPCM-based decoder in the receiving unit after a period of silence. The method includes: the encoder performing a first syncless reset operation after receiving audio data; the encoder using the audio data and the decoder performing a second syncless reset operation; the encoder operating on the audio data; the transmitting unit transmits the content of the buffer of samples; the receiving unit receiving the content of the buffer of samples; and the decoder decoding the received content.

A device that separates a sampled sound signal into a high frequency signal and a low frequency signal, individually encrypts each signal, and generates error detection code specific to the high frequency ADPCM data and the low frequency ADPCM data was developed in[4]. The device transmits the error detection code in place of data applicable to some of the multiple bits used to configure the low frequency ADPCM data. The high frequency ADPCM data and the low frequency ADPCM data are received by a receiver side, which then individually processes each set of data in accordance with the error detection code value. The current invention proposes

a wireless wideband voice. An error detection code is delivered after replacing some low range ADPCM data bits, and it is used to analyze voice communication, high frequency ADPCM data, and low frequency ADPCM data separately. A fixed-size packet can therefore retain wideband sound quality even in poorer connectivity settings without affecting the sound's data rate.

The shape of encoding noise during the ADPCM encoding of a digital audio input signal is controlled using a technique and equipment in [5]. Through the use of feedback, which includes noise filtering, noise is shaped. The process consists of the following steps: obtaining a parameter to indicate a high spectral dynamic range of the signal, the parameter indicating a risk of feedback instability; detecting a risk of instability by comparing the indication parameter to at least one predetermined threshold; limiting the feedback in the event that a risk of instability is detected; and gradually reactivating the feedback over a predetermined number of frames after the current frame for which the feedback is limitedA feedback encoder with a control module that uses the described control mechanism is also offered. As a result, the method enables quick and accurate detection of potentially troublesome signals that run the risk of causing feedback instability phenomena. As a result, this occurrence is prevented because the feedback is limited as soon as these risky signals appear. Even total deletion of this feedback may constitute this restriction. Therefore, the technique acts as a preventative measure against the emergence of problematic events. After that, the feedback loop is gradually activated so as not to cause the coded signals to change in an unnaturally abrupt way.

The primary issue with ADPCM is that, even at high data rates, it adds significant nonlinear distortion to the voiceband data signal. This issue can be resolved either by changing the ADPCM algorithm [6–9] or the model of the data transmission system [10–12].

2. Structure of ADPCM

The 32 kb/s ADPCM algorithm used in this document is the same as that in CCITT G.726 [1]. ADPCM codec's simplified block diagram is shown in Fig. 1. The algorithm is made up primarily of two elements: an adaptive quantizer and an adaptive predictor. Also shown is the relationship between the encoder and the decoder. The encoder has an adaptive quantizer (Q) and an inverse adaptive quantizer (Q-1) which makes a distinction between them. In contrast, the decoder merely features an inverse adaptive quantizer. The decoder merely transmits $r(n)$ as opposed to $c(n)$ as its output. It is a subset of the encoder. The two poles and six zeros of the adaptive predictor compute an input signal estimate, or (n), which is then subtracted from the input signal, or $s(n)$, to produce a difference signal, or $d(n)$. The transmission facility converts

d(n) into the 4-bit codeword c(n), which is then transferred. An ADPCM decoder employs c(n) to try to reconstruct the original signal s(n) at the receiving end. Actually, only r(n), which is connected to the initial input signal s(n), may be recovered as follows:

$$r(n) = s(n) + e(n) \tag{1}$$

where

$$e(n) = dq(n) \quad d(n) = r(n) \quad s(n) \tag{2}$$

is the error introduced by the quantizer, and dq(n) is the output of inverse adaptive quantizer.
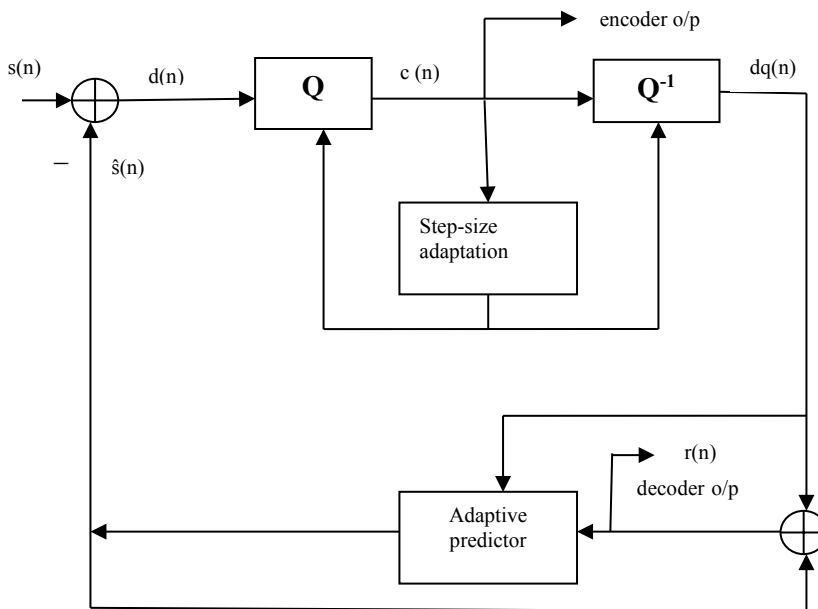
Figure 1. ADPCM Codec

A typical measure of the ADPCM performance is given by signal-to-noise ratio (SNR)

$$SNR= E[s^2(n)]/E[e^2(n)] = \sigma_s^2/ \sigma_e^2 \tag{3}$$

Where E denotes expectation, σ_s^2 is the power (or variance) of input signal, & σ_e^2 is the power (or variance) of the error signal.

3. Standard and modified modem

When trellis coding is removed, the conventional QAM modem V.32 bis [13] works at a symbol rate of 2400 baud with a six-bit representation for each symbol, giving it a data rate of 2400x6=14.4 kb/s. The M-ary QAM constellation contains 64 points total, or 26 points. In order to lessen the impact of channel noise and the distortion of ADPCM, the QAM constellation design is crucial. Fig. 2 depicts some of the 64-point, rectangular, and (6,12,19,27) circular constellations that are taken into consideration in this article. Parts of rectangular and circular constellations are drawn due to symmetry.

The modified QAM modem runs at a symbol rate of 2880 baud with a five-bit representation for each symbol (trellis coding is removed), providing a data throughput of 2880x5=14.4kb/s with a 25=32-point constellation. Fig. 3 displays some 32-point constellations, including circular, rectangular, and (4,11,17), and (5,11,16).

4. Model of data transmission

The data transmission model used to assess the effectiveness of ADPCM is shown in Fig. 4. There are four pieces to this model. Each 6-bit/5-bit of binary data is mapped into one of the 64-point or 32-point QAM constellations in the first component, which is a random data generator. The second component is a QAM transmitter with a symbol output speed of 2400/2880 baud and a data rate of 2400 6 bits 2880 5 bits 14.4 kb/s. The third component is an ADPCM codec that has an input (s(n)) and an output (r(n)) for calculating the SNR specified in Eq. (3). The QAM receiver is the fourth component.

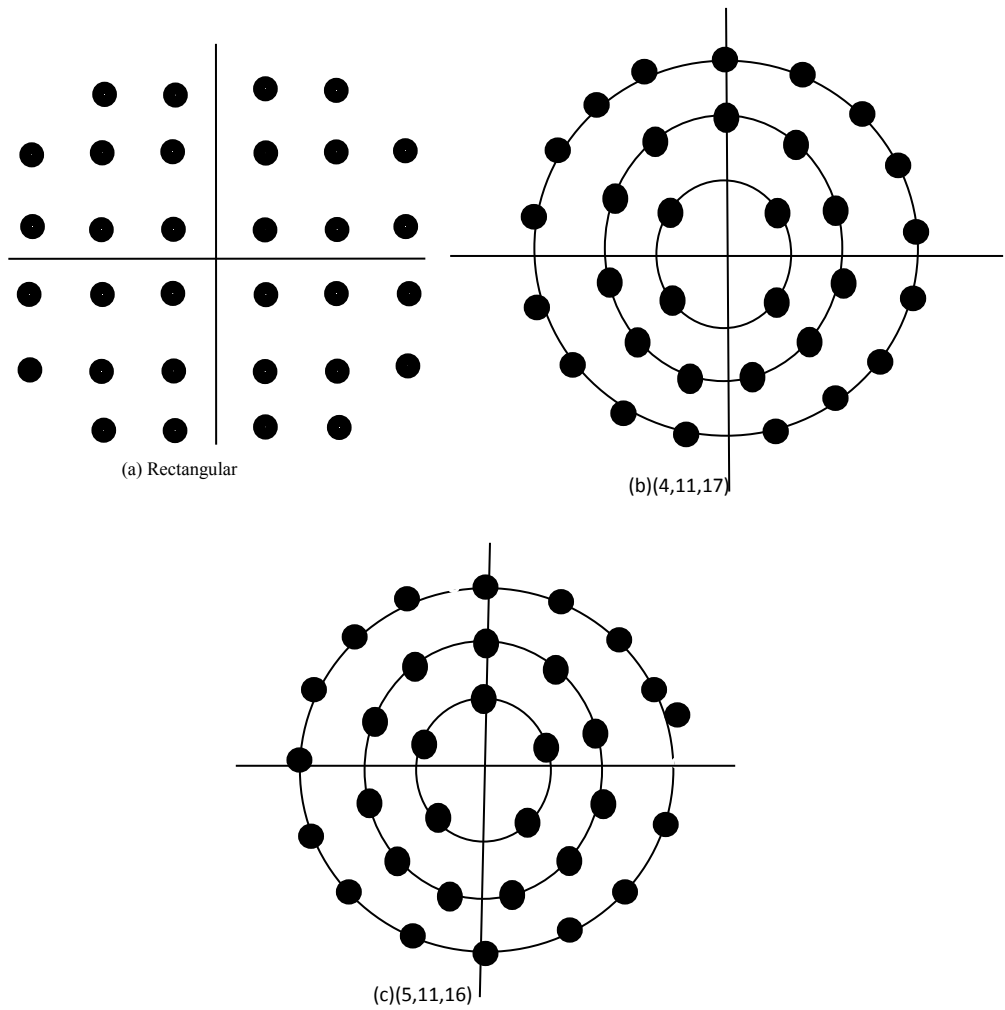## 5. Computer simulation test

ADPCM codec has been put through a number of computer simulation tests utilizing both standard and customized QAM modem signals at 14.4 kbps with the constellations seen in Figs. 2 and 3. SNR in equation 3 is used to determine ADPCM performance.
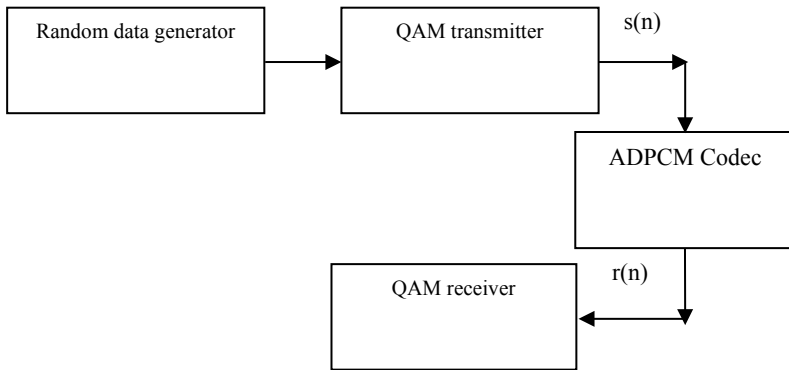
Rectangular

(b) (6,12,19,27)
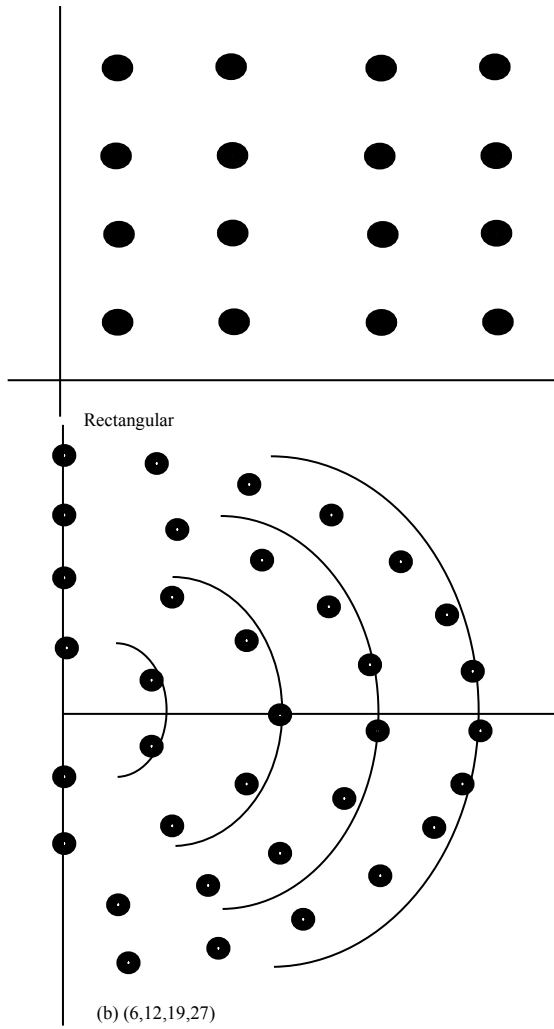
Figure 2. 64-ary QAM constellations

(a) Rectangular

(b)(4,11,17)

(c)(5,11,16)

Figure 3. 32-ary QAM constellations

Figure 4. Model of data transmission

Tables 1 and 2 display the outcomes of the ADPCM testing. ADPCM with a circular constellation performs somewhat better for regular modems by around 0.4 dB—than one with a rectangular constellation. ADPCM with a circular constellation performs somewhat better than one with a rectangular constellation for modified modems (by about 0.5 dB).

The performance of ADPCM with modified modem is superior to standard modem by roughly 0.9dB for rectangular constellation and 1dB for circular constellation, according to the comparison between them.

Table 1. Performance of ADPCM with standard QAM

	Standard QAM	
	Rect	(6,12,19,27)
SNR (db)	20.9	21.3

Table 2. Performance of ADPCM with modified QAM

	Modified QAM		
	Rect	(4,11,17)	(5,11,16)
SNR (db)	21.8	22.2	22.3

6. Conclusion

In order to lessen the nonlinear distortion of ADPCM, a modified QAM modem that transmits data at a rate of 14.4kb/s has been developed. According to the simulation results, ADPCM with a modified QAM modem performs better than a conventional QAM modem. Additionally, a circular constellation performs better than a rectangular one.

References

1. *40, 32,24,16 kb/s ADPCM,* CCITT Recommendation G.726-1990.
2. Z. Markus, *Method of packet loss concealment in ADPCM Codec and ADPCM decoder with PLC circuit*, U.S. Patent 20160148619, 2016.
3. A. Gur, *Non-synchronized ADPCM with discontinuous transmission*, U.S. Patent 9332585, 2016.
4. A. Shibuta, *Wireless communication device and communication terminal*, U.S. Patent 9270419, 2016.
5. S. Ragot, *Controlling a noise-shaping feedback loop in a digital audio signal encoder avoiding instability risk of the feedback*, U.S. Patent 9489961, 2016.
6. *Comparison of ADPCM algorithm*s, ITU-T Recommendation G.726 Appendix III-1994.
7. M. AL-Rawi, M. AL-Rawi, Modified 24kb/s ADPCM System, *Journal of the Institution of Engineers (India): Series B (Springer)*, Vol.94(3), 2013.
8. M. AL-Rawi, M. AL-Rawi, Comparative study of 24kb/s ADPCM algorithms, *Radioelectronics and Communications Systems (Springer)*, 57(6), 2014.
9. M. AL-Rawi, M. AL-Rawi, Modified algorithm of 16kb/s ADPCM, *Pacific Science Review (Elsevier)*, 17(3), 2015.
10. M. AL-Rawi, Detection techniques for mitigating the nonlinear distortion of ADPCM link, *Australian Journal of Multi-disciplinary Engineering (Taylor and Francis),* 14(1), 2018.
11. M. AL-Rawi, M. AL-Rawi, Analysis and design of ADPCM system, *Journal of Advanced Engineering*, 10(3), 2015.
12. M. AL-Rawi, M. AL-Rawi, Performance study of multistage of 40kb/s ADPCM systems, *International Review of Applied Sciences and Engineering (Akademiai Kiado)*, 6(2), 2015.
13. *A duplex modem operating at data signalling rates of up to 14400bit/s for use on the general switched telephone network and on leased point-to-point 2-wire telephone-type circuits*, CCITT Recommendation V.32 bis-1991.

Address:

- Muhanned AL-Rawi, Bandung Institute of Technology, Indonesia,
  muhrawi@yahoo.com

Determining the optimum severity of damage using model performance analysis methods

Santatra Mitsinjo Randrianarisoa*, Gilbert-Rainer Gillich ⬛

Abstract. *In this work, we have considered a cantilever beam with a rectangular plastic cross-section, reinforced by four wire reinforcements made of ductile Iron. It was studied using numerical resolution based on theoretical formulae and then simulated using Solidworks software. A comparison of the results on the frequency ratios between the theoretical and numerical by Solidworks models gave a low error of 1.389% with a high correlation coefficient of around 0.959. Then, two top reinforcements inside the beam were cut in order to study the behavior of the intact beam and the damaged beam. Using the simulation results, we found an accurate damage severity using a mathematical method based on error deviation indicators or Model Performance Analysis (MPA).*

Keywords*: cantilever beam, frequencies, RMSE, SolidWorks, vibration modes.*

1. Introduction

SOLIDWORKS is a computer-aided design (CAD) software package developed by Dassault Systèmes and used mainly in the mechanical engineering industry. Since its arrival in 1993, this software has revolutionized the engineering world and become the most widely used modeling tool in the industrial sector [1]. Adopted mainly in the automotive and aerospace industries, SolidWorks allows designers to visualize an accurate, to-scale representation of the final product [2] and examine its static and dynamic behavior.

In this work, we propose exploiting the powerful features of the SolidWorks software to study the behavior of a cantilever plastic beam reinforced with four reinforcements inside. The study focuses on the out-of-plain vibrations. The dynamic response of cantilever beams with and without cracks is well-known and comprehensively described in [3]-[5].

The severity of damage is defined in [6], and a mathematical model of beams with cracks is proposed in [7]. In order to obtain reliable results with the model presented by the authors in previous research, it is essential to have a good correlation between the crack depth and the severity.

The contribution of this paper consists of extending the mathematical model's availability for reinforced beams and defining a methodology to find the severity of reinforcement wire damage accurately.

2. Theoretical background and methodology

2.1. *About the vibration of beams*

We consider the Euler-Bernoulli beam theory, which formulates the problem of the transversely vibrating beam with constant cross-section and rigidity in terms of the partial differential equation of motion [8]:

$$\frac{\partial^4 v}{\partial x^4} + \frac{\rho S}{EI} \frac{\partial^2 v}{\partial t^2} = 0, \tag{1}$$

where v is the vertical displacement of the beam at distance x measured from the clamped end. Considering that v depends on distance x and time t, and the evolution in time is harmonic, the expression of displacement is :

$$v(x,t) = \phi(x).y(t) = \phi(x).\sin(\omega t + \varphi) \tag{2}$$

After derivation of relation (2) and substitution in relation (1), one obtains :

$$\phi^{iv}(x)\sin(\omega t + \varphi) - \frac{\rho S \omega^2}{EI}\phi(x)\sin(\omega t + \varphi) = 0 \tag{3}$$

and, after simplifying by $sin(\omega t + \varphi)$, we have :

$$\frac{d^4\phi(x)}{dx} - \frac{\rho S \omega^2}{EI}\phi(x) = 0 \tag{4}$$

with the well-known solution [8]:

$$\phi(x) = A\sin(kx) + B\cos(kx) + C\sinh(kx) + D\cosh(kx) \tag{5}$$

In the above equation, we denoted:

$$\frac{\rho S \omega^2}{EI} = k^4 \tag{6}$$

The constants A, B, C, and D are determined from the boundary conditions. These derivatives are proportional to the vertical displacement $v(x)$, deflection $\theta(x)$, bending moment $M(x)$, and shear force $T(x)$. Putting the boundary condition for the clamped cantilever beam, given by mechanical reasons :

$$\phi(0) = \phi^i(0) = \phi^{ii}(L) = \phi^{iii}(L) = 0 \qquad (7)$$

to find the constants A^*, B^*, C^* and D^* we obtain the equation :

$$\cos(\alpha L) * \cosh(\alpha L) + 1 = 0 \qquad (8)$$

We can find the n solutions to equation (8) by solving it graphically:
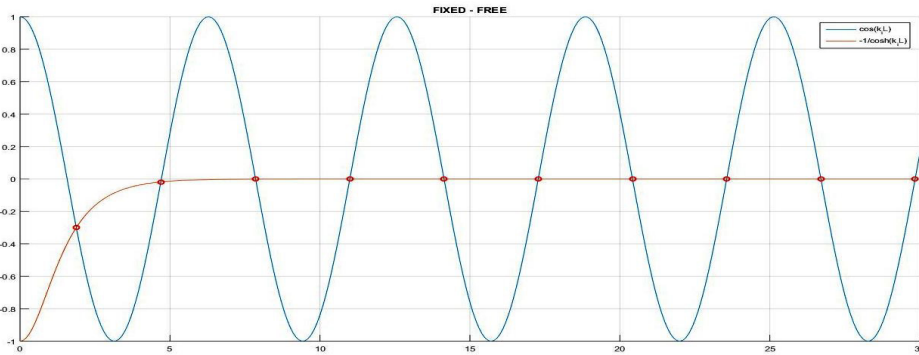
Figure 1. Graphical resolution of the characteristic equation of a cantilever beam

The adimensional wave numbers for the first $n = 6$ modes of vibration of a beam are given in the following table:

Table 1. Wave numbers of a cantilever beam

Modes i	1	2	3	4	5	6
αL	1,8751	4,6941	7,8548	10,9955	14,1372	17,2788

We denote $\lambda = \alpha L$, and calculate the angular frequencies ω_i by multiplying the relation of k^4 by L^4 and substituting the values of λ_i. It results:

$$\omega_i = \frac{\lambda_i^2}{L^2}\sqrt{\frac{EI}{\rho S}}\,(rad\,/\,s) \tag{9}$$

Finally, we find the natural frequencies:

$$f_i = \frac{\omega_i}{2\pi}\,(hertz) \tag{10}$$

and the periods:

$$T_i = \frac{1}{f_i}\,(\sec) \tag{11}$$

Obviously, for each angular frequency ω_i there is a corresponding mode shape ϕ_i. The mode shape for the cantilever beam is found, according to [9], with the mathematical relation:

$$\phi(x) = \cosh(\alpha x) - \cos(\alpha x) - \frac{\cos\lambda + \cosh\lambda}{\sin\lambda + \sinh\lambda}[\sinh(\alpha x) - \sin(\alpha x)] \tag{12}$$

The second derivative of the mode shape represents the mode shape curvature. For a particular bending vibration mode, it can be expressed:

$$\phi''(x) = \cosh(\alpha x) + \cos(\alpha x) - \frac{\cos\lambda + \cosh\lambda}{\sin\lambda + \sinh\lambda}[\sinh(\alpha x) + \sin(\alpha x)] \tag{13}$$

2.2. The expression of the severity

This section presents a method for determining the deflection at the free end of a cantilever beam with a crack. In our case, the crack consists of two cuttings in the reinforcement wires that are located inside the beam (Figure 2).

a) Intact beam   b) Damaged beam
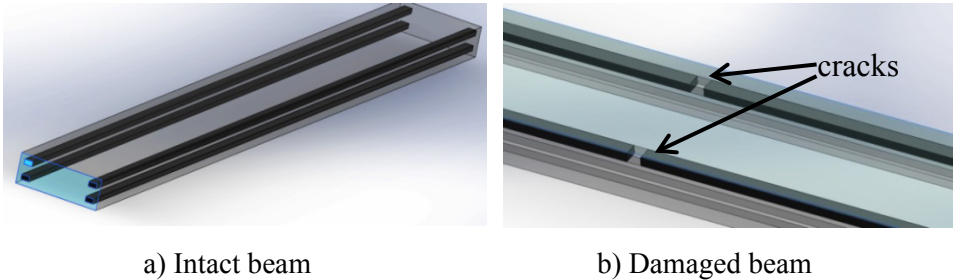
Figure 2. Presentation of the intact beam and damaged beam

The challenge faced when attempting to evaluate damages is that the effect of the crack, both on the deflection and the natural frequencies, is different when it is placed in different positions along the beam [9]. In prior research [7], we have determined a method for assessing the severity of transverse cracks, considering the deflection of a cantilever beam in the intact state and when it is altered by a breathing crack of known depth located at the fixed end. This mathematical relation is:

$$\gamma(a) = 1 - \frac{\sqrt{\delta_U}}{\sqrt{\delta(a,0)}} \tag{14}$$

In Eq.(14), we denoted $\gamma(a)$ the severity of a crack with depth a located at the fixed end; $\delta(a,0)$ the deflection at the free end of the cantilever beam having a crack with depth a at the fixed end (index 0 stays for location $x = 0$ mm); δ_U the deflection of the intact beam at the free end.

In [6], it is presented how to determine the deflection at the free end for the intact beam with a constant cross-section subjected to dead mass:

$$\delta_U = \frac{\rho g S L^4}{8EI}, \tag{15}$$

and the frequency of the undamaged beam becomes:

$$f_{1U} = \frac{\lambda_1^2}{2\pi} \sqrt{\frac{g}{8\delta_U}} \tag{16}$$

Here, ρ is the volumetric mass density, S is the cross-sectional area, g is the gravity, E is Young's modulus, and I is the second moment of inertia.

Similarly, the deflection at the free end for the damaged beam is :

$$\delta_{D\max} = \frac{\rho g S L^4}{8EI_D} \tag{17}$$

and the frequency of the damaged beam [6]:

$$f_{1D} = \frac{\lambda_1^2}{2\pi} \sqrt{\frac{g}{8\delta_{D\max}}} \tag{18}$$

The ratio of the two frequencies gives :

$$\frac{f_{iD}}{f_{iU}} = \frac{\sqrt{\delta_{U\max}}}{\sqrt{\delta_{D\max}}} \tag{19}$$

Consequently, we obtain:

$$f_{iD}(0,a) = f_{iU} \frac{\sqrt{\delta_{U\max}}}{\sqrt{\delta_{D\max}(0,a)}} \tag{20}$$

with:

$$\Delta f_{iD}(0,a) = f_{iU} - f_{iD}(0,a) = f_{iU}\left(1 - \frac{\sqrt{\delta_{U\max}}}{\sqrt{\delta_{D\max}(0,a)}}\right) \tag{21}$$

The severity is given by:

$$\gamma(a) = \frac{\Delta f_{iD}(0,a)}{f_{iU}} = \frac{f_{iU} - f_{iD}(0,a)}{f_{iU}} = 1 - \frac{f_{iD}(0,a)}{f_{iU}} \tag{22}$$

Thus, we have:

$$f_{iD}(0,a) = f_{iU}\left(1 - \gamma(a)\right) \tag{23}$$

The authors [9] established a relationship indicating the change in frequency for any vibration mode i, damage depth a, location x, and any types of bar fixation:

$$f_{iD}(x,a) = f_{iU}\left[1 - \gamma(0,a) * \left(\overline{\phi''(x)}\right)^2\right] \tag{24}$$

which makes use of the natural frequency of the intact beam f_{iU}, the damage severity $\gamma(a)$, and the normalized mode shape curvature $\overline{\phi''(x)}$.

2.3. The Model Performance Analysis (MPA) method

This analysis proposes a series of performance indicators to assess the predictive power of a model. The proposed indicators make it possible to evaluate a model's fidelity, exactitude, and accuracy [10].

The bias or Fidelity criteria is the first condition for validating a model, which is that the average of all the deviations e_i should be as close as possible to zero, i.e. an unbiased model. The bias can be calculated as follows:

$$bias = \frac{1}{n}\sum_{i=1}^{n}\left(Y_{real} - Y_{predict}\right) = \frac{1}{n}\sum_{i=1}^{n}e_i \tag{25}$$

The RMSE (Root Mean Square Error), or Exactitude criteria, characterizes the size of the differences between observations and measurements.

The bias indicates differences but does not give us any information about the amplitude of these differences since the positive and negative values of e_i compensate for each other in the mean.

$$RMSE = \sqrt{\frac{1}{n}\sum_{i=1}^{n} e_i^{2}} \qquad (26)$$

The variance of the term e_i over the entire simulation time interval will be defined as the "accuracy" of the model. It can be calculated using the following equation:

$$\sigma_e^2 = RMSE^2 - bias^2 \qquad (27)$$

The equations (25), (26), (27) will be used to assess the optimum severity of damaged in order to obtain a high-performance model.

3. Numerical simulations

This work considers a plastic rectangular (6x20 mm²) beam reinforced by four rectangular (1x2 mm²) wires with ductile Iron inside. The length of the cantilever beam is 500 mm.
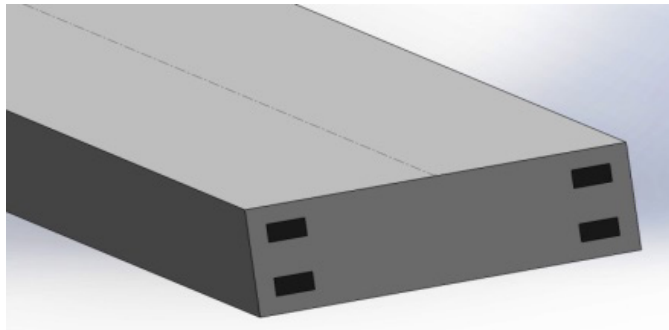
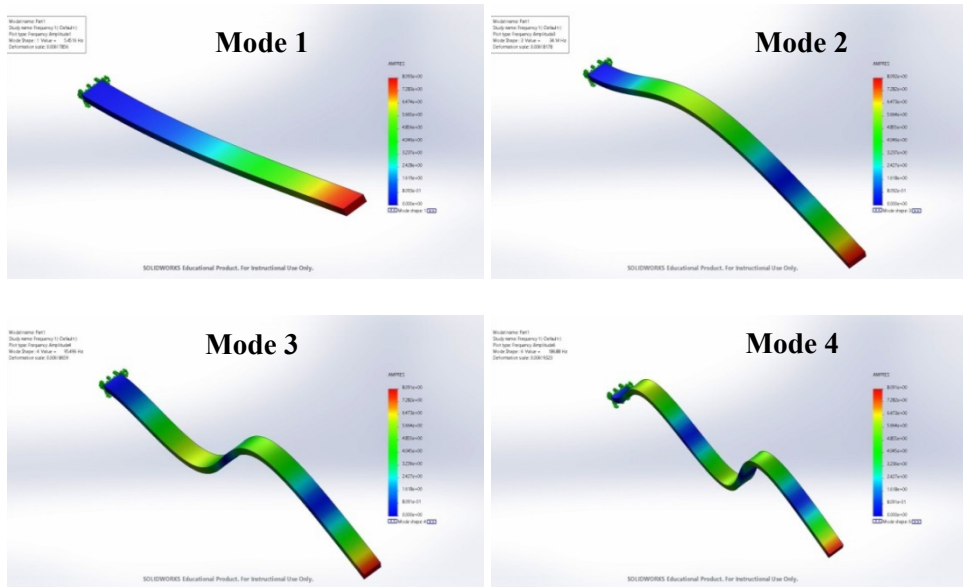**Figure 3.** Presentation of the cross-section of the test beam

3.1. Simulation of the intact beam

Using Solidworks with standard parameters, the following table summarises the simulation results for the first six vibration-relevant modes (out-of-plane bending):

Table 2. Frequencies of the intact beam for the first six vibration modes

Modes	1	2	3	4	5	6
ω_i (rad/sec)	58.227	363.45	1011.3	1964	3209.9	4730.9
f_i (Hz)	9.267	57.844	160.95	312.58	510.87	752.95
T_i (sec)	0.10791	0.017288	0.006213	0.003199	0.001957	0.001328

The following figure shows the stresses for the first four vibration modes for the intact beam :

Figure 4. Modes shape of the intact beam using Solidworks

3.2. Simulation of the damaged beam

Now, we cut two of the reinforcements inside the beam. The width of the cut is 2 mm, and *X[mm]* is the location from the fixed end of the beam. Using Solidworks with standard parameters, the following table summarises the simulation results for the first four vibration-relevant modes:

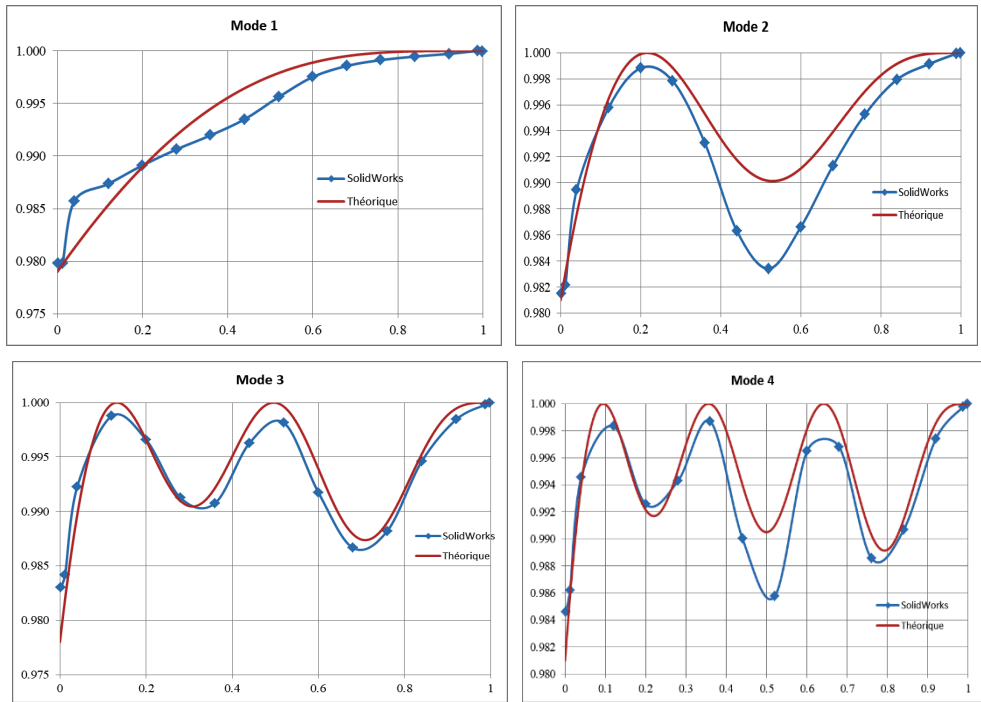**Table 2.** Frequencies of the damaged beam for the first four vibration modes

X (mm)	Mode 1	Mode 2	Mode 3	Mode 4
1	9.091	56.844	158.41	308.14
6	9.091	56.883	158.6	308.64
20	9.146	57.305	159.9	311.25
60	9.162	57.672	160.95	312.44
100	9.178	57.848	160.6	310.63
140	9.192	57.79	159.74	311.17
180	9.204	57.515	159.66	312.55
220	9.219	57.124	160.55	309.84
260	9.238	56.956	160.85	308.5
300	9.256	57.142	159.82	311.86
340	9.266	57.414	159	311.96
380	9.271	57.642	159.25	309.38
420	9.274	57.797	160.28	310.04
460	9.276	57.866	160.9	312.15
494	9.279	57.912	161.12	312.89
499	9.279	57.916	161.15	312.96

Figure 5 shows the curves given by Solidworks (blue) from Table 2 compared with the theoretical (red) for the first four modes of vibrations.

After cutting the reinforcement of the beam, we confirm that the results found on Solidworks with the damaged beam allow us to have a curve shape that is well synchronized with the theoretical but with errors that oscillate between [0 : 0.0050], which is accepted.

Table 3. Error indicator values for each vibration mode

Modes	1	2	3	4
MAE	0.00126	0.00184	0.00132	0.00146
RMSE	0.00168803	0.00239106	0.00157144	0.00197598
Correlation coefficient	0.9784	0.9437	0.9731	0.9409

Figure 5. Frequencies of the damaged beam plotted with results from Solidworks (blue line) and calculus (red line)
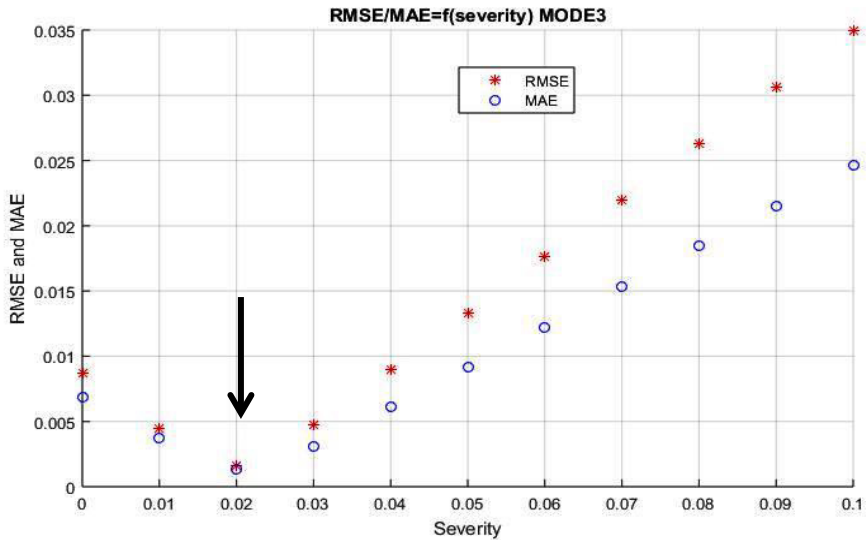
We conclude that for each vibration mode, the values of the error deviation indicators are acceptable. Solidworks can generate the theoretical results well, with an average correlation coefficient of 0.9590, which is satisfactory.

3.3. Severity assessment using the MPA method

Figure 6 shows that the values of the indicators (MAE and RMSE) change as a function of the damage severity coefficient. Therefore, we propose the following approach to determine the optimum value for severity:
- plotting a points cloud of MAE and RMSE as a function of the severity coefficient,
- the optimal coefficient corresponds to the minimum value of MAE (Mean Absolute Effor) and RMSE (Root Mean Square Error) together.

The following example was made using vibration mode number 3:

Figure 6. Points cloud for determining optimum severity

We deduce that for mode number 3, the optimum severity is 0.020. We found the optimum severity values for each vibration mode using the same procedure. The results are presented in Table 4.

Table 4. Optimum severity values for each vibration mode

Modes	Mode 1	Mode 2	Mode 3	Mode 4
Optimum severity	0.020	0.022	0.020	0.019

From the values in Table 4, we estimate the optimum severity as the average of the severities for the considered modes, which is 0.02025. We chose a single value for the severity for all modes since this was demonstrated in [6].

4. Conclusion

We used SolidWorks to accurately model and analyze the behavior of a rein-forced cantilever beam subjected to vibration. The simulations showed perfect syn-chronization between the theoretical vibrations of the beam and the SolidWorks sim-ulation results. Thus, we confirmed the reliability of the models developed in Solid-Works for structural dynamics applications.

We also determined the severity value for the considered damage using a probabilistic approach based on error indicators, and the results are demonstrated as very satisfactory.

References

1. B. Brejcha, *From Origins To Now: The History Of The SolidWorks Saga*, Available online: https://design-engine.com/from-origins-to-now-the-history-of-the-solidworks-saga/ (downloaded on 14 September 2024).
2. D. Planchard, *Engineering Design with SOLIDWORKS 2020*, SDC Publications, USA, 2019.5
3. G.R. Gillich, M. Tufoi, Z.I. Korka, E. Stanciu, A. Petrica, The relations between deflection, stored energy and natural frequencies, with application in damage detection, *Romanian Journal of Acoustics and Vibration*, 13(2), 2016, pp. 87-93.
4. L.V. Tran, H.A. Ly, J. Lee, M.A. Wahab, H. Nguyen-Xuan, Vibration analysis of cracked FGM plates using higher-order shear deformation theory and extended isogeometric approach, *International Journal of Mechanical Sciences*, 96, 2015, pp. 65-78, https://doi.org/10.1016/j.ijmecsci.2015.03.003
5. G.R. Gillich, N.M.M. Maia, M.A.Wahab, C. Tufisi, Z.I. Korka, N. Gillich, M.V. Pop, Damage detection on a beam with multiple cracks: a simplified method based on relative frequency shifts, *Sensors*, 21(15), 2021, Art. ID 5215, https://doi.org/10.3390/s21155215
6. G.R. Gillich, N. Maia, I.C. Mituletu, M. Tufoi, V. Iancu, Z. Korka, A new approach for severity estimation of transversal cracks in multi-layered beams, *Latin American Journal of Solids and Structures*, 13(8), 2016, pp. 1526-1544, https://doi.org/10.1590/1679-78252541
7. C. Tufisi, C.V. Rusu, N. Gillich, M.V. Pop, C.O. Hamat, C. Sacarea, G.R. Gillich, Determining the severity of open and closed cracks using the strain energy loss and the Hill-Climbing method, *Applied Sciences*, 12(14), Art. ID 7231, https://doi.org/10.3390/app12147231
8. G. Szeidl, L.P. Kiss, *Mechanical Vibrations*, Springer Nature Switzerland AG, Zurich, Switzerland , 2020.
9. G.R. Gillich, Z.I. Praisach, Modal identification and damage detection in beam-like structures using the power spectrum and time-frequency analysis, *Signal Processing,* 96, 2014, pp. 29-44, https://doi.org/10.1016/j.sigpro.2013.04.027

10. Critères et indicateurs d'auto-évaluation des modèles, Available online: https://www.graie.org/graie/graiedoc/reseaux/autosurv/GRAIE-Criteres-indicateurs-autoevalutiondesmodeles-autosurveillance-web18-v1.pdf (downloaded on 14 September 2024).

Addresses:

- Postdoc. Dr. Eng. Santatra Mitsinjo Randrianarisoa, Institut Supérieur de Technologie d'Antananarivo, Ecole du Génie Civil, Rue Dr Rasoamiaramanana Iadiambola, Ampasapito RN2, Antananarivo 101, Madagascar ramitsinjo@yahoo.fr (*corresponding author*)
- Prof. Dr. Eng. Gilbert-Rainer Gillich, Department of Engineering Science, Faculty of Engineering, Babeș-Bolyai University Cluj-Napoca, Romania, Piața Traian Vuia, nr. 1-4, 320085, Reșiţa, gilbert.gillich@ubbcluj.ro

Dynamic behavior of a simply supported circular plate

Ionela Harea 🄳, Zeno-Iosif Praisach* 🄳

Abstract. *The paper presents a study regarding the dynamics behavior of thin circular plate simply supported with a relation obtained analytically and the graphic representation of the modal shapes. The modal shapes are obtained using Bessel functions and their graphic representation are compared with Finite Element Method (FEM) by using modal analysis. For the analyzed case, the first 70 eigenvalues and natural frequencies are calculated.*

Keywords*: Bessel functions, circular plate, mode shape, eigenvalue.*

1. Introduction

Thin plates are used in architecture, civil construction design, industrial plant and machinery, oil platforms, hydraulic structures, aerospace and mechanical engineering.

Study of plates and dynamic behavior has been of scientific interest since the 18th century. The first researchers to offer mathematical approaches to plate and free vibration analysis were L. Euler [1], J. Bernoulli [2], E. Chladni, C.L. Navier, G.R. Kirchhoff, Ventsel and Krauthammer [3], S.P. Timoshenko [4], J.V. Boussinesq, S.G. Lekhnitskii, A. Leissa [5].

The problem of vibration analysis was analyzed using different numerical methods: Boundary element method [6], Finite element method [7, 8], Finite difference method.

The paper is focused on the analytical approach by using Bessel function solution and the comparison with the numerical results of the dynamic behavior for a simply supported circular plate. The considered plate is homogeneous, of constant thickness and is subject to the action of its dead weight.

The frequency equation is deduced from which the first 70 eigenvalues and natural frequencies were calculated, the modal functions are presented and illustrated using the Excel software and compared with the modal shapes obtained from Solid-Works software.

2. Analytical approach

The origin 0 of a thin circular plate, in polar coordinates is defined by the radius r=a=0.4 m and the angle θ (fig. 1). The plate is made of structural steel with constant thickness h=0.002 m and having the modulus of elasticity E=2.1·10^{11} N/m^2, Poisson coefficient ν=0.28 and density ρ=7800 kg/m^3.
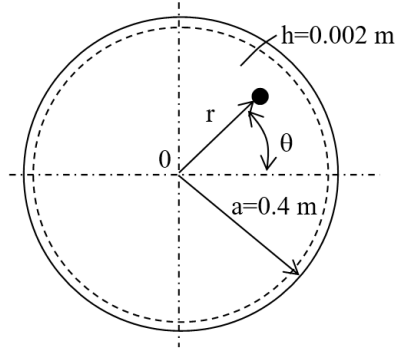
Figure 1. Simply supported circular plate defined by polar coordinates.

The flexural rigidity of the considered circular has the value:

$$D = \frac{Eh^3}{12(1-v^2)} = 151.91 \text{ Nm} \qquad (1)$$

To obtain the analytical solution of the dynamic behavior of the simply supported circular plate, it starts from the general solution [5] of the equation in polar coordinates:

$$\begin{cases} W(r,\theta) = \sum_{n=0}^{\infty}[A_n J_n(kr) + B_n Y_n(kr) + C_n I_n(kr) + D_n K_n(kr)]\cos(n\theta) + \\ \quad + \sum_{n=0}^{\infty}[A_n{}^* J_n(kr) + B_n{}^* Y_n(kr) + C_n{}^* I_n(kr) + D_n{}^* K_n(kr)]\sin(n\theta) \end{cases} \qquad (2)$$

where,

r, θ are polar coordinates;
a [m] is the circular plate radius;
h [m] is the thickness of the plate;
E [N/m^2] is the Young's modulus;
ν is the Poisson coefficient;
n = 0, 1, …, ∞ is the number of nodal diameters, or the order of the Bessel function;
$k = \sqrt[4]{\frac{\rho\omega^2}{D}}$ is a parameter of convenience.
$J_n(k\cdot r)$, $Y_n(k\cdot r)$ are the Bessel functions of the first and second kind;

$I_n(k \cdot r)$, $K_n(k \cdot r)$ are the modified Bessel functions of the first and second kind;

A_n, B_n, C_n, D_n, A_n^*, B_n^*, C_n^*, D_n^* are coefficients that are obtained from boundary conditions.

The considered circular plate does not have a central hole and to avoid deformations and infinite stresses at r=0, the terms $Y_n(kr)$ and $K_n(kr)$ are not taken into account [5].

In addition, the boundary conditions present symmetry in relation to one or more diameters of the simply supported circular plate and in this case the terms involving the term $\sin(n\theta)$ are not necessary.

The general solution of the equation in polar coordinates (2) becomes:

$$W(r,\theta) = [A_n J_n(kr) + C_n I_n(kr)]\cos(n\theta) \tag{3}$$

The boundary condition for the simply supported plate are:

$$\begin{cases} W(a) = 0 = [A_n J_n(\lambda) + C_n I_n(\lambda)]\cos(n\theta) \Rightarrow C_n = -A_n \frac{J_n(\lambda)}{I_n(\lambda)} \\ \frac{\partial^2 W(a,\theta)}{\partial r^2} = 0 = \lambda^2 A_n \left[\left(J''_n(\lambda) + \frac{v}{\lambda}J'_n(\lambda)\right) - \frac{J_n(\lambda)}{I_n(\lambda)}\left(I''_n(\lambda) + \frac{v}{\lambda}I'_n(\lambda)\right)\right]\cos(n\theta) \end{cases} \tag{4}$$

where, $\lambda = k \cdot a$ is the eigenvalue.

By using the recurrence relations [9]:

$$\begin{cases} J'_n(\lambda) = -J_{n+1}(\lambda) + \frac{n}{\lambda}J_n(\lambda) = J_{n-1}(\lambda) - \frac{n}{\lambda}J_n(\lambda) \\ I'_n(\lambda) = I_{n+1}(\lambda) + \frac{n}{\lambda}I_n(\lambda) = I_{n-1}(\lambda) - \frac{n}{\lambda}I_n(\lambda) \end{cases} \tag{5}$$

and

$$\begin{cases} J_{n+2}(\lambda) = \frac{2}{\lambda}(n+1)J_{n+1}(\lambda) - J_n(\lambda) \\ I_{n+2}(\lambda) = -\frac{2}{\lambda}(n+1)I_{n+1}(\lambda) + I_n(\lambda) \end{cases} \tag{6}$$

it will be obtained:

$$\begin{cases} J''_n(\lambda) = \left(\frac{n^2}{\lambda^2} - 1\right)J_n(\lambda) + \frac{1}{\lambda}J_{n+1}(\lambda) \\ I''_n(\lambda) = \left(\frac{n^2}{\lambda^2} + 1\right)I_n(\lambda) - \frac{1}{\lambda}I_{n+1}(\lambda) \end{cases} \tag{7}$$

which replaced in the second relationship (4) give us the frequency equation:

$$\frac{J_{n+1}(\lambda_{n,s})}{J_n(\lambda_{n,s})} + \frac{I_{n+1}(\lambda_{n,s})}{I_n(\lambda_{n,s})} = \frac{2\lambda_{n,s}}{1-v} \tag{8}$$

The solutions of the frequency equation (8) give us the eigenvalues $\lambda_{n,s}$. It can be observed that in the case of the circular plate simply supported, the frequency equation takes into account Poisson's ratio ν.

The normalized mode shape function can be written as:

$$
\begin{cases}
W(r,\theta)_{n,s} = A_n \left[J_n\left(\lambda_{n,s},\frac{r}{a}\right) - \frac{J_n(\lambda_{n,s})}{I_n(\lambda_{n,s})} I_n\left(\lambda_{n,s},\frac{r}{a}\right) \right] \cos(n\theta) \\
W(r,\theta)_{n,s} = A_n \left[J_n\left(\lambda_{n,s},\frac{r}{a}\right) - \frac{J_n(\lambda_{n,s})}{I_n(\lambda_{n,s})} I_n\left(\lambda_{n,s},\frac{r}{a}\right) \right] \sin(n\theta)
\end{cases}
\tag{9}
$$

and the natural frequencies are expressed with relationship:

$$
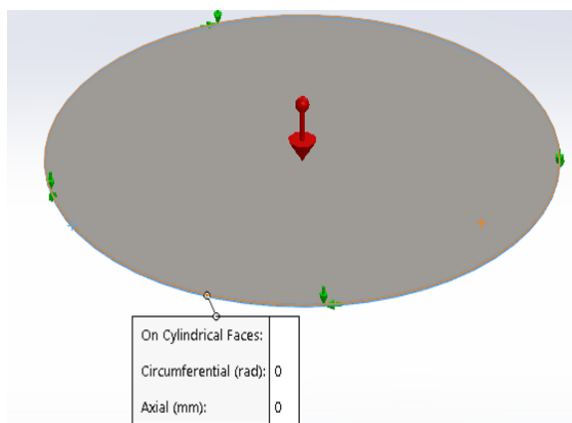f_{n,s} = \frac{\lambda_{n,s}{}^2}{2\pi \cdot a^2} \sqrt{\frac{D}{\rho \cdot h}}
\tag{10}
$$

where,

s is the number of nodal circles;

$\lambda_{n,s}$ is the eigenvalue as a function of n and s.

3. Modal analysis by using FEM

The modal analysis used for Finite Element Method (FEM) simulation was performed using the SolidWorks software. The boundary conditions applied to the 3D circular plate model for simply supported conditions are presented in figure 2.

The dimensions of the elements (mesh) and the details provided by SolidWorks can be seen in figure 3. The dimensions of the circular plate and the physical characteristics and mechanical properties are the same as presented in Chapter 2.

Figure 2. Boundary condition for simply supported circular plate.

Figure 3. Mesh details.

4. Results

The eigenvalues $\lambda_{n,s}$ depending on the number of nodal diameters n, respectively the number of nodal circles s, solutions of relation (8), calculated for 70 vibration modes are presented in the table 1 and the natural frequencies calculated with relation (10) are shown in table 2.

Table 1. Eigenvalues $\lambda_{n,s}$.

s	Nodal diameters n						
	0	1	2	3	4	5	6
0	2.215	3.725	5.059	6.319	7.538	8.728	9.898
1	5.449	6.961	8.372	9.723	11.031	12.308	13.562
2	8.610	10.137	11.588	12.987	14.347	15.677	16.982
3	11.760	13.296	14.771	16.201	17.595	18.961	20.303
4	14.906	16.448	17.939	19.390	20.809	22.201	23.571
5	18.051	19.597	21.100	22.567	24.004	25.416	26.807
6	21.194	22.744	24.255	25.734	27.186	28.614	30.022
7	24.337	25.890	27.407	28.896	30.359	31.800	33.222
8	27.480	29.034	30.557	32.053	33.526	34.978	36.412
9	30.623	32.178	33.706	35.208	36.689	38.150	39.594

Table 2. Natural frequencies $f_{n,s}$ [Hz].

s	Nodal diameters n						
	0	1	2	3	4	5	6
0	15.23	43.06	79.43	123.96	176.37	236.47	304.11
1	92.18	150.41	217.58	293.42	377.71	470.26	570.92
2	230.12	318.95	416.80	523.51	638.91	762.85	895.19
3	429.28	548.74	677.25	814.70	960.98	1115.94	1279.50
4	689.70	839.79	998.95	1167.10	1344.15	1529.99	1724.53
5	1011.39	1192.11	1381.91	1580.74	1788.51	2005.14	2230.55
6	1394.35	1605.70	1826.14	2055.63	2294.09	2541.46	2797.68
7	1838.57	2080.56	2331.64	2591.78	2860.92	3139.01	3425.98
8	2344.07	2616.69	2898.41	3189.20	3489.00	3797.78	4115.48
9	2910.84	3214.09	3526.45	3847.88	4178.35	4517.81	4866.21

The $\lambda_{n,s}$ values were obtained by iterative calculation. For example, for n=0, the first s=0, ..., 9 solutions of the frequency equation (8) resulted, respectively the values: $\lambda_{0,0}$, ..., $\lambda_{0,9}$, after which the number of n was increased from 1 to 6.

In the numerical modal analysis, the first 30 natural frequencies and vibration modes were obtained and they are shown in figure 4.

The natural frequencies obtained from FEM analysis, with identical values that appear at different vibration modes in figure 4, are due to the terms cos and sin from the analytically derived modal function (9). The natural frequency deviations ($\varepsilon_{n,s}$) obtained by the two calculation methods are very small and can be seen in table 3.

Table 3. Natural frequencies deviations $\varepsilon_{n,s} = f_{FEM}/f_{n,s} - 1$ [%].

s	Nodal diameters n						
	0	1	2	3	4	5	6
0	-0.0197	0.0046	-0.0013	0.0081	-0.0113	-0.0127	-0.0164
1	-0.0011	0.0000	-0.0094	-0.0102	-0.0132		
2	-0.0043	-0.0094	-0.0096				
3	-0.0093						

Study name:Frequency 1

Mode No.	Frequency(Rad/sec)	Frequency(Hertz)	Period(Seconds)
1	95.675	15.227	0.065672
2	270.57	43.062	0.023222
3	270.57	43.062	0.023222
4	499.07	79.429	0.01259
5	499.07	79.429	0.01259
6	579.18	92.179	0.010848
7	778.81	123.95	0.0080677
8	778.81	123.95	0.0080677
9	945.03	150.41	0.0066486
10	945.03	150.41	0.0066486
11	1,108.1	176.35	0.0056704
12	1,108.1	176.35	0.0056704
13	1,367	217.57	0.0045963
14	1,367	217.57	0.0045963
15	1,445.8	230.11	0.0043458
16	1,485.6	236.44	0.0042294
17	1,485.6	236.44	0.0042294
18	1,843.4	293.39	0.0034084
19	1,843.4	293.39	0.0034084
20	1,910.5	304.06	0.0032888
21	1,910.5	304.06	0.0032888
22	2,003.9	318.92	0.0031355
23	2,003.9	318.92	0.0031355
24	2,372.9	377.66	0.0026479
25	2,372.9	377.66	0.0026479
26	2,382	379.1	0.0026378
27	2,382	379.11	0.0026378
28	2,618.6	416.76	0.0023995
29	2,618.6	416.76	0.0023995
30	2,697	429.24	0.0023297

**Figure 4.** Natural frequencies f_{FEM} obtained by FEM.

Examples of modal shapes obtained analytically (left) and FEM (right) are presented in the figures 5 – 12. Figures 9 – 12 show the modal shapes of the circular plate simply supported that take into account both the cos function and the sin function, according to (9).
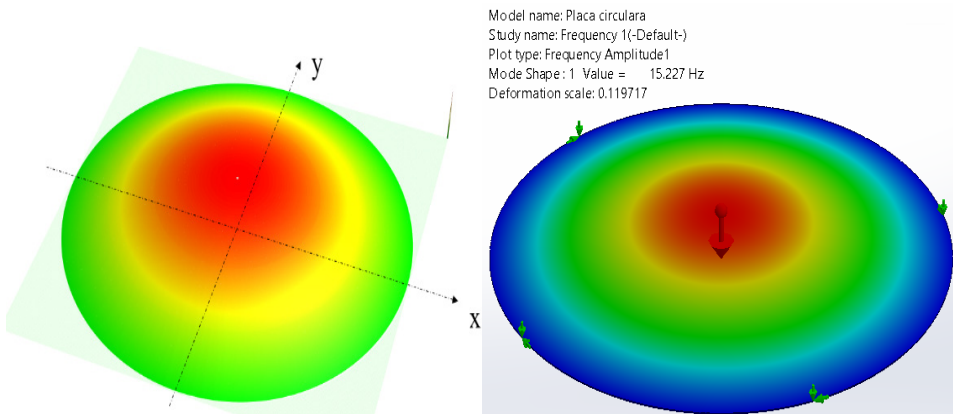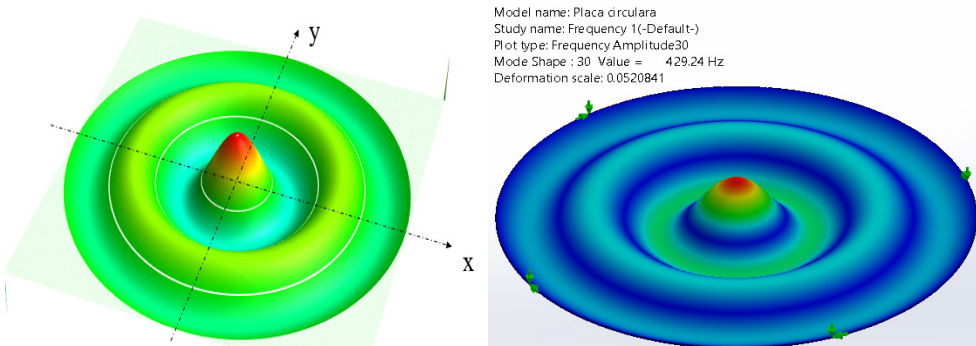

Figure 5. Simply supported circular plate. Mode shape for n=0 and s=0.
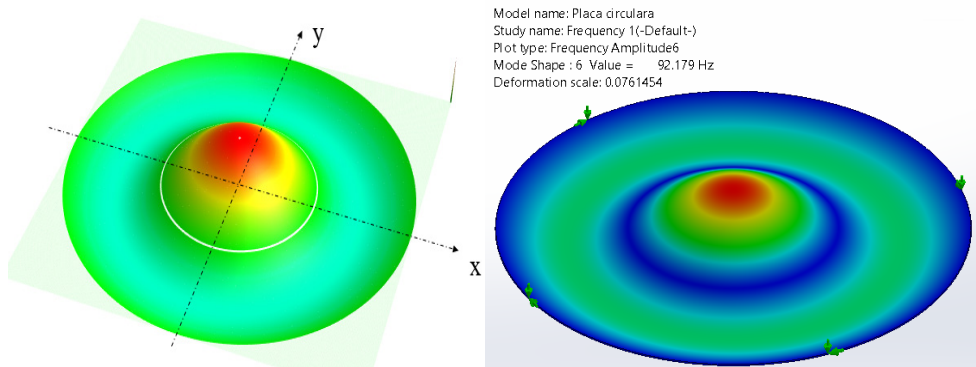
Figure 6. Simply supported circular plate. Mode shape for n=0 and s=1.
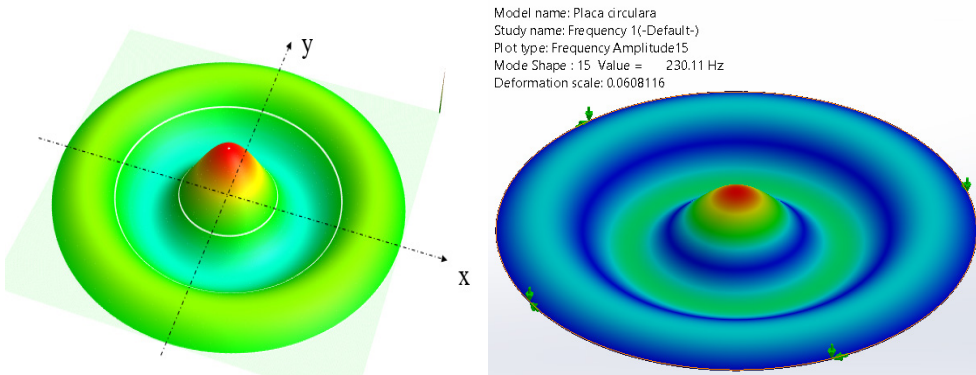
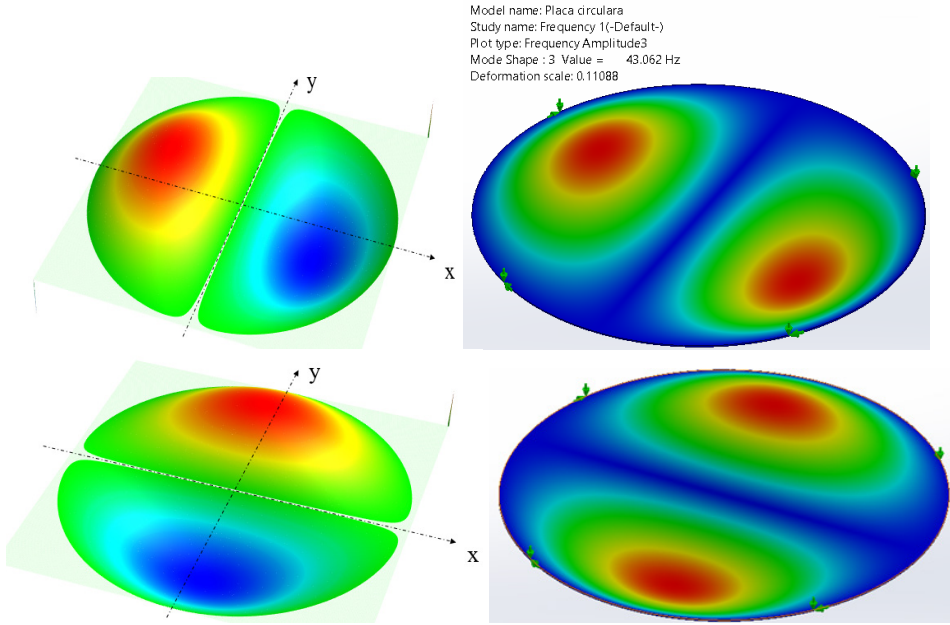

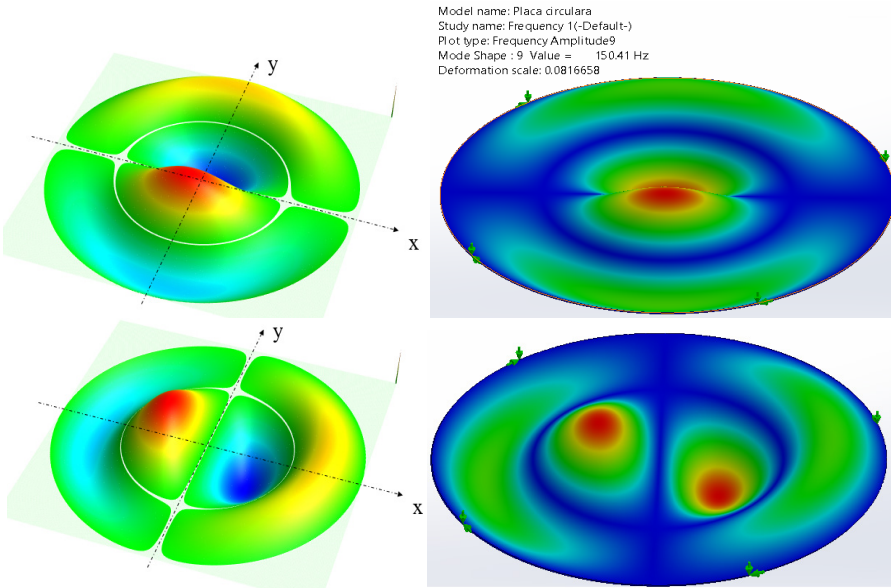**Figure 7.** Simply supported circular plate. Mode shape for n=0 and s=2.

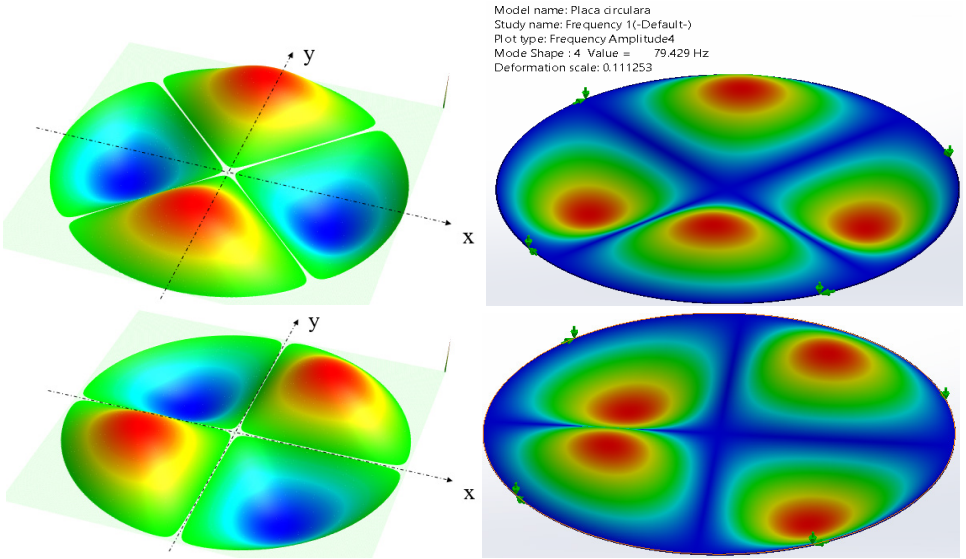**Figure 8.** Simply supported circular plate. Mode shape for n=0 and s=3.
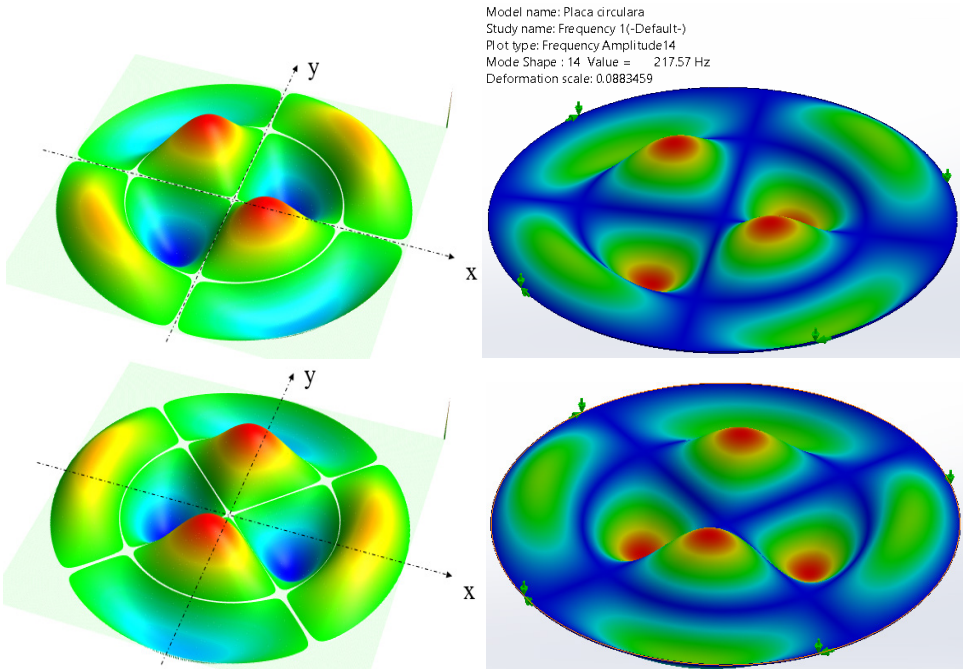
Figure 9. Simply supported circular plate. Mode shape for n=1 and s=0.

Figure 10. Simply supported circular plate. Mode shape for n=1 and s=1.

Model name: Placa circulara
Study name: Frequency 1(-Default-)
Plot type: Frequency Amplitude4
Mode Shape : 4 Value =   79.429 Hz
Deformation scale: 0.111253

Figure 11. Simply supported circular plate. Mode shape for n=2 and s=0.

Model name: Placa circulara
Study name: Frequency 1(-Default-)
Plot type: Frequency Amplitude14
Mode Shape : 14 Value =   217.57 Hz
Deformation scale: 0.0883459

Figure 12. Simply supported circular plate. Mode shape for n=2 and s=1.

5. Conclusions

The paper presents the vibration modes for a simply supported circular plate in a 3D representation using MS Excel software and the comparison with modal shapes obtained from the modal analysis obtained using SolidWorks software.

The eigenvalues $\lambda_{n,s}$ were calculated for seven values of the nodal diameters n=0, 1, .., 6 and ten values of the nodal circles s=0, 1, ..., 9. For these values the natural frequencies were calculated.

The large number of natural frequencies (70) was chosen to illustrate the ease with which the natural frequencies, respectively the vibration modes, can be calculated by the analytical method compared to the modal numerical method. For example, out of the 30 results obtained by the numerical modal analysis, only the first 16 natural frequencies can be compared with the analytically determined natural frequencies which are presented in Table 3.

It should be taken into account that the results obtained from the modal numerical analysis give us the vibration modes for both variants of the modal function (9): $\cos(n\theta)$ and $\sin(n,\theta)$, vibration modes for which the natural frequency has the same value, respectively the same eigenvalue $\lambda_{n,s}$, according to (10).

The numerical results by FEM for the first 30 vibration modes of the circular plate have highlighted the fact that the natural frequency deviations obtained by the two methods are less than 0.02%.

From the analysis of figures 5 – 12, a very good correlation of the modal shapes obtained both analytically and through FEM can be observed.

References

1. L. Euler, De motu vibratorio tympanorum. Vol. 10, *Novi Commentarii academiae scientiarum Petropolitanae,* 1766, pp. 243-260.
2. Diarmud O. Mathuna, (1994), *Jacques II Bernoulli and The Problem of the Vibrating Plate.* Dublin Institute for Advanced Studies. Ireland.
3. E. Ventsel, T. Krauthammer, *Thin Plates and Shells Theory, Analysis, and Applications*. 1st Edition. The Pennsylvania State University Park, Pennsylvania, Copyright 2001 by Marcel Dekker, Inc. U.S.A.
4. S.P. Timoshenko, S. Woinowsky-Krieger, *Theory of Plates and Shells*, Copyright by McGraw-Hill Book Company, second edition, 1989, U.S.A.
5. A.W. Leissa, *Vibration of Plates,* NASA SP-160. Washington, DC U.S. Government Printing Office. Special Publication 2013.

6. J.R. Hutchinson, *Analysis of plates and shells by boundary collocations. In: Boundary Element Analysis of Plates and Shells*, Ed. D.E. Beskos, Springer-Verlag, Berlin, 1991, pp. 341–368.
7. I. Fried, *Linear and Nonlinear Finite Elements*, Boston University Department of Mathematics Boston, U.S.A, 1984.
8. T.Y. Yang, *Finite Element Structural Analysis.* Pearson College Div, New Jersey. U.S.A. 1985.
9. Bessel Functions of the First and Second Kind, https://pub.me755_web.tex (uwaterloo.ca), (downloaded at July 20rd, 2018)

Addresses:

- PhD. Stud. Eng. Ionela Harea, Doctoral School of Engineering, Babeș-Bolyai University, Cluj-Napoca, Romania, Piaţa Traian Vuia, nr. 1-4, 320085, Reşiţa
  ionela.harea@ubbcluj.ro
- Lect. PhD. Habil. Zeno-Iosif Praisach, Department of Engineering Science, Faculty of Engineering, Babeș-Bolyai University Cluj-Napoca, Romania, Piaţa Traian Vuia, nr. 1-4, 320085, Reşiţa
  zeno.praisach@ubbcluj.ro
  ([*]*corresponding author*)

Reverse engineering of a toothed gear

Antonio-Patrik Nedelcu, Cristian Tufisi*

Abstract. *With the rapid development of modern industry, the need for spare parts has increased. Most mechanical systems have transmission components which are composed of toothed gears. In most cases, the manufacturer of the spare part does not exist on the market and the need to reproduce the failed part needs to be met. Usually, toothed gears are obtained using special cutting machines, like Gleason, Lees-Bradner, and Pfauter. To be able to reproduce the part by using a common manufacturing process, the current paper presents a RE method for obtaining the 3D geometry of a toothed gear in the scope of machining the part using a CNC 3-axis mill. CAD software and 3D scanning technology is used to recreate the gear's 3D model and ensure accurate dimensions for the gear teeth, including tooth spacing, depth, and angle.*

Keywords: *reverse engineering, computer aided design, toothed gear insert, 3D scanning, point clouds*

1. Introduction

The current paper aims to showcase the generation of the 3D model of a toothed gear, by applying Reverse Engineering methods, like 3D scanning technology. Reverse engineering is the process of analyzing a physical object to identify and understand the relationship between its functioning principles and components, in order to reproduce the object in another form or of superior quality. It can also be described as the process of duplicating an existing component by capturing the physical dimensions of its parts. The main purpose of this method is to create models as precise as possible of an object that reflect its basic geometry through scanning. [1]

Other research has concluded that through reverse engineering, it is possible to reconstruct the tooth profile using point clouds obtained through a non-contact methodology. The basic settings of the reconstructed gear machines were estimated based on derived data from the original gear and were compared with those of a specific

model. The results indicate that most of the basic settings of the gear machine are well estimated, although precise estimation of the root cone angle is necessary for an accurate determination of the base pitch and machine root angle settings. [2]

In other research such as [3], an attempt was made to create a gearbox with a parallel shaft and two speeds. They succeeded with reverse engineering to reach the conclusion that they could scan and generate a model of this already used unit. After finding out the necessary data for operation, they calculated the ideal model for a new unit and rebuilt the assembly. And the paper [4] also describes the scanning of a gear wheel with the help of Artec space spider & Geomagic Design X software.

As a brief historical overview, gears are one of the ancient tools, having first appeared as early as the 27th century BCE in China. Aristotle provided the earliest description of gears in the 4th century BCE, noting that the direction of rotation is reversed when one toothed wheel drives another toothed wheel.

Straight gears, as in this work, have teeth parallel to the axis of rotation; they are used to transmit rotation between parallel shafts. Compared to other types, straight gears are the simplest. [5]
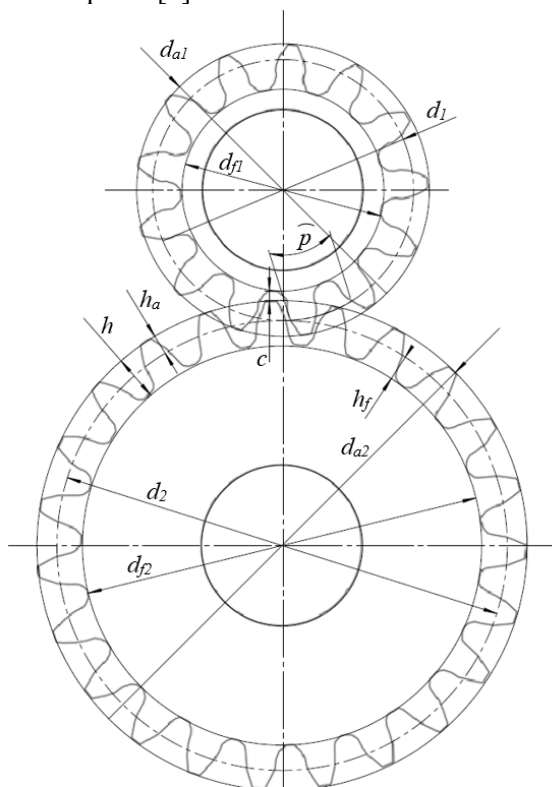
Figure 1. Main gear parameters

2. Materials and methods

The gear we aim to reverse engineer using 3D scanning technology is part of a classical mill's gearbox, a component vital for the machinery's operation. Over time, due to wear and tear or other factors, some of its teeth have become damaged or broken, impairing its functionality, as seen in Figure 2.

Figure 2. The damaged part

By employing 3D scanning technology, we intend to capture the precise geometry of the intact portions of the gear, as well as the damaged areas. Through this method, we can accurately map out the contours and dimensions of the gear, including the intact teeth and the areas where damage has occurred.

Once the 3D scan is completed, we can utilize reverse engineering techniques to analyze the scanned data and reconstruct the original design of the gear. This involves identifying the parameters and specifications of the gear, such as tooth profile, pitch diameter, and helix angle. With this information, we can create a virtual model of the gear, incorporating the necessary adjustments to compensate for the damaged or missing teeth.

The goal of this reverse engineering process is to produce a functional replacement gear that seamlessly integrates with the existing gearbox.

First, we have defined the main parameters of the gear, through measurement. The essential component elements of gears are module (1), pitch (2), number of teeth (3), clearance (4), pitch diameter (5), addendum (6), dedendum (7), total depth (8) as follows:

$$m = \frac{(d_2 - 2)}{z} = \frac{(86 - 2)}{42} = 2 \tag{1}$$

$$p = \pi \cdot m = \pi \cdot 2 = 6.28 \, \text{mm} \tag{2}$$

$$N = \frac{d_0 - 2 \cdot m}{m} = \frac{88 - 2 \cdot 2}{2} = 42 \tag{3}$$

$$c = 0.1 \cdot m = 0.1 \cdot 2 = 0.2 \, \text{mm} \tag{4}$$

$$d = m \cdot N = 2 \cdot 42 = 84 \, \text{mm} \tag{5}$$

$$h_a = m = 2 \, \text{mm} \tag{6}$$

$$h_d = m + c = 2 + 0.2 = 2.2 \, \text{mm} \tag{7}$$

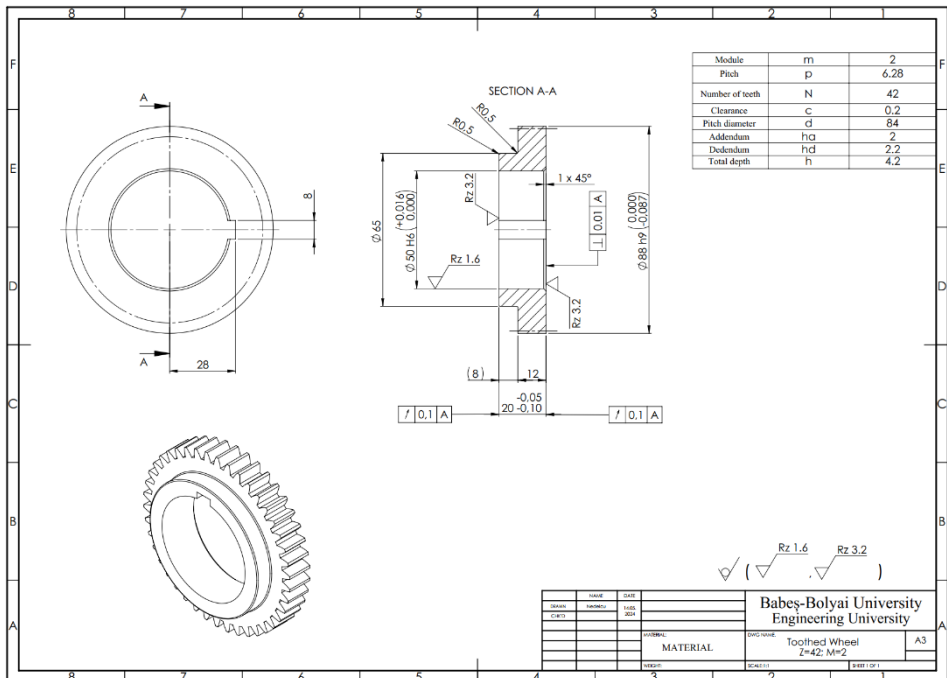$$h = 2 \cdot m + c = 2 \cdot 2 + 0.2 = 4.2 \, \text{mm} \tag{8}$$

Figure 3. Execution drawing

2.1. The 3D scanning of the toothed gear

The equipment utilized comprises a POP 3D Scanner, a rotary table, and the necessary computer. The POP handheld 3D scanner integrates a proprietary 3D camera module and embedded chip to deliver precise and rapid 3D scans, designed to be compact and portable with multi-mode scanning capabilities suitable for product development, prototyping, 3D printing, and artistic creation. Utilizing Binocular Structured Light technology, the Revopoint POP 3D Scanner ensures high-accuracy 3D point cloud data acquisition with a single-frame precision of up to 0.15mm. Equipped with depth cameras including two IR sensors and a projector, it swiftly captures object shapes, while an RGB camera captures texture details. This device supports high-precision and texture scanning modes, facilitating the direct generation of vivid 3D models.

Figure 4. 3D scanner

The first stage consisted in positioning the component on a rotary table, it was tried to be as centered as possible and in a horizontal position. The 3D scanner was turned on and the rotary table too. The table rotated at 2.5 RPM during the entire operation. The scanner was fixed at a distance of about 40 centimeters. During the data were entered on a computer. For scanning, the color scanning module and the normal one were used.

## 3. Obtaining the 3D model from the scanned data

In the Geomagic design X software, I introduced the 3D scans that are initially brought as a cloud of points, the Mesh Buildup Wizard is used, from here there are several stages that consist of the selection of elements that are not aligned correctly

and adjustments. After corrections, a model is made only as a surface. And the last stage is making a solid model according to the surface generated after processing.

Scanning can be done in different profiles, directions, angles and depths, and what is very important, in the end, a combination of scans can be performed in a unitary whole, of great resolution and finesse, being the most recommended application in the field reverse engineering.

The procedure for obtaining a 3D model from 3D scan data, as can be seen in Figure 4, consists of the actual object scan, division of the scanned model into regions, virtual extrusion of regions, superposition of surfaces on the network of scanned points, volume processing of surfaces and filling design with scanned parameters.

First the point cloud data of the gear is obtained by 3D color scanning or RGB-D scanning, which is a technique used to capture three-dimensional objects along with their color information.
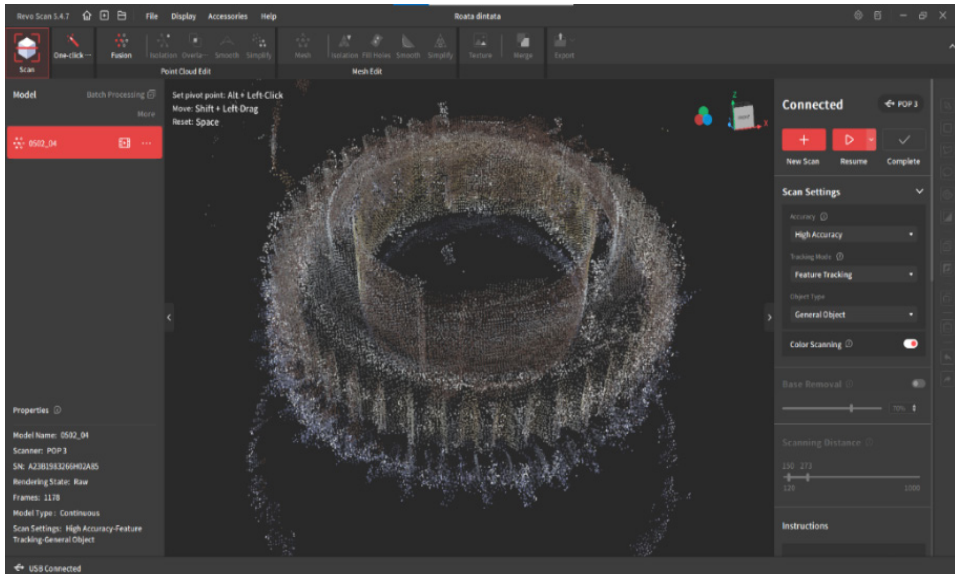

Figure 5. Point cloud data of the toothed gear using color scanning

A second set of point cloud data of the gear is obtained by normal 3D scanning, which is the process of collecting XYZ points in space to represent an existing physical object. It results in a cloud of points, a collection of data stored as a matrix of discrete coordinates, which define the shape and dimensions of the object. At this stage, a preliminary graphic description of the object on the computer is possible.
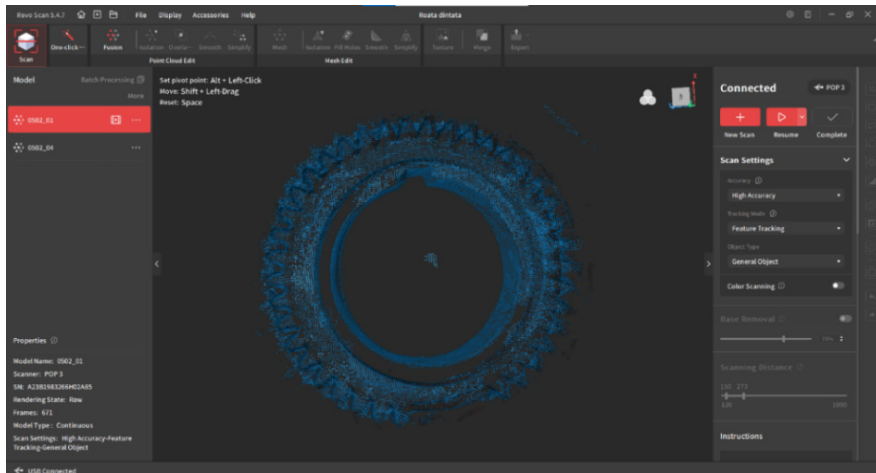
Figure 6. Point cloud data of the toothed gear without color scanning

The mesh buildup wizard in Geomagic Design X is employed for processing the scanned data. First, the two scans are opened, and the type of scanner is selected and afterwards the point cloud data is cleaned by deleting unnecessary data.
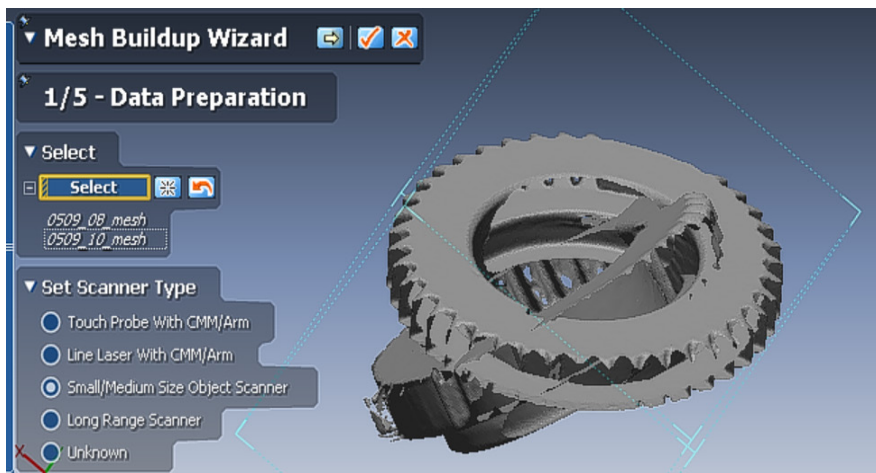

Figure 7. 3D scan data preparation

The scans are aligned by using the Best-Fit-Aligning method and data merging is applied.
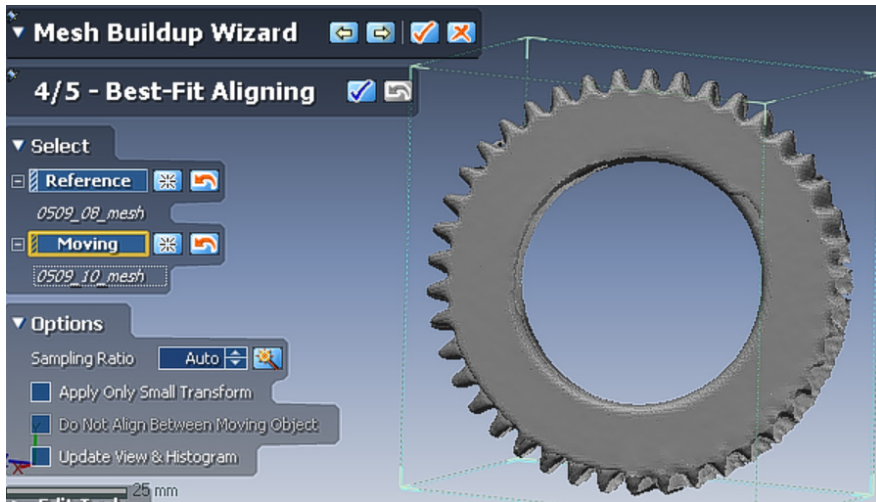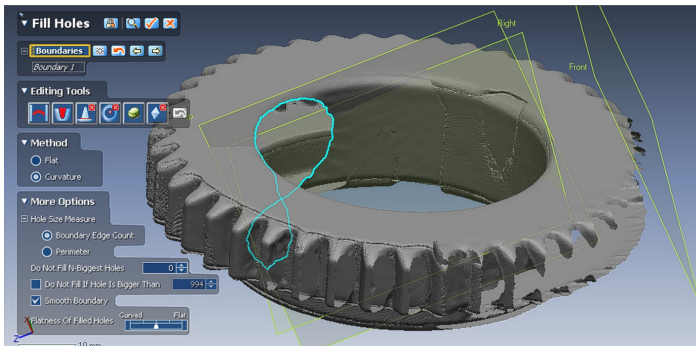
Figure 8. Aligned scans

After the volume processing is finished, Geomagic Design X Healing Wizard is used for reverse engineering and converting the 3D scan data into usable CAD models. The Healing Wizard is a tool designed to automate and simplify the process of fixing imperfections and errors in scanned data.
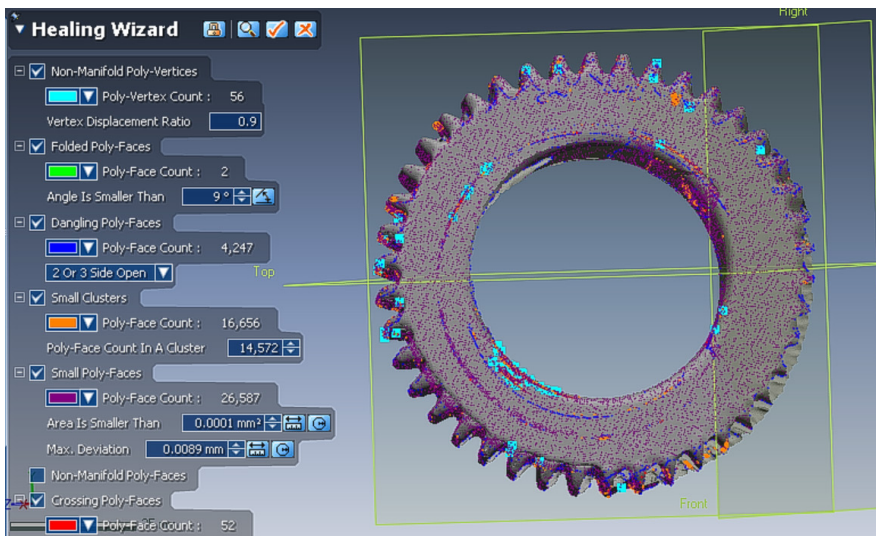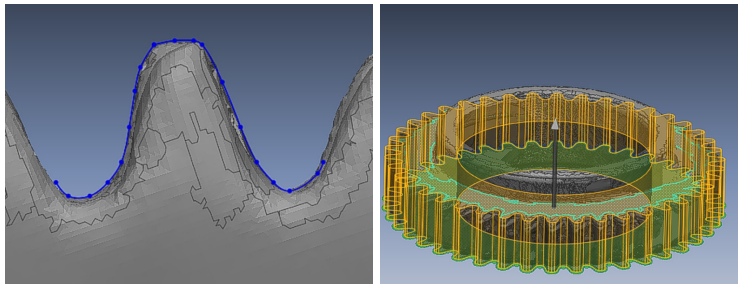

Figure 9. Healing wizard

Figure 10. Creating the mesh file and filling the holes

The geometry of the part is reconstructed based on the obtained mesh file.

Figure 11. Reconstruction of the geometry

4. Determining the precision of the scanned model of the toothed gear

After the 3D model is generated from scanning and converted into a solid representation using the software Geomagic Design X, it undergoes a process of comparison with an ideal 3D component. This comparison involves assessing the accuracy and fidelity of the scanned model relative to a reference or ideal model.
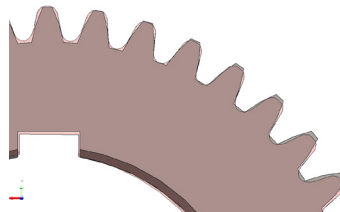
Figure 12. Comparison of the tooth profile
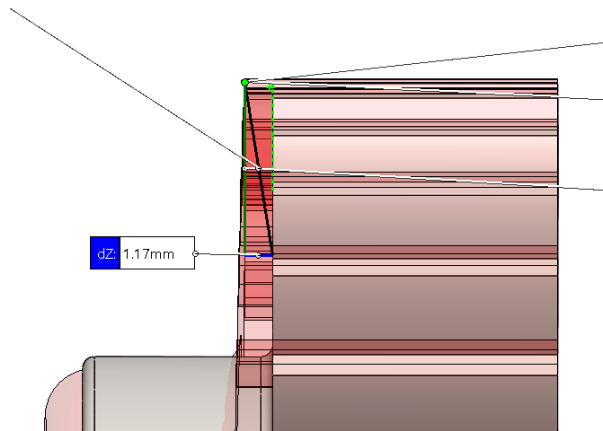
Figure 13. Maximum deviation

5. Conclusion

Despite the short processing time of just 20 minutes, our analysis reveals that the accuracy achieved in comparing the scanned model to the ideal component is exceptionally high. This underscores the efficiency and effectiveness of the scanning and processing methodologies employed. The rapid turnaround time, coupled with the attainment of precise results, not only demonstrates the advancements in technology but also highlights the feasibility of integrating 3D scanning into various applications where speed and accuracy are paramount. This success opens up avenues for expedited workflows and enhanced productivity across industries, promising substantial benefits in design, manufacturing, and quality control processes.

References

1. K. Khairul, *Revers Engineering of Spur Gearbox*, UTeM, 2015.
2. I. Gonzalez-Perez, A. Fuentes-Aznar, *Reverse engineering of spiral bevel gear drives reconstructed from point clouds*, Department of Mechanical Engineering, Materials and Manufacturing, Universidad Politécnica de Cartagena, Spain, Department of Mechanical Engineering, Rochester Institute of Technology, USA, 2022.
3. O. Ibhadode, A. Adekunle, *Reverse Engineering Approach for the Design of Gear-box for a Hand-guided Vibratory Roller Soil-Compactor*, Nigerian Building and Road Research Institute, 2020.

4. H. Alhafeiti, A. Ziout, A. Alsaadiya, A. Alhebsi, *Re-designing a gear using reverse engineering*, Department of Mechanical Engineering, United Arab Emirates University, Alain, United Arab Emirates, 2019.
5. F. Alsaid, S. Sultan, *Reverse Engineering for Gearbox*, Palestine Polytechnic University, 2019.
6. https://www.goengineer.com/blog/geomagic-design-x-features-and-tutorials (downloaded on 13.05.2024).
7. https://www.dicarlotech.com/products/software/modeling/geomagic-designx (downloaded on 13.05.2024).

Addresses:

- Stud. Antonio-Patrik Nedelcu, Babeș-Bolyai University, Faculty of Engineering, Piaţa Traian Vuia, nr. 1-4, 320085, Reşiţa, Romania
  antonio.nedelcu@stud.ubbcluj.ro
- Ş.l. Dr. Eng. Cristian Tufişi, Department of Engineering Science, Faculty of Engineering, Babeș-Bolyai University Cluj-Napoca, Romania, Piaţa Traian Vuia, nr. 1-4, 320085, Reşiţa
  cristian.tufisi@ubbcluj.ro
  ([*]*corresponding author*)

Simulation of a serial topology robot operation using the 3DEXPERIENCE platform

Razvan-George Olingheru* ID, Adrian-Bogdan Olariu ID,
Calin-Octavian Miclosina ID

Abstract. *The paper presents the assembling of a 3D model serial topology robot, the definition of kinematical joints of the guiding device mechanism and the simulation of robot operation, using the 3DEXPERIENCE platform. In the end, there are presented different positions of the robot during simulation.*

Keywords*: serial topology, robot, 3DEXPERIENCE platform.*

1. Introduction

Serial topology robots are widely used in industrial and service applications.
The guiding device mechanism of this type of robots contains an open kinematical chain, the links being connected by the kinematical joints one after another. An example is shown in fig. 1.
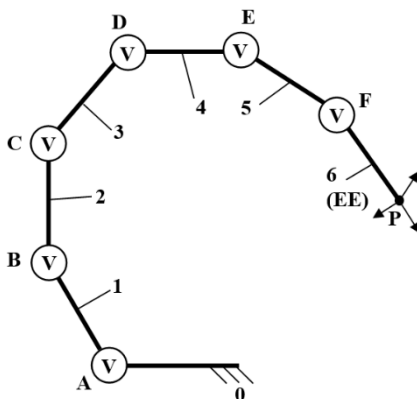
Figure 1. Structural scheme of a serial topology mechanism [1].

The mechanism has 7 binary links (0 - 6) and 6 kinematical joints of fifth class (A – F).

The serial topology robot which will be simulated is presented in fig. 2. The components were obtained by 3D printing [2].

Figure 2. The serial topology robot [2].

2. The 3DEXPERIENCE Platform

3DEXPERIENCE (3DX) is a business and innovation platform that provides organizations with a holistic, real-time vision of their business activity and ecosystem. It connects people, ideas, data and solutions in a single collaborative environment [3].

It includes many design applications and modules, as Design with CATIA V5, Part Design, Assembly Design, Design with Solidworks, xDesign, etc.

The files can be created on a PC using a design software as CATIA V5 [4], [5], and then uploaded on the platform, or can be created, edited and saved directly in cloud.

Nowadays, the 3DEXPERIENCE platform is used for various engineering design projects [6], [7].

3. Assembling the 3D Model

The 3D models of the components were uploaded on the 3DEXPERIENCE platform and assembled in CATIA Assembly Design module.

First, the robot base with its motor were inserted in the new file, rigidized one to another, and then fixed in the virtual space using the *Fix* connection type, as shown in fig. 3.
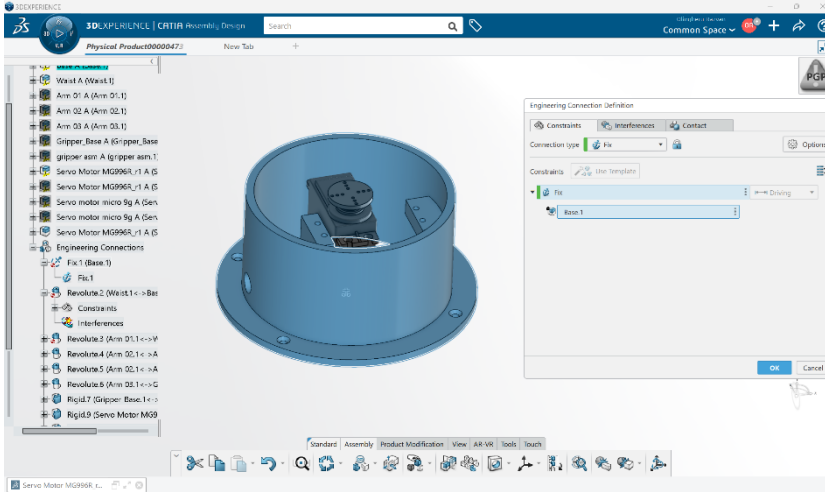
Figure 3. Inserting and fixing the robot base.

Then, the second component with its motor were inserted and connected to the base by a revolute joint with a 360° stroke, as shown in fig. 4.
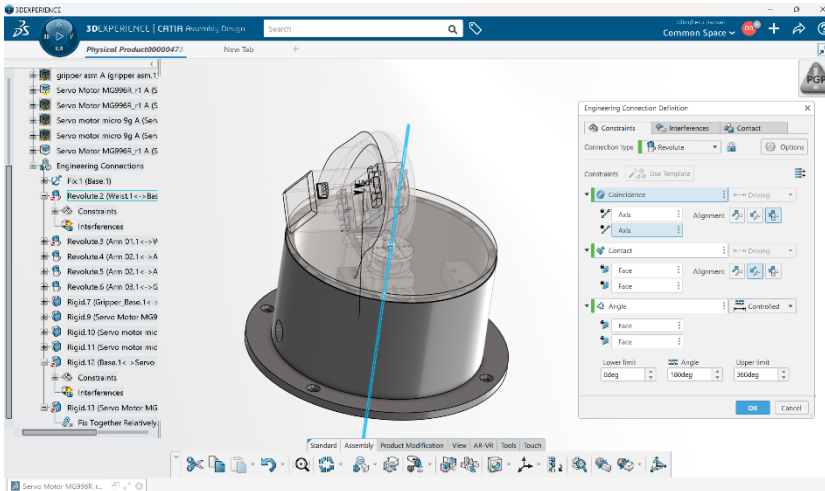
Figure 4. Defining a revolute joint between the base and the second component.

The third component was inserted next and connected to the second component by a revolute joint with a 180° stroke, as shown in fig. 5.
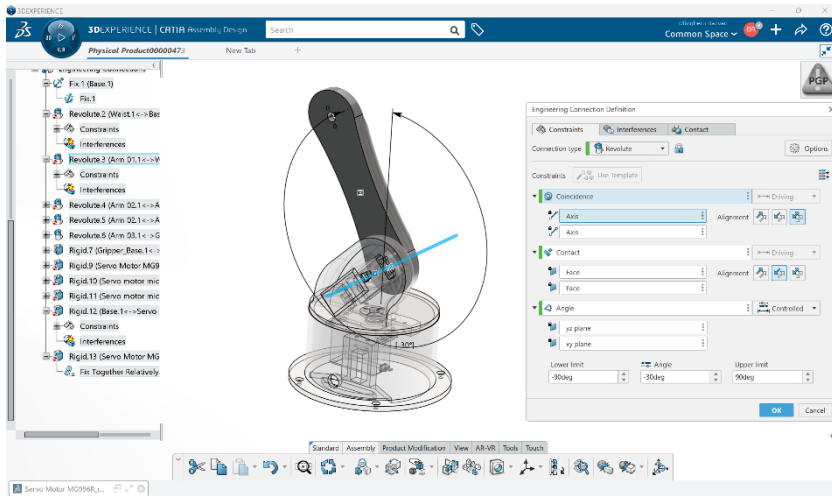
Figure 5. Defining a revolute joint between the second and the third components.

Next, the fourth component with its two motors were inserted and connected to the third component by a revolute joint with a 248° stroke, as shown in fig. 6.
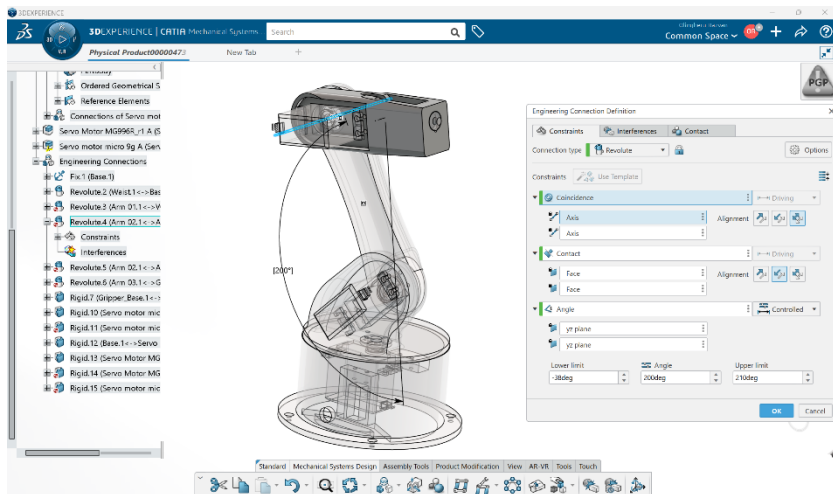
Figure 6. Defining a revolute joint between the third and the fourth components.

Then, the fifth component with its motor were inserted and connected to the fourth component by a revolute joint with a 360° stroke, as shown in fig. 7.

Figure 7. Defining a revolute joint between the fourth and the fifth components.

The sixth component (the end effector) with its motor were inserted and connected to the fifth component by a revolute joint with a 180° stroke, as shown in fig. 8.
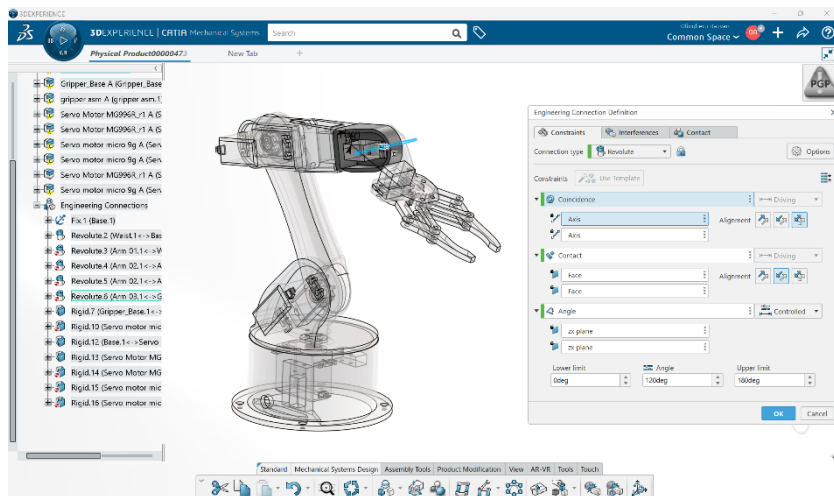
Figure 8. Defining a revolute joint between the fifth and the sixth components.

4. Simulation of the Robot Operation

The simulation of the 3D model of the serial topology robot operation was accomplished using the Mechanical Systems Design module.

Different positions of the robot during simulation are shown in fig. 9, 10 and 11.
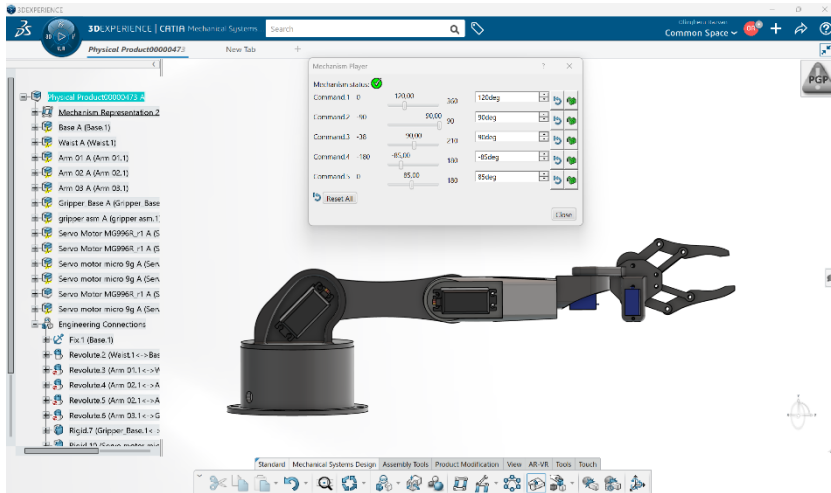
Figure 9. Horizontal position of the robot.
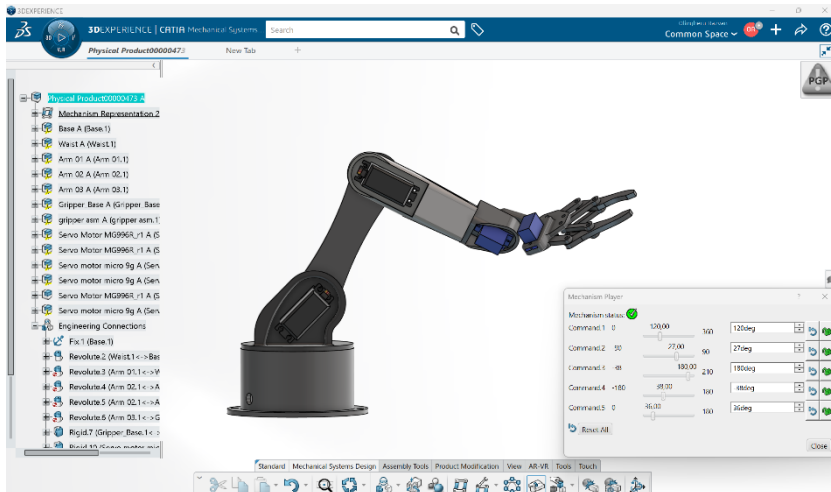
Figure 10. Intermediate position of the robot.
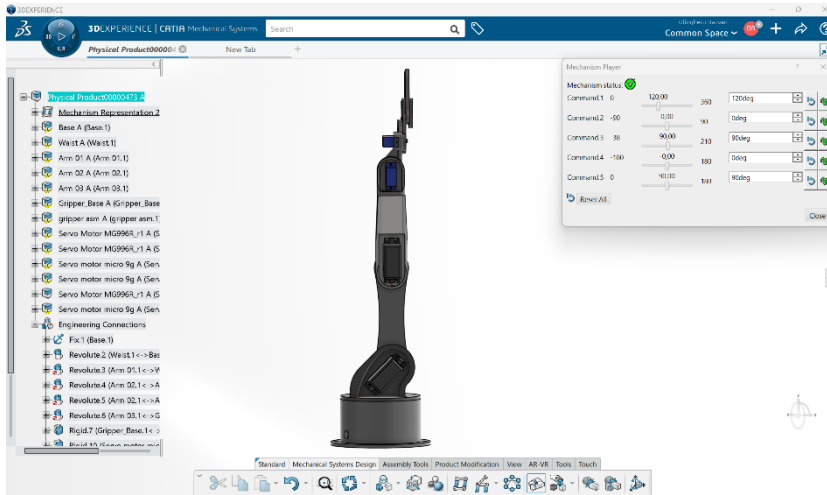
Figure 11. Vertical position of the robot.

4. Conclusions

The 3DEXPERIENCE platform represents a powerful tool for engineering design and simulation.

Using the steps presented in this paper, the operation of different types of mechanical systems can be done.

References

1. C.O. Miclosina, *Roboţi Industriali şi Linii Flexibile*, Editura Eftimie Murgu, Reşiţa, 2009.
2. A.B.Olariu, R.G. Olingheru R.G., C. Sandor, D.D. Ardeljan, *Realizarea unui robot cu topologie serială*, SSING 2024 - Cercetare şi inovare în inginerie mecanică, Apr. 18-19, 2024, Transilvania University of Braşov, Scientifical Coordinator - Assoc. Prof. Dr. Eng. Calin-Octavian Miclosina.
3. The 3DEXPERIENCE Platform, https://www.3ds.com/3dexperience (downloaded on 7.05.2024)
4. I.G.Ghionea, *CATIA V5. Aplicatii in Inginerie Mecanică,* Editura Bren, Bucuresti, 2007.
5. C.O. Miclosina, *Bazele Proiectării Asistate de Calculator*, Editura Eftimie Murgu, Reşiţa, 2018.

6. S.M. Kumar, B.S.D.Sagar, V. Prema, A.R.A.Chandra, B.G. Suhas, *Modelling and Simulation of Bifurcated Winding Induction Generator using 3DEXPERIENCE*, 2022 IEEE 4th Global Power, Energy and Communication Conference (IEEE GPECOM2022), Jun. 14-17, 2022, Cappadocia, Turkey, pp. 216-221.
7. C.R. Rao, V. Prema, A.N. Nagashree, R.S. Geetha, *Development of virtual lab module for wind and solar energy systems using 3DEXPERIENCE platform of Dassault Systemes*, International Conference on Sustainable Materials, Manufacturing and Renewable Technologies (I-SMaRT), Apr. 22-23, 2021, Materials Today Proceedings, vol. 7, part 15, pp. 4978-4987,

Addresses:

- Stud. Razvan-George Olingheru, Faculty of Engineering, Babeş-Bolyai University Cluj-Napoca, Romania, Piaţa Traian Vuia, nr. 1-4, 320085, Reşiţa
  razvan.olingheru@stud.ubbcluj.ro
  (*corresponding author*)
- Stud. Adrian-Bogdan Olariu, Faculty of Engineering, Babeş-Bolyai University Cluj-Napoca, Romania, Piaţa Traian Vuia, nr. 1-4, 320085, Reşiţa,
  adrian.olariu@stud.ubbcluj.ro
- Assoc. Prof. Dr. Eng. Calin-Octavian Miclosina, Department of Engineering Science, Faculty of Engineering, Babeş-Bolyai University Cluj-Napoca, Romania, Piaţa Traian Vuia, nr. 1-4, 320085, Reşiţa
  calin.miclosina@ubbcluj.ro

FocusedDFT: A DFT implementation for vibration-based structural damage detection

Petar Prvulović ID

Abstract. *This paper introduces focusedDFT, a novel Discrete Fourier Transform (DFT) implementation optimized for short signals with low frequency components, particularly where a single frequency component is of interest. The results suggest focusedDFT as a viable and efficient solution for vibration-based damage detection methods, offering improved execution times compared to traditional DFT approaches.*

Keywords: *focusedDFT, DFT, frequency bins, vibration-based damage detection*

1. Introduction

Detecting structural defects and cracks is crucial in mechanical engineering, impacting safety, reliability, and the longevity of structures. Damage from stress, fatigue, environmental factors, material flaws, or vibrations can lead to serious failures, making early detection essential. Vibration-based damage detection has emerged as a valuable non-destructive method, leveraging a structure's dynamic response to identify potential defects. Vibration-based damage detection involves analyzing changes in natural frequencies, typically by recording vibrations with sensors and extracting frequency components using Fourier transforms. The Discrete Fourier Transform (DFT) converts signals from the time domain to the frequency domain, which allows engineers to pinpoint frequency components that may indicate structural damage. However, precise frequency detection is challenging due to the discrete nature of digital computation.

One way to improve precision is to adjust the signal length by cropping or padding, which changes the frequency bin resolution and moves the bins closer to the actual monitored frequency. This approach can reduce spectral leakage and increase spectral amplitudes, as signal energy is less dispersed to neighboring bins. Methods

based on this idea iteratively recalculate the DFT for various signal lengths. A drawback of standard Fast Fourier Transform (FFT) implementations in this case is that they often split the signal into chunks of specific lengths, typically powers of two, in order to improve the efficiency, which can introduce unwanted effects like spectral leakage and interfere with intended signal length manipulation.

In vibration-based damage detection, high precision is required, and it often involves short signals with low frequency components and non-integer number of periods. A "clean" DFT algorithm is preferred in this case as it doesn't interfere with signal length manipulation. The challenge with DFT is its order of complexity which can be slow when used in iterative signal length manipulation.

This paper introduces *focusedDFT*, a DFT implementation suited for processing short signals with low frequency components, targeting a single frequency component. This implementation processes only a specified range of frequency bins around the targeted frequency, offering execution times practical for the intended application.

The paper is organized as follows: Section 2 discusses background information and related work. Section 3 introduces the algorithm implementation and helper functions in Python. Section 4 presents the results of testing the helper functions and implemented DFT algorithm output, comparing execution times to NumPy's FFT. Section 5 discusses the results and the potential for *focusedDFT* use in methods for improving DFT precision.

2. Background and Related Work

Vibration-based structural damage detection requires precise analysis of acquired signals, as damage is detected by noticing changes in the natural frequencies of the structure. In these cases, signals are often short and contain low-frequency components, typically below 100 Hz [1]. The discrete nature of the Discrete Fourier Transform (DFT) results in a set of discrete frequency bins, where the exact frequency may not be captured, causing the signal's energy to be spread to neighboring bins, leading to spectral leakage. Various interpolation methods can mitigate this issue to some extent. However, these methods may produce poor results when low-frequency components are close and neighboring bins overlap. One possible approach involves gradually changing the signal length by cropping or padding to adjust the frequency bin resolution, moving frequency bins closer to the actual frequency of the targeted component [1-4]. Standard Fast Fourier Transform (FFT) implementations enhance efficiency by chunking the signal into lengths that are powers of two, but this can interfere with the aforementioned approach [5], The DFT's complexity is generally acceptable for processing short signals, but it becomes problematic with iterative signal length manipulation as execution time increases.

Focusing on the frequency range of interest can reduce the number of iterations and provide a faster DFT implementation without compromising precision. This paper introduces focusedDFT, a targeted approach to processing short signals with low-frequency components efficiently and accurately.

3. Discrete Fourier Transform

Discrete Fourier transform formula is:

$$X_k = \sum_{n=0}^{N-1} x_n e^{-i2\pi\frac{k}{N}n} \tag{1}$$

where N represents number of samples in the signal and X_k represents the value of k-th frequency bin in signal spectrum. This sum can be implemented as a for loop which n over the range [0, N-1] for each k frequency bin. The part $\frac{2\pi}{N}$ can be extracted into variable D, which is calculated before the loop, to save on total execution time, as defined in formula 2:

$$D = \frac{2\pi}{N} \tag{2}$$

By applying the Euler's formula (3) e^{ix} can be replaced with sum of sines and cosines. This improves the DFT implementation in two ways: sinus and cosines in Python are using native C functions which use precalculated tables, which should be faster than calculating the power of e, and imaginary and real part are separate so there is no need to introduce additional libraries or helper functions to deal with that part.

$$e^{ix} = \cos(x) + i\sin(x) \tag{3}$$

After applying formulas 2 and 3 into formula 1 we get the following expression:

$$X_k = \sum_{n=0}^{N-1} x_n \cdot \cos(-knD) + ix_n \cdot \sin(-knD) \tag{4}$$

which can be further simplified by identities:

$$\cos(-\alpha) = cos(\alpha)$$
$$\sin(-\alpha) = -sin(\alpha) \tag{5}$$

which brings the following formula:

$$X_k = \sum_{n=0}^{N-1} x_n \cdot \cos(knD) - ix_n \cdot \sin(knD) \tag{6}$$

X_k values are complex numbers and need to be converted to real numbers to form the signal spectrum. As each X_k contains real and imaginary part, which are on their respective axes, Euclidean distance of the (Re,Im) coordinate from x axis is calculated and used for signal spectra. If formula 6 is represented as

sum of Real and Imaginary parts, as shown in formula 7, k-th frequency bin value is calculated per formula 8.

$$X_k = \sum_{n=0}^{N-1}(Re - Im) = \sum_{n=0}^{N-1}Re - \sum_{n=0}^{N-1}Im = SRe - SIm \qquad (7)$$

$$X'_k = \sqrt{SRe^2 + SIm^2} \qquad (8)$$

This can be implemented as a double for loop which iterates k over the range [0, length(signal)) and for each k iterates n over the range [0, N-1]. As we are concerned about only a specific range of frequency bins around the targeted frequency, outer loop can iterate over that range only, which is a basis for the FocusedDFT.

4. Methodology and materials

The FocusedDFT was implemented as a function *focused_dft* in Python. To test the function, we created a test script, and a helper function called generateSignal to generate sinusoidal signals with desired frequency components, amplitudes, and phase shifts for a given sampling rate. This function generates an array of double-type values.

FocusedDFT was designed to calculate the DFT in a straightforward manner, looping through the signal with two nested loops to compute the spectrum. This function returns an array of double-type values representing the spectrum. To save on computation time, the function supports limiting the frequency range for calculation. For iterative signal length manipulation, the function also supports signal padding and cropping for the desired number of samples from the start or end of the signal array.

We used the standard FFT function from the numpy package, *numpy.fft.fft,* to test the correctness of the implemented function. An experiment was designed to generate simple and complex sinusoids, calculate the DFT and FFT of these generated signals, and compare the resulting spectra. Execution time of *focused_dft* and *numpy.fft.fft* was compared for short and long signals, both for signals whose lengths are powers of 2, which are typically suitable for FFT, and for slightly different lengths. Below is the description of each segment of the experiment. Section 4 provides the results.

4.1. Signal generation function

The signal generation function creates a sinusoid with specified frequency components, phase offsets, amplitudes, sample rate, and duration in seconds. The function signature is:

```
generateSignal(frequencyComponents, phaseOffsets, amplitudes,
                sample_rate, duration)
```

The return value is an array of double values with *sample_rate * duration* elements. The function returns an array of double values with sample_rate * duration elements. It starts with an array of zeros and iterates through each frequency component, adding the appropriate value to the corresponding index based on the given parameters. Below is the Python implementation of the function:

Code Listing 1: Function for Signal Generation

```
def generateSignal(frequencyComponents, phaseOffsets, amplitudes,
                    sample_rate, duration):
  numSamples = sample_rate * duration
  signal = [0] * numSamples
  sampleX = [i/sample_rate for i in range(sample_rate * duration)]
  for i in range(0,len(frequencyComponents)):
    for j in range(0,numSamples):
      signal[j] += amplitudes[i]
              * math.sin(2*math.pi*frequencyComponents[i]*sampleX[j]
                         + phaseOffsets[i] )
  return signal
```

The function was tested by generating sinusoidal signals with integer and non-integer numbers of periods, featuring 1, 2, and 3 frequency components, with and without phase shifts. Table 1 lists all the parameters, and Figure 1 shows the generated signals. The sample rate is 10,000 samples/sec in all cases.

Table 1. Results for DFT and FFT

Signal	Duration (sec)	No. of periods	Frequency components	Amplitudes	Phases
I1	1	Integer	10	1	0
I2	1	Integer	10	1	π
I3	1	Integer	10, 50	5, 1	0, 0
I4	1	Integer	10, 50	5, 1	$\pi, \pi/2$
I5	1	Integer	5, 10, 50	1, 5, 2	$0, \pi, \pi/2$
N1	1.03	Non-integer	10	1	0
N2	1.03	Non-integer	10	1	π
N3	1.03	Non-integer	10, 50	5, 1	0, 0
N4	1.03	Non-integer	10, 50	5, 1	$\pi, \pi/2$
N5	1.03	Non-integer	5, 10, 50	1, 5, 2	$0, \pi, \pi/2$
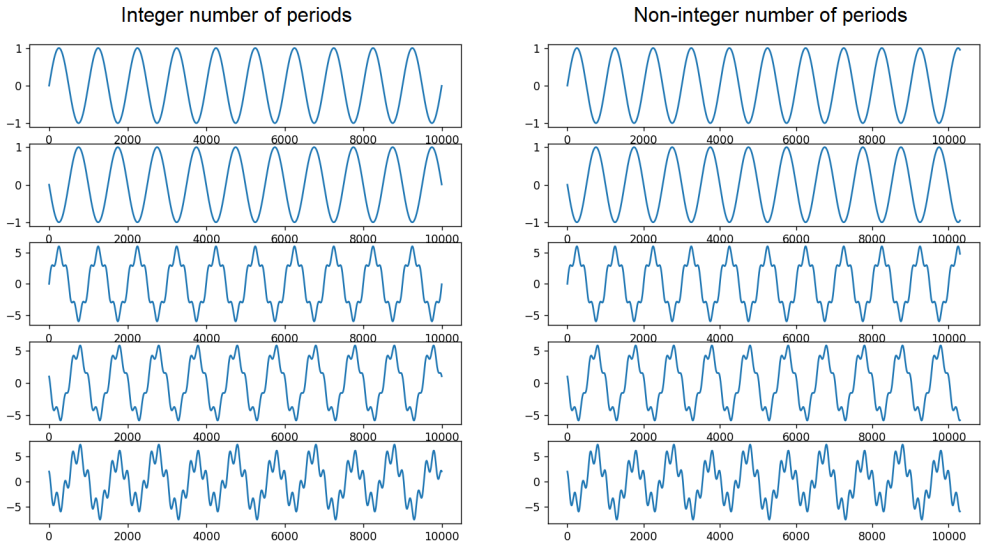
Figure 1. Output of generateSignal() function

### *4.2. DFT function*

The experiment used two functions for computing Fourier Transforms: a custom DFT implementation and the standard FFT from the numpy package. The DFT function has the following signature:

```
focused_dft(signal, freq_from=None, freq_to=None, sample_rate=None,
            left_padding=0, right_padding=0)
```

The parameters include: the signal (an array of double values), an optional frequency range to calculate the DFT (to accelerate computation when interested in a specific spectral component), the sample rate (needed when frequency range is provided), and optional sample counts to add to the beginning or end of the signal (left and right padding). The return value is an array of double values representing the left half of the spectrum, as DFT generates a symmetric spectrum.

Figure 2 shows the spectra obtained from the FocusedDFT and FFT functions for generated signals noted in Table 1, zoomed in on the parts with frequency components. FocusedDFT was used without focusing on a specific frequency to obtain a full spectrum. It is evident that both FocusedDFT and FFT produce the same spectra, detecting the same frequency components as expected from the generated signals.
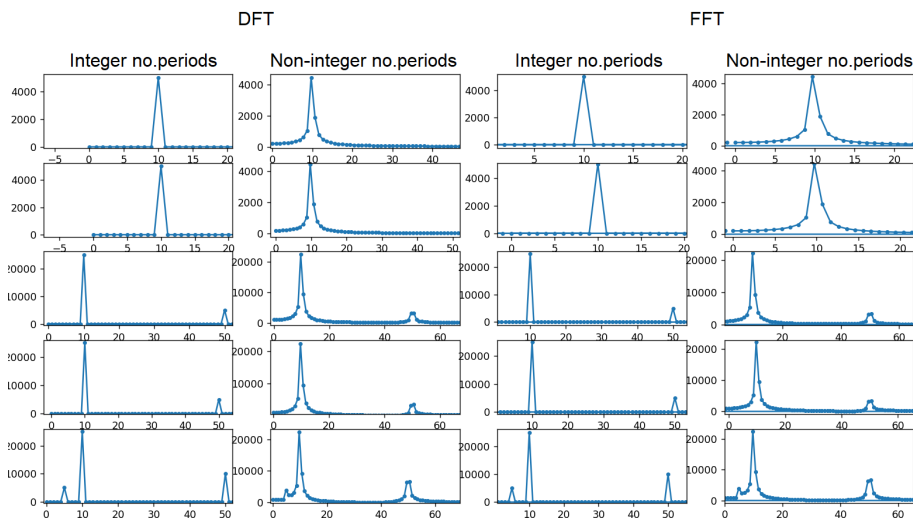
Figure 2. DFT and FFT spectra of generated signals

To test the FocusedDFT with focus on a specific range of frequencies, spectra of DFT and FocusedDFT for range [8.5, 11.5] Hz was calculated over the generated signals noted in Table 1. The resulting spectra, zoomed in on the parts where frequency components are present, are shown in Figure 3. It can be seen that FocusedDFT produces accurate spectra with only 10Hz component, ignoring the rest of the frequency bins, as intended.
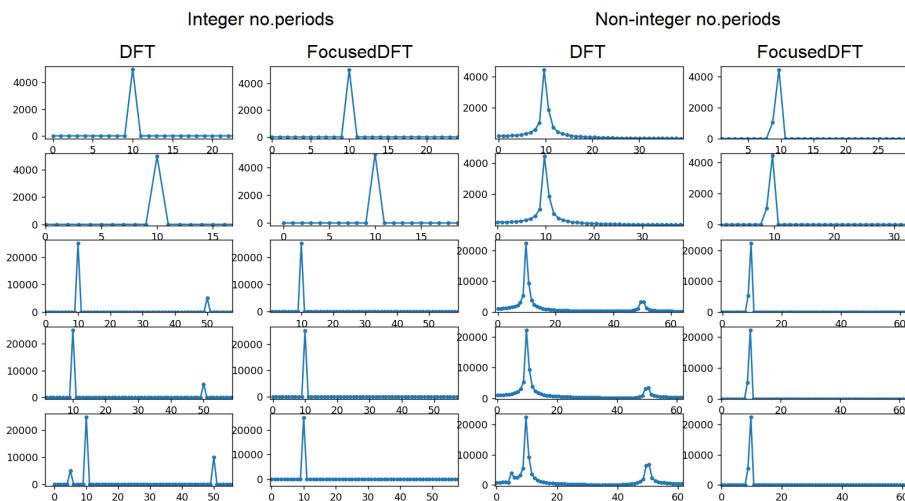
Figure 3. FocusedDFT and DFT spectra of generated signals

The DFT function implementation includes logic for signal padding and cropping based on the provided parameters. It then uses two nested loops to calculate the real and imaginary components, which are combined using Euclidean distance to produce the resulting spectrum, as derived in formula 8. The core of the code for the DFT function is shown in Code Listing 2.

Code listing 2. FocusedDFT function

```
def focused_dft(signal_original, freq_from=None, freq_to=None,
                sample_rate=None, left_padding=0, right_padding=0):
  # left and right signal padding and cropping ...
  # dft
  Xreal = numpy.zeros(N)
  Ximag = numpy.zeros(N)
  X = numpy.zeros(N)
  for k in range(k_range_from, k_range_to):
    for n in range(0, N):
      Xreal[k] = Xreal[k] + signal[n]*math.cos(k*n*2*math.pi/N)
      Ximag[k] = Ximag[k] - signal[n]*math.sin(k*n*2*math.pi/N)
    X[k] = math.sqrt( Xreal[k]**2 + Ximag[k]**2 )
  return X
```

To generate the frequency array (x-axis) for the frequency bins, a function called *frequencyBins* was implemented, which calculates these values based on the length of the spectrum array and the sample rate. The function is provided in Code Listing 3.

Code Listing 3: Frequency Bins Function

```
def frequencyBins(dft_spectrum, sample_rate):
  N = len(dft_spectrum)
  frequencyResolution = sample_rate / N
  frequencyBins = [ i * frequencyResolution for i in range(N) ]
  return frequencyBins
```

4.3. Execution time

To measure and compare the execution time, FocusedDFT and FFT were executed over 4 generated signals: a short signal, simulating the expected case in vibration-based damage detection; a long signal, for comprehensive measurement; a signal

whose length is a power of 2, which is supposedly suitable for FFT; and a signal whose length is a slightly different from the previous one, which should be unsuitable for FFT but indifferent for FocusedDFT. The generated signals are listed in Table 2.

Table 2. Test signals

Signal	Sample rate	Length (sec)	Frequency components	Amplitudes	Phases
S1 - Short	1000	1	10, 50	5, 1	1, 2
S2 - Long	22000	1	10, 50	5, 1	1, 2
S3 - FFT suitable	1024	1	10, 50	5, 1	1, 2
S4 - FFT unsuitable	1027	1	10, 50	5, 1	1, 2

5. Results

In the experiment, 4 signals were generated, followed by applying the DFT over entire spectrum, FocusedDFT around the target component of 10Hz, and FFT. Experiment was run on Intel i5-1035G1 CPU, on Windows 10. To avoid possible increase in execution time due to randomly activated background processes, each test was executed 4 times. Measured execution times and calculated average times are listed in Table 3.

Table 3. Execution times in ms

DFT type	Signal	Test 1	Test 2	Test 3	Test 4	Rounded average
DFT	S1	380419.7	376956.7	370383.1	366535.3	373573
	S2	169263715.6	172438375.3	171855072.3	172453596.9	171502690
	S3	378081.9	380420.5	378003.3	377855.1	378590
	S4	379929.9	377849.8	387159.4	385697.9	382659
Focused DFT	S1	2950.9	3111.1	2905.2	2986.2	2988
	S2	56586.3	54741.4	59146.4	58865.2	57335
	S3	2561.9	3020.4	2321.4	2268	2543
	S4	3034.4	2442.3	3016.0	2762.7	2814
FFT	S1	188.2	142.4	149.7	143.9	156
	S2	2768.6	2229	2379.5	3081.8	2615
	S3	104.4	75	90.1	107.1	94
	S4	135.5	92.9	141.5	150.9	130

As expected, execution time for DFT is significantly longer then Focused DFT and FFT. In case of S3-signal with 1024 samples, which should be suitable for FFT, and S4-signal with 1027 samples, which should be unsuitable for FFT, it is visible that DFT execution time proportionally increases, which is not the case with FFT.

6. Discussion

The implemented DFT produces accurate results, aligning closely with the Fast Fourier Transform (FFT) in identifying frequency components, as depicted in figures 2 and 3. Table 3 illustrates that the Focused DFT is approximately 20 times slower than FFT for signals containing 1000 samples.

The primary application for the Focused DFT lies in vibration-based damage detection methods, which prioritize precision in identifying specific frequency components. These methods manipulate signal length to refine frequency binning, a process where FFT implementations often fall short due to inherent signal chunking. By adjusting the signal length to accommodate an integer number of periods of the targeted frequency, precision is optimized. For instance, for a 10Hz signal, adjustments up to 1/10th of the original length may be necessary, requiring several hundred iterations and potential DFT recalculations. However, experiments demonstrate that executing Focused DFT for a 1000-sample signal takes approximately 3ms, allowing for 300 iterations per second. With a total execution time of several seconds, the Focused DFT emerges as a viable solution in this context

7. Conclusion

Vibration-based damage detection is a popular non-intrusive approach which heavily relies on precise signal processing. DFT is an important part of this process. Small frequency changes are important and need to be captured. The discrete nature of computer systems and data acquisition poses challenges to precision, particularly regarding frequency bin resolution. While spectral interpolation may seem like a solution, in some specific cases it falls short in practice. Manipulating signal length to align with frequency bin resolution proves to be a successful strategy, albeit one that demands multiple DFT calculations across varying signal lengths. FFT implementations in this case fail to provide good results due to inherent signal chunking. Traditional DFT implementation is slow and total execution time can be problematic.

In the case of vibration-based damage detection FFT can be used for an initial processing of the acquired signal to get the quick insight of the spectra and spectral components present. The engineer can then focus on a specific frequency component and direct the algorithm to provide the precise frequency within that focused frequency range, by manipulating the signal length and frequency bin resolution. FocusedDFT

execution time is acceptable, it doesn't suffer from long execution time like DFT does and doesn't interfere with signal length as FFT does. FocusedDFT can be used as a viable alternative in such methods.

Future research efforts could be directed to employ FocusedDFT in PyFEST and similar methods in order to improve their execution time without compromising the precision.

References

1. X. Sun, S. Ilanko, Y. Mochida, R.C Tighe., A Review on Vibration-Based Damage Detection Methods for Civil Structures, *Vibration*, 6(4), Art. no. 4, Dec. 2023, doi: 10.3390/vibration6040051
2. D. Nedelcu, G.-R. Gillich, A structural health monitoring Python code to detect small changes in frequencies, *Mech. Syst. Signal Process.*, vol. 147, p. 107087, Jan. 2021, doi: 10.1016/j.ymssp.2020.107087.
3. G.-R. Gillich, N.N.N. Maia, I.C. Mituletu, *Problem of Detecting Damage Through Natural Frequency Changes*, in Computational and Experimental Methods in Structures, vol. 10, WORLD SCIENTIFIC (EUROPE), 2018, pp. 105–139. doi: 10.1142/9781786344977_0004.
4. C. Chioncel, N. Gillich, O. Tirian, J.L Ntakpe, Limits of the Discrete Fourier Transform in Exact Identifying of the Vibrations Frequency, *Romanian J. Acoust. Vib.*, 12(1), pp. 16–19, Jan. 2015.
5. L. Jin, L. Liang, A power-of-two FFT algorithm and structure for DRM receiver, *IEEE Trans. Consumer Electron*., 56(4), pp. 2061–2066, Nov. 2010, doi: 10.1109/TCE.2010.5681072.

Address:

- Petar Prvulović, School of Computing, Union University, Kneza Mihaila 6/6, Belgrade, Serbia
  pprvulovic@raf.rs

The effect of the signal initial phase on the amplitudes of a DFT spectrum

Daniela Giorgiana Burtea [ID], Nicoleta Gillich* [ID], Gilbert-Rainer Gillich [ID]

Abstract. *Knowing the amplitudes in a spectrum calculated using the Discrete Fourier Transform (DFT) algorithm is essential for precisely estimating the frequencies of a real-valued signal. Since the amplitudes are affected by the signal's initial phase, it is crucial to consider this aspect when estimating the signal frequencies. This paper presents the initial signal phase's effect on the values calculated for the real and imaginary parts and the magnitudes in the DFT of a real-valued signal. Analyzing the evolution of the amplitudes with the initial phase for a complete cycle for the initial phase, we found that the values in the magnitude DFT are subject to minor alteration, while the values of the real and imaginary parts of the DFT are strongly affected by the initial phase.*

Keywords: *Discrete Fourier Transform, amplitude spectrum, frequency estimation, initial phase*

1. Introduction

The literature is rich with studies on accurately estimating the frequencies and amplitudes of signals [1]. Most often, the frequencies are located on an inter-beam position in the spectrum, thus requiring supplementary processing such as interpolation algorithms for finer frequency estimation. An in-depth approach to this topic is presented in [2]. The interpolation is made using two or three points in the real part of the DFT or the magnitude DFT. The main idea is to find a correction coefficient, which represents the distance between the actual frequency and the frequency found using a standard DFT. Several papers presenting these algorithms are [3]- [13]. Thus, knowing the amplitudes for a given context is crucial for the precision of frequency estimation algorithms. However, no papers have considered the initial phase of the signal in a special way when estimating the frequencies.

In our previous research [14]-[16], we developed a frequency estimation technique supported by Machine Learning (ML) to find the frequency at an inter-line position. This technique finds the correction coefficient using an Artificial Neural Network (ANN) that has as inputs the biggest values in the magnitude DFT.

By applying the ANN-supported algorithm, we observed that the estimation precision decreases if the signal has the initial phase differing from zero. The inaccuracy occurs because the amplitudes in the magnitude DFT present slight changes if the signal has an initial phase. To better train the network, we propose using as input in the ANN not just the biggest values in the magnitude DFT but also those real and the imaginary parts of the DFT. This paper presents the spectral values' dependency on the initial signal phase.

2. Theoretical background

The real Discrete Fourier Transform decomposes an input signal $x[n]$, having N discrete samples taken over time into two output signals that contain the amplitudes of the component sine and cosine waves. The output signals have $N/2+1$ points that represent the frequencies of the sine and cosine waves in which the input signal $x[n]$ is decomposed. The input signal is said to be in the time domain, while the output signals are representations in the frequency domain. A schematic of the process is presented in Figure 1.
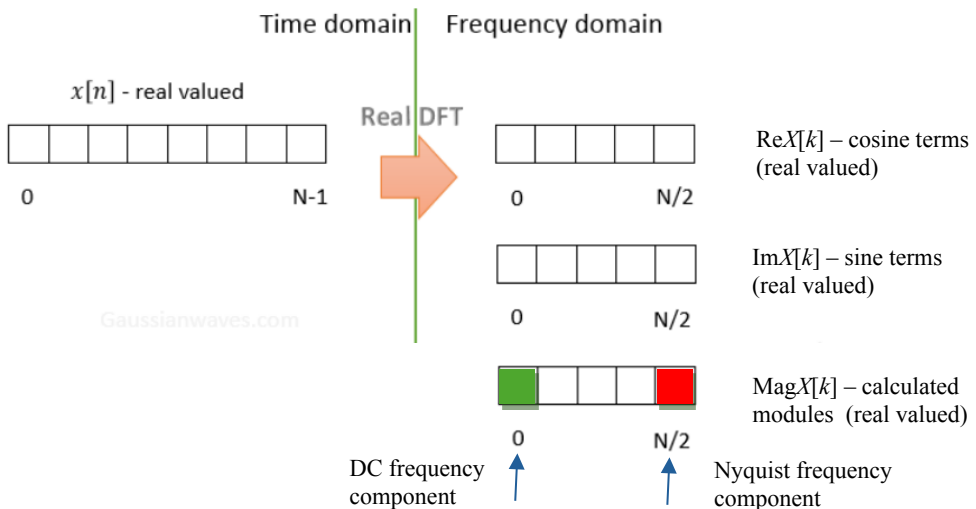
Figure 1. The real DFT

Let us consider the discrete-time sinusoid. It can be expressed

$$x[n] = A\sin(2\pi f_R \frac{n}{f_S} + \varphi_0) \tag{1}$$

where A is the signal amplitude, f_R is the actual signal frequency, f_S is the sampling rate, and φ_0 is the initial phase expressed in radians. In the above equation, n is the sample number, which takes values between 0 and N-1.

The mathematical relation to calculate the values for the amplitude on the k-th spectral bin of the real part is

$$\operatorname{Re} X[k] = \frac{2}{N} \sum_{n=0}^{N-1} x[n]\cos(2\pi k \frac{n}{N}) \tag{2}$$

while the amplitude on the k-th spectral bin of the imaginary part is calculated with the mathematical relation

$$\operatorname{Im} X[k] = -\frac{2}{N} \sum_{n=0}^{N-1} x[n]\sin(2\pi k \frac{n}{N}) \tag{3}$$

With these two sets of values, the $N/2+1$ values of the magnitude DFT for the individual spectral bins are calculated with the mathematical relation

$$\operatorname{Mag} X[k] = \sqrt{\left(\operatorname{Re} X[k]\right)^2 + \left(\operatorname{Im} X[k]\right)^2} \tag{4}$$

We denote the biggest amplitude in the magnitude DFT as A_{max}, the value found at its left as $A_{pre\text{-}max}$, and the value found at its right as $A_{post\text{-}max}$. Similarly, for the amplitudes in the real part, we use $R_{pre\text{-}max}$, R_{max}, and $R_{post\text{-}max}$; for the imaginary part, we use $I_{pre\text{-}max}$, I_{max}, and $I_{post\text{-}max}$.

3. Numerical simulation

To find the effect of the initial phase on the amplitudes, we first consider a sinusoidal signal with a given frequency and length and with the initial phase set to zero. For this signal, we calculate, with equations (2)-(4), the values of the real part Re$X[k]$, the imaginary part Im$X[k]$, and the magnitudes Mag$X[k]$. Note that we normalized the values of Re$X[k]$ and Im$X[k]$ by multiplication with 2/N in order to obtain all amplitudes related to the signal.

Next, we iteratively increase the initial phase with a small step until the initial phase achieves 2π. For each step, we identify the picks and its neighbors in the real, imaginary, and magnitude DFT. We associate these values with the frequency f_E found on the spectral line of A_{max} and the actual frequency f_R.

The identified values are stored in a database with the structure presented in Table 2. The database aims to provide data for training an ANN to estimate the correction coefficients and the signal's frequencies accurately. Numerous initial phases are considered in this analysis to complete the database.

Table 1. The structure of the database realized for training the ANN

Role	Parameter	Symbol	Initial phase [rad]		
			0	…	2π
ANN Input	Amplitude [m/s²]	$R_{pre\text{-}max}$			
		R_{max},			
		$R_{post\text{-}max}$			
		$A_{pre\text{-}max}$			
		A_{max}			
		$A_{post\text{-}max}$			
		$I_{pre\text{-}max}$			
		I_{max}			
		$I_{post\text{-}max}$			
Support	Actual frequency [Hz]	f_R			
	Estimated frequency [Hz]	f_E			
ANN Target	Correction coefficient [Hz]	δ			

First, we exemplify the evolution of the amplitudes in several cases. The first signal contains $N = 207$ samples by a sampling rate $f_S = 167$ Hz, resulting in a signal time length $t = 1.23353$ sec, a time resolution $\Delta t = 0.00599$ sec, and a frequency resolution $\Delta f = 0.81068$ Hz. The signal amplitude is $A = 1$ m/s², and the frequency is $f_R = 5$ Hz. As mentioned, we set the initial phase $\varphi_0 = 0$ rad for the first simulation. Afterward, we increase the value of the initial phase with 0.1π until the initial phase achieves 2π.

To have an image of the amplitude/initial phase dependency, we consider it sufficient to present the evolution of the picks in the real part, imaginary part, and magnitude DFT, namely R_{max}, I_{max}, and A_{max}. Note that while the values of R_{max} and I_{max} can be real positives or negatives, the values of A_{max} are always real positives. Figure 2 presents this evolution.

We observe in Figure 2 that the evolution of the picks is sinusoidal/cosinusoidal, which is justified by the mathematical relations that express the real and imaginary part terms.
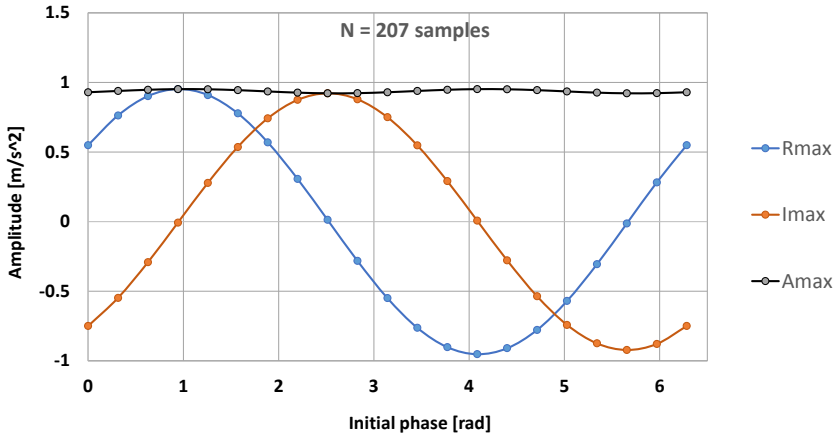
Figure 2. The evolution of the picks with the initial phase for a signal generated with $N = 207$ samples

We now consider a signal generated with $N = 201$ samples to get a more complete image of the phenomenon. This signal length is chosen because it comprises six sinusoids, so its DFT gives a good frequency estimate. The signal amplitude $A = 1$ m/s², the frequency $f_R = 5$ Hz, the sampling rate $f_S = 167$ Hz, and the time resolution $\Delta t = 0.00599$ sec remain unchanged. For these parameters, the length of the second signal becomes $t = 1.1976$ sec, which results in the new frequency resolution $\Delta f = 0.835$ Hz. As in the first case, we set the initial phase $\varphi_0 = 0$ rad for the first simulation and increase it with 0.1π until the initial phase achieves 2π.
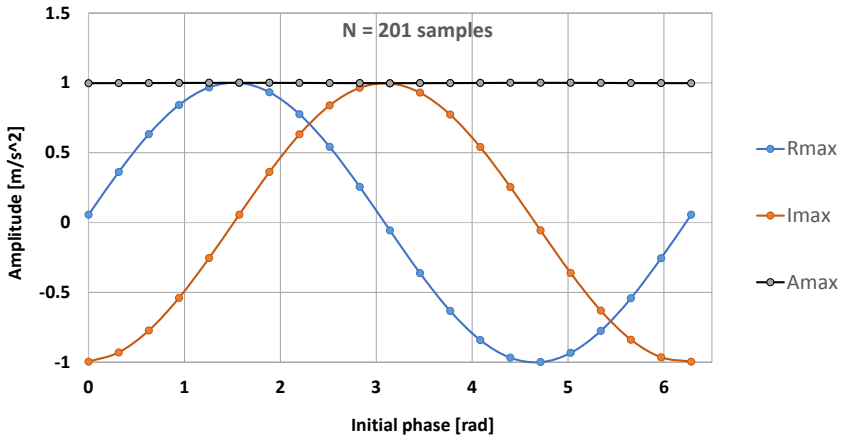
Figure 3. The evolution of the picks with the initial phase for a signal generated with $N = 201$ samples (signal contains six entire cycles)

Figure 3 depicts the pick evolution for the real part, imaginary part, and magnitude DFT, namely R_{max}, I_{max}, and A_{max}, for the signal generated with 201 samples. It can be observed that the A_{max} is much closer to the actual amplitude, and it has a more minor variation.

To have consistent results, we analyze a third signal generated with $N = 204$ samples by maintaining the amplitude, the frequency, the sampling rate, and the time resolution. For these parameters, the signal length becomes $t = 1.21557$ sec and the frequency resolution $\Delta f = 0.82266$ Hz. As in the first case, we set the initial phase $\varphi_0 = 0$ rad for the first simulation and increase it with 0.1π until the initial phase achieves 2π. The obtained results are presented in Figure 4.
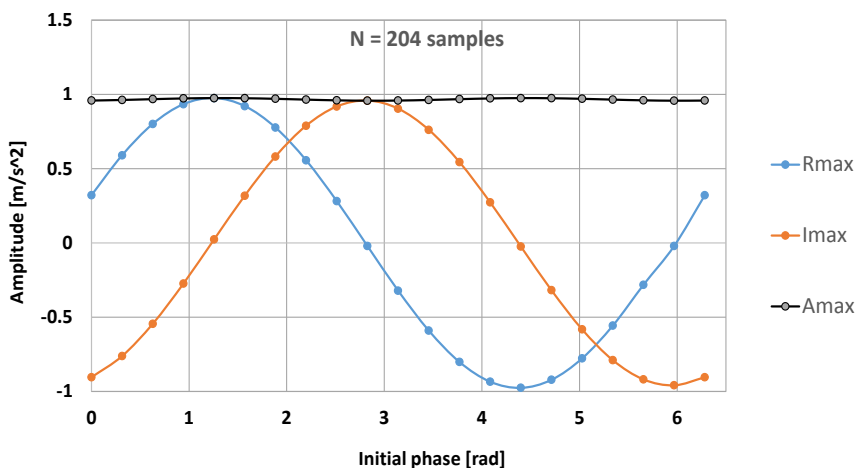

Figure 4. The evolution of the picks with the initial phase for a signal generated with $N = 204$ samples

In Figure 4, we observe that A_{max} is closer to the actual amplitude when compared to the signal containing 207 samples but not so close as those for the signal generated with 201 samples. The amplitude variation is also between the two previously studied cases. This demonstrates that the closer the signal length is to a multiple of the period T, the better the amplitude is found.

A more explicit evolution of A_{max} is shown in Figure 5. It can be observed that, for all signals, the biggest amplitude was not obtained for the initial phase set at zero. It is also remarked that the amplitudes for the signal generated with 207 samples vary between 0.92205 and 0.95195, so the absolute difference is less than 0.015, which means a difference of 1.5%. This difference is relevant for frequency estimation so that the training of the ANN must contain the sets of values derived for all initial phases.

For the shorter signal generated with 204 samples, the amplitudes A_{max} vary between 0.95821 and 0.97535, so the absolute difference is 0.00857, which means a difference of less than 0.857%.
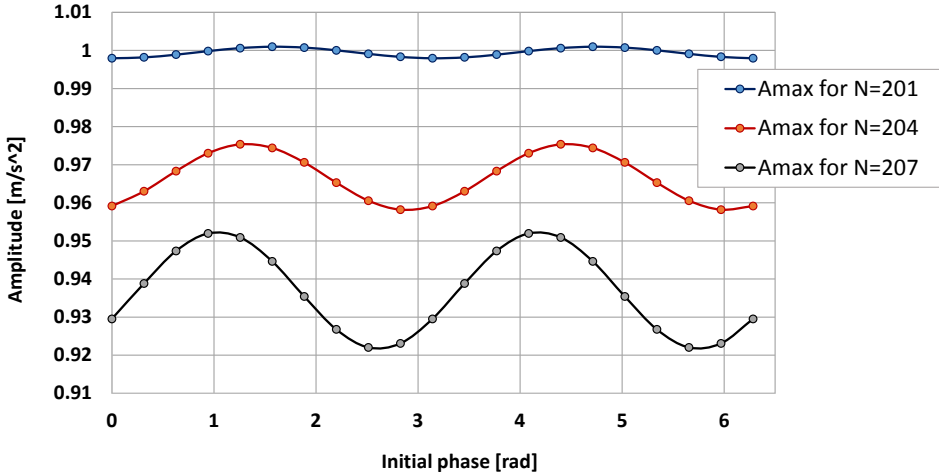
Figure 5. The evolution of A_{max} with the initial phase for different signal lengths

The signal containing six cycles provides the most accurate amplitudes A_{max}, varying between 0.99797 and 1.00096. The absolute difference is 0.0015, which can be neglected in practical applications. However, because the initial phase is not known *a priori*, the input data for the training of the ANN must comprise scenarios for different signal lengths and initial phases.

4. Conclusion

The initial phase influences the amplitudes shown in the magnitude spectrum and the spectra of the real and imaginary parts. For a signal that is a multiple of the signal period T, all amplitudes calculated in the DFT magnitude spectrum, regardless of the initial phase, vary very little around the actual signal amplitude. We found a variation of less than $\pm0.15\%$ for the studied signal.

When the signal is not a multiple of the signal period T, all the calculated amplitudes are smaller than the actual signal amplitude, and the amplitude variation is more significant than in the particular case when the signal comprises an entire number of cycles. For such signals, we found an amplitude variation due to the initial phase change of up to $\pm1.5\%$ for the analyzed signals, but we presume it can be more extensive than that when the signal length is t = $T(m+0.5)$ cycles.

In the following study, we will approach more signal lengths to cover an entire cycle of length *T* representing a signal period. This study, in correlation with the phase shift analysis, will permit the creation of a robust database for ANN training and accurate frequency estimation.

References

1. I. Santamaria, C. Pantaleon, J. Ibanez, A comparative study of high-accuracy frequency estimation methods, *Mechanical Systems and Signal Processing*, 14(5), 2000, pp. 819-834.
2. A.A.Minda, C.I.Barbinita, G.R. Gillich, A Review of Interpolation Methods Used for Frequency Estimation, *Romanian Journal of Acoustics and Vibration*, 17(1), 2020, pp. 21-26.
3. B.G. Quinn, Estimating Frequency by Interpolation Using Fourier Coefficients, *IEEE Transactions on Signal Processing*, 42, 1994, pp. 1264-1268.
4. E. Jacobsen, P. Kootsookos, Fast, accurate frequency estimators, *IEEE Signal Processing Magazine*, 24(3), 2007, pp. 123-125.
5. C.Candan, A method for fine resolution frequency estimation from three DFT samples, *IEEE Signal Processing Letters*, 18(6), 2011, pp. 351-354.
6. J.L Ntakpe, G.R. Gillich, I.C. Mituletu, Z.I. Praisach, N. Gillich, An Accurate Frequency Estimation Algorithm with Application in Modal Analysis, *Romanian Journal of Acoustics and Vibration*, 13(2), 2016, pp. 98-103.
7. T. Grandke, Interpolation Algorithms for Discrete Fourier Transforms of Weighted Signals, *IEEE Transactions on Instrumentation and Measurement*, 32, 1983, pp. 350-355.
8. P. Voglewede, Parabola approximation for peak determination, *Global DSP Magazine*, 3(5), 2004, pp. 13-17.
9. V.K. Jain, W.L. Collins, D.C. Davis, High-Accuracy Analog Measurements via Interpolated FFT, *IEEE Transactions on Instrumentation and Measurement*, 28, 1979, pp. 113-122.
10. G.R. Gillich, I.C. Mituletu, Z.I. Praisach, I. Negru, M. Tufoi, Method to Enhance the Frequency Readability for Detecting Incipient Structural Damage, *Iranian Journal of Science and Technology, Transactions of Mechanical Engineering*, 41(3), 2017, pp. 233–242.
11. E. Aboutanios, B. Mulgrew, Iterative frequency estimation by interpolation on Fourier coefficients, *IEEE Transactions on Signal Processing*, 53(4), 2005, pp. 1237-1242.
12. K. Ding, C. Zheng, Z. Yang, Frequency Estimation Accuracy Analysis and Improvement of Energy Barycenter Correction Method for Discrete Spectrum, *Journal of Mechanical Engineering*, 46(5), 2010, pp. 43-48.

13. J.Z. Xiang, S. Qing, C. Wei, A novel single tone frequency estimation by interpolation using DFT samples with zeropadding, in: Proc. IEEE ICSP, Chengdu, China, Mar. 2017, pp. 277-281.
14. C. Tufisi, A.A. Minda, D.G. Burtea, G.R. Gillich, Frequency Estimation using Spectral Techniques with the Support of a Deep Learning Method, *Romanian Journal of Acoustics and Vibration*, 19(1), 2022, pp. 49-55.
15. D.G. Burtea, G.R. Gillich, C. Tufisi, Estimating the frequencies of vibration signals using a machine learning algorithm with explained predictions, *Vibroengineering Procedia*, 51, 2023, pp. 160-166.
16. D.G. Burtea, E.V. Gillich, C. Tufisi, Tudor L., Estimation of The Frequency of Very Short Signals by Involving Artificial Neural Networks, *Romanian Journal of Acoustics and Vibration*, 20(2), 2023, pp. 157-161

Addresses:

- Ph.D. Stud. Eng. Daniela Giorgiana Burtea, Doctoral School of Engineering, Babeş-Bolyai University, Cluj-Napoca, Romania, Piaţa Traian Vuia, nr. 1-4, 320085, Reşiţa
  daniela.burtea@ubbcluj.ro
- Prof. Dr. Eng. Nicoleta Gillich, Department of Engineering Science, Faculty of Engineering, Babeş-Bolyai University Cluj-Napoca, Romania, Piaţa Traian Vuia, nr. 1-4, 320085, Reşiţa
  nicoleta.gillich@ubbcluj.ro
  (*corresponding author*)
- Prof. Dr. Eng. Gilbert-Rainer Gillich, Department of Engineering Science, Faculty of Engineering, Babeş-Bolyai University Cluj-Napoca, Romania, Piaţa Traian Vuia, nr. 1-4, 320085, Reşiţa
  gilbert.gillich@ubbcluj.ro

Dynamic behavior of a Warren truss beam upon loosening of a bolt in a truss node

Dan Alexandru Pîrşan

Abstract. *The present work aims to show our practical achievements made in the laboratory of the UBB Resita faculty, where on Warren truss hinged at both ends, we studied the negative impact of loosening a bolt in a truss node that has them on natural frequency. Based on the bolt tightening, the specimen had three different states: healthy state, damage state I, and damage state II.*

Keywords: *Warren truss, mode shape, natural frequency*

1. Introduction

Warren truss are popularly used in various engineering fields [1, 2, 3, 4], through experimental tests in the laboratory of Babes-Bolyai University we tested the dynamic behavior of a truss Figure 1, by gradually tightening a screw from the node .and among them, steel tubular trusses have been widely applied in large engineering structures, such as the International Space Station, bridges, concert halls and electricity poles, thanks to their architecturally attractive and favorable forms structural properties [5]. The geometry of the truss elements and the properties of the material are modified, and with them, the modal parameters of the structure are also changed [6]

With the help of LabVIEW data acquisition mode, which receives the signal from the 2 accelerometers [7], and transmits it to the compact NI cDAQ-9172[8] chassis, we export the extracted data in the PyFEST program, developed in the research center of UBB Resita [9].

The elements in truss were numbered with numbers and the nodes were assigned letters. The fastening of the truss was done with screws M6.

I extracted the natural frequencies on a warren truss, articulated at both ends, where each element is 500 mm long. The free length of the truss are L=1000 mm. The cross-section area is 30 mm and the thickness is 5 mm.
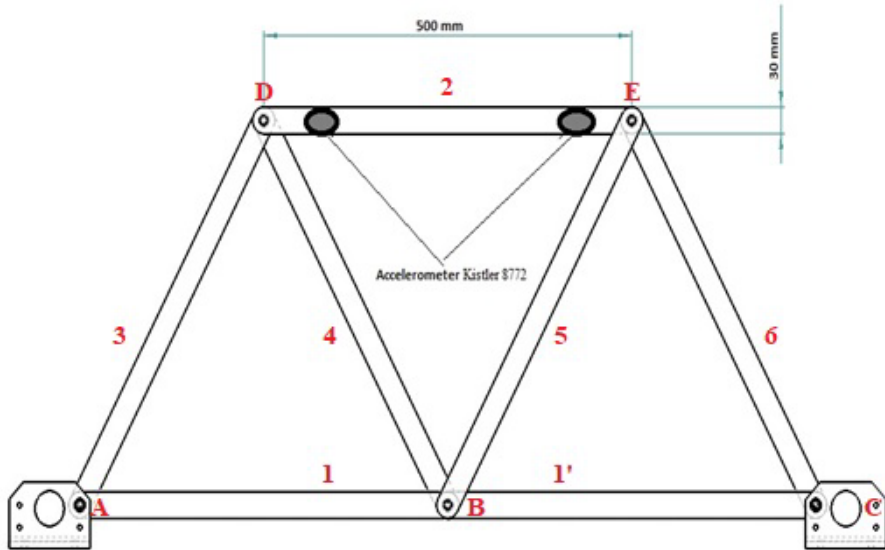

Figure 1. Seven-bar truss

Table 1. The physical-mechanical properties

| Mass density ρ [kg/m³]	Young modulus E [N/m²]	Poisson ratio [-]	Tensile strength [MPa]	Yield strength [MPa]	Min. elongation [%]
7850	$2 \cdot 10^{11}$	0.3	470-630	355	20

2. Steps taken in the laboratory

We fix the beam with the truss on the support then on the number two bar we fix two accelerometers. With the help of the Program implemented in LabVIEW Figure 2, we acquire the signal after which the extracted signal is imported into PyFEST Figure 3, which was developed at UBB Resita.

The data reported from LabVIEW were exported in PyFEST and the resulting data were extracted and presented in the Tables 2 and 4.
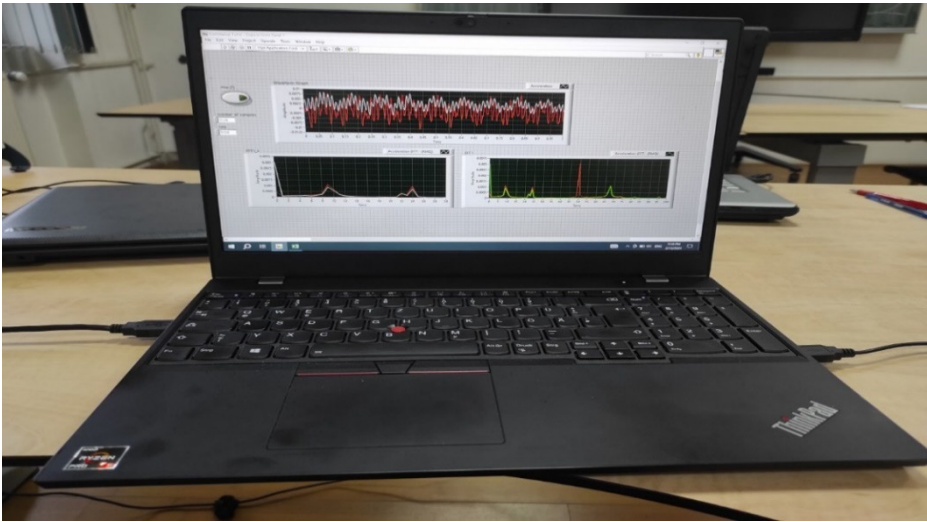
Figure 2. Signal extracted using LabVIEW
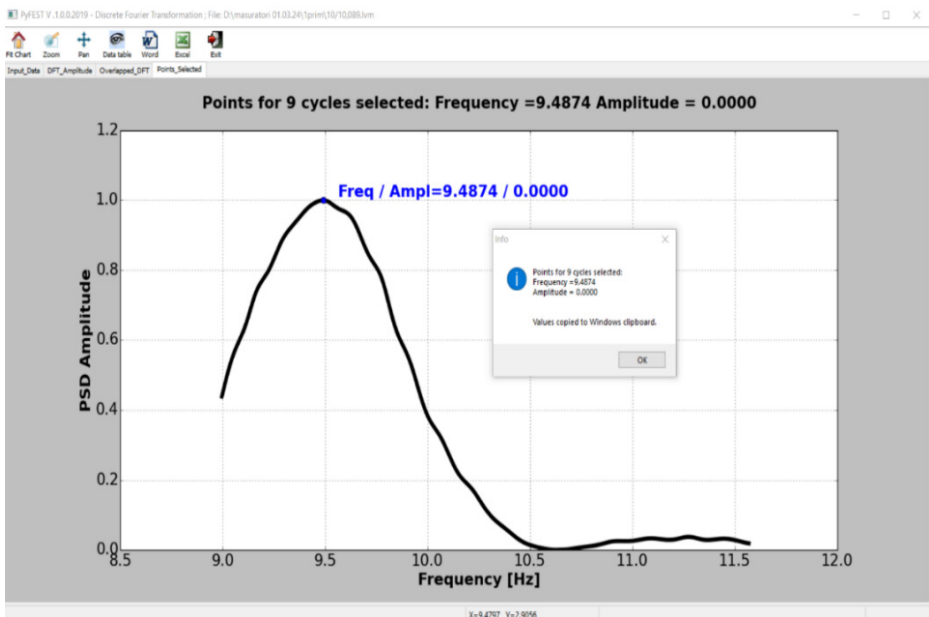
Figure 3. Frequency found with PyFEST

F - Excited frequency in LabVIEW
Fpy- Frequency measured in PyFEST

117

Table 2. Analyzed cases healthy state 20 Nm

Case	Mode 1		Mode 2		Mode 3		Mode 4	
	F [Hz]	Fpy [Hz]	F [Hz]	Fpy [Hz]	F [Hz]	Fpy [Hz]	F [Hz]	Fpy [Hz]
1	10,089	9,377	22,197	21,790	25,003	25,3992	70	73,401
2	10,160	9,379	23,297	21,556	25,103	24,0618	72,003	73,904
3	10,200	9,358	23,397	22,086	25,597	24,1394	72,203	74,706
4	10,321	9,388	23,497	21,766	25,603	25,4479	72,300	73,981

Table 3. Analyzed cases damage state 10 Nm

Case	Mode 1		Mode 2		Mode 3		Mode 4	
	F [Hz]	Fpy [Hz]	F [Hz]	Fpy [Hz]	F [Hz]	Fpy [Hz]	F [Hz]	Fpy [Hz]
1	10,089	9,3849	22,197	21,8112	25,003	21,7628	70	74,099
2	10,160	9,4172	23,297	21,8001	25,103	21,7486	72,003	72,489
3	10,200	9,291	23,397	21,4163	25,597	21,8065	72,203	74,056
4	10,321	9,4051	23,497	21,4605	25,603	23,3408	72,300	72,568

Table 4. Analyzed cases damage state 0 Nm

Case	Mode 1		Mode 2		Mode 3		Mode 4	
	F [Hz]	Fpy [Hz]	F [Hz]	Fpy [Hz]	F [Hz]	Fpy [Hz]	F [Hz]	Fpy [Hz]
1	10,089	10,7096	22,197	22,5186	25,003	24,3441	70	69,033
2	10,160	9,0154	23,297	21,1198	25,103	24,3843	72,003	69,041
3	10,200	9,0164	23,397	23,3739	25,597	25,3486	72,203	69,022
4	10,321	9,0559	23,497	23,9939	25,603	25.3658	72,300	69,025

Table 5. The average of the analyzed cases

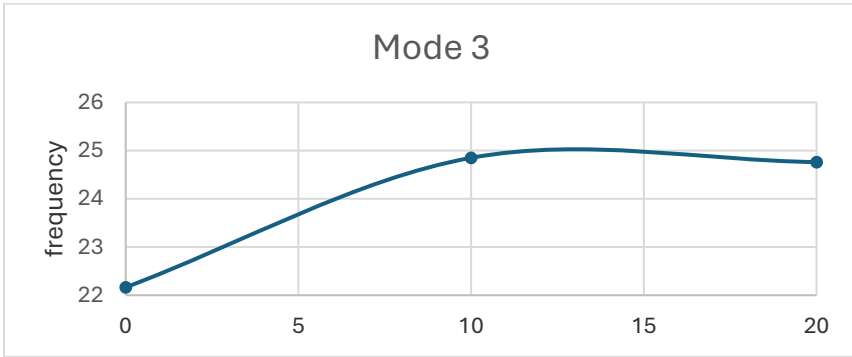| Case	Mode 1	Mode 2	Mode 3	Mode 4
20 Nm	9,368	21,79988	24,76208	73,998425
10 Nm	9,37455	21,81203	24,85065	73,2694
0 Nm	9,449325	22,75155	22,16468	69,03063
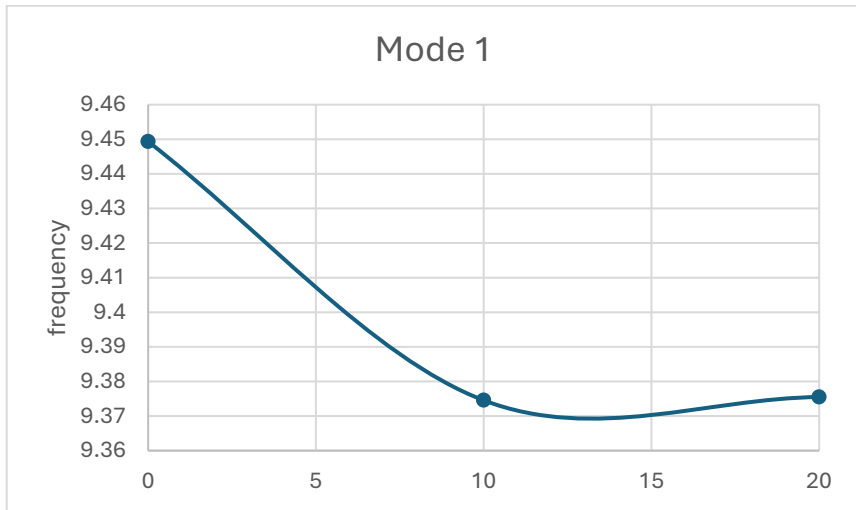
Figure 4. The first mode of vibration
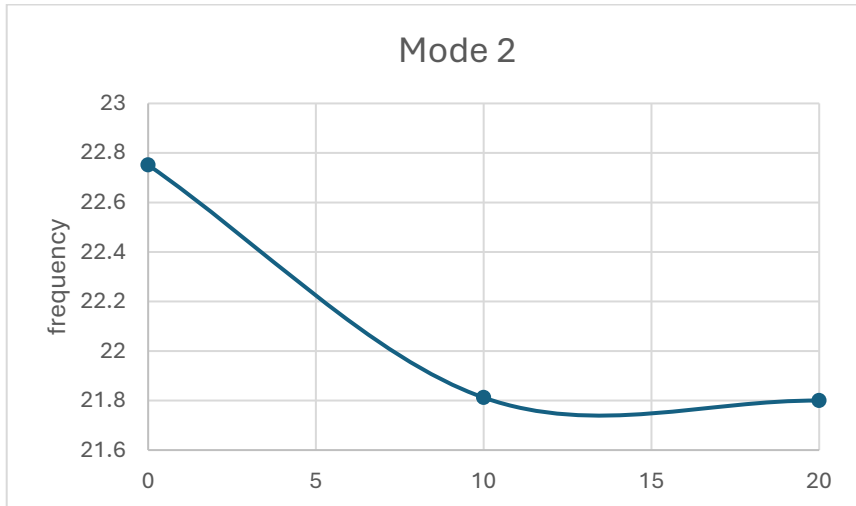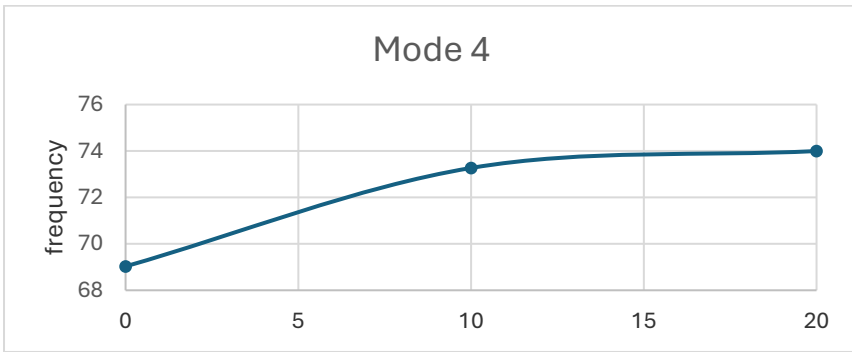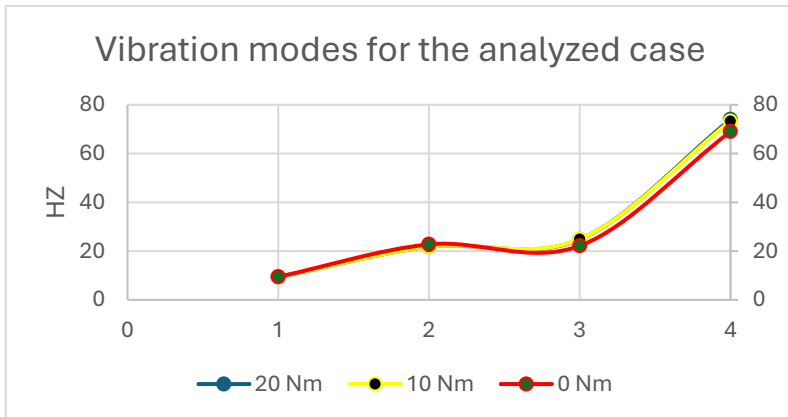

Figure 5. The second mode of vibration

Figure 6. The third mode of vibration

Figure 7. The fourth mode of vibration

Figure 8. Vibration mode

3. Conclusion

The paper presents the eigenfrequencies measured on a Warren beam for the first four modes of vibration, to which for node E a tightening moment was applied from 0 to 20 Nm.

It was established that the natural frequencies of a structure are directly related to its stiffness. As the stiffness increases, the natural frequencies also increase. This means the truss will resonate at higher frequencies when its screws are tightened.

References

1. G.R. Gillich, Z.I. Praisach, Damage-patterns based method to locate discontinuities in beams, *SPIE Smart Structures and Materials& Nondestructive Evaluation and Health Monitoring*, Vol. 8695, March 2013, San Diego CA, 2013;
2. Z.I. Praisach, D.A. Pîrşan, The influence of the change of the lon-gitudinal modulus of elasticity on the dynamic behavior of a Warren truss, *Studia Universitatis Babeș-Bolyai Engineering,* 67(1), 2022, pp. 201-208, DOI: 10.24193/subbeng.2022.1.19
3. G.R. Gillich, Z.I. Praisach, Modal identification and damage detection in beam-like structures using the power spectrum and time–frequency analysis, *Signall Processing,* Elsevier, Vol. 96, 2014, pp. 29-44.
4. D.A. Pîrşan; Z.I. Praisach., Natural frequencies and mode shapes in zero-force members of a truss, *Studia Universitatis Babeș-Bolyai Engineering,* 66(1), 2021, pp. 94-99, DOI: 10.24193/subbeng.2021.1.9
5. J. Wardenier, J.A. Packer, X.L Zhao, G.J.V.D. Vegte, *Hollow Sections in Structural Applications*, CIDECT: Geneva, Switzerland, 2010.
6. L.F. dos Santos Souza, D. Vandepitte, V. Tita, R. de Medeiros, .Dynamic response of laminated composites using design of experiments: an experimental and numerical study, *Mech. Syst. Signal Process*. 115, 2019 pp. 82–101, https://doi.org/10.1016/j.ymssp.2018.05.022.
7. DBK8.8772M10e-12.01.pdf (intertechnology.com) (downloaded on 12.05. 2024)
8. National Instruments Cataloque: NI-9234 Specifications - NI
9. G.R. Gillich, D. Nedelcu, V. Iancu, N. Gillich, About the accuracy of estimated frequencies with the PyFest software, *Annals of the „Constantin Brancusi" University of Targu Jiu, Engineering Series*, No. 4, 2019, pp. 13-18.

Address:

- PhD. Stud. Eng. Dan Alexandru Pîrşan, Doctoral School of Engineering, Babeș-Bolyai University, Cluj-Napoca, Romania, Piaţa Traian Vuia, nr. 1-4, 320085, Reşiţa dan.pirsan@ubbcluj.ro

Eigenvalues of a continuous beam with two spans

Patric-Timotei Stan[ID], Zeno-Iosif Praisach*[ID]

Abstract. *Continuous beams can be found in various engineering applications. The dynamic behavior of continuous beams is strongly influenced by the location of the intermediate support. The paper presents the determination of the frequency equation depending on the location of the intermediate support for a continuous beam with two openings for the case that this support can be placed in any position along the length of the beam. Finally, the obtained curves of the eigenvalues for the first six vibration modes are represented.*

Keywords: *eigenvalues, continuous beam, dynamic behavior*

1. Introduction

The dynamics of structures has as its main purpose the development of methods for determining efforts and deformations in the structure subjected to dynamic actions. A dynamic action is an action whose magnitude, direction or point of application varies over time. Dynamics of structures develops specific calculation methods considering the time variation of the response of a subjected structure to dynamic loads and actions [1 – 5].

Continuous beams are placed on more than two supports, one of these supports is fixed (joint or embedded), and the others are mobile (simple supports). These supports do not prevent the variation of the length in the direction of the axis of the bar, it results that the axial effort does not represent a static indeterminacy of the structures [6 – 8].

Continuous beams are widely used in various engineering applications to effectively support loads. Some engineering applications include bridge structures, building frames, and transportation systems.

The paper presents the determination of the frequency equation depending on the location of the intermediate support for a continuous beam with two openings for the case that this support can be placed in any position along the length of the beam.

2. Euler-Bernoulli theory

To determine the transverse frequency equation for a continuous beam with two openings, the Euler-Bernoulli theory is considered. The continuous beam is a simple beam supported on three supports, and the model of the beam is shown in figure 1.
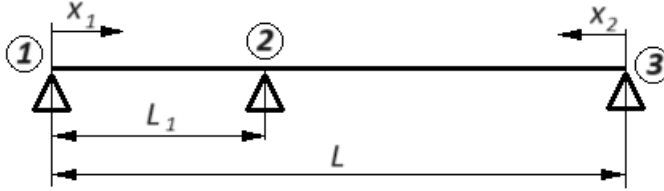
Figure 1. Continuous beam with two spans.

For transverse vibrations, the Euler-Bernoulli model takes into account the bending moment and lateral displacement, and does not take into account the shear deformation and rotary inertia [9 – 10].

The spatial solution of transverse (bending) vibrations, free and undamped, for the Euler-Bernoulli model, has the expression (1):

$$W(x) = A sin(\alpha x) + B cos(\alpha x) + C sinh(\alpha x) + D cosh(\alpha x) \tag{1}$$

where,

A, B, C, D are the integration coefficients;

α is the eigenvalue;

$W(x)$ is the modal wave function.

Since the continuous beam has two openings, a modal wave function is considered for each span (fig. 1): $1 - 2, 3 - 2$ (2).

$$\begin{cases} W_1(x_1) = A_1 sin(\alpha x_1) + B_1 cos(\alpha x_1) + C_1 sinh(\alpha x_1) + D_1 cosh(\alpha x_1) \\ W_2(x_2) = A_2 sin(\alpha x_2) + B_2 cos(\alpha x_2) + C_2 sinh(\alpha x_2) + D_2 cosh(\alpha x_2) \end{cases} \tag{2}$$

where,

$x_1 \in (0, L_1)$ is variable along the length of span $1 - 2$;

$x_2 \in (0, L - L_1)$ is variable along the length of span $3 - 2$;

According to the Euler Bernoulli model, the boundary conditions for each support, taking into account (2) can be written as follows:

$$\begin{cases} W_1(0) = 0 \\ W_1''(0) = 0 \\ W_2(0) = 0 \\ W_2''(0) = 0 \\ W_1(L_1) = 0 \\ W_2(L - L_1) = 0 \\ W_1'(L_1) = -W_2'(L_2) \\ W_1''(L_1) = W_2''(L_2) \end{cases} \tag{3}$$

where,

W$_1$, W$_2$ is the deflection;

W$_1$', W$_2$'is the slope;

W$_1$", W$_2$" is directly proportional to bending moment.

$L_1 \in (0, L)$ is the location of the intermediate support.

3. The frequency equation

By solving the system (3) and taking into account (2), the integration constants (4) and the frequency equation (5) are obtained:

$$\begin{cases} B_1 + D_1 = 0 \\ B_1 - D_1 = 0 \Rightarrow \boxed{B_1 = D_1 = 0} \\ B_2 + D_2 = 0 \\ B_2 - D_2 = 0 \Rightarrow \boxed{B_2 = D_2 = 0} \\ A_1 sin(\alpha L_1) + C_1 sinh(\alpha L_1) = 0 \Rightarrow \boxed{C_1 = -A_1 \frac{sin(\alpha L_1)}{sinh(\alpha L_1)}} \\ A_2 sin(\alpha(L - L_1)) + C_2 sinh(\alpha(L - L_1)) = 0 \Rightarrow \boxed{C_2 = -A_2 \frac{sin(\alpha(L-L_1))}{sinh(\alpha(L-L_1))}} \\ A_1 cos(\alpha L_1) + C_1 cosh(\alpha L_1) = -[A_2 cos(\alpha(L - L_1)) + C_2 cosh(\alpha(L - L_1))] \\ -A_1 sin(\alpha L_1) + C_1 sinh(\alpha L_1) = -A_2 sin(\alpha(L - L_1)) + C_2 sinh(\alpha(L - L_1)) \end{cases} \tag{4}$$

By solving the last two equations in system (4) it obtains the integration coefficient A$_2$ and the frequency equation:

$$\begin{cases} \boxed{A_2 = A_1 \frac{sin(\alpha L_1)}{sin(\alpha(L-L_1))}} \\ Z_{11} \cdot Z_{22} + Z_{12} \cdot Z_{21} = 0 \end{cases} \tag{5}$$

where it was denoted,

$$\begin{cases} Z_{11} = cos(\alpha L_1) - \frac{sin(\alpha L_1)}{sinh(\alpha L_1)} cosh(\alpha L_1) \\ Z_{12} = sin(\alpha L_1) \\ Z_{21} = cos\big(\alpha(L - L_1)\big) - \frac{sin(\alpha(L - L_1))}{sinh(\alpha(L - L_1))} cosh\big(\alpha(L - L_1)\big) \\ Z_{22} = sin\big(\alpha(L - L_1)\big) \end{cases} \tag{6}$$

4. Results

For a normalized length of the continuous beam ($L=1$) for which the cross-section is constant having the moment of inertia I [m^4] and is made of a material with modulus of elasticity E [N/m^2], the eigenvalues obtained as solution of frequency equation (5), starting from $L_1=0.001$ till $L_1=0.999$, with step of 0.001, for the first six vibration mode, are presented in the figures 2 - 7.

Table 1 presents the eigenvalues for the first six vibration modes for $L_1=0.001$, $L_1=0.150$, $L_1=0.325$ and $L_1=0.500$. Due to the symmetry of the supports, the eigenvalues for $L_1 =0.001$ are the same with $L_1=0.999$, for $L_1=0.150$ are the same with $L_1=0.850$ and $L_1=0.325$ are the same with $L_1=0.675$.

Table 1. Eigenvalues for the first six vibration modes for different values of L_1

| L_1	0.001 / 0.999	0.150 / 0.850	0.325 / 0.675	0.500
α_1	3.9292235	4.40911578	5.28238731	6.2831853
α_2	7.07330383	7.98600823	9.41313727	7.85320462
α_3	10.216999	11.5834823	11.26626	12.5663706
α_4	13.3606957	15.1779383	14.6365202	14.1371655
α_5	16.5043945	18.7173101	18.8061283	18.8495559
α_6	19.6480955	21.929824	20.815083	20.4203522

125
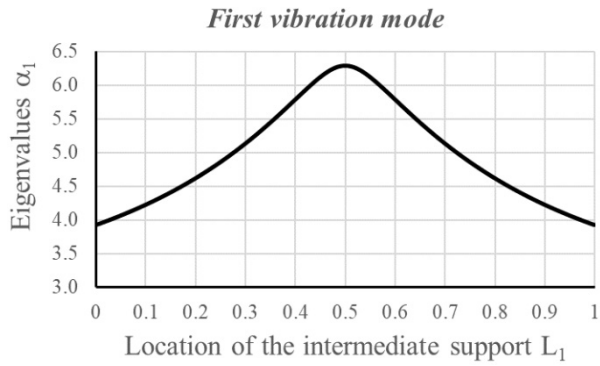
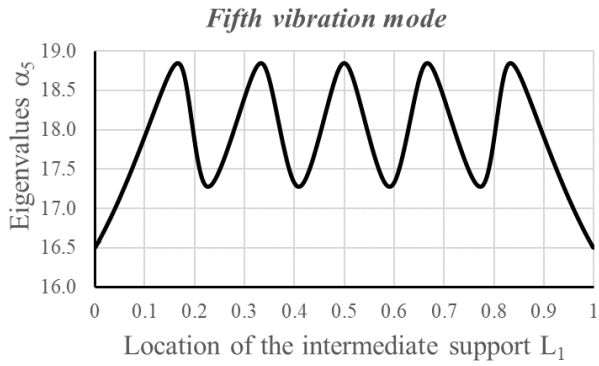**Figure 2.** Eigenvalues for the first vibration mode.
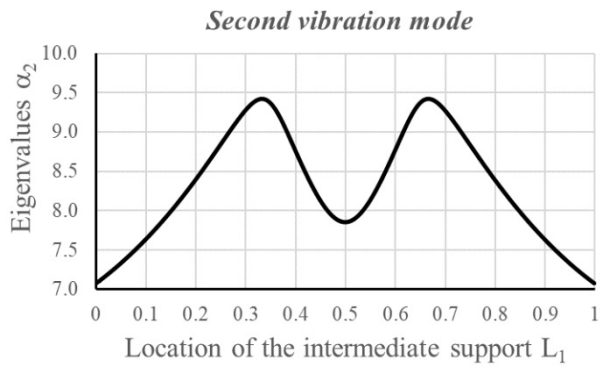
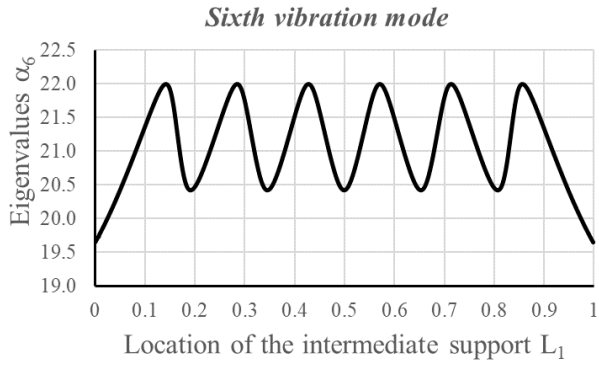**Figure 3.** Eigenvalues for the second vibration mode.
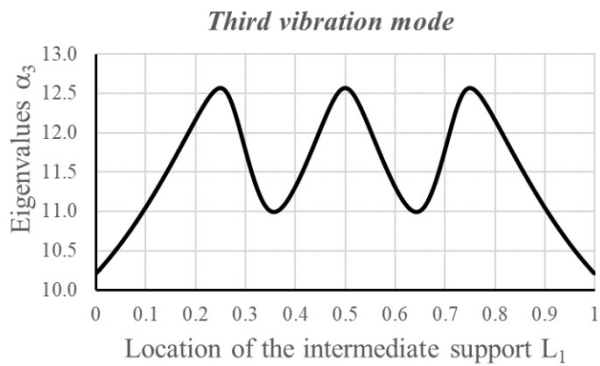
Figure 4. Eigenvalues for the third vibration mode.
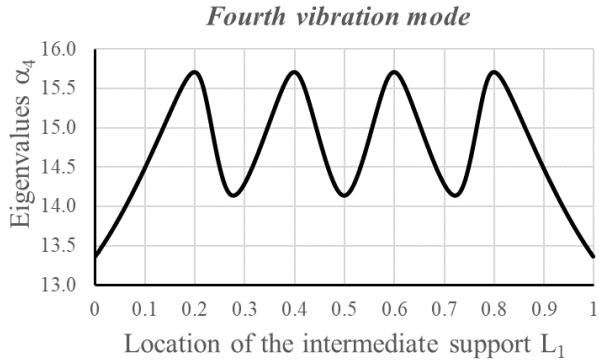
Figure 5. Eigenvalues for the fourth vibration mode.

Figure 6. Eigenvalues for the fifth vibration mode.

Figure 7. Eigenvalues for the sixth vibration mode.

5. Conclusions

The results obtained for the eigenvalues of the continuous beam with two spans, assuming that the intermediate support can occupy any position along the length L of the beam, is important for calculating the natural frequencies of the beam, considering that the natural frequency of the beam is directly proportional to the square of the eigenvalue.

Knowing the eigenvalues of the continuous beam and the values of the integration coefficients from system (2) we can write the modal function that allows us to draw the modal shapes for the vibration modes of the beam.

From the analysis of figures 2 - 7, it can be seen that the eigenvalues obtained, compared to the middle location of the intermediate support, are symmetrical regardless of the mode of vibration.

When $L_1 = 0.5$, the eigenvalues, respectively the natural frequencies, for the odd vibration modes have maximum values. Minimum values are obtained when the intermediate support is positioned very close to the ends of the continuous beam.

As a particularity, the maximum value of the eigenvalues is equal to $(n+1) \cdot \pi$, where n represents the number of the vibration mode.

When the intermediate support is positioned very close to the beam ends, the dynamic behavior of the continuous beam can be associated with a beam clamped at one end and hinged at the other. For these cases, the clamped end is not perfect, it can be considered a weak clamp, because the boundary conditions for the end point are for a hinge end and not a clamp end. In other words, in the hinged end of the continuous beam, the slope does not have zero value as in the case of a clamped end, all the more so as the boundary condition for this hinge imposes a bending moment with zero value.

References

1. A. Popovici, C. Ilinca, *Dinamica structurilor și inginerie seismică, Aplicații*, Vol. 1, Ed. Conpress, București, 2011.
2. K.C. Anil, *Dynamisc of structures – Theory and Applications to Earthquake Engineering*, Pearson Education Limited, 2014.
3. W.C. Ray, P. Joseph, *Dynamisc of structures,* Computers&Structures, Inc.1995 University Ave. Berkeley, 1995.
4. J.C. Andesron, *Dynamic Response of Structures*, http://civilwares.free.fr/The%20Seismic%20Design%20Handbook/Chapter%2004-Dynamic%20Response%20of%20Buildings.pdf (downloaded on 13.05.2024).

5. A. Stratan, *Dinamica structurilor şi inginerie seismică Note de curs*, Timişoara 2021.
6. C. Nicolae, B. Roxana, C. Alexandru, M. Aliz, M. Cristian, M. Ioana, *Statica construcţiilor. Structuri static nedeterminate – Îndrumător pentru lucrări*, U.T. PRESS Cluj-Napoca, 2014.
7. E.T. Mircea, *Statica construcţiilor. Structuri static nedeterminate*, Ed. Conpress, Bucureşti, 2005
8. S. Carlos, *Introduction to the theoretic-practical classes of Strength of Materials*, Faculdade de engeneria, Universidade de Porto, 2022.
9. G.R. Gillich, I. Negru, E. Stanciu, C. Protocsil, F.P. Minda, *Evaluarea Integritatii Structurilor Mecanice*, Editura Eftimie Murgu, Reşiţa, 2018.
10. M.S. Han, H. Benaroya, T. Wei, Dynamics of transversely vibrating beams using four engineering theories, *Journal of Sound and Vibration*, 225(5), 1999, pp. 935-988.

Addresses:

- PhD. stud. Eng. Patric-Timotei Stan, Doctoral School of Engineering, Babeş-Bolyai University, Cluj-Napoca, Romania, Piaţa Traian Vuia, nr. 1-4, 320085, Reşiţa
  patric.stan@ubbcluj.ro
- Lect. PhD. Habil. Zeno-Iosif Praisach, Department of Engineering Science, Faculty of Engineering, Babeş-Bolyai University Cluj-Napoca, Romania, Piaţa Traian Vuia, nr. 1-4, 320085, Reşiţa
  zeno.praisach@ubbcluj.ro
  ([*]corresponding author)

The influence of stiffness on the dynamic behavior of a PCB enclosure

Razvan-George Olingheru* ⓘD, Adrian-Bogdan Olariu ⓘD,
Zeno-Iosif Praisach ⓘD

Abstract. *The paper presents the modification of the first 6 natural frequencies for a PCB case where the material quality was modified from Ultradur B4300 G6 material in AlSi12Cu1 aluminum alloy. Following the change in the quality of the materials, the natural frequency of the 1ˢᵗ vibration mode changed from 164 Hz to 378 Hz, as a consequence of the change in the modulus of elasticity, respectively the stiffness.*

Keywords: *natural frequencies, moment of inertia, longitudinal modulus of elasticity, ultradur B4300 G6, AlSi12Cu1*

1. Introduction

The work appeared as a result of the competition [1] organized by the Continental company in which the goal was to modify the spectrum of natural frequencies so that for mode I vibration, the resulting natural frequency is higher than 300 Hz.

The Continental company provided the 3D model of the PCB case and the initial materials of the assembly, and the research theme was to modify the frequency spectrum only by increasing the stiffness.

In fig. 1 shows the sectional view of the PCB case, and figure 2 shows the materials that make up the case.

In the work, it was aimed to increase the rigidity of the casing on the one hand by modeling internal and external ribs, respectively by increasing the moment of inertia, on the other hand by changing the quality of the material from Ultradur B4300 G6 to AlSi12Cu1. For each stage, the obtained results are presented.
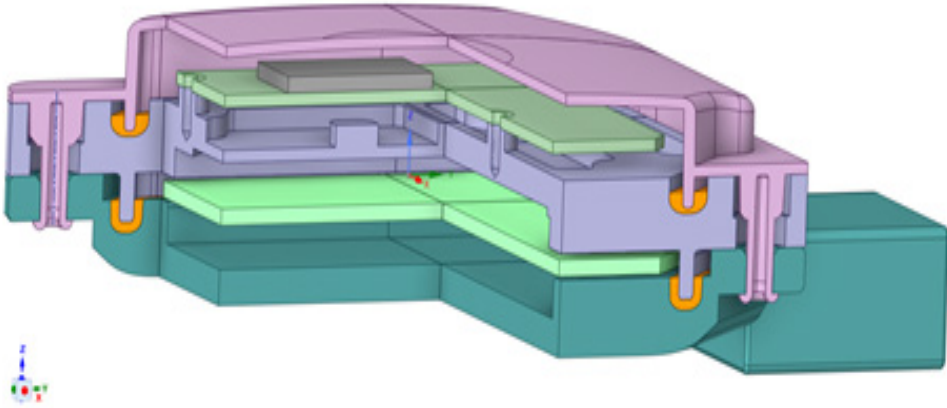
Figure 1. PCB housing detail

Part	Material	Young's Modulus [MPa]	Poisson's ratio [-]	Density [g/cm3]	Yield strength [MPa]	Strain limit [µstrain] / [-]
Cover, Housing	B4300 G6	8500	0.35	1.35	70	/
Screws	Steel	200000	0.3	7.85	250	/
PCBs	FR-4	X:20400 / Y:18400 / Z:15000	XY: 0.11 YZ:0.09 XZ:0.14	1.84	/	700 µstrain / 0.0007
Chip	Chip encapsulant	25000	0.35	1.7	/	/
Seallings	Glue	10	0.45	1.35	/	/
Carrier	AlSi12Cu1	73000	0.33	2.65	140	/

Figure 2. Material list

2. Increasing stiffness by changing the moment of inertia.

In the first step, for increasing of the natural frequencies, especially for the first vibration mode, we considered that by introducing additional ribs [2], [3] in the PCB case we will obtain the minimum of 300 Hz for the vibration module.

The introduction of additional ribs leads to an increase in the moment of inertia or stiffness [4].

The adopted solutions are presented in figures 3 and 4.
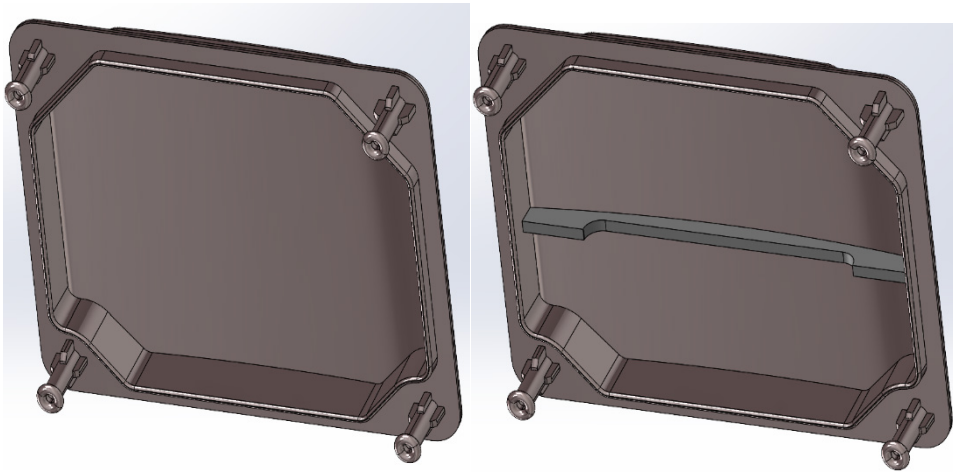
Figure 3. The constructive solution without a rib (left) and the constructive solution with an internal rib (right)
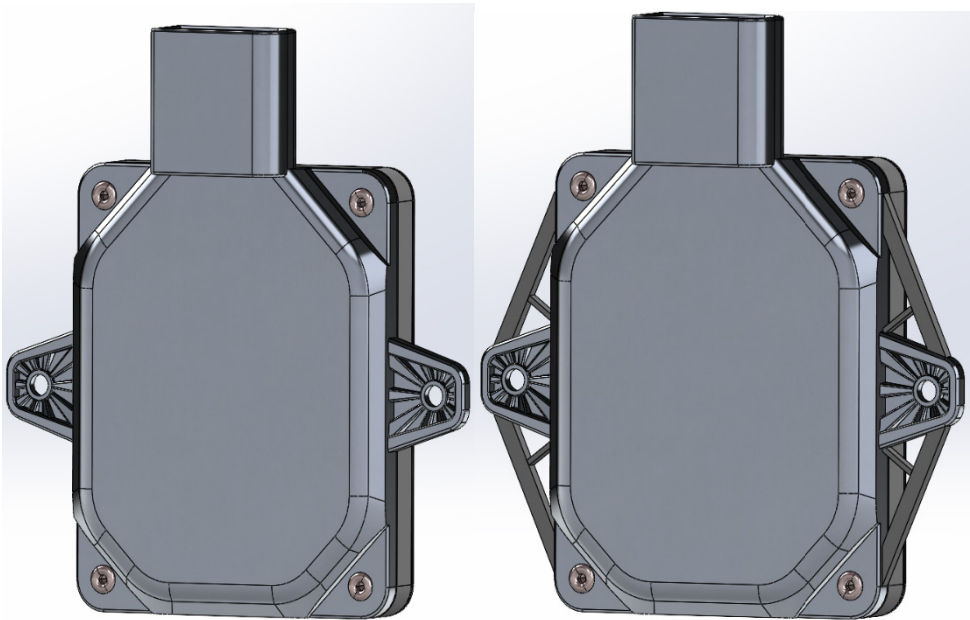
Figure 4. The constructive solution without a rib (left) and the constructive solution with an external rib (right

3. Increasing stiffness by changing the longitudinal modulus of elasticity

In order to increase our own frequencies, we considered that by changing the quality of the material [5], [6], respectively the longitudinal modulus of elasticity, we will reach the threshold of 300 Hz required in fear.

Property	Value	Units
Elastic Modulus	73000	N/mm^2
Poisson's Ratio	0.33	N/A
Shear Modulus		N/mm^2
Mass Density	2650	kg/m^3
Tensile Strength		N/mm^2
Compressive Strength		N/mm^2
Yield Strength	140	N/mm^2
Thermal Expansion Coefficient		/K
Thermal Conductivity		W/(m·K)
Specific Heat		J/(kg·K)
Material Damping Ratio		N/A

Figure 5. AlSi12Cu1 alloy properties

The initially provided Ultradur B4300 G6 material was replaced by an AlSi12Cu1 aluminum alloy. The Ultrahard material B4300 G6 according to figure 2 has the Modulus of elasticity E= 8500 MPa, and the proposed material has the modulus of elasticity E= 73000 MPa.

The material was chosen from the SolidWorks library shown in figure 5, the program with which the modal analysis [7] was performed to determine the natural frequencies.

4. Results

The natural frequencies for the unmodified PCB housing are presented in table 1.

For the variants in the case of the modified PCB housing and following the modal analysis, the following natural frequencies for the first 6 vibration modes were obtained.

Table 1. Unmodified PCB housing natural frequencies

Vibration mode	Angular frequency ω [rad/sec]	Frequency f [Hz]	Period T [s]
1	1.030,5	164,01	0,006097
2	3.853,9	613,37	0,0016303
3	4.868,7	774,87	0,0012905
4	6.265,8	997,23	0,0010028
5	8.165,4	1.299,6	0,00076949
6	8.726,9	1.388,9	0,00071998

Table 2. PCB case natural frequencies with increasing moment of inertia

Vibration mode	Angular frequency ω [rad/sec]	Frequency f [Hz]	Period T [s]
1	1.169,6	186,15	0,0053721
2	3.527,2	561,37	0,0017814
3	4.585,9	729,87	0,0013701
4	6.579,5	1.047,2	0,00095496
5	8.680,6	1.381,6	0,00072382
6	10.151	1.615,6	0,00061897

For the case where we considered the increase of the moment of inertia by introducing internal and external ribs in the PCB case, the obtained natural frequencies are shown in table 2.

It can be seen from the results obtained that the natural frequency in the 1st vibration mode increased from 164.01 Hz to 186.15 Hz. The results obtained are both for the version with internal ribs (Fig. 3) and with external ribs (Fig. 4).

The natural frequencies obtained for the variant with an increase in the longitudinal modulus of elasticity can be found in table 3.

Table 3. PCB case natural frequencies with increasing modulus of elasticity

Vibration mode	Angular frequency ω [rad/sec]	Frequency f [Hz]	Period T [s]
1	2.376,7	378,26	0,0026437
2	4.197,8	668,1	0,0014968
3	5.393,8	858,45	0,0011649
4	8.527,9	1.357,3	0,00073678
5	11.246	1.789,8	0,00055872
6	12.411	1.975,3	0,00050625

4. Conclusion

Following the numerical modal analyzes performed, we obtained the natural frequencies for the first 6 vibration modes for the initial version, the version with internal and external ribs and the version with material modification.

For the initial variant, the 1st natural frequency obtained from the numerical analysis has the value of 164.01 Hz, far below the value required in the research topic of 300 Hz.

By increasing the moment of inertia, i.e. adding inner and outer ribs, the 1st natural frequency increased by approximately 11%, i.e. to the value of 184.15 Hz. This value also did not meet the 300 Hz minimum threshold requirement.

The only acceptable solution to reach the minimum threshold of 300 Hz was to increase the longitudinal modulus of elasticity from 8500 MPa to 73000 MPa, respectively by replacing the Ultradur B4300 G6 material with the AlSi12Cu1 alloy. The natural frequency obtained in 1st vibration mode is 378.26 Hz, a value that exceeds the minimum threshold of 300 Hz.

References

1. *TIE M+ 2024 Structural Analysis Subject Development Committee, Finite Element Analysis Engineering Team,* 1st April 2024, Sibiu
2. C. Tufişi, C. Haţiegan, *Product Design Techniques Using SolidWorks*, Editura Eurostampa, Timişoara, 2023.
3. *SolidWorks, Fundamentals of 3D design and simulations, SolidWorks Educational Edition 2020-2021*, Dassault Systemes, 2020.
4. G.R. Gillich, I. Negru, E. Stanciu, C. Protocsil, F.P. Minda, *Evaluarea integrităţii structurilor mecanice,* Editura Eftimie Murgu, Reşiţa, 2018.
5. D.C. Planchard, *SolidWorks 2020 Tutorial*, SDC Publications, 2020.
6. D.C. Planchard, *SolidWorks 2022 Tutorial, A step-by-step Based Approach Utilizing 3D Modelling,* SDC Publications, 2022.
7. P.M. Kurowski, *Engineering analysis with SolidWorks'Simulation 2015*, SDC Publications, 2015.

Addresses:

- Stud. Razvan-George Olingheru, Faculty of Engineering, Babeş-Bolyai University Cluj-Napoca, Romania, Piaţa Traian Vuia, nr. 1-4, 320085, Reşiţa razvan.olingheru@stud.ubbcluj.ro
  (*corresponding author*)

- Stud. Adrian-Bogdan Olariu, Faculty of Engineering, Babeș-Bolyai University Cluj-Napoca, Romania, Piaţa Traian Vuia, nr. 1-4, 320085, Reşiţa
adrian.olariu@stud.ubbcluj.ro
- Lect. PhD. Habil. Zeno-Iosif Praisach, Department of Engineering Science, Faculty of Engineering, Babeș-Bolyai University Cluj-Napoca, Romania, Piaţa Traian Vuia, nr. 1-4, 320085, Reşiţa
zeno.praisach@ubbcluj.ro

Analysis of methods of hardening and restoration of worn parts

Iskakova Dinara* [ID], Kasenov Asylbek [ID], Magellan Dariya [ID],
Zoltan-Iosif Korka [ID]

Abstract. *The restoration of worn parts is an important aspect in the field of machine repair and maintenance of machinery. It allows you to significantly reduce repair costs and is a priority issue in the development of a machine maintenance and repair system. The main causes of performance loss products are abrasive wear, fatigue breakdowns, corrosion and other types of destruction. When choosing a recovery method, the type of coupling, types of friction and operating conditions of the machines are important factors. An increase in wear resistance can be achieved by changing the chemical composition of the material, mechanical influences and the application of wear-resistant coatings.*

Keywords*: wear resistance, restoration, surfacing.*

1. Introduction

In the structure capital cost repairs of machines, 60-70 % of the costs are accounted for by the cost of spare parts [1]. At the same time, the cost of restoring most parts does not exceed 25-40 % of the price of a new part [2]. Currently, advanced restoration technologies have been developed, which, in addition to restoration, strengthen it, significantly increasing wear resistance [3]. Restoration of worn parts is one of the main ways to save material and energy resources, solve environmental problems, since the cost of energy, metals and other materials is 25-30 times less than the cost of manufacturing new parts. When remelting worn parts, up to 30 % of the metal is irretrievably lost.

The restoration of worn-out parts can significantly reduce the cost of repairing machinery and is therefore a priority issue in the development of a machine maintenance and repair system [4].

Methods for restoring machine parts provide for compensation of surface layers of the main structural material lost during operation (restoration of nominal drawing dimensions and operational properties) by applying new masses (layers) of material of the same or another brand to worn areas. In some cases, when restoring, the boring method is used for the next repair size, while changing the mating part. Special treatments are also required – annealing to relieve stress, hardening to increase wear resistance [5].

The rapid destruction of products operating at high speeds, loads and temperatures, as well as under conditions of abrasive, corrosive and other types of exposure, requires the development and introduction into production of new methods for their hardening and restoration. The main causes of loss of performance of products are abrasive and other types of wear, fatigue breakdowns and discoloration of the material, various kinds of corrosion and cavitation damage, liquid and gas erosion and various combinations of the above reasons [6], [7].

2. Analysis

The various details in mechanical engineering are characterized by shape, dimensions, materials, weight, balance, as well as tolerances (shapes and locations of surfaces): straightness, flatness, roundness, cylindricity, parallelism, perpen-dicularity, alignment, symmetry, positional deviation, axis intersection, radial and end runout, tilt, shape of a given profile. During operation, in addition to changing the shape, size, weight and location of surfaces, cracks, fragments, chips, nicks occur, and balancing is disrupted. Of all the surfaces to be restored, the outer and inner cylindrical surfaces make up 53.3 %, threaded – 12.7 %, spline – 10.4 %, toothed – 10.2 %, flat – 6.5 %, all others – 6.9 %. Except for the parameters of the surfaces to be restored (shape, dimensions, physical and mechanical properties, accuracy, roughness, integrity, type of thermal or chemical-thermal treatment, the presence and material of the coating) to choose the recovery method, very important factors are: the type of coupling, types of friction and relative movement of surfaces during the operation of machines. These factors are combined by a common concept – indicators of working conditions [8].

It is possible to increase the wear resistance of the working surfaces of products by changing the chemical composition of the surface material by introducing alloying components to form structures that resist wear processes well; by mechanical and thermal effects on the metal surface, which lead to structural and substructural transformations that increase resistance to various wear processes; by applying wear-resistant coatings on the friction surfaces of parts. According to the above, it is possible to classify a variety of technological methods for increasing wear resistance (Figure 1), considering that they are based on factors of chemical, thermal and mechanical influences that can significantly change the surface properties of

products. A variety of operating conditions of machines and mechanisms, combined with modern requirements, necessitate the development and improvement of technological methods for applying wear-resistant coatings in order to obtain bimetallic products and for restoration operations. Among the variety of methods of applying wear-resistant coatings, a special place is occupied by surfacing, in which the surface of the coated material and the deposited alloy are melted due to the heat of an external source, as a result of which their interaction occurs with the formation of a metallurgical bond [9].
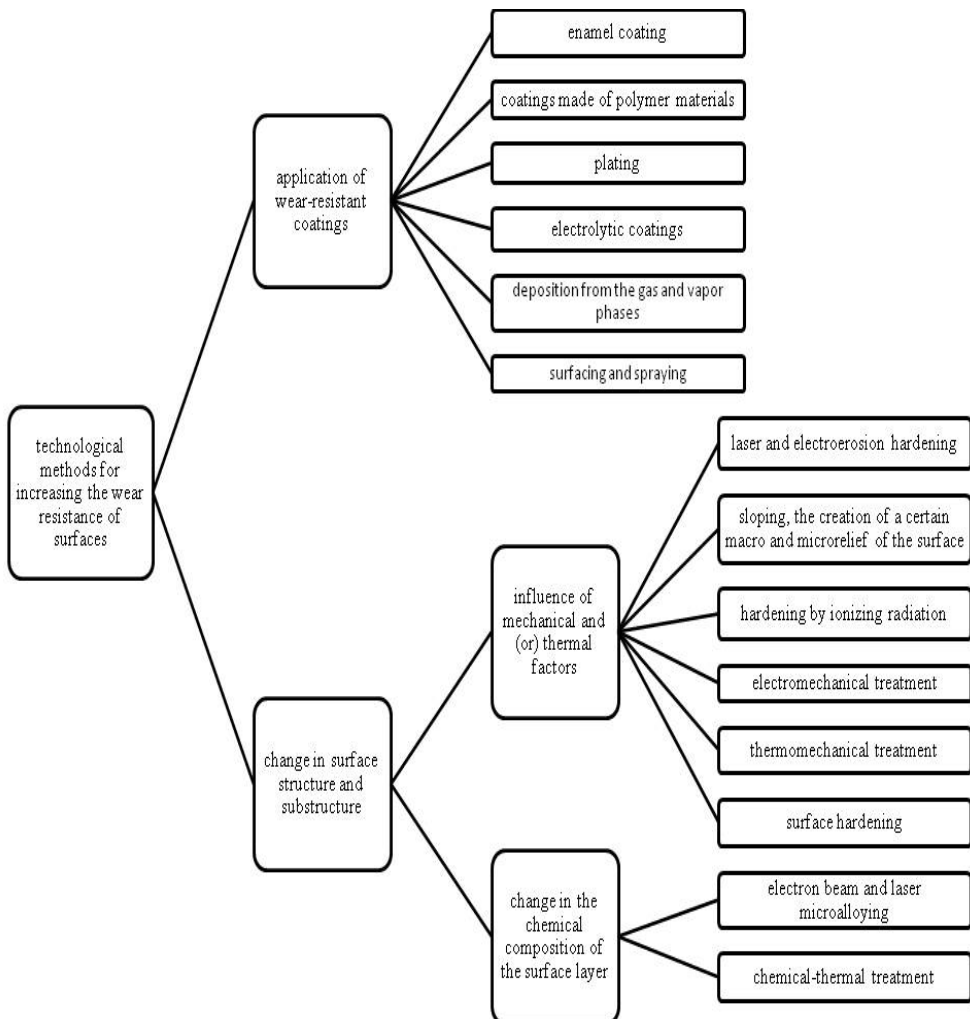
Figure 1. Technological methods of increasing wear resistance

The surfacing technology has the advantages of obtaining a sufficiently large coating thickness, high productivity, and no restrictions on the size of the surfaced surfaces. In this case, a layer with the required chemical composition, high hardness and wear resistance is formed. In the total volume of work on the restoration of parts at repair enterprises, surfacing of various types accounts for about 77%, electrocontact baking — 6 %, electroplating methods – 5 %, electromechanical processing – 4 %, pouring with liquid metal – 2 %, polymer reduction – 4 %, other methods – 5 % (Tables 1 and 2). Currently, many technological methods are widely used for surfacing materials on the surface of the part to be restored. Most of them are quite close in terms of energy parameters (Figure 2).

Table 1. Technical and economic indicators of coating methods

The method of application	Performance coefficient	Coefficient of technical and economic efficiency	Applicability in repair (shaft-sleeve connection)
Surfacing			
under the flux layer	1,62-1,45	0,436	
vibration arc	0,85-0,72	0,25	limited
in the environment of carbon dioxide	1,82-1,77	0,403	wide
electrical contact	2,3-2,1	0,66	
with powder wires	1,75-1,54	0,4	wide
manual arc	1	0,314	-
plasma	2,2-1,9	0,56	
Spraying			
gas flame	1,68-1,47	0,39	limited
plasma	1,76-1,68	0,4	limited
Electroplating coatings			
chrome plating	0,32-0,022	0,087	-
ironization	1,93-1,77	0,064	-

Restoration of a part is a complex of technological operations to eliminate defects in a part, ensuring the resumption of its operability and geometric parameters established by regulatory and technical documentation.

Recovery methods are conditionally divided into two categories: methods of building up and processing methods.

Depending on the physical nature of the processes, technological and other features, the existing methods are divided into ten groups (Table 3).

Mechanical machining eliminates signs of wear and restores the shape of the part. At the same time, the dimensions after processing differ from the nominal ones. To ensure the necessary fit, mating parts with changed parameters are used or a wear compensator is installed (rings, bandages, bushings, threaded spiral inserts, etc.).

Table 2. Indicators of the restoration of parts in various ways.

The method	Estimated indicators			
	Material consumption, kg/m	Specific labor intensity, h/m	Unit cost, USD/m	Specific energy intensity, kWh/m
Surfacing				
manual electric arc	43-57	30-38	0.65-0.93	580
manual argon	30	23-30	0.64-0.70	520
arc manual gas	38-51	36-33	0.82-0.88	80
electric arc under a layer of flux	38-51	21-24	0.42-0.55	286
vibrating arc	35-30	33-36	0.73-0.77	234-240
electric arc in carbon dioxide environment	30-45	14-21	0.28-0.48	250
Electroplating coatings				
chrome plating	20-24	72-129	0.88-1.48	324
ironization	28-43	15-19	0.32-0.38	120
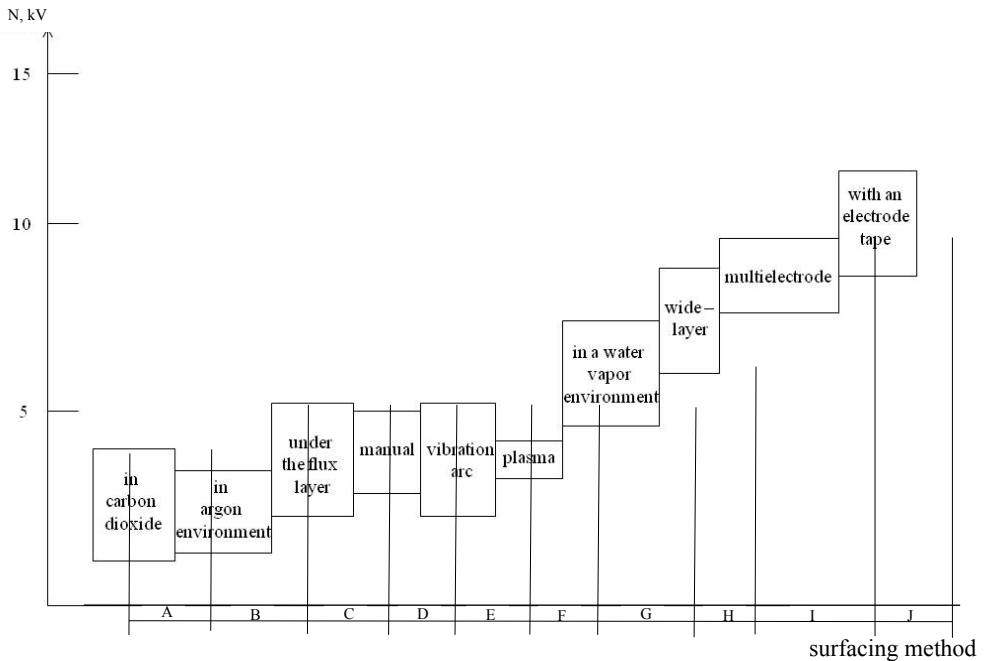
Figure 2. The dynamics of the growth of the working power of the arc from the method of surfacing: N – is the working power of the welding arc, kilovolts; A, B, C, D, E, F, G, H, I, J - surfacing methods

Table 3. Ways to restore parts

Group number	A group of methods	Method
1	Locksmith and mechanical processing	1. Processing for repair size 2. Setting up an additional repair part 3. Processing before removing signs of wear and giving the correct geometric shape 4. Re-assembly
2	Plastic deformation	1. Hood, drawbar 2. Editing (on presses, by riveting) 3. Mechanical distribution 4. Hydrothermal distribution 5. Electrohydraulic distribution 6. Rolling out 7. Mechanical compression 8. Thermoplastic compression 9. Precipitation 10. Extrusion 11. Knurling 12. Electromechanical disembarkation
3	Application of polymer materials	1. Spraying: flame gas, in a pseudo-liquefied layer (vortex, vibratory, vibratory), etc. 2. Crimping 3. Injection molding 4. Application with a spatula, roller, brush, etc.
4	Manual welding and surfacing	1. Gas 2. Arc 3. Argon arc 4. The Blacksmith Shop 5. Plasma 6. Thermite 7. Contact information
5	Mechanized arc welding and surfacing	1. Automatic submerged 2. In the environment of protective gases: argon, carbon dioxide (carbon dioxide), water vapor, etc. 3. With combined protection 4. Arc with flame protection 5. Vibration arc

Group number	A group of methods	Method
		6. With a powder wire or tape 7. Wide - layer 8. With a recumbent electrode 9. Plasma (compressed arc) 10. Multielectrode 11. With simultaneous deformation 12. With simultaneous machining
6	Mechanized arcless welding and surfacing methods	1. Induction (high frequency) 2. Electroslag 3. Contact welding and welding 4: By friction 4. Gas 5. Electron beam 6. Ultrasonic 7. Diffusion 8. Laser 9. Thermite 10. By explosion 11. Magnetic pulse 12. Furnace welding
7	Thermal gas spraying (metallization)	1. Arc 2. Gas flame 3. Plasma 4. Detonation 5. High frequency 6. Electric pulse 7. Ion-plasma
8	Electroplating and chemical coatings	1. Direct current hardening 2. Periodic current hardening 3. Flow-through hydration 4. Local (untreated) ironification 5. Chrome plating 6. Chrome plating is flow-through, jet 7. Copper plating 8. Galvanizing 9. Application of alloys 10. Application of composite coatings 11. Electrocontact application (electronic abrasion)

Group number	A group of methods	Method
		12. Galvanomechanical method 13. Chemical nickel plating
9	Thermal and chemical heat treatment	1. Tempering, vacation 2. Diffusion boration 3. Diffusion galvanizing 4. Diffusion titration 5. Diffusion chrome plating 6. Diffusion chromo-titanization 7. Diffusion chromoazotization 8. Cold treatment
10	Other methods	1. Pouring with liquid metal 2. Freezing 3. Criticism 4. Soldering 5. Soldering welding 6. Electric spark buildup and alloying

Plastic deformation recovery methods are based on the plasticity property of metals. During plastic deformation, the metal of the part is redistributed from non-working parts of the part to the working ones, thereby restoring the dimensions of worn surfaces. The volume of the part remains constant. The advantages include the following: no additive material is required, simplicity of methods, relatively high productivity. Disadvantages include: the need for heat treatment of ferrous metals, changes in linear dimensions (for example, the piston pin is shortened after distribution).

The technology of restoring parts with polymer materials is characterized by simplicity and accessibility (used in the field), low cost, high productivity and good quality. The durability of bearing seats increases many times after restoration with polymer materials.

Manual welding and surfacing methods are widely used due to the simplicity and possibility of performing the process in hard-to-reach places. The disadvantages include: low productivity, material consumption and not always high quality.

Mechanized welding and surfacing methods can be automatic and semi-automatic. Most of these methods provide high performance and quality.

In arc methods, the heat source for melting the filler material and the surface of the part is the heat of the electric arc. In arcless methods, such a source is losses from eddy currents (HDPE), Joule heat (electroslag surfacing, contact welding), heat of combustible gases, etc.

Manual and mechanized welding and surfacing methods have received the greatest application (75–80% of the total recovery volume). Their disadvantages are thermal effects on the base metal, including non–recoverable surfaces, deformation of parts, significant allowances for machining. The use of most of these methods is advisable for the restoration of heavily worn parts [10].

During spraying, the molten filler material (wire or powder) is sprayed with compressed air and applied to the prepared surface of the part. Spraying methods are distinguished depending on the heat source: arc – the heat of an electric arc, gas– flame – the heat of a gas flame, etc. The process of metal spraying is called metallization. Most spraying methods are characterized by high performance, which allows you to accurately adjust the thickness of the coating and the allowance for machining. A serious disadvantage of spraying is the low adhesion of coatings to the substrate. To increase it, a special sublayer is applied, followed by reflow, etc.

Electroplating methods are based on the phenomenon of electrolysis. They are distinguished by the type of metal deposited, the type of current used, the method of deposition, etc. Electroplating methods are high-performance, do not have a thermal effect on the part, allow you to accurately adjust the thickness of coatings and minimize or completely eliminate mechanical processing, ensure high quality coatings with cheap starting materials. Such methods are used to restore poorly worn parts. The disadvantages of electroplating are the multi–operability, complexity and environmental harmfulness of the technology [11].

Heat treatment is used to harden and restore the physical and mechanical properties of parts (spring elasticity, etc.). With chemical thermal methods, diffuse saturation of the surface of the part with refractory metals (chromium, titanium, etc.) occurs with some size change. These methods are used to restore and increase the wear resistance of poorly worn parts (plungers, etc.).

Figure 3 shows the distribution of methods for restoring worn machine parts.
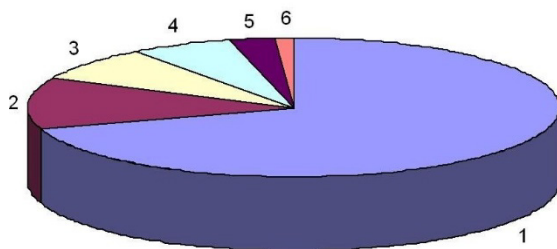
Figure 3. Distribution of methods for restoring worn machine parts: 1 – surfacing and welding (70 %); 2 – repair dimensions (12 %); – electrolytic coatings (8 %); 4 – polymer materials (6 %); 5 – installation of an additional repair part (3 %); 6 – surface plastic deformation (1 %).

As follows from Figure 3, more than 70 % of worn parts are restored by surfacing and welding.

3. Conclusion

An analysis of methods and methods for restoring machine parts, classifications used for restored parts, and principles of production organization allows us to draw the following conclusions:

– the share of parts restored at enterprises of the agro-industrial complex by gas-thermal methods is 26.1 %;

– the most promising methods for restoring machine parts are gas-thermal spraying, which make it possible to ensure the life of the restored parts at and above the level of new parts;

– the organization of the processes of restoration of parts, based on the use of classification of elements of mating parts, is the most cost-effective, since it allows the development of modular technological restoration processes.

References

1. D.A. Iskakova, A.Zh. Kasenov, D.A. Magellan, *Comparison and analysis of the technological process of repair of pipe fittings*, "XXIV Satpayev readings" International Scientific Conference, 19 April 2024, Pavlodar, Kazakhstan, pp. 23-30.
2. D.A. Magellan, D.A. Iskakova, J.K. Musina, *Investigation of the influence of surfacing modes on wear resistance*, "XXIV Satpayev readings" International Scientific Conference, 19 April 2024, Pavlodar, Kazakhstan, pp. 38-41.
3. D.A. Iskakova, A.J. Kasenov, A.U. Kabulova, *The study of tribotechnical characteristics of surfaces by various processing methods. Theoretical and practical aspects of the development of modern science* [Electronic resource] / SORoS Publishing House, Scientific Publishing Center "World of Science"– The electron. text. data. (1.70 Mb.).–Neftekamsk: Scientific Publishing Center "World of Science", 2023. pp. 18-26.

4. W. Feng, Research on microstructure of the auto-restoration layer of worn surface of metals, *Materials Science and Engineering: A*, 399(1–2), 2005. pp. 271-275.
5. V.I. Chernoivanov, Organizatsiya i tekhnologiya vosstanovleniya detaley mashin / Chernoivanov V. I. – M. : *Agropromizdat,* 1989. – 334 p.
6. Z.H. Wu, Z.X. Li, Q.Y. Zhang, Y. Jiang, Z.G. Liu, Y.D. Yuan, Y. Xue, X.N. Wang, Effect of microstructure on wear resistance during high temperature carburization heat treatment of heavy-duty gear steel, *Materials Today Communications*, Vol. 40, 2024, 109486.
7. J. Li, Y. Jiao, C. Xu, L. Zhang, Q. Li, L. Ren, Study on the multi-environmental wear resistance of a shell-imitating multilayer multimaterial composite carbon fiber, *Tribology International*, Vol. 198, 2024, 109930.
8. I.I. Drakonov, Innovative methods of hardening and restoration of machine parts / I.I. Dragunov, V.V. Evenko // *New materials and technologies in mechanical engineering*. – 2022. – No. 36. – pp. 14-18.
9. E.V. Treshcheva, Analysis of the features of coating by gas thermal spraying in the processes of restoration and hardening of parts of transport and technological machines / E. V. Treshcheva // Students of Russia: Century XXI *Proceedings of the VI All-Russian International Scientific and Practical Conference: in 4 parts*, Orel, 13 December, 2018. Vol. Part 4. – Orel: N.V. Parakhin Oryol State Agrarian University, 2019. – pp. 370-378.
10. Y.M. Kuskov, I.L. Bogaychuk, N.P. Shevchenko, M.A. Fesenko, Electroslag surfacing of 110G13L steel using various types of surfacing material, *Welding International*, 2021, DOI 10.1080/09507116.2021.1945321.
11. V.G. Burov, A.A. Bataev, Kh.M. Rakhimyanov, D.O. Mul, Technology of Strengthening Steel Details by Surfacing Composite Coatings, *IOP Conference Series: Materials Science and Engineering*, 7, Kemerovo, Russia, September 23-25, 2015.

Addresses:

- PhD. stud. Iskakova Dinara, Toraighyrov University, Kazakhstan, Pavlodar, 64 Lomova Street.
  iskakovada@mail.ru
  ([*]corresponding author)
- Candidate of Technical Sciences, Professor Kasenov Asylbek, Toraighyrov University, Kazakhstan, Pavlodar, 64 Lomova Street.
  asylbek_kasenov@mail.ru

- Master stud. Magellan Dariya, Toraighyrov University, Kazakhstan, Pavlodar, 64 Lomova Street.
  ematador@list.ru
  - Assoc Prof. PhD. Eng. Habil. Zoltan-Iosif Korka, Department of Engineering Science, Faculty of Engineering, Babeş-Bolyai University Cluj-Napoca, Romania, Piaţa Traian Vuia, nr. 1-4, 320085, Reşiţa
    zoltan.korka@ubbcluj.ro

Organization of truck maintenance

Bulbul Umarova* ⓘ, Nurbolat Sembayev ⓘ, Zoltan-Iosif Korka ⓘ

Abstract. *Increased maintenance performance is able to contribute in growing the profitability of a transport company. Maintenance produces financial costs as well as losses in terms of availability. While the financial costs are a direct economic loss, availability losses causes indirectly an economic loss. Therefore, proper maintenance of trucks leads to high availability, thus increasing short-term profit of a transport company. This paper deals with the development production and technological tasks development of innovative system of vehicle operating in the Republic of Kazakhstan, due to the centralized specialized technical repair organizations or auto services in the context of the specific modifications of trucks together with the manufacturers. It presents a methodology for assessing the operational efficiency of contemporary commercial vehicles from different brands and manufacturers for which there isn't yet a legal framework.*

Keywords: *car, exploitation, efficiency, profit, service.*

1. Introduction

Road transport plays an important role in the transport complex of the Republic of Kazakhstan, regularly servicing millions of enterprises, organizations, and the population. More than 70% of goods are transported by road annually, and more than 65% of passengers are transported by public transport. At the same time, road transport is the main consumer of resources consumed by the transport complex: 66% of fuel is of petroleum origin, 70% of labor resources and 50% of all capital investments [1].

As shown by the study of the existing management system, the least studied tasks were operational planning. It is known from management theory that optimization problems are considered the most difficult and effective of the tasks of this class.

On the other hand, in Kazakhstan, the fleet of commercial trucks is being intensively updated due to modern Russian, Chinese and other foreign models. At the same time, owners of transport enterprises make a choice of cars, focusing on the prestige of the brand, the availability of certain models on the market, cost, etc. But during operation, it often turns out that such a car has high operating costs compared to competitors, although it meets the requirements of the technological transportation process. In most cases, this is due either to car failures or to the high cost of spare parts, consumables, and lubricants.

2. The purpose of the work

The study of a methodology for evaluating the efficiency of operation of modern commercial vehicles of various manufacturers and brands, for which there is currently no regulatory framework.

The efficiency of the operation of vehicles in the implementation of commercial cargo transportation for the owner of trucks is ultimately determined by the maximum profit received.

The latter depends on the efficiency of using cars and the cost of transporting cargo, which in turn depends on the amount of operating costs.

Managing a complex system with continuously changing parameters of individual elements is quite a difficult task, its solution by standard optimization methods in production conditions in some cases do not give positive results, in others they require large expenditures of funds and resources. Therefore, to solve this problem, we have proposed a method of operational redundancy based on decomposition ideas, which will solve the problem of ensuring a high level of reliability of trucks of various brands at relatively low cost.

Effectively managing a motor transport company and the transportation process in market conditions means fully satisfying the effective demand for transportation and reducing the transport component in the final price of transported goods. All this can be considered a common management goal. To fulfill the purpose of operational management in it, a tree of goals is proposed (Figure 1).

The following symbols were used in Figure 1:
1- increase in profit;
2.1- increase in income;
2.2- reduction of financial costs;
3.1- reducing the cost of own resources
4.1- offering new services
4.2- increase in transportation tariffs
4.3- attracting new customers;

4.4- maintaining income at the planned level;
4.5- reducing the cost of an auto-hour;
4.6- reduction of the cost per man-hour;
4.7- reducing the cost of own resources;
5.1- compliance with the terms of delivery of goods;
5.2- compliance with cargo delivery addresses
5.3- compliance with the conditions of loading according to the nomenclature
    of goods;
5.4- reducing the cost of car watches;
5.5- reducing the cost of man-hours;
6.1- reduction of the empty mileage coefficient;
6.2- reducing vehicle downtime;
6.3- reducing the labor intensity of the transport company.
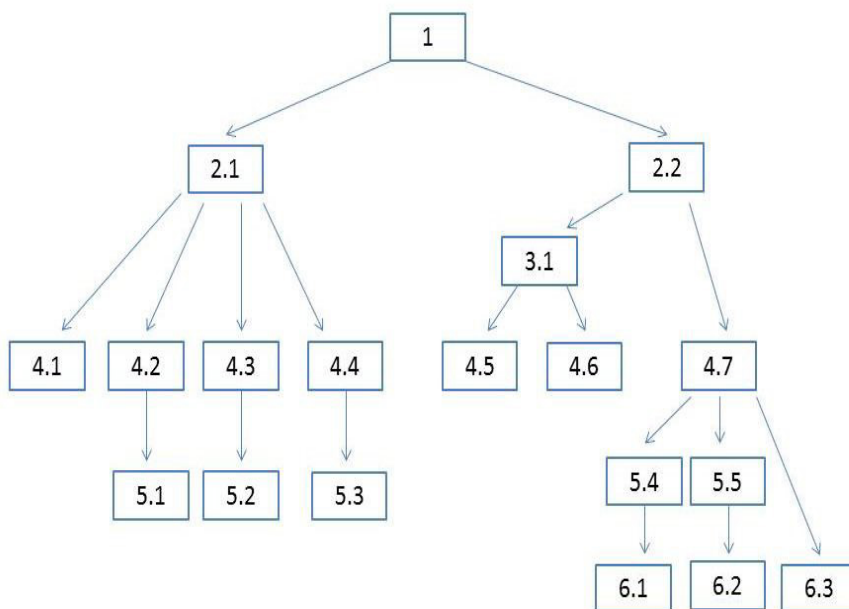
Figure 1. A tree of goals for effective management of road transport enterprises

Components such as maintaining revenues at the planned level; reducing the cost of preparing rolling stock for transportation, repairs and transportation proper belong to both levels of the formulated service facility. Based on the research conducted, it has been established that one of the most important problems facing road transport is to increase the operational reliability of cars. The research used

materials from surveys of motor transport enterprises, regardless of the form of ownership and affiliation, scientific and technical reports on the development and implementation of technological processes and mechanization tools for the maintenance and repair of trucks of various brands and industries, as well as the results of a survey among drivers of heavy-duty vehicles performing intercity and international road transport.

In order to increase operational reliability and reduce maintenance and repair costs, it is necessary, first of all, to improve the design and manufacturing technology of the car. On the one hand, the solution to this problem is provided by the automotive industry through the production of more reliable rolling stock, on the other – by improving the methods of technical operation. Unfortunately, this requires the creation of the necessary base to maintain the rolling stock in good condition, the use of advanced resource-saving technological maintenance processes directly in motor transport enterprises. Since the creation of optimal modes of operation and maintenance will reduce the intensity of changes in the technical condition of the car, which, ultimately, will lead to an increase in the durability of the car, the main indicator of which is the resource.

However, in motor transport enterprises, the insufficiency of their own working capital does not allow for proper investments (investments) for the development and maintenance of the necessary technical base for maintenance and repair, as well as aimed at replacing rolling stock and equipment. The renewal of fixed assets is one of the main factors in the effectiveness of their use, improvement of the quality characteristics of the services provided and, ultimately, economic recovery, sustainable development of the country's industry. Therefore, it is currently necessary to organize specialized enterprises with modern rolling stock and technological equipment for the maintenance and repair of a certain brand of cars.

Specialization is understood as an increase in the services provided, carried out by increasing the investment of resources per unit of production area, equipment, and vehicles.

The main indicator in determining the range of works and services provided is the coefficient of specialization and is calculated according to the formula [2]:

$$K_c = \frac{100}{\Sigma YB(2i-1)} \qquad (1)$$

where:

YB - the specific weight of types of services, %;

i – the ordinal number of the specific weight of services in the ranked series;

100 – the sum of the specific weights of services in individual industries.

For this purpose, the analysis of the fleet's activities for all groups of rolling stock together and the types of services provided is carried out. In the analysis, we use such indicators as the total and average daily mileage, car-days at

work, at the enterprise, in repair and other indicators, and the coefficients given in Table 1, as well as the volumes performed by the auxiliary structural units of the motor transport enterprise.

The production program for the operation of a transport company is calculated based on its production capacity and productivity and expressed in operational meters. Calculations are carried out for each car model separately, and then summarized throughout the fleet.

The production capacity of the fleet is determined by the car days at the enterprise. The initial data for its planning is the average number of used cars since the beginning of operation.

Table 1. Fleet performance indicators

№	Indicators
1	Cargo transported, thousand tons
2	Mileage utilization factor
3	Total mileage, thousand km
4	Average daily mileage, km
5	Rolling stock
6	Car-days at the enterprise
7	Car-days at work
8	Car-days in repair
9	Output ratio
10	Technical readiness coefficient
11	Income from car services, thousand tenge.

The calculation of the production program is based on the mileage for the year. To reduce the volume, cars were combined into technologically compatible groups [3].

On the other hand, modern car operating conditions place increased demands on its technical and operational properties. The requirements for increasing savings and improving environmental friendliness when using fuels and lubricants come out on top today. Optimization of measures to improve the work of the maintenance and repair department is one of the main tasks for the development of any motor vehicle enterprise since many times more labor and money are spent on car maintenance than on its production.

Technical service is a complex of works and services for the effective use of equipment and maintaining them in good condition throughout the entire period of operation. The operation of the product includes intended use, storage, maintenance, and repair. The purpose of technical operation of machines is to maintain, preserve and restore serviceability, operability, and resource. It includes the performance of works on refueling machines with fuel and lubricants, cleaning, regulation, replacement of wear-out machine elements, their restoration, checking and diagnosing the condition of machines and components, determining residual life, environmental impact control, restoration of worn parts, modernization of machines in operation.

In conditions of shortage and limited renewal of rolling stock at motor transport enterprises, the importance of repair and maintenance production of car owners and the entire repair and maintenance base increases significantly. However, the increase in the number of cars and the increase in traffic safety and environmental safety requirements create the need to improve the management system of the technical condition of the car fleet.

3. The results of the study

Operational reliability and the level of quality of services provided depend on the rationality and scientific organization of maintenance and repair. Because modern economic conditions objectively change the relationship between consumers and service providers. Motor transport companies, in conditions of intense competition and escalating need for systematic improvement of technological processes, inevitably strive to rationalize and increase the productivity of car maintenance and repair services as much as possible.

When repairing trucks, it is most often necessary to repair the engine, suspension, transmission and electronic systems. It is clear that thousands of miles of mileage can render unusable even such powerful engines that are installed on cars from leading countries of the world. Therefore, it is necessary to increase the operational and technical reliability of cars, by improving the organization and increasing the level of maintenance and repair at specialized motor transport enterprises, for further economic development of the enterprise and increasing its competitiveness. For this purpose, a special technological map of cars is compiled, depending on the technical condition and the amount of work performed. The calculation is carried out in the context of specific car brands [4].

We will determine and adjust the inter-repair mileage before major repairs according to the formula:

$$L_{KP} = L_{KP}^H * K_1 * K_2 * K_3 \tag{2}$$

where: L_{KP}^H – standard mileage before major repairs, thousand km;

K_1 – mileage correction factor depending on the operating conditions;

K_2 – correction factor depending on the modification of the rolling stock;

K_3 – the coefficient of correction depending on natural and climatic conditions.

Trucks have been attracting freight carriers for a long time with their reliability and increased comfort, but even such an automobile giant as Mercedes Benz breaks down sooner or later. In order to repair it in a short time and at minimal cost, you need to know the car service stations where it is produced. After all, the repair of a truck will differ from a passenger car not only in the spare parts used, but also in the repair technology [5-8]. Trucks must have increased reliability and resistance to breakage. This is the main requirement for a machine that is designed for everyday use in the harshest conditions.

4. Conclusions

In order to be sure that a truck after repair will serve faithfully for a long time, it must be repaired in a professional car service center, which has a team of highly qualified specialists who can work at the highest level, have specialized equipment and a modern technological base. In addition, they must conduct a reasonable pricing policy, and a wide range of spare parts must be present in the assortment.

It is necessary and advisable to organize centralized specialized repair and technical enterprises or car service centers in the context of specific modifications of trucks together with manufacturers, depending on their number and market demand levels.

References

1. *An annual report of Committee Ministry of Transport is Republics of Kazakhstan*, Astana, 2012.
2. L.B. Mirotin, *Perfection of operating work motor-car transport - M.*: 2000.
3. S.A. Zernishki, *Economy of motor transport.* - M.: Higher school, 2005.
4. M.I. Ydin *Technical service of machines and basis of planning of enterprises. it is Krasnodar*, 2007.
5. X. Tao, J. Mårtensson, H. Warnquist, A. Pernestål, Short-term maintenance planning of autonomous trucks for minimizing economic risk, *Reliability Engineering & System Safety*, 220, 2022, 108251.

6. C.P.Y. Ayala, S.M. Gallego, M.V.C. Mesa, C.E.P. Rodríguez, F.J.G. Carazas, Excellence model for the maintenance area in Heavy-Duty Truck Company, *IFAC-PapersOnLine*, 55(19), 2022, pp. 163-168.
7. A.R.Z. Hossein, A.R. Sayadi, M.J. Rahimdel, M.R. Moradi, Human reliability analysis in maintenance and repair operations of mining trucks: A Bayesian network approach, *Heliyon*, 10(15), 2024, e34765.
8. Y. Hao, Z. Chen, J. Jin, X. Sun, Joint operation planning of drivers and trucks for semi-autonomous truck platooning, *Transportmetrica A Transport Science*, 2023.

Addresses:

- PhD. stud. Umarova Bulbul, Toraighyrov University, Kazakhstan, Pavlodar, 64 Lomova Street
  bulbul186@mail.ru
  (*corresponding author*)
- Candidate of Technical Sciences, Assoc. Prof. Nurbolat Sembaev, Toraighyrov University, Kazakhstan, Pavlodar, 64 Lomova Street
  n.sembaev@mail.ru
- Assoc. Prof. PhD. Habil. Eng. Zoltan-Iosif Korka, Department of Engineering Science, Faculty of Engineering, Babeş-Bolyai University Cluj-Napoca, Piaţa Traian Vuia, nr. 1-4, 320085, Reşiţa,
  zoltan.korka@ubbcluj.ro

Aspects from the Museum of the Faculty of Engineering in Reşita

Eugen Răduca [iD], Cornel Haţiegan* [iD],
Petrişor Dorel Ţăran, Roberta Răduca

Abstract. *The work presents elements of the professional activity carried out within the institution of higher technical education in Reşita, since its establishment (year 1971) and in the following 50 years of existence. The framework that was chosen is that of the establishment of a museum. Some significant devices and equipment worked with in the students' laboratory works, two stands made by students in the graduation projects, and two laboratory works made by students in some profile disciplines are presented.*

Keywords: *museum, faculty, engineering, laboratory, devices.*

1. Introduction

The engineering profession is an essentially applied one that is the theoretical knowledge and experience gained by each graduate during the years of study is expected to be materialized in a series of technical and execution projects, realization of stands and products, mainly industrial, concrete improvements of achievements of the type mentioned.

Reşiţa has a long industrial tradition, over 250 years (in 1771 the first metallurgical furnace was built) [1]. In the more than 50 years of operation of the higher technical education in Reşiţa [2], first as the Institute of Subengineering (ISR), part of the Polytechnic Institute Traian Vuia in Timişoara (IPTVT), in the field of engineering, many were trained at a high level generations of graduates.

The students carried out the applied activities in the institution's own laboratories, but also in two flagship Romanian factories, Uzina Constructoare de Maşini Reşita (UCMR) and Combinatul Siderurgic din Reşiţa (CSR), benefiting from the valuable experience of their specialists. UCMR and CSR are direct descendants of the famous interwar factory, Uzinele Domeniile Reşita (UDR) [3], a joint-stock company with Romanian, English, French and German shareholders. The UDR had direct origins from 1771 [1].

The name Faculty of Engineering (FI) appeared for the first time in 1991, initially as a component of IPTVT (today Politehnica University Timişoara-UPT-). Since 1992, it has been part of the recently established "Eftimie Murgu" University of Reşita (UEMR) [4], which, during its operation in this structure, continued to function, essentially, with similar specializations and derived from those existing at the time of its establishment higher education in Reşita: mechanical, electrical, metallurgical.

From the year 2020, UEMR merged, through absorption, with Babeş-Bolyai University from Cluj-Napoca [5]. Currently, the Faculty of Engineering in Reşita is part of the Reşita University Center of the Babeş-Bolyai University in Cluj-Napoca (CUUBB in Reşita) [6].

2. Organization of the museum

Considering the long industrial tradition in Reşita, of the functioning of a quality technical higher education in Reşita, I had the initiative to establish a museum of the Faculty of Engineering (internal address No. FI 493/20.10.2023). The UBB management, visionary and efficient, immediately approved funds, and the CUUBB and FI management ensured the progress of the works so that at the beginning of the summer of 2024, a first room of about 105 m was made available to the museum, in the E body. A sketch is presented in Figure 1.
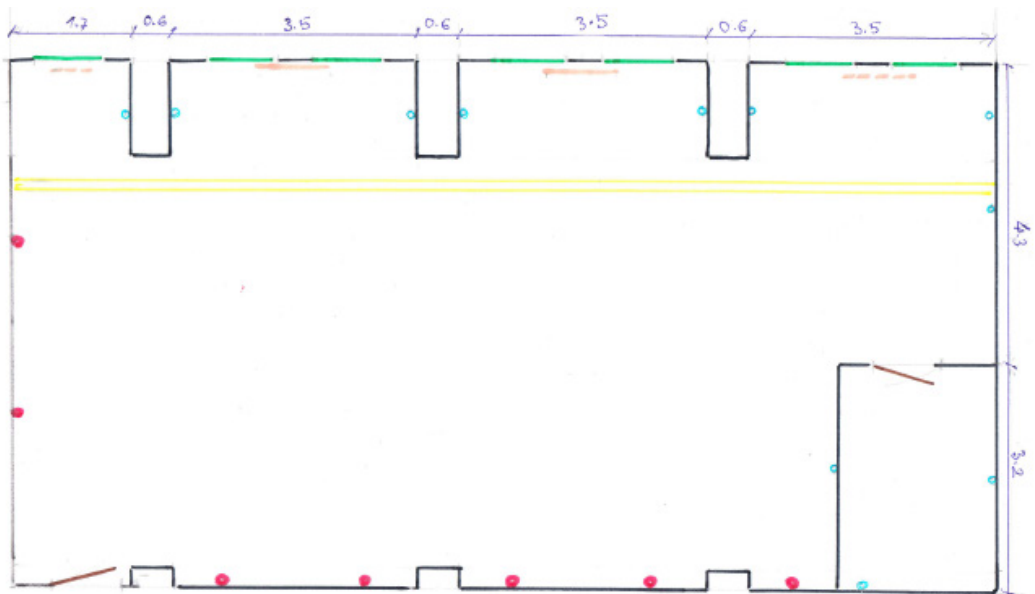
Figure 1. Exhibition hall sketch ● set of single-phase and three-phase sockets, ◉ single-phase socket, ▬ existing radiator, - - - installing radiator, ▬ window, ▬ pipes

Exhibits are presented in the museum, which, in one form or another, have been a component of the didactic activity carried out in the engineering field since its establishment (year 1971), in the following 50 years of existence (1971-2021). The exhibits are grouped by engineering fields that were studied at Reșita: mechanical, electrical, metallurgical, and by types:

- devices/installations/stands with which the activity was carried out in the laboratories;

- practical achievements (projects) of students/graduates during the didactic process.

It is desired that each exhibit be associated with some information, considered significant, as the case may be, such as name, year of manufacture, technical characteristics for devices/installations/stands, respectively name, author(s), year of completion for students' practical projects/graduates. This process has been initiated and is in progress for some of the pieces already on display.

Many of the devices, installations, industrial stands, and projects of students and graduates, following the checks carried out, were found to be at least partially functional and work is being done to improve their condition.

In the museum there are also pieces that could be considered auxiliary, such as 2 chalkboards - still used sometimes even today -, laboratory tables on which the equipment used to work was arranged, chairs on which the students sat in laboratory, a cupboard existing in laboratories since the foundation of the institution, (year 1971), for storing tools and laboratory equipment.

Considering that many of the devices, equipment, and stands used were produced in Romania, this fact is distinctly highlighted. As many know, Romania had - until the mid-1990s, at least - a consistent industry of its own, which contributed essentially to the development of the country and which was also able to provide products suitable for applied training in university engineering.

In Figure 2 and Figure 3 are presented images from which you can see the current organization of the museum, which, according to its expansion, will be adjusted, and in

Figure 2. Overview of the museum

Figure 3. Image from the entrance to the museum

Figure 4 part (shelf) of a cupboard from 1971 where devices/equipment were placed / auxiliaries used in laboratories. In the museum, we temporarily arranged some of the inventoried pieces. Currently, more than 100 pieces are exhibited, and several dozen more will follow.

Figure 4. Part (shelf) of a 1971 laboratory cabinet, now with some of the inventoried parts.

3. Exhibits

The paper then presents some exhibits considered representative of the activity carried out in the laboratories, with 3 exceptions (Figures 6, Figures 8, Figure 14), Romanian. Also, on display are (for now) two experimental stands used for laboratory work, reconstructed with the original equipment, as part of a Diploma Thesis [7].

The inventory numbers from that time are still visible in some of the exhibits.

Oscilloscopes are essential devices in any laboratory because practically, all mechanical, optical, thermal, chemical, etc. They can be converted with suitable transducers into electrical signals, and these can be visualized and measured with the oscilloscope.

Figures 5. The oscilloscope E-0101

The oscilloscope E-0101 [8] is the first oscilloscope for industrial use, Romanian - made in the 1970s - with the first electronic amplifier components in history (electronic tubes), used in laboratories for visualizing and measuring periodic electrical and electronic signals The oscilloscope [8] has a single channel of signal and allows the visualization of periodic electrical signals of direct and alternating current with frequencies up to $f = 5$ MHz and amplitudes from approx. 1mVvv to 250 Vvv.

Figures 6. HC3502 the analogue oscilloscope

HC 3502 is the first analog oscilloscope with two independent channels for synchronous measurement of two electrical signals up to 20 MHz frequencies - South Korea production-present in FI laboratories since the mid-1990s, which made it possible to carry out laboratory work and more complex research. Technical drawing was and remains one of the basic disciplines in the training of an engineer.

Figures 7. Drawing board

The drawing board was used for making all types of technical drawings, used before the advent of computers, in all institutions that had as their object of activity research and design in the engineering field.

Figure 8. Electromechanical graphics printer in two axes

An electromechanical graphics printer, in two axes, was used, before the advent of today's computers, for plotting on paper the graphics and characteristics of some components/equipment in XOY coordinates. It has been widely used in the study of systems of any type.

Figure 9. Handmade electric oven with resistors

The furnace was made as part of research-design activities in ISR and used for heating metallurgical samples at temperatures of the order of hundreds of degrees Celsius.

Figure 10. Electronic thermometer

This electronic thermometer is used to measure the temperature of mechanical, electrical, and metallurgical samples in the range 0...150 degrees Celsius.

Figures 11. E-4109 triple stabilized DC power supply with short circuit protection

The E-4109 source [9] provides three electrical voltages (5V/2A,+15V/0.4A, -15V/0.4A) stabilized, direct current, which is protected against short circuit. The voltage of 5 V/2A is a fixed one, being used in particular to power digital circuits made in TTL technology, but it can be used to power any analog or digital circuits that require this value. Each of the voltages of +15V/0.4 A, -15V/0.4A are actually variable, their values can be changed from 0V by the user by means of a multi-turn type fine-tuning potentiometer. The two sources can also be connected in series, thus obtaining a variable voltage between 0 and 30 V. The two sources can also work in differential mode, a useful situation especially in the case of powering circuits containing differential amplifier type components.

Figure 12. MAVO 35 analog laboratory multimeter

MAVO 35 analog laboratory multimeter produced since the 1970s, at IAEM Timișoara, was used for low-error measurements of direct and alternating voltages and currents, as well as electrical resistors. Direct and alternating current voltages can be measured in the range 1mV–1000 V, direct and alternating currents can be measured in the range 25uA–5A, and electric resistors in the range 0.2 Ω –50 MΩ. It enjoyed great success in foreign markets as well, today a clone is still manufactured in China, also exhibited in the museum.

Figures 13. Digital laboratory multimeter,

Laboratory digital multimeter presented is a stationary device produced at IEMI Bucharest, which was used in the ISR laboratories in the 1980s, and then, later, also in FI.

Figures 14. Portable digital multimeters

The presented multimeters are part of the first batch, from the beginning of the 1990s, with which the engineering faculty laboratories were equipped, used to measure voltages, currents, resistors and as the case may be, other parameters of electrical and electronic components.

In the higher engineering education in Reșita, it was a tradition that most graduation papers were completed with a practical achievement. The components of the graduation works came largely, until the mid-1990s, from donations of the two large factories in Resita. In many cases, these works were even carried out at the students' practice places in the two factories. Later, private companies sponsored the realization of the practical works. Several such practical works by students/graduates are exhibited in the museum, and in the present work two of them.

Figures 15. Inverter with transistors. The practical implementation of a Diploma Thesis from 1983
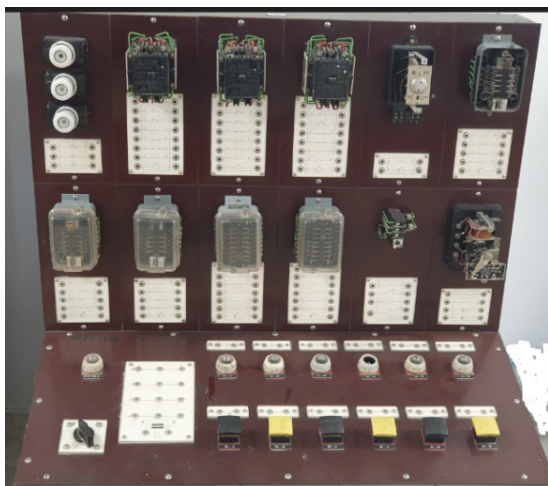
Figures 16. Stand for the study of electromagnetic relays Practical realization of a Diploma Thesis from around the 1990s

In the work [7], two of the laboratory works carried out by students, in relevant disciplines, were reconstructed and described, being now functional: 1. Measurement of voltage and currents in electric current circuits, carried out since the 1970s 2. Stand for determination of active filter parameters, carried out since the 1990s. Both are exhibited in the museum.

a   b

Figures 17. Experimental part of the laboratory work Measurement of voltage and currents in electric current circuits **a.** the direct current circuit **b.** the alternating current circuit

Figures 18. Experimental circuit of the laboratory work Study of active filters with operational amplifiers

In the Figures 17, Figures 18 can be noted, being additionally inserted for an easier follow-up of the tests, in addition to the original components (test circuits, analog measuring devices, rheostat) and devices currently used in laboratories in framework of these works: Fluke 177 multimeter, Tektronics TDS2004 oscilloscope.

4. Conclusions and perspectives

Starting from the thoughts of the illustrious Nicolae Iorga: "A people who do not know their history is like a child who does not know their parents" and "Knowing history, heroes, tradition, we become more sociable, more altruistic, more loving to people and life", we considered that creating such a museum is a necessary, useful and responsible act.

Among the actions scheduled for the future, we mention:

- expanding the exhibition space, which is currently insufficient even for the existing pieces;

- increasing the number of exhibits with pieces from the mentioned period, which are still found in the laboratories;

- increasing the number of exhibits with pieces that have already been brought to the museum space, but which have not been exhibited for various reasons: inadequate condition, lack of space for exhibition;

- repair / reconditioning / putting back into operation some pieces that want to be exhibited;

- supplementing the exhibits with additional, basic information and exhibition of technical bibliographic materials for museum exhibits.

It is desired that, in the end, the Museum of the Faculty of Engineering can be visited by a wide category of public. At present, it is only at the beginning and there is still much to be done before reaching a state of it that is considered to be satisfactory to enter such a circuit.

References

1. https://gugulanul.ro/monografia-istorica-a-resitei-istoria-industriala-a-resitei/ (downloaded on 18.09.2024)
2. HCM no. 321 of March 29, 1971, Bucharest
3. http://enciclopediaromaniei.ro/wiki/Uzinele_%C8%99i_Dome-niile_Re%C8%99i%C8%9Ba (downloaded on 18.09.2024)
4. MO No. 140 of July 21, 1992, pg. 15-16, Bucharest
5. MO No. 92 of January 28, 2021, pg. 6-23, Bucharest
6. https://eng.ubbcluj.ro/, (downloaded on 17.09.2024)
7. P.-D. Țaran, Scientific coordinator prof.univ.dr.ing. Răduca Eugen, *Study and actions for the establishment of a Museum of the Faculty of Engineering in Reşiţa*, Diploma Thesis, Faculty of Engineering in Reşiţa, Babeş-Bolyai University Cluj-Napoca, 2024.
8. IEMI Bucureşti-E-0101, *The service oscilloscope*, Technical book, Bucureşti, 1975.
9. ICSIET Bucureşti–E4109, *Triple stabilized voltage source*, Technical book, Bucureşti, 1975.
10. IAEM Timişoara-*MAVO-35*, Technical book Timişoara, 1978.

Addresses:

- Prof. Dr. Eng. Eugen Răduca, Department of Engineering Science, Faculty of Engineering, Babeş-Bolyai University Cluj-Napoca, Romania, Piaţa Traian Vuia, nr. 1-4, 320085, Reşiţa
  eugen.raduca@ubbcluj.ro
- Assoc. Prof. Dr. Cornel Haţiegan, Department of Engineering Science, Faculty of Engineering, Babeş-Bolyai University Cluj-Napoca, Romania, Piaţa Traian Vuia, nr. 1-4, 320085, Reşiţa
  cornel.hatiegan@ubbcluj.ro
  *(*corresponding author)*
- Stud. Eng. Petrişor-Dorel Ţăran, Faculty of Engineering, Babeş-Bolyai University Cluj-Napoca, Romania, Piaţa Traian Vuia, nr. 1-4, 320085, Reşiţa, petrisor.taran@stud.ubbcluj.ro
- Stud. Roberta Răduca, Faculty of Architecture and Urbanism, Politehnica University of Timisoara, Romania, Str. Traian Lalescu 2, Timişoara 300223
  roberta.raduca@student.upt.ro

An assessment of the impact of commercial land use on residential housing. A case study of Auchi, Edo State

Lucky Eboreime[*], Munirat Monisola Bejide,
Imiewan Roland Erayanmen, Kenneth Alenbalulu Ewah

Abstract. *Auchi's strategic location as a commercial hub has led to a significant expansion of its economy, resulting in a complex interplay between residential living conditions and economic development. The goal of this study was to determine how commercial activity affects residential housing in Auchi in order to raise the standard of housing there. In order to raise Auchi's housing quality, this study aims to evaluate how commercial activity affects residential housing. In order to accomplish this goal, the following goals were taken into account: figuring out why residential housing in Auchi was converted to commercial use; figuring out what mixed-use housing Auchi has; figuring out what commercial activity is currently taking place on the city's stock of residential housing; figuring out how these commercial activities affect Auchi's residential housing; and figuring out the overall effects of commercial activity on Auchi's residential housing. 155 questionnaires were distributed to various study areas' quarters as part of a quantitative research methodology. The basic percentage method was employed to analyze the gathered data. The research findings indicate that although commercial activities have created job opportunities and drawn many individuals and families to Auchi, there are drawbacks as well. Firstly, there is an increasing demand for space, which results in the conversion of residential properties into commercial establishments. This reduces the supply of residential housing for locals, causing a shortage and an increase in housing prices. Based on the research's findings, the following recommendations were made: the government should enact laws regulating property prices and rentals to ensure that they stay within the reach of locals; collaborate with private developers to construct affordable housing units in Auchi in order to alleviate the city's housing scarcity; enforce laws governing noise pollution in order to reduce disturbances caused by commercial activity in residential areas; and promote mixed-use development in Auchi, which enables locals to live close to places of employment while preserving their ability to balance their personal and professional lives.*

Keywords: *Residential housing, Commercial, Activity, Private developer, Housing scarcity, Auchi.*

1. Introduction

Urban development is dynamic, with the intersection of residential and commercial activity influencing many facets of community life. The growing commercial activity in Auchi, a town in Nigeria's Edo State, has generated a lot of interest in terms of how it will affect residential housing. Auchi, which was formerly well-known for its importance in trade and agriculture, is currently undergoing fast urbanization and commercial growth, which has an impact on its residential landscapes [1]. This introduction aims to investigate the complex effects of these commercial operations on Auchi's residential housing market, with particular attention to property values, community dynamics, infrastructure, and socioeconomic conditions. Auchi's commercial activity has increased as a result of several factors, such as infrastructural development and population growth. Land use patterns are changing significantly as markets and businesses expand. Due to the large land requirements of commercial enterprises, residential areas may be relocated or the demand for housing may change [2]. The spread of commercial zones may raise the value of nearby properties, which could result in higher rent and property prices. These factors would then have an impact on the accessibility and affordability of housing for locals [3].

The transformation of neighborhood character is one of the main issues with commercial encroachment on residential areas. A neighborhood's peaceful residential character can be disrupted by the presence of commercial buildings like stores, eateries, and offices, which can lower the standard of living for those who live there. Common problems resulting from such changes include increased foot traffic, noise, and pollution [4]. These elements have the potential to lessen the residential allure of neighborhoods that are generally regarded as peaceful and suitable for residential use. Another important area that is impacted by the increase in commercial activity is infrastructure. The augmented need for roadways, parking areas, and communal facilities frequently puts pressure on the current infrastructure, resulting in gridlock and a reduction in the caliber of services [5]. For Auchi, the challenge lies in balancing commercial growth with the maintenance and enhancement of infrastructure to support both residential and commercial needs adequately [6].

Attention should also be paid to the effects on nearby companies and job prospects. Commercial operations frequently promote economic expansion and job creation, which helps residential communities by supplying employment opportunities and promoting stability in the economy [7]. However, there may be unevenness to this economic boost, which could result in income inequality and socioeconomic divisions within the community (Ifeanyichukwu, 2018). Furthermore, social dynamics in Auchi may be impacted by the interplay between the residential and commercial sectors. Social structures and community cohesion may change as a result of commercial activities drawing in a diverse range of people and businesses. Although the influx of new businesses and residents may enhance the local culture, it can also cause tensions and conflicts between long-term locals and recent arrivals [8]. Land use conflicts, in which businesses may invade or disturb existing residential areas, are a

major source of concern. Conflicts over land use and rights may result from this encroachment, which may have negative social and legal repercussions [9]. In order to resolve these conflicts and guarantee the peaceful coexistence of residential and commercial uses, effective urban planning and regulatory measures are needed.

The growth of commercial activity can have indirect effects on real estate development trends in addition to direct ones. It is possible that developers will prioritize investing in properties with commercial potential over residential needs, thereby contributing to a real estate priorities shift [10]. The area's supply and caliber of residential housing may be impacted by this change. A thorough analysis of how Auchi's commercial activities influence residential housing is necessary to comprehend these effects. For a comprehensive understanding of the community's challenges and changes, this analysis needs to take into account both quantitative and qualitative data. The research will provide insightful information about urban development and planning tactics designed to successfully strike a balance between residential and commercial demands [11]. In conclusion, Auchi's residential housing is affected by commercial activity in a way that is consistent with global urban trends. This study attempts to provide useful suggestions for controlling urban growth while maintaining the standard and stability of residential environments by analyzing these effects. To promote sustainable and peaceful urban living, commercial development and residential needs must be balanced.

2. Research methodology

2.1. Research design

According to [12], research design is defined as a framework that shows how problems under investigation will be solved. [13] stated that the research design is a way to accomplish the research objectives through empirical evidence that is obtained economically. The considerations that determine the research design to be used include: research purpose, categories of data required, data sources, and the cost implications. According to [14], descriptive research is a process of collecting data in order to answer questions concerning the current status of the subjects in the study. They point out that the purpose of descriptive research is to determine and report the way things are done. Descriptive research is used to obtain information concerning the current status of the phenomena to describe what exists with respect to variables or conditions in a situation. The methods involve a range of activities, from the survey, which describes the status quo, to the regression study, which investigates the relationship between variables. The primary use of descriptive statistics is to describe information or data through the use of numbers (create a number of pictures of the information). The characteristics of groups of numbers representing information or data are called descriptive statistics. According to [13], this type of research attempts to describe such things as possible behavior, attitudes, values, and characteristics.

The description of this research design matches with the objective of this study, as the study sought to investigate the impact of commercial activities on residential housing in the Auchi community.

2.2. Data required and sources

The task of data collection begins after a research problem has been identified and a research design plan has been checked out. The method of data collection used for this study was both primary and secondary data, which was obtained through the use of a questionnaire, personal observation, and an oral interview.

2.2.1. Primary data

The primary data are those that are collected afresh and for the first time and thus happen to be original in character. Primary data was collected during the course of the study. It was obtained through observation, which is one of the major instruments for primary data collection in research generally. It is one of the earliest instruments used for scientific research in the process of carrying out reconnaissance surveys on the study area. Observation that was beneficial to this work was employed on the motorcycle transport conditions. Also, the researcher used a standard set of questionnaires and personal interviews as an instrument for data collection, which represent personal contact between the researcher and the respondent with the aim of getting reliable and valid information from the respondent on the situation of motorcycles and institutions that are related to transportation issues in the area under study.

2.2.2. Secondary data

These data were obtained second-hand from publishers or record sources and used for a purpose different from that of the agency that initially collected them from the field. It could be gotten quickly and cheaply compared with data collected specially for the problem at hand. The secondary source of data collected for this study will include books such as journals, research reports, maps, and publications of various scholars in related fields regarding the subject matter of the study. Also, dissertations, seminar papers, and internet materials were sourced for the study.

2.3. Research population

The population of the study consists of Eight Thousand, Two Hundred and Sixty (8,260) residential buildings in the five major quarters in Auchi; this was obtained from the record of Benin Electricity Distribution Company (BEDC) Auchi Branch (2023). A breakdown of the population is shown in Figure 1.

Table 1. Sample Size and sampling

S/N	QUARTER	Housing unit
1	AKPEKPE	2,400
2	IYEKHEI	3,000
3	UTSOGUN	1,300
4	IGBEI	800
5	AIBOTSE	760
	TOTAL	**8,260**
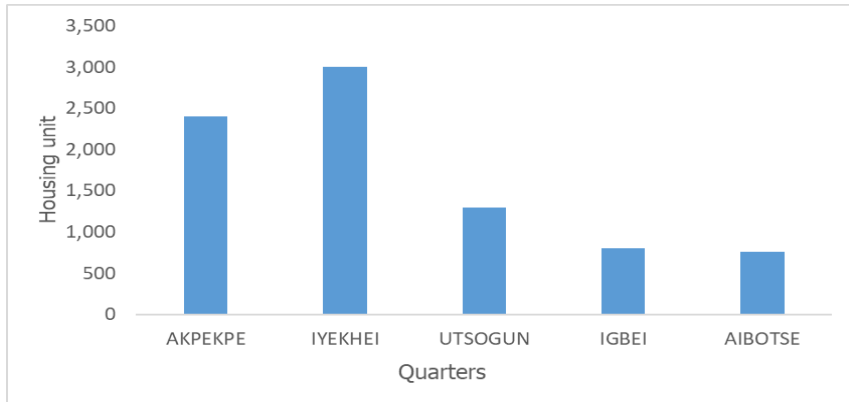
Figure 1. Population of housing unit

2.4. Sample size

The use of stratified sampling technique was used to divide the population into five (5) quarters (strata), and 155 questionnaires were distributed as represented in Table 1. The sample size was calculated using equation 1 and as shown in Table 2.

$$n_o = \frac{Z^2 P(1-P)}{e^2}$$ (1)

where,

e: desired level of precision, the margin of error
p: the fraction of the population (as percentage) that displays the attribute
z: the z-value, extracted from a z-table

Table 2. Sample Size and sampling

S/N	QUARTER	Housing unit	Sample size	Percentage (%)
1	AKPEKPE	2,400	45	29
2	IYEKHEI	3,000	56	36
3	UTSOGUN	1,300	24	15
4	IGBEI	800	15	10
5	AIBOTSE	760	15	10
	TOTAL	**8,260**	**155**	**100**

3. Results and Discussion

3.1. Data presentation

Based on the data presented in Table 3 and Figure 2, it can be observed that of the 150 respondents, 54 (or 36%) are female and 96 (or 64%) male. Most of the respondents from the study area are male, according to the distribution. 59 respondents, or 39% of the population, are single, 76 respondents, or 51% of the population, are married, and 15 respondents, or 10% of the population, are divorced, according to Table 4. As can be seen, married people make up the majority of the respondents. According to Table 5, 30 respondents, or 20% of the population, are between the ages of 20 and 29; 80 respondents, or 53% of the population, are between the ages of 30-39; and 40 respondents, or 27% of the population, are between the ages of 40 and above. Figure 3 shows the educational status of the respondents. 32 of them, representing 21%) of the population, attained primary education. 42 of the respondents, representing 28% 28% of the population, attained secondary education. 55 of them, representing (37%) of the population, attained tertiary education, while 18 of the respondents, the respondents, representing (12%) of the population, did not get any formal education. The above indicates that the greater percentages of the respondents are well educated. The good academic background of most respondents gave them the good disposition to respond objectively to the questions regarding the subject of the research. Figure 4 shows the number of years the respondents have spent in the study area. 30 of them representing (20%) of the population have spent 1-5 years, 44 of the respondents representing (29%) of 40 have spent 6-10 years, 59 of them representing (37%) of the population have spent 11-20 years, and 17 of the respondents the respondents representing (11%) of the population have spent 20 and above years in the study area.

	Frequency	Percentage
Male	96	64
Female	54	36
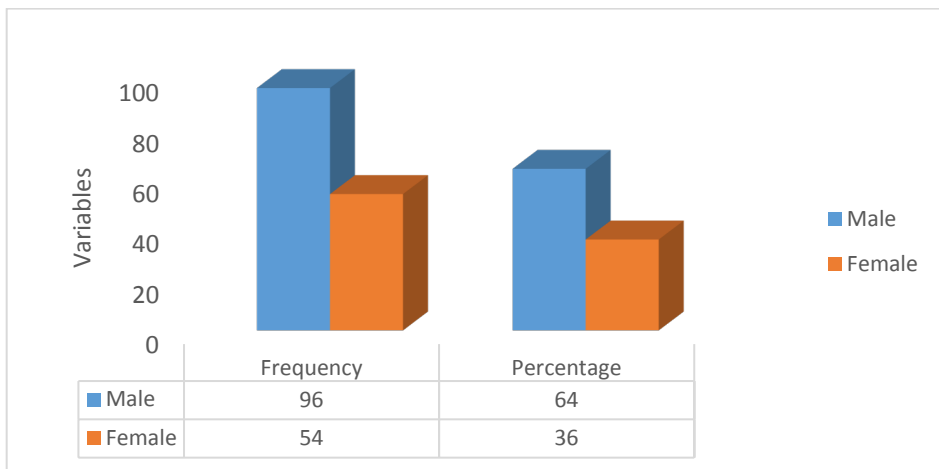
Figure 2. Sex distribution

Table 3. Respondent demograph

Option	Frequency	Percentage
Male	96	64
Female	54	36
Total	150	100

Table 4. Sex Distribution of Respondents

Option	Frequency	Percentage
Single	59	39
Married	76	51
Divorced	15	10
Total	150	100

Table 5. Age distribution of respondents

Option	Frequency	Percentage
20-29	30	20
30-39	80	53
40 and above	40	27
Total	150	100
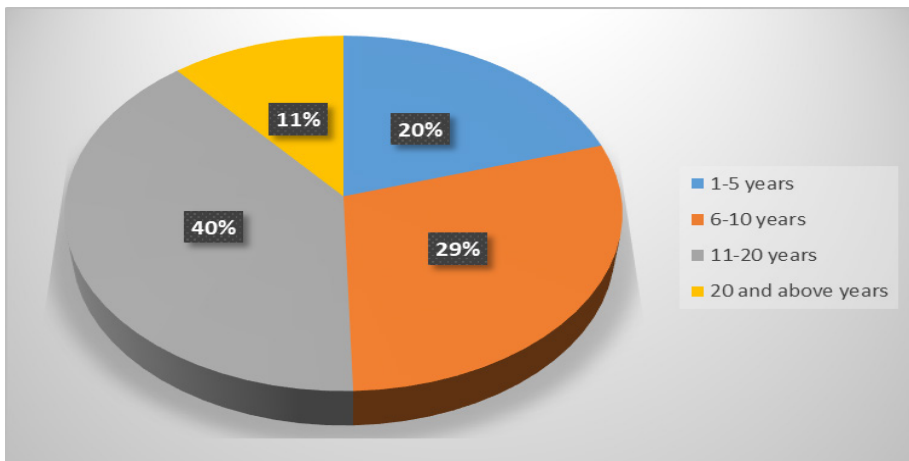
Figure 3. Sex distribution
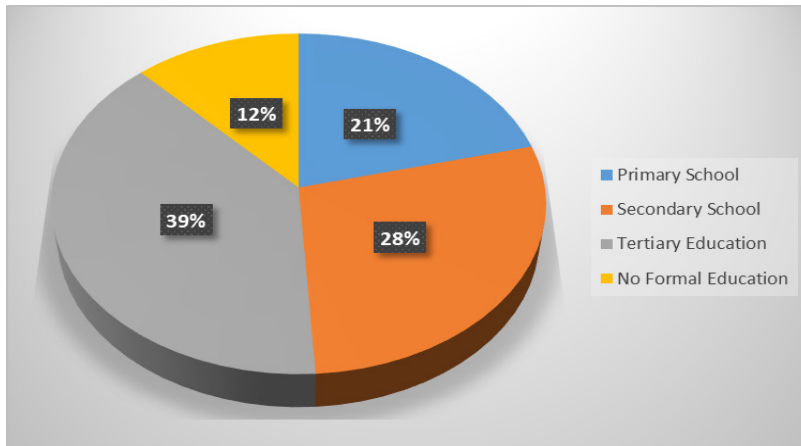
Figure 4. Number of years spent in Auchi

3.2. Evaluation of commercial activities and residential properties

According to Figure 5, 115 respondents, or 80% of the population, concur that Auchi's commercial activity has caused residential properties to be converted into commercial ones, while 33 respondents, or 20% of the population, disagree for the same reason. According to Figure 6, 116 respondents, or 77 percent of the population, concur that Auchi's commercial activity contributed to the rise in traffic congestion in residential areas, while 34 respondents, or 23 percent of the population, disagree. Table 4.2.8 shows that, of the respondents, 117 (or 80%) agree that commercial activities in Auchi have raised the levels of noise and pollution in residential areas of Auchi, while 33 (or 20%) disagree. Table 4.2.8 shows that, of the respondents, 100 (or 66%) agree that Auchi's commercial activities have reduced the availability of amenities for residential areas, while 50 (or 34%) disagree.

The finding revealed that the respondents, 98 (or 65%) agree that the actions taken by the local authorities to address the impact of commercial activities on residential housing have been successful, while 52 (or 35%) disagree. The result indicates that 115 respondents, or 79% of the population, concur that there has been an increase in commercial activity on study area residential property, while 32 respondents, or 21% of the population, concur. This suggests that the rise in commercial activity on residential buildings within the study area is driving up demand for housing. In addition, among the respondents, 30 respondents (20%) agree that commercial activities have had a very positive impact on the residential housing in the study area; 33 respondents (22%) agree that commercial activities have somehow positively impacted the residential housing in the study area; 25 respondents (22%) agree that commercial activities have had a neutral impact on the residential housing in the study area; and 62 respondents (41%) agree that commercial activities have negatively impacted the residential housing in the study area. This suggests that the rise in commercial activity on residential buildings

in the study area is driving up housing demand. The research also showed that the presence of commercial buildings among residential properties has resulted in a housing scarcity and a migration of residents from the area's center to its outskirts in pursuit of more hospitable and suitable housing.
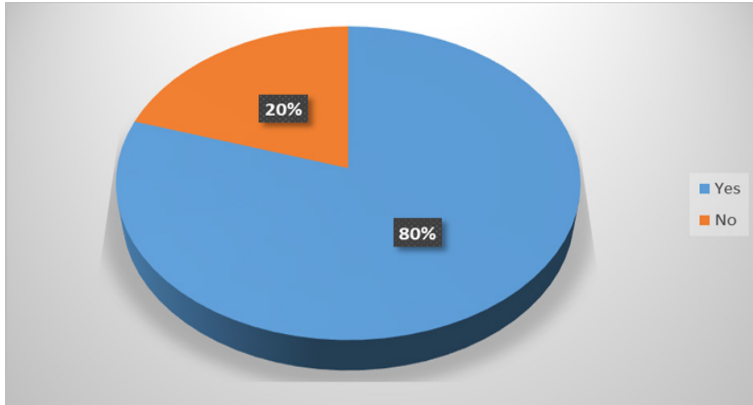
Figure 5. Response of respondents to commercial activities on residential properties
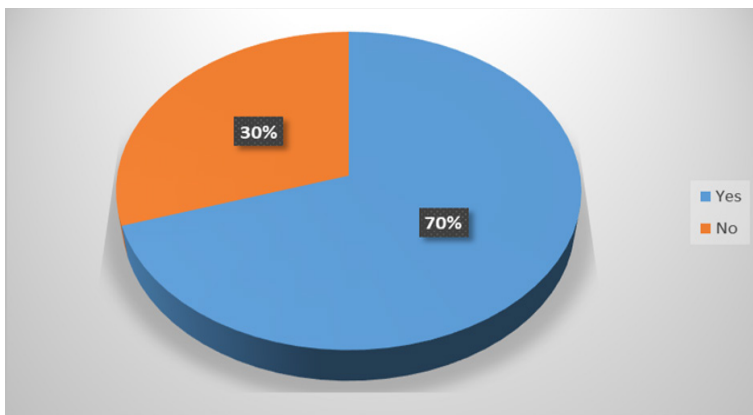
Figure 6. Response of respondents to commercial activities on traffic congestion

The assessment of the impact of commercial land use on residential housing in Auchi, Edo State reveals a complex interplay between commercial activities and residential living conditions. The findings indicate that the expansion of commercial land use significantly influences various aspects of residential housing, including property values, accessibility to amenities, and overall quality of life for residents. Commercial land use often leads to an increase in property values in adjacent residential areas. This phenomenon can be attributed to improved infrastructure and enhanced accessibility that commercial

establishments bring. However, this increase can also lead to gentrification, where long-term residents may find themselves priced out of their neighborhoods due to rising costs associated with increased demand for housing. The proximity of commercial establishments provides residents with easier access to goods and services. This convenience can enhance the quality of life by reducing travel time and costs associated with accessing essential services such as grocery stores, healthcare facilities, and recreational areas. However, it is crucial to balance this accessibility with potential drawbacks such as noise pollution and traffic congestion that may arise from increased commercial activity. While commercial land use can improve certain aspects of living conditions through better amenities and services, it can also detract from the quality of life if not managed properly. Issues such as overcrowding, environmental degradation, and loss of green spaces are significant concerns that need addressing. Effective urban planning strategies must be employed to mitigate these negative impacts while maximizing the benefits derived from commercial developments. In conclusion, the relationship between commercial land use and residential housing in Auchi is multifaceted. It necessitates careful consideration by policymakers to ensure sustainable development that benefits both commercial interests and residential communities. Future research should focus on long-term impacts and explore strategies for harmonizing these two critical aspects of urban development.

4. Conclusions

In assessing the impact of commercial land use on residential housing in Auchi, Edo State, it becomes evident that the interplay between these two types of land use significantly shapes the socio-economic landscape of the area. commercial land use has the potential to stimulate economic growth and improve living standards in Auchi, it also poses challenges that require careful management through strategic planning and community engagement. Balancing these factors will be essential for ensuring that both commercial enterprises and residential neighborhoods thrive harmoniously.

Author Contributions: Conceptualization, L. Eboreime, methodology, M.M. Bejide, writing-review, I.R. Erayanmen and editing, K.A. Ewah
All authors have read and agreed to the published version of the manuscript.

Conflicts of Interest: The authors declare no conflict of interest.

References

1. T. Ezekiel, Infrastructure and Urban Growth: Balancing Commercial and Residential Needs, *Nigerian Journal of Urban Planning*, 12(1), 2019, pp. 54-67
2. A. Obayelu, Urbanization and Economic Development in Nigeria, *African Development Review*, 31(1), 2019, pp. 62-79.
3. W. Stull, Community Environment, Zoning, and the Market Value of Single Family Homes, *The Journal of Law and Economics* 18(2), 2007, pp. 535- 557.
4. J. Adeniran, G. Okafor, Urban Property Markets in Nigeria: Trends and Implications, *Journal of Real Estate Research*, 41(3), 2020, pp. 405-420.
5. L. Ijeoma, E. Ezeani, Neighborhood Changes Due to Commercial Development: A Case Study, *Journal of Housing and the Built Environment*, 32(2), 2017, pp. 150-165.
6. T. Oluwole, Urban Infrastructure Development in Growing Towns: A Case Study of Auchi. *Urban Planning International*, 29(2), 2021, pp. 92-104.
7. K.A. Okete, J. Braimah, U. Justin, Investigating the causes and impact of gulley in Auchi Nigeria, *Journal of Geography, Environment and Earth Science International,* 4(4), 2016, pp. 10-16.
8. A. Okonkwo, K. Eze, Real Estate Development Trends in Emerging Urban Areas, *Journal of Property Investment & Finance*, 39(4), 2021, pp. 320-335.
9. N. Agbonifo, O. Akinbo, Urban Planning and Development Strategies: Lessons from Auchi, *Journal of Urban Affairs*, 45(1), 2023, pp. 78-95.
10. O.A. Aliu, Urban land use planning and management in Nigeria: A case study of Minna Niger State. *Journal of Environmental and Earth Sciences,* 5(4), 2015, pp. 28-36.
11. A. Ayotamuno, A.E. Gobo, O.B. Owei, The impact of land use conversion on a residential district in Port Harcourt, Nigeria, *Environment and Urbanization: Institute for Environment and Development* (IIED), 22(1), 2010, pp. 259–265.
12. I. Duru, M. Okechukwu, Land Use Conflicts in Urban Areas: Case Studies and Solutions, *Urban Studies Review*, 37(4), 2019, pp. 241-260.
13. K.A. Umar, J. Braimah, Investigating the causes and impact of gulley in Auchi Nigeria, *Journal of Geography, Environment and Earth Science*, 4(4), 2016, pp. 5-8.

Addresses:

- Lucky Eboreime, Department of Urban and Regional Planning, Auchi Polytechnic, Auchi, Edo State, Nigeria.
  luckyeboreime01@gmail.com
  (*corresponding author)
- Munirat Monisola Bejide, Department of Urban and Regional Planning, Auchi Polytechnic, Auchi, Edo State, Nigeria. monibejide@yahoo.com
- Imiewan Roland Erayanmen, Department of Urban and Regional Planning, Auchi Polytechnic, Auchi, Edo State, Nigeria
  erayanmenroland@gmail.com
- Kenneth Alenbalulu Ewah, Department of Estate Management and Valuation, Auchi Polytechnic, Auchi, Edo State, Nigeria.
  ken.ewah@gmail.com

Development and Evaluation of a COOI24m Pelletizer

Yahaya Olotu* ⓘ, Afolabi Adeniyi Rodiya ⓘ, Victor Ndaraba Haruna,
Benjamin Chukwutem Ikwuebene

Abstract. *It is essential to formulate appropriate feeding pellets with the required nutrient compositions for poultry animals to meet the growing demand for protein through the provision of eggs and meat. Forming the required feed concentrates into pellet-mash requires a pelletizing machine, which is, in most cases, very expensive for the local farmers due to the high foreign exchange rate. Based on this, the study focuses on the development of a simple and affordable pelletizing machine from locally sourced materials. The machine consists of a frame, hopper, die roller, pelletizer, and internal combustion (5.5 hp), and it was run at 950, 600, and 450 revolutions per minute. The formation and discharge of pellets from the machine increased with the pelletizing efficiency (Pe) of 70.3% to 84.6% at a moisture content (MC) of 15.8% to 27.1%, and the Pe decreased at a moisture content above 29.0%. Also, the drying temperature (DT) has a significant effect on the pellet moisture content (MC) and bulk density at P > 0.05. The effects of weather conditions on pellets produced using the COOI24m pelletizer were assessed in this study. The analysis showed that changes in weather conditions had an insignificant effect on the quality and properties of the pellets. The machine is highly recommended for use by small-scale livestock farmers for the local production of pellet-mash of different compositions because of its affordability, ease of use, and high working efficiency.*

Keywords: *Machine, pellets, pelletizing, moisture content, compositions, pellet-mash, local, farmers.*

1. Introduction

A range of basic ingredients are used in the production of compound meals for animals. The feeds are defined in accordance with precise guidelines for physical, sanitary, and nutritional quality, as well as guidelines on their nutritive composition.

In order to optimise processing while preserving or regulating nutritional quality for a particular feed form, these requirements collectively necessitate understanding of a wide range of distinct constituent qualities. Thus, it may now be necessary for the fields of "feed science and technology" and "nutritional science" to work together in order to advance cattle production. It has been observed that animals fed pelleted feeds perform better than those fed mash feeds in terms of average daily gain and feed conversion [1,2] in both the case of pigs and poultry [3]. Feed processing affects how quickly feed components break down and move through ruminants [4]. For example, pelleting decreases starch's resistance to ruminai degradation by around 15% [5]. Pellets must also possess a fundamental physical property, such as durability and hardness, in order to endure the rigours of transportation. Durability is the amount of particles that return from pellets following mechanical or pneumatic agitation, whereas hardness is the force required to smash a pellet or a batch of pellets at once. The impacts of feed composition, conditioning, expander treatment, pellet binders, die selection, etc., can also be assessed using these quality parameters [6].

A pelletizer, also called a pellet machine, is specialised equipment used to create feeds (feed pellets and feed mash) for animals like sheep, pigs, cattle, pets, fish, birds, chickens, poultry, and other livestock. A roller and a flat die are the machine's essential components. The feed stock enters the pelleting chamber directly and uniformly, and the feeding of flat-die tiny feed machinery is dependent on material weight. The raw materials will be forced through the pellet die's perforations during the pelletizing process by the pressure created between the dies and rollers. Additionally, the mash components will be compressed into uniform pellet particles.

Specific machinery for making feeds (feed pellets & feed mash) for animals such as sheep, pig, cattle,pet, fish, hource, chicken, poultry and other livestock is known as pelletizer or pellet machine. The key parts of the machine are flat die and roller. The feeding of flat die small feed machinery relies on materials weight and the feed stock enters into the pelleting room directly and evenly. While pelletizing, the pressure generated between the dies and rollers will force the raw materials through the holes in the pellet die. And mash materials will be pressed into regular pellet particles. It is known for the features of easy operation, greater mobility, low noise, low price, low energy consumption and relatively low productivity when compared with ring die feed mills. Some of the materials usually used for pelleting are wheat, rice, corn, soya expeller, maize, sorghum, broomcorn, e.t.c. It is well-known for having simple operation, increased mobility, little noise, low cost, low energy usage, and, in comparison to ring die feed mills, comparatively low productivity. Typically, pelleting involves the use of wheat, rice, corn, soy extract, maize, sorghum, broomcorn, and other materials.

Nutritionists specify objective parameters for animal feed, which include certain moisture needs. In addition to being necessary for diets, moisture is also necessary for the pelleting of animal feed. Particle binding, gelatinization, pellet quality, mill

energy consumption, and profitability are all facilitated by enough moisture. Elevated moisture levels may result in "plug-ups" and decreased mill throughput, which can drive up energy costs and accelerate microbial development. Low feed moisture, on the other hand, causes brittle pellets, which raise fines and result in inefficient use of feed on farms. Controlling moisture is essential to the financial success of producers. Even moisture distribution and absorption inhibit unchecked microbial load growth, promoting feed utilisation and pellet quality while lowering shrink and loss in the production process. One important criterion for selecting premium pellets is moisture content. Producers must guarantee uniform moisture absorption in order to protect feed shape.

Additionally, as feed pelleting progresses, temperature changes. In order to encourage moisture absorption into the feed, high temperatures are employed during conditioning. Temperatures between 50°C and 90°C have been shown to improve pellet quality and increase the digestibility of crude protein, dry matter, and starch. Although this varies by kind of feed, such as high starch, fibre, or protein, heat-sensitive, and more, most manufacturers condition feed around 78–80 °C. This temperature range allows feed to absorb steam moisture sufficiently, which promotes particle binding, starch gelatinization, and improved digestibility. When feed is pushed into the die, pressure is created. The friction that results flashes off any water that hasn't been fully absorbed, affecting the feed's moisture content. The thermal energy produced by this friction can occasionally surpass the heat applied during conditioning. However, by lowering or raising the processed pellet's weight excessively, relative humidity and ambient temperature have a substantial impact on its quality and can lead to contamination and blockage. The rising reliance on exogenous enzymes in animal nutrition has led to a greater body of research on the impact of pelleting on enzyme stability in recent years [7,8]. There hasn't been much research done on how ambient temperature and relative humidity affect pellet quality, though. This brings up the main goal of the study, which is to evaluate how weather impacts the quality of pellet mash.

2. Materials and Methods

2.1. Design consideration

The following factors were taken into considerations in designing, fabrication and testing of the pellet machine: weight of the machine, physical characteristics of the feed materials (rolling resistance, friction), screw auger speed, prime mover power output and the selection of fabrication materials in line with the approaches of [9] and [10].

2.2. Description of the component parts of the pellet milling machine

COOI24 pellet machine is composed of the following component parts as shown in Figure 1: 1. Frame, 2. Hopper, 3. Die roller, 4. Pelletizer plate, 5.Bearing, 6. Bolt and nut, 7. Internal combustion(5.5hp)

2.2.1. Design for pelletizer hopper

The hopper of the pelletizer was designed as indicated as follows:

$$W = f\left(\frac{D}{B}\right)^{t_{B\,2.5}} \qquad (1)$$

T = time in minute for the flow
B = Orifice diameter
W = bulk density of the concentrate
D = Average diameter of the concentrate [11].

2.2.2. Design for pelletizer extrusion pressure

The pelletizer extrusion pressure is the pressure that force concentrate through a die at a high pressure. The pelletizer extrusion pressure was designed as expressed in equation (2):

$$P = \frac{W}{A} \qquad (2)$$

where:
W = Thrust force
A = Area of the extruder $= A = (N\,\frac{\pi D^2}{4})$
N = Number of holes
D = Hole diameter

2.2.3. Design for propeller shaft

The pelletizer shaft was designed using the expression as follows:

$$T = N\frac{60}{2\pi N} \qquad (3)$$

where:
T = Transmitting force (N)
P = Power (Watts)
N = Number of holes [12].

2.2.4. Design for volume of barrel (Extrusion Chamber)

The volume of the extrusion barrel was computed using the relationship given as:

$$V = \pi r^2 h \qquad (4)$$

where:
V = volume of extrusion barrel
r = radius of barrel, and
h= height of barrel [13]

2.2.5. Design for tangential force

Tangential force of the pellet machine was designed using equation

$$F = W\tan\Phi \qquad (5)$$

where:
F = Tangential force
W = Thrust force
Φ = Helix angle [14].

2.2.6. Die plate

It is the process that turns the prepared feeds into solids with a cylinder shape, or pellets. When the internal combustion engine is turned on, the die plate can rotate because it is bolted perpendicular to a vertically positioned diameter shaft. It has 400 holes with a 6 mm diameter, all of which are evenly spaced.

2.2.7. Discharge chute

The pelletized feeds are released for collection at this point. Gauge number 2 mm stainless steel sheet is used to construct the inclined discharge chute. To reduce the amount of pelleted feed that spills unintentionally, a flapper is hinged close to the chute opening as described by [15].

2.3 Concentrates formulation

Rice and maize husks were mixed with maize grain and eggs at different mixing ratios. Water was added to reach a moisture content level of 15%. Five (5) levels of concentrate formulation of 2, 4, 6, 8, and 10 kg were used for the testing of the machine, as follows:

i. $\frac{1}{2}$ kg of rice husk, $\frac{1}{2}$ kg of maize husk, 1 kg of maize grain and two (2) eggs;
ii. 1 kg of rice husk, 1 kg of maize husk, 2 kg of maize grain and (4) eggs;

iii. $1\frac{1}{2}$ kg of rice husk, $1\frac{1}{2}$ kg of maize husk, 2 kg of maize grain and (6) eggs;

iv. 2 kg of rice husk, 2 kg of maize husk, 2 kg of maize grain and (8) eggs; and

v. $2\frac{1}{2}$ kg of rice husk, $2\frac{1}{2}$ kg of maize husk, 5 kg of maize grain and 10 eggs.

The chicken and bird feed pelletizing machine was evaluated in terms of pelleting efficiency, as described by [16] and [17]. The pelleting efficiency of the machine was calculated and expressed as follows:

$$P_e = \frac{W_{fp}}{W_{fc}} * 100 \qquad (6)$$

P_e = Pelletizing efficiency (%);
W_{fp} = Weight of formed pellets (Kg); and
W_{fc} = Weight of feed concentrates (Kg)

The pellet moisture content (PMC) at each 5-minute interval was computed to achieve a relative safe moisture content of 10% for storage as recommended by [18] and [17]. Pellet Drying Time (PDT): This is the time taken in drying the pellets for each treatment combination to the desired safe storage moisture content. The oven was set at a drying temperature of 105 °C and the drying was monitored at intervals of 10 minutes to ascertain the changes in their weights as follows

i. $\quad PMC_{5min} = \frac{IWP_{5min} - FWP_{5min}}{IWP_{5min}} * 100 \qquad (7)$

ii. $\quad PMC_{10\,min} = \frac{IWP_{10min} - FWP_{10min}}{IWP_{10min}} * 100 \qquad (8)$

iii. $\quad PMC_{15\,min} = \frac{IWP_{15min} - FWP_{15min}}{IWP_{15min}} * 100 \qquad (9)$

iv. $\quad PMC_{n\,min} = \frac{IWP_{n\,min} - FWP_{n\,min}}{IWP_{n\,min}} * 100 \qquad (10)$

where:

IWP is the initial moisture content of the pellet;
FWP is the final moisture content of the pellet;
Time interval: 5 minutes, 10 minutes, 15 minutes …………….. *n* minutes.

2.3.1. Bulk density

The produced pellet was loosely poured in a 250 ml beaker till was full, so as to get the bulk volume, then the feed inside the beaker was weighed to get the mass. The bulk density be calculated as follows:

$$BD = \frac{BMP}{BVP} \qquad (11)$$

where:

BD = Bulk density;

BMP = Bulk Mass of the pellet;

BVP = Bulk volume of the pellet

The MC differential in response to the temperature and relative humidity of the storage environment was used to assess the quality of the pellet at 10% moisture content (MC).
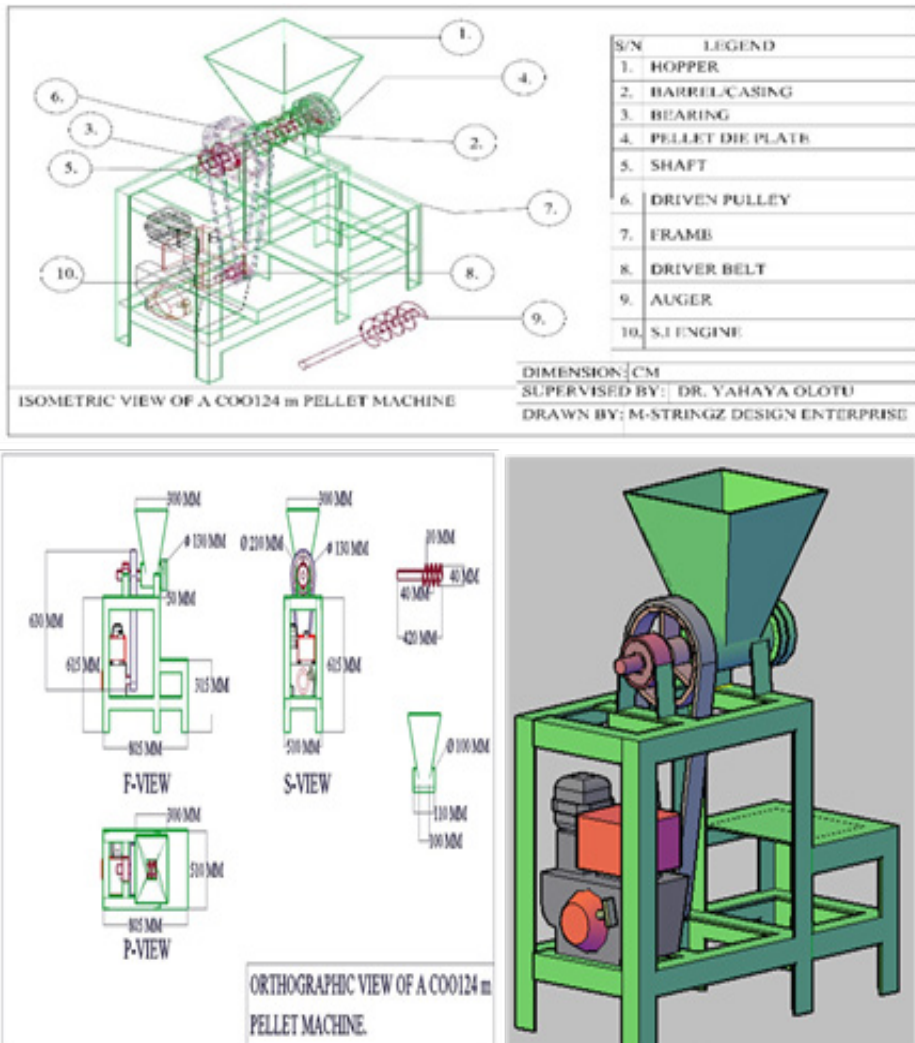
Figure 1. Isometric view and section drawing of a COOI24m pellet machine

3. Results and Discussion

3.1. Pelletizing efficiency and moisture content

Pellet moisture content (MC) varied from 15.8% to 27.1%, with an increase in pelletizing efficiency (Pe) from 70.3% to 84.6%. Figure 2 an illustrates the directional proportional relationship that was found between the pelletizing functional efficiency and the pellet's moisture content. Raising the pelletizing moisture reduced the specific energy consumption while increasing the capacity for pellet production. The physical quality of the pellet improved with the decrease in moisture content. Heat is produced while the raw materials are being ground because of the impact and friction between the material and the fast-moving hammer. The temperature inside the crushing chamber is typically between 45 and 50 ºC, which is higher than the outside temperature. In that process, moisture loss typically ranges from 0.5% to 1.5%. The temperature, type of hammer mill, and particle size all affect the degree of loss. Feed conditioning and tempering is the process of hydrothermally treating the materials by adding steam prior to their entry into the granulator, which enhances the material's chemical and physical characteristics. After conditioning, the material's moisture content is reasonable, ranging from 14% to 15.5%. The finding is line with the studies of [19] and [20]. This is because the pellet feed produced and processed under these conditions has good processing quality, making it easy for the finished product's moisture content to meet standards. It is challenging to maintain 14% moisture content after conditioner during dry and hot seasons. The limited moisture content of the feed concentrates at low moisture content (15.3%) was insufficient to bind the feed constituents together for appropriate pellet production and discharge. Pellet formation was moderate, ranging from 18.0% to 28.0% MC in moisture content. However, when the machine was run at 950, 600, and 450 revolutions per minute, the formation and discharge of pellets from the machine decreased at a moisture content above 29.0%.

3.2. Formation of pellet mash

Figure 3 presents the relationship between the feed concentrates and pellets produced by the pelletizing machine. The modelling expression revealed that the coefficient of determination (R^2) value of 0.999 showed that a strong and positive relationship existed between *PP* (pellet produced) and *FC* (feed concentrates). The results demonstrate that, as a result of the feed concentrates' moisture content and the operating machine speed, the majority of the formulated concentrates were converted to pelletized mash in every experimental trial with very little loss.
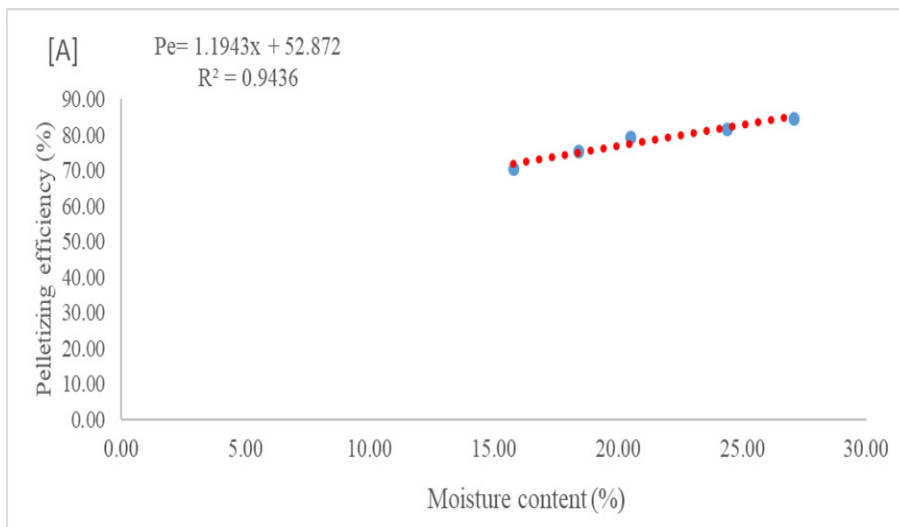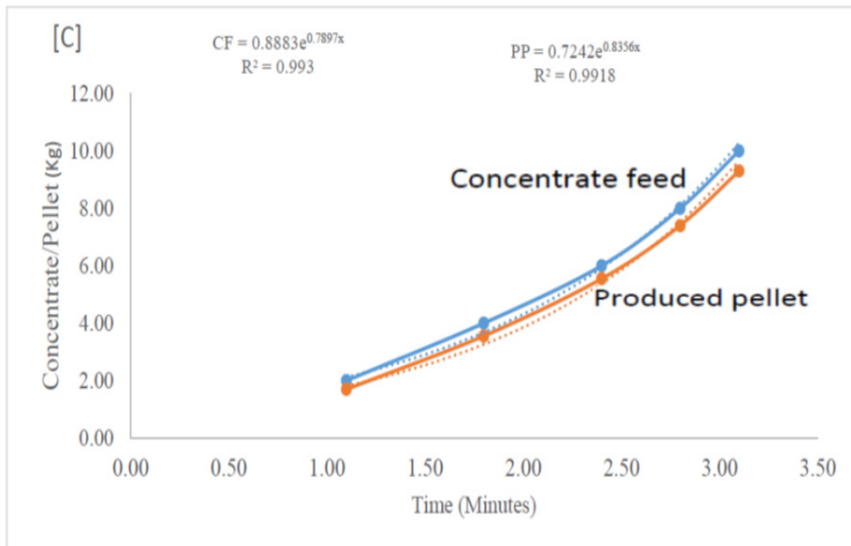
Figure 2. Moisture content and pelletizing efficiency
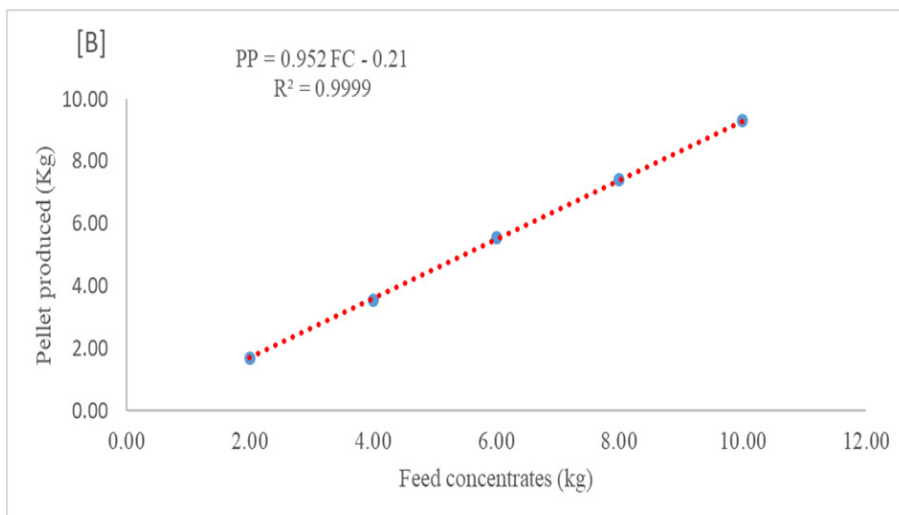
Figure 3. Moisture content and pelletizing efficiency

3.3. Pellet machine arrangement and loading

The COOI24m pelletizing machine developed from locally-sourced is used to convert formulated feed concentrates into mash pellets for chicken. The pellet machine adopts a large modulus hard toothed helical gearbox, strengthened spindle, strong power output, equipment stable operation, low failure rate, low production cost as shown in plate 1 a-b. Pellet machine was applied to a wide variety of many different applications, and the drive loading was varied from an easy, uniform load to severe shock loading. The power transmission was developed for more severe conditions, safety, reliability and overall longevity. Generally, the gearing used in a typical gear-driven pellet machine is life and durability limited, not shock load limited. Therefore, the tooth design is more than adequate to handle any shock loading. In the case of belt drives, the shock resistance of the belts is limited by a combination of heat dissipation capacity, the tensile strength of the reinforced strands and the durability of the friction surfaces in contact with the sheaves. The average pellet size of 8 mm was formed with operational capacity of 188 kg/hr or 7.5 bags of pelletized feed mash per hour as shown in Figure 4 and plate 1 a-b. Plate 2a-b shows the freshly produced pellet-mash at 27.1% moisture content and oven-dried pellet-mash at 15.1% moisture content.

Figure 4. Pellet machine arrangement, loading and milling time

Plate 1. The developed COOI24m pellet machine before operation (a) and the pelletizing machine during operation (b).

Plate 2. Freshly produced pellet-mash at 27.1% moisture content (a) and oven-dried pellet-mash at 15.1% moisture content (b).

The relationship between pellet moisture content (MC) and drying temperature (DT) is demonstrated by the results shown in Figures 5 and 6. At the drying temperature (DT) of 30°C, the pellet-mash moisture content decreased to 27.1°C; at the DT of 40°C, it decreased to 24.4%. At 70 °C DT, the moisture content steadily decreased to 15.8%. If the drying temperature is kept at 70°C for an extra five minutes after the pre-set fifteen minutes of drying time, it is anticipated that the pellet moisture content could be lowered to 10.0%. The variation in moisture loss is depicted in Figure 5 following the production of a pellet that was dried at different temperatures. The relationship between the DT and MC is inverse, as demonstrated by the modelling expression shown in Figure 5.
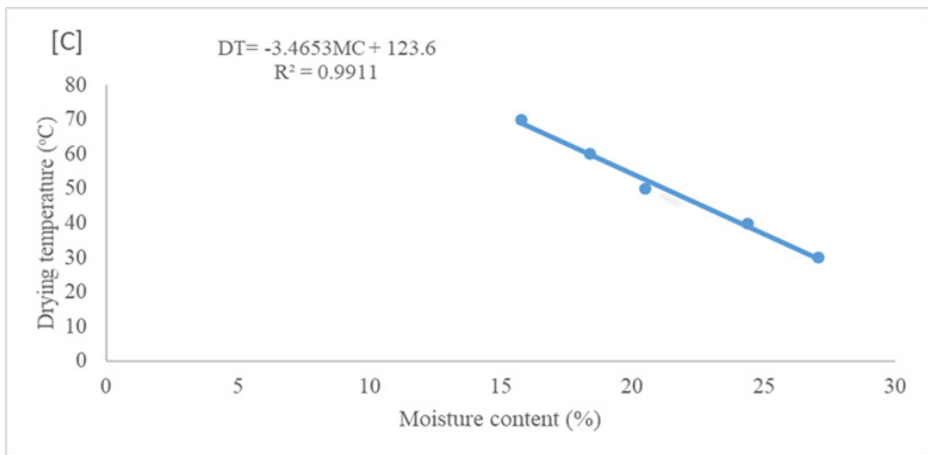
Figure 5. Pellet moisture content and drying temperature
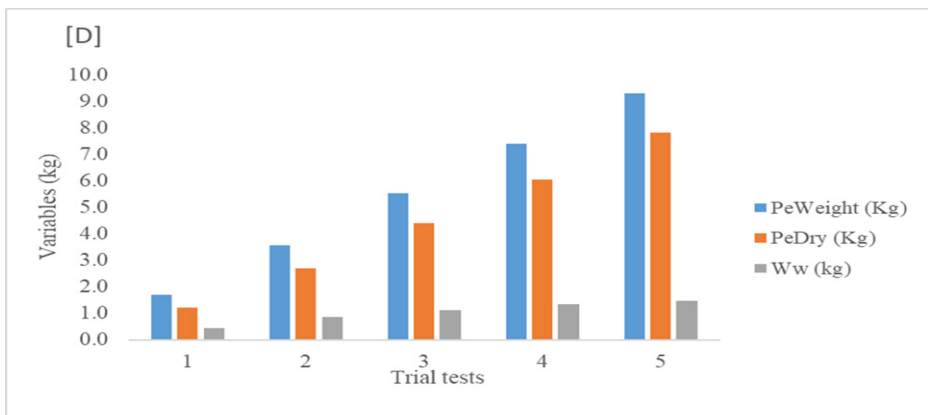
Figure 6. Variation of pellet-mash moisture loss in response to drying temperature

192
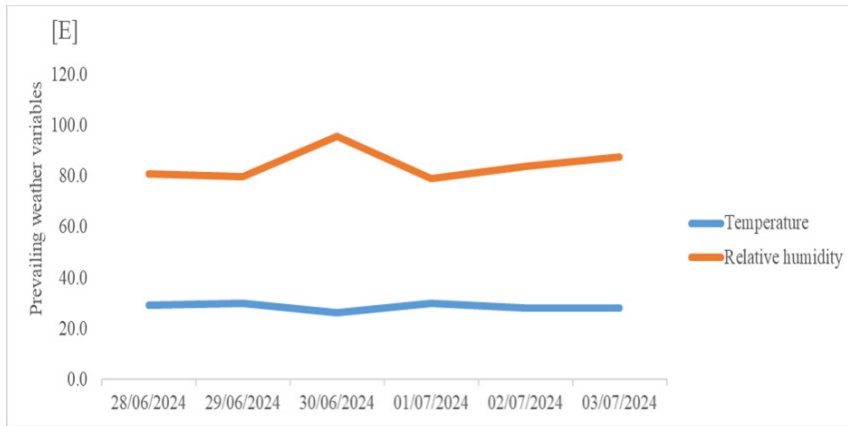
Figure 7. Prevailing weather variables of the storage facility

The outcome in Figure 7 depicts the six (6) days of average weather in the pellet-mash storage facility. The air temperature was 28.1°C on 02/07/2024 and 30.2°C on 01/07/2024, respectively, and the greatest and lowest relative humidity readings, of roughly 79.5% and 97.0%, were recorded on 01/06/2024. Climate variability, however, has no appreciable impact on variations in the product's volume, weight, size, or general quality.

3.4. Effect of drying temperature on the pellet bulk density and moisture content

The effects of the drying temperature (DT) on the pellet moisture content (mc) and bulk density (BD) as presented in Table 1-3. The highest bulk density of the formed pellets was recorded as 244.2 kg/m^3 at a moisture content of 27.1 % (db) and drying temperature of 30°C while the lowest bulk density was recorded as 200.1 kg/m^3 at a moisture content of 15.8 %(db) and 70°C DT as shown in Table 1. It is generally observed that increase in drying temperature led to decreases in bulk density and pellet moisture content which is significant at $P > 0.05$. This led to reduction in weight, size, and volume of the formed pellet-mash.

Table 1. Effects of drying temperature on pellet

Drying temp (°C)	Moisture content (%)	Bulk density (kg/m^3)
30	27.1	244.2
40	24.4	230.6
50	20.5	220.2
60	18.4	210.6
70	15.8	200.1

193

Table 2. Summary data

Treatments				
	Drying temp	**Moisture content**	**Bulk density**	**Total**
N	5	5	5	15
$\sum x$	250.0	106.2	1105.7	1461.9
Mean	50.0	21.2	221.4	97.5
$\sum X^2$	13500.0	2338.2	245690.4	261528.6
Std. Dev	15.8	4.5	17.1	92.2

Table 3. Result Details

Source	**SS**	**df**	**MS**	**F**
Between treatment	116793.4	2	58396.71	310.28
Within treatment	2258.4	12	188.2	
Total	119051.9	14		

4. Conclusions

The pelletizing machine COOI24m was developed for the production of poultry pellet mash using locally sourced materials. The machine has a milling and production capacity of 188.5 kg/hr of pellet-mash equivalent of 7.5 bags/hour on the basis of 25 kg per bag. The highest pelletizing efficiency of 84.4% was at 27.1%, while the lowest *Pe* at 70.3% was obtained at the *MC* value of 15.8%. It is estimated that the functional efficiency of the machine increases with the increased moisture of the feed concentrates used to form the pellet-mash. Thus, the bulk density decreased with the increase in drying temperature of the pellet-mash. This demonstrates that the drying temperature has a significant effect on moisture content and bulk density at $P > 0.05$. To enhance the formation of pelletized feeds, binding materials ought to be incorporated into feed concentrates. Small- and medium-sized fish farmers would benefit greatly from the adoption of the pelletizing machine as it would enable them to generate their own feed and reduce the issues related to obtaining imported feeds. Engineers can use the information in this study to enhance the efficiency of pelletizing machines.

I appreciate my family for their unwavering encouragement during this challenging journey.

Conflicts of Interest: The authors declare no conflict of interest.

References

1. F. Vanschoubroeck, L. Coucke, R. Spaendonck, The quantitative effect of pelleting feed on the performance of piglets and fattening pigs. *Nutr. Abstr. Rev.* 41, 2021, pp.1-9.
2. W.G. Pond, J.G. Maner, *Swine Production and Nutrition Animal Science*, Textbook series AVI Publ.Co., Inc., Westport, Connecticut, USA. 2014, 646pp.
3. C. Calet, The relative value of pellets versus mash and grain in poultry nutrition, *World. Poult.* 21: 2005, pp.23–52.
4. A.F.B. Van der Poel, M.W.A. Verstegen, S. Tamminga, *Chemical, physical and nutritional effects of feed processing technology*, 16"' Western nutrition conference, Sept. 13-14, 2015, Saskatoon, Saskatchewan, Canada. pp. 266.
5. J. S. Tumuluru, Effect of process variables on the density and durability of the pellets made from high moisture corn stover, *Biosystems Engineering*, 119, 2014, pp.44 – 57.
6. H.B. Pfost, Testing the durability of pelleted feed, *Feedstuffs. World. Poult.* 21, 2013, pp. 66 –68.
7. J.T. Pope, *Non-conditioning factors affecting enzyme thermostability during feed processing* [PhD dissertation]. Raleigh (NC): North Carolina State University, Department of Poultry Science, 2019.
8. C.N. Truelock, *Influence of exogenous enzymes and pelleting on feed manufacturing and broiler performance*, [PhD dissertation]. Manhattan (KS): Kansas State University, Department of Grain Science, 2020.
9. L.E. Heffner, H.B. Pfost, Gelatinisation during pelleting, *Feedstuffs*, 2013. pp. 45:32.
10. H.S. Bayley, J.D Summers, S.J. Slinger, The effect of steam pelleting feed ingredients on chick performance: Effect on phosphorous availability, metabolizable energy value and carcass composition, *Poult. Sci.*, 47, 2018, pp. 1140–1148.
11. D.E. Maier, J. Gardecki, Evaluation of pellet conditioning: Understanding steam, *Feed Manage.*, 2013, 44:15.

12. E.R. Skoch, K.C. Behnke, C.W. Deyoe, .F. Binder, The effect of steam conditioning rate on the pelleting process, *Anim. Feed Sci. Technol*. 6, 2018, pp. 83-90.
13. M. Thomas, A.F.V. van der Poel, Fundamental factors in feed manufacturing: Towards a unifying conditioning/pelleting framework. *Anim. Feed Sci. Technol.,* 268, 2020, pp.1-8.
14. C.R. Stark, *Feed Processing to Improve Poultry Performance*, Arkansas Nutrition Conference, Rogers, AR, 2012.
15. L. Reimer, Conditioning. Northern Crops Institute, Feed Mill Management and Feed Manufacturing Technology Short Course. California Pellet Mill Co., 2022 Pg. 7.
16. E.R. Skoch, K.C. Behnke, C.W. Deyoe, S.F. Binder, The effect of steam conditioning rate on the pelleting process, *Anim. Feed Sci. Technol*., 6, 2018, pp. 83-90.
17. A.T. Ishola, A.R. Busari, O.S. Aboyeji, Effects of Operating Parameters on the Performance of a Mixer cum Pelletizer for Livestock Feeds, *Journal of Research Information in Civil Engineering,* 18 (2), 2021, pp. 4116-4132.
18. D. Ziggers, Die determines pellet production. *Feed Technol.,* 7. 2013, pp. 17-19.
19. A.A. Balami, D. Adgidzi, A. Mua'zu. Development and Testing of an Animal Feed Mixing Machine, *International Journal of Basic and Applied Science,* 1(3), 2013, pp. 491-503.
20. N.N. Collins, O.A. Olasunkanmi, Development of a Dual-Mode Laboratory-Sized Pelletizing Machine, *Leonardo Journal of Sciences*, 13: 2008, pp. 22 - 29.

Addresses:

- Yahaya Olotu, Department of Agricultural & Bio-Environmental Engineering, Auchi Polytechnic, Auchi, Edo State, Nigeria.
  realyahaya@yahoo.com
  (*corresponding author*)
- Afolabi Adeniyi Rodiya, Department of Agricultural and Bio-Environmental Engineering,The Federal Polytechnic Ado-Ekiti, Nigeria.
- Victor Ndaraba Haruna, Department of Mechanical Engineering, Federal Polytechnic, Bida, Niger State, Nigeria
- Benjamin Chukwutem Ikwuebene, Department of Mechanical Engineering, Delta State Polytechnic, Ogwashiuku, Nigeria

Development and Calibration of a Solar-Powered Egg Incubator

Yahaya Olotu* , Abdurrahman Ismail Omoakhalen,
Reuben Ishiekwene, Benjamin Chukwutem Ikwuebene

Abstract. *This study evaluated the effects of various climatic variables on the efficiency of a solar-powered egg incubator. Results showed that generated incubation temperature (GIT) and relative humidity (GIRH) all significantly impacted the incubator's performance. Low temperatures negatively affected egg embryonic formation and hatching rates, while high humidity levels resulted in poor egg quality. Additionally, it demonstrated that the incubator could be kept at the desired temperature of 34–38 °C and relative humidity of 56–86% for high efficiency. The study also discovered that more solar radiation resulted in more reliable and effective temperature control inside the incubator. The findings of this study offer significant contributions to the enhancement of solar-powered egg incubator designs and the optimisation of their efficiency under diverse climate scenarios.*

Keywords: *Egg, Incubator, Efficiency, Temperature, Humidity, Solar-powered.*

1. Introduction

In the past twenty years, the amount of chicken meat produced worldwide has climbed by over 108%, from 54 to 112 million tonnes, meaning that its percentage of total meat production has increased by 36% [1; 2]. It is projected that the global population will continue to expand and that the average person's consumption of meat will double by 2020–2022. This trend indicates that by 2022, the world's poultry meat consumption is expected to reach 128 million tonnes [3]. Hatcheries must maximise chick output, which involves more than just incubating more fertile eggs, in order to fulfil the increasing demand for poultry meat. Increasing the hatchability of healthy chicks with high survival rates and optimising the expression of their genetic growth potential under all field conditions are two things we believe are essential to hatcheries achieving high production efficiency in a sustainable manner today.

A technique called egg incubation allows eggs to be produced from chicks without the need for the mother hen to be present during the hatching process. In the normal process of egg incubation, the hen protects the eggs by producing warmth, which promotes the growth of the embryo [5;6]. However, as technology advances, incubation eggs to produce chicks at the appropriate time requires the use of artificial methods. For millennia, this man-made procedure has been refined to achieve increased effectiveness [7]. Despite numerous initiatives, epileptic power supply remains an issue in the majority of developing nations [8]. Low productivity and industry folding result from the production of poultry. Therefore, new energy sources are necessary for the poultry business to progress. For this reason, specialists in energy prefer using renewable energy, which has low production costs and is comparatively environmentally beneficial [9]. Although electrical incubators are effective, a sizable portion of the population in poor countries does not have access to the grid [10]. Poultry farmers use bush lamps to heat their farms in rural areas where 80% of the population lives. This practice poses environmental and health risks, as evidenced by high mortality rates, low feed conversion efficiency, and high rates of parasite and disease infection [11].

Having the proper, controlled temperature and relative humidity at various stages of the egg embryo's growth is one of the most important conditions for a successful incubation process. Solar energy is an endless resource that can thus supply this need with almost no risk to the environment [11]. Numerous studies have looked into how temperature affects the ability of viable eggs to hatch, as reported by [12]. The growth of embryos, their capacity to hatch, and their performance after hatching are all significantly influenced by temperature [3]. Throughout the incubation of about 21 days of fertilised eggs in an incubator, temperature is crucial, particularly in the first week. According to numerous studies, the most crucial elements influencing the quality of chicks and their capacity to hatch are the incubation conditions, which include temperature, humidity, ventilation, and turning.

This research study focuses on developing a solar-powered egg incubator with integrated sensors to control the climate parameters inside the incubating chamber, having theoretically taken into account the significance of consistent and regulated heat during the egg incubation process.

2. Materials and methods

The solar powered incubator with capacity of hatching 90 chicken eggs were fabricated and tested for efficient performance. The incubator has dimension of 1.05 m height and 0.65 m width constructed of insulated metal sheet. One tungsten bulb of 250 Watt was incorporated to heat up the eggs, a rheostat switch was also incorporated to regulate the temperature of the incubator between 34ºC to 37°C, the fan was installed to ventilate and control the air needed by the incubator. A water tray was fabricated with thin sheet and placed on the bottom of the cabinet to increase and recover humidity in the incubator during the experimental period. A solar panel of 200W, 12V battery and a DC to AC converter (inverter) is also incorporated. The 12V battery connected to the inverter to convert the DC to AC current and the inverter is

connected to the bulb through the rheostat. The charged solar supplies the required energy to heat up the incubator. The materials used for the development of the solar-powered egg incubator are: solar panel, 12 V battery, charge controller, temperature sensor, humidity sensor, fan, insulator, egg tray, thermostat; cables (wires and connectors), timer; water reservoir; solar charging indicator; heating source (250w) as shown in Figure 1.
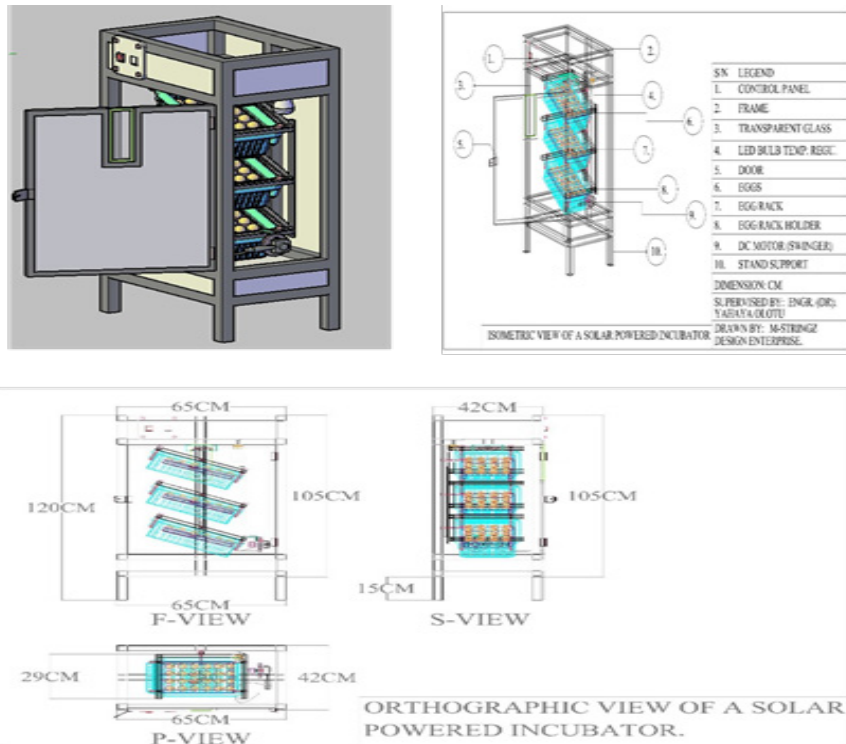
Figure 1. Sectional drawing of solar-powered egg incubator

2.2. Design consideration for solar-powered egg incubator

Incubator capacity

The capacity of the solar-powered egg incubator was designed using the expression as follows:

$$A = B \times C \times D \tag{1}$$

where:
A = Capacity of the solar-powered egg incubator
B = Height of the incubator

C = Width of the incubator

D = Breadth of the incubator

Design egg tray

A 90-egg capacity tray was designed using the equation 2:

$$P = Q \times R \tag{2}$$

where:

P = Cross sectional area of the egg tray

Q = Length of the egg tray

R = Width of the egg tray

2.3. Development relative humidity for solar-powered egg incubator

The relative humidity required for the incubation of eggs was calculated as the mass of water vapour (MVP) per unit volume over unit volume of air as shown in equation 3:

$$H = \frac{m_v}{V} \tag{3}$$

where:

H = relative humidity inside the incubating chamber,

m_v = Molar mass of water,

V = speed of fan [13].

2.4. Design for heat generation

Heat generated from the incubator was determined as $MC\Delta T$, which implies that the heat required to raise the temperature of the incubator. as shown in equation 4:

$$Q_I = M_I C_I \Delta T \tag{4}$$

where:

Q = heat quantity,

C = specific heat capacity,

ΔT = change in temperature,

M_1 = molar mass.

2.5. Design of ventilation hole

Incubation ventilation was designed as the product of the volume of mass flow in and out and cross sectional area of the incubator as follows:

$$V = (\textstyle\prod d2/4)V \tag{5}$$

where:

V = Volume flow rate
A = Cross sectional area
V = Velocity

2.6. Working principle of the incubator

The temperature of incubator was maintained between 34-37°C using a set of pre-set temperature sensors which regulate and control the temperature and the relative humidity. Adequate control of the heat was maintained to avoid overheating and under heating which can affect the hatchability of the embryo. The moisture level was also maintained around using the creation of water vapour within the incubating chamber at 52-56% and later increased to around 87% in the last three (3) days at the hatcher tray. Water surface was maintained as large as the wideness of the egg tray and positioned inside a pan under the egg tray, this helps to humidify the system. This air regulation is necessary during embryo development for efficient output. This was achieved by using the fan to effectively circulate the air. The eggs were placed inside the trays and automatically turned at an interval three (3) minutes so that all sides get exposed to heat. This process continues and temperature regulated until the eggs are hatched. Plate 1 a-d show the assemblage of the solar powered incubator. The adopted circuit diagram for heating system for a solar-powered egg incubator is depicted in Figure 2.
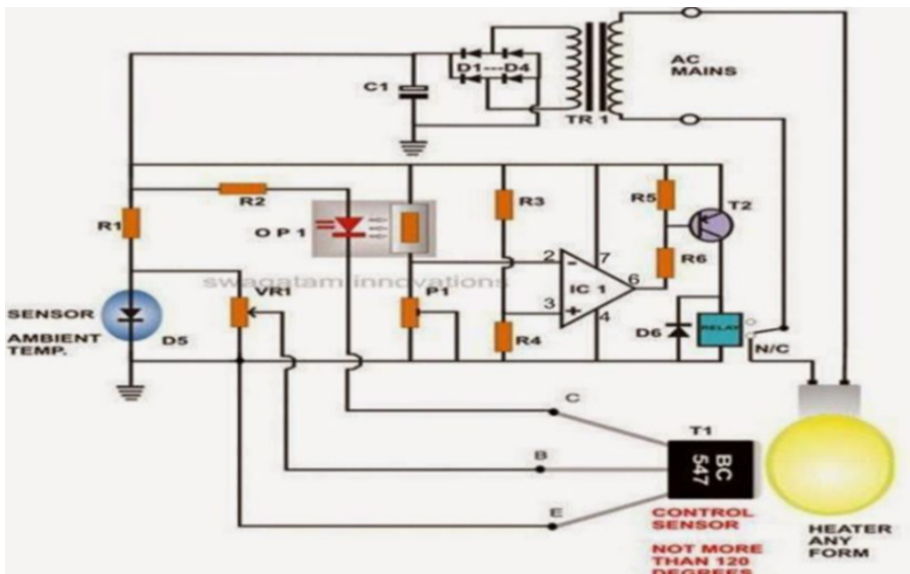
Figure 2. Circuit diagram for heating incubator
Source: [14]

Plate 1. Arrangement of incubator skeleton (a), assemble of incubator members (b), rotating egg tray inside incubating chamber (c), and completed solar-powered incubator connected to the solar power

3. Results and discussion

3.1. Calibration of solar-powered incubator

An evaluation of the system's performance was conducted by testing the egg incubator. 2024 July was the test month. Egg incubator was used for the preliminary test, which was carried out to determine the system's effectiveness. Temperature adjustments were made to the incubator using a thermostat. To prevent harming the eggs, the thermostat is designed to turn off and close the air duct when the incubating chamber reaches approximately 37 °C, as depicted in plate 2 a-b. This stops hot air from the thermal storage unit from entering the chamber. Likewise, if the temperature drops below 34 °C, the thermostat is supposed to activate and begin supplying hot air to the incubating chamber because a temperature lower than that will cause the chick's metabolism to slow down. The incubating unit's evaporative moisture pan is utilised to supply the necessary humidity. The incubating unit's evaporative moisture pan is taken out when the hygrometer reading reaches 65% or higher. Likewise, the evaporative moisture pan is returned if the hygrometer reading falls below 60%. At a predetermined 3-minute interval, the eggs in the incubating chamber are automatically turned.

Plate 2. Incubating eggs with temperature and relative humidity datalogger

3.2. Generated climatic variables in incubation chamber

A 10-day average of relative humidity and temperature inside the incubating chamber was collected within 15- minutes through the built-in data logger. The result presented in Figure 3a showed that the generated incubation temperature (GTI) of 29.0 °C was recorded at 07:50 am, and the GTI increased steadily to 38 °C at 10:25 am, dropped to 34 °C at 11:35 am through 11:50 am, and rose to 36 °C at 12:20 pm through 12:35 pm, while at 01:05 pm the GTI declined to 35 °C. The regression line for the generated incubation and time showed that there was no relationship between GIT and the time of incubation with r and r^2 of 0.37 and 0.14, respectively. The fluctuations in the temperature of the incubating chamber could be attributed to possible heat loss or transfer to the surrounding incubator wall and the environment. Also, the possibility of energy drops and low solar radiation due to continuous rainfall could cause the heating element or bulb not to work perfectly. However, the fluctuation in the generated temperature does not have a significant effect on the performance of the solar-powered egg incubator. The finding is consistent with the study of [16], which revealed that a drop in temperature could have resulted from the poor performance of the solar PV system due to heavy overcast weather on that day. Despite this trend, the results generally showed that steady incubation operating conditions could be achieved and maintained using solar energy for sustained egg

incubation. The embryonic formation of the eggs inside the incubator was measured starting on day 5 of the incubation process. The result showed that 85% of the eggs showed about 30% embryonic formation. Several studies have supported that 30% of egg embryonic formation at the initial 5-day incubation period is a good development for a higher hatchery rate. Figure 3b shows the effect of an average relative humidity on the incubation chamber for the ten (10) days of the experiment. It was observed that the average relative humidity of the incubation chamber ranged from 55–86%.
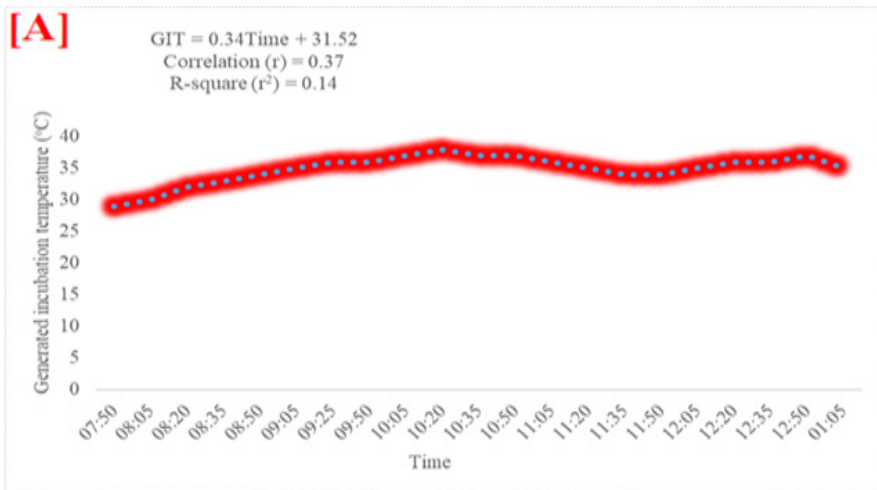
Figure 3.a. Generated incubation temperature
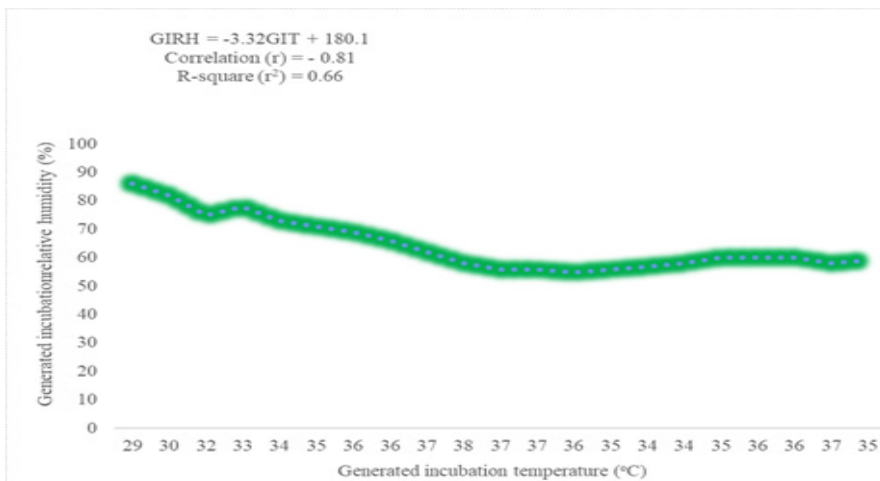
Figure 3.b. Effect of an average relative humidity on the incubation

The regression line between the generated relative humidity and the incubating time shows a correlation (r) and coefficient of determination (r^2) of -0.42 and 0.17, respectively. Low humidity will cause the eggs to lose too much weight, which means the air space will be larger than what is ideal. A large air space also means the chick will be smaller than normal. Small chicks are weak chicks, and weak chicks cannot always hatch on their own, and they may die just before or just after hatching. High relative humidity (RH) appears to have a detrimental effect on embryonic development, as evidenced by several studies.

Humidity and temperature have an inversely proportional relationship. Relative humidity will decrease with rising temperatures, making the air drier. Relative humidity rises as a result of the air becoming wetter as the temperature drops. 50% humidity at 21.1 °C and 50% humidity at 32 °C are not the same. Elevating the temperature in an incubator without adding water will result in a decrease in the relative humidity (RH%) because the maximum possible water vapour capacity increases with temperature. Both models experienced condensation on the cold portions of the canopy when the incubator's humidity level was high, but the sealed cavity wall's increased insulation lessened the likelihood of this issue.

4. Conclusions

The egg incubation system powered by solar photovoltaics designed and developed was evaluated with fertile eggs to ascertain its ability to incubate and hatch fertile eggs. The system was developed using locally sourced materials. During the first five days of incubation, 30.3% of the eggs showed signs of embryonic formation, according to tests conducted on the solar-powered incubator. Furthermore, it is anticipated that by the end of the sixteen (16) day incubation period, over 95% of embryos will have developed. Additionally, it demonstrated that the incubator could be kept at the desired temperature of 34–38 °C and relative humidity of 56–86%. The egg incubator was equipped with an automatic turning system, and it has been determined that this method of rotating the eggs throughout incubation is efficient. It was discovered that the incubator system is capable of successfully hatching chicken eggs. The use of solar incubators would provide an answer to a significant problem of power shortages for commercial chicken egg incubation in Nigeria.

Author contributions: Conceptualization, Y. Olotu, methodology, A.I. Omoakhalen, writing-review, R.I. Ishiekwene and editing, B.C. Ikwuebene .All authors have read and agreed to the published version of the manuscript.

Conflicts of Interest: The authors declare no conflict of interest.

References

1. M.M Abu, A. Adamu,). Construction of an Electrically Operated Egg Incubator, *International Journal of Modern Engineering Sciences*, 5(1), 2016, pp. 1-18.
2. C. AviSite, A evolução em uma década, segundo a. Available from: http://avisite.com.br/noticias/index. php?codnoticia=15871
3. D.C. Deeming, M.W.J. Ferguson, *Physiological effects of incubation temperature on embryonic development in reptiles and birds*. In: Deeming DC, Ferguson MJW, editors. Egg incubation. Cambridge: Cambridge University Press, 2012, pp.147–172.
4. M. L. Alvarado, *Processo de incubação artificial de ovos desenvolvimento de sistemas de medição de temperatura e massa* [dissertação]. Campinas (SP): Universidade Estadual de Campinas; 2008.
5. N. Benjamin, N.D. Oye, Modification of the Design of Poultry Incubator, *International Journal of Application or Innovation in Engineering and Management,* 1(1), 2012, pp.90-102.
6. D.C. Deeming, M.W.J. Ferguson, *Physiological Effects of Incubation Temperature on Embryonic Development in Reptiles and Birds*, Cambridge University Press, Cambridge, UK, 2011, pp 147-172.
7. R. Meijerhof, G. vanBeek, Mathematical modeling of temperature and moisture loss of hatching eggs, *Journal of Theoretical Biology*,165. 2013, pp. 27-41.
8. SNA News Boletim Semanal da Sociedade Nacional de Agricultura. FAO: produção mundial de carne de frango dobrou em apenas duas décadas [cited 2016 Maio 8]. Rio de Janeiro; 2015. Available from: http://sna. agr.br/fao-producao-mundial-de-carne-de-frango-dobrou-em-apenasduas-decadas/
9. F.U. Okeoma, *Design, Construction and Performance Evaluation of a Liquefied Petroleum Gas Incubator*, Department of Mechanical Engineering, Faculty of Engineering, Ahmadu Bello University, Zaria, Nigeria, 2016, 159 pp.
10. D.O. Ojo, H.D. Shaid, Proposed Development of a Solar Powered Automated Incubator for Chickens, *International Journal of Engineering and Techniques,* 4 (1), 2018, pp. 517-524.
11. J.A. Oluyemi, F.A. Roberts, *Poultry Production in Warm Wet Climates,* Macmillan Publishers Limited, London and Basingstoke, United Kingdom 1988, 102 pp.
12. M.O. Oseni, Improving households' access to electricity and energy consumption pattern in Nigeria: Renewable energy alternative. *Renewable and Sustainable Energy Reviews*. 16(6), 2012, pp. 3967-3974

13. Y. Oznurlu, E. Sur, T. Ozaydin, I. Celik, D. Uluisik, Histological and histochemical evaluations on the effects of high incubation temperature on the embryonic development of tibial growth plate in broiler chickens, *Microscopy Research and Technique,* 79, 2016, pp. 106-110.
14. F.E. Robison, G.M. Fasenko, R.A. Renema, *Optimizing chick production in broiler breeders*, Alberta: Poultry Research Centre; 2013, v.1.
15. B.C. Roy, H. Ranvig, S.D. Chowdhury, M.M. Rashid M.R. Faruque, Production of day-old chicks from crossbred chicken eggs by broody hens, rice husk incubator and electric incubator and their rearing up to 6 weeks, *Livestock Research Rural Development,*16(2). 2014, pp. 67.

Addresses:

16. Yahaya Olotu, Department of Agricultural & Bio-Environmental Engineering, Auchi Polytechnic, Auchi, Edo State, Nigeria.
    realyahaya@yahoo.com
    (*corresponding author*)
17. Abdurrahman Ismail Omoakhalen. Department of Mechatronics, Auchi Polytechnic, Auchi, Edo State, Nigeria.
18. Reuben Ishiekwene, Department of Electrical/Electronic Engineering Delta State Polytechnic, Ogwashiuku, Nigeria.
19. Benjamin Chukwutem Ikwuebene, Department of Mechanical Engineering Delta State Polytechnic, Ogwashiuku, Nigeria

Estimation of consumptive water use for Watermelon in Auchi, Nigeria

Yahaya Olotu* ⓘD, Dauda Aluyah Okodugha, Olasimbo Olarinde,
Vivian Enyopo Momoh, Rasheed Ibrahim

Abstract. *This study aims to estimate the consumptive water use (CWU) for watermelon production in Auchi, Edo State, Nigeria. The research was conducted over a period of eight months (March–October) and used data collected from the watermelon field at the Demonstration and Research Farm of Auchi Polytechnic, Auchi. The result of the experiment revealed the estimation of CWU and watermelon water requirements (CWR) of 175.9 mm and 195 mm for the 62-day (August to October) vegetation stage of watermelon, with a CROPWAT projected harvest on November 20, 2022. The finding also revealed that the mean annual consumptive water use for watermelon production was 520.7 mm. The mean seasonal water use for watermelon production was higher in the dry season (March to June, 488.7mm) than in the wet season (July to October, 390.6mm). However, based on this harvest date, the model predicted irrigation requirements of 23.1 mm and 59.4 mm in October and November. Additionally, this study offers proof that management strategies for water use efficiency and irrigation scheduling can dramatically lower water losses and boost efficiency. The findings of this study can be applied to the Auchi region's water management decision-making procedures as well as to help watermelon farmers reduce their water consumption levels while maintaining output.*

Keywords: *Crop water use, Watermelon production, CROPWAT, Watermelon, Auchi.*

1. Introduction

Watermelon, (Citrullus lanatus) is cultivated throughout the tropics and subtropics and has a worldwide distribution [1]. Its world production had expanded from 2.917 to 3.7 million ha in the period from 1999 to 2003 [2]. In Nigeria, though there are no

official figures recorded for its production, the crop has a wide distribution as a garden crop, while as a commercial vegetable production; its cultivation is confined to the drier savanna region of Nigeria [3]. It is a crop with high economic value and is grown and traded for export. Most as well drained-soils, clayey or sandy, can be used to produce the crop. Its fruit has a moisture content of about 92% and sometimes serves as a source of water for human consumption [4]. Despite high water content, its seasonal water requirement is between 400 and 600 mm under tropical climates [4]. It is of much importance to assess the effects of water consumptive use, water stress and mulch on production, yield and quality of certain crops both at the experimental level as well as to farm level and integrate new knowledge with the traditional farmers' knowledge through participating, research and extension [4]. Accurate knowledge of the impact of reduced water supply on yield and quality is required to define appropriate strategies to optimize crop production and economic benefits, while maintaining environmental requirements. Many studies were reported on the irrigation of watermelon [5]. The available information shows that fruit yield response to water is usually highest when watermelon is adequately irrigated.

Scarce water resources and growing competition for water reduce its availability for irrigated agriculture. Achieving high water use efficiency is a primary challenge in irrigated agriculture, irrigation practices and techniques aimed at maximizing crop production with minimum water utilization are fast evolving, and there is a need for evaluation of these practices before adoption, which include the employment of techniques and practices that deliver a more accurate water supply to crops [4]. Studies are needed to increase the efficient use of the available water. A regulated irrigation system with mulching is one among many practices that are fast gaining ground, and it appears a very promising option at achieving the goal of more crops per unit volume of water, if properly adopted. The development of new irrigation scheduling and identifying the sensitive crop growth stage to water consumptive use is one way to enhance crop productivity with less water [7]. This study is designed to estimate water melon crop water use using CROPWAT software and establish the relationship between crop water use and growth parameters.

2. Materials and methods

2.1. Study area

A field experiment was carried out at the mini Teaching and Demonstration Farm located in between the E-Learning Centre and Alumni Drawing Studio at Campus-One, Auchi Polytechnic at latitude 7.04°N and longitude 6.27°E. Auchi is classified as a savanna with an average mean temperature and precipitation of 28.5oC and 1201.3 mm.

209

February is the driest period with an average air temperature of 29.5°C, whereas the Months of July and September indicate a low mean temperature of 26.6°C and 27.8°C respectively. The watermelon was planted on sandy loamy soil on 3rd August 2022 at a planting depth of 2.5 cm and 75% of the plant germinated after eight days of planting over a plot area of 5m * 5m. A spacing of 15 cm x 15 cm was adopted with a plant density of 8000 per acre on the average. Plate 1 a – e shows some of the field activities.

2.2. Estimation of Consumptive Water Use of Water Melon

Phocaides [7] mentioned that the consumptive water use of crop is the quantity of water used by the vegetative growth of a given area in transpiration or building of plant tissue and that evaporated from the soil or intercepted precipitation on the area in any specific time. It is expressed in water depth per unit of time (consumptive use or evapotranspiration). This study applied CROPWAT AND AQUACROP to estimate consumptive water use(CWU) and some other parameters. Hence, the inbuilt mechanism of the selected process-based models estimates the (CWU) as shown in equation 1-4:

$$CWU = ET_0 * K_c * K_s \qquad (1)$$
At initial growth phase

$$CWU = ET_{0i} * K_{ci} * K_{si} \qquad (2)$$
At developmental growth phase

$$CWU = ET_{0d} * K_{cd} * K_{sd} \qquad (3)$$
At maturity growth phase

$$CWU = ET_{0m} * K_{cm} * K_{sm} \qquad (4)$$

where:

ETo is reference evapotranspiration (mm/day)
Kc is the crop coefficient
Ks is the crop stress factor
i, d and m are the initial, developmental and maturity of watermelon growth

Figure 1. Map of Edo State showing the study area
Source: https://www.owogram.com/edo-state/

Plate 1. Field cultivation and planting of water melon (a), growth of watermelon at fourteen days (14) after planting (b) growth of watermelon at forty-five (45) days after planting (c) growth of watermelon at seventy days after planting (d and e).

2.3. CROPWAT Model

FAO's CROPWAT 8.0 model is a computer program used in estimating and modelling crop water requirements, irrigation requirements and consumptive water use of different crops based on soil- climate-crop data [8]. The program allows the development of irrigation schedule for different management conditions and the calculation of scheme water supply for different areas under different crops. The CROPWAT model was selected based on its ability to simulate the impact of various climate change scenarios on the consumptive use of water. The consumptive water use of watermelon was estimated using the inbuilt CROPWAT mechanism. Table 1 shows the input and output parameters of the CROPWAT model for simulating the consumptive water use of watermelon.

Table 1. The input and output of the CROPWAT model

Dataset	Input Parameters	Output Parameters
Climatic data	Rainfall	Solar radiation
	Minimum temperature	Reference evapotranspiration
	Maximum temperature	Crop water requirement
Crop datasets	Sowing data	Actual crop evapotranspiration
	Crop description (phenology)	
	Crop coefficient (K_c)	
Soil	Soil texture	Soil moisture deficit
	Available moisture	Estimated yield reduction
	Infiltration rate	

Source: Nyatuame et al., 2013

2.4. Measurement of Phenological Parameters of Watermelon

The control of weeds on the plot where watermelon was planted was achieved through the combination of manual and chemical operations. The phenological growth was evaluated by measuring the plant height from the soil surface to the emergence point of the youngest leaf, counting the number of living leaves, measuring the length and width of the youngest fully developed leaf.

The relationship of plant phenological parameters such as plant height, leaf breadth, and number of leaf emergences was evaluated using statistical metrics such as mean, median, variance, regression coefficient, and T-test of SPSS software.

3. Results and Discussion

3.1. Calibration meteorological variables

The climatic variables such as rainfall, minimum temperature (Tmin), relative humidity (RH), wind speed (WS), maximum temperature (Tmax), and evaporation rate (EVR) were measured during the 76-day field experimentation of watermelon (Citrullus vulgaris, cv. Crimson Sweet). Mean temperature (Tmean oc) and effective rainfall (EffRain) were calculated using the empirical relationship between Tmin, Tmax, and CLIM module in CROPWAT software, as shown in the CROPWAT interface window. The results in Figure 2 show the lowest and highest relative humidity of 63% and 90%, respectively, were recorded on 08/07/2022 and 03/09/2022. However, the RH fluctuated throughout the period of experimentation.

The coefficient of determination $R^2 = 0.016$ demonstrated no link between the relative humidity and the watermelon growing duration (days) (Figure 2). Therefore, it could be determined that higher RH values corresponded to the period of high rainfall intensity and duration. This supports the finding of [2], which revealed that
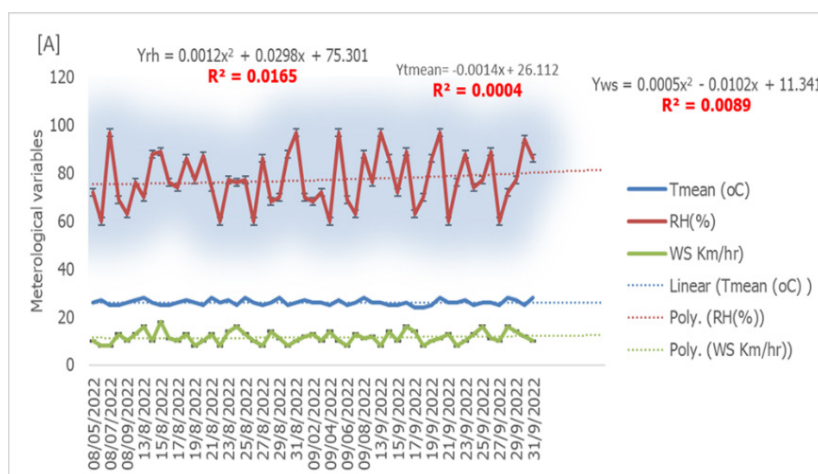
Figure 2. Relationship of meteorological variables

rainfall is anticipated when relative humidity and temperature are high, and minimal precipitation is anticipated when both of these factors are low. Figure 3 shows the rate of evaporation during the crop's growing cycle. The evaporation rate (EVR) changed from 0.1 cm to 0.3 cm.

The highest EVR of 3 cm/day was obtained on 08/06/2022 and 20/08/2022, respectively. The driver of the evaporation rate is not limited to temperature but includes sunshine hours, wind speed, and relative humidity. Poos and Varju (2020) revealed that evaporation is dependent on the properties of the materials and the conditions of the environment, such as air temperature, air humidity, air speed, and turbulence. Figure 4 presents the simulated effective rainfall at the study area (campus-one-Auchi Polytechnic, Auchi).
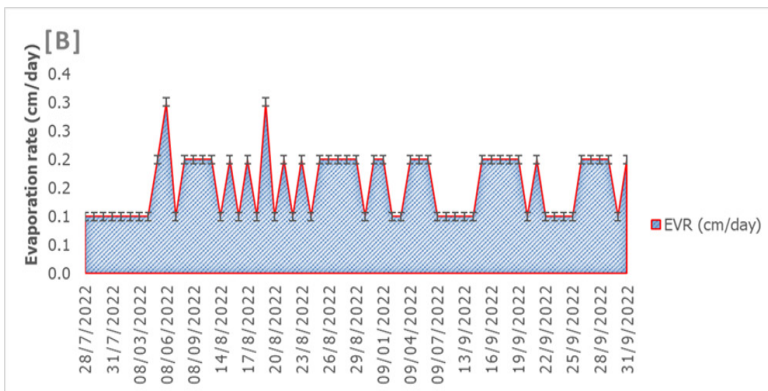
Figure 3. Evaporation rate

	Rain	Eff rain
	mm	mm
January	2.5	2.5
February	15.2	14.8
March	43.2	40.2
April	83.8	72.6
May	124.5	99.7
June	162.5	120.3
July	185.4	130.4
August	200.7	136.3
September	213.4	140.5
October	137.2	107.1
November	30.5	29.0
December	5.1	5.1
Total	1204.0	898.4

Station: Campus 1-Auchi Poly Eff. rain method: USDA S.C. Method
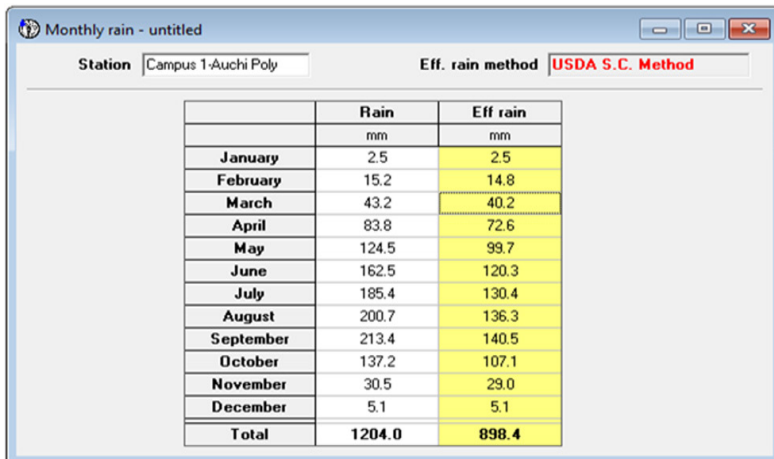
Figure 4. Simulation of effective rainfall
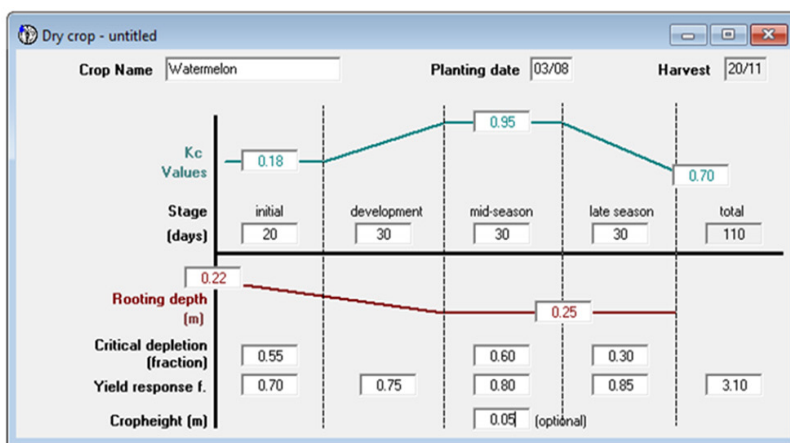
Figure 5. Simulation of watermelon growing cycle length

3.2. Estimation of Consumptive Water Use

A combination of reference evapotranspiration (ETo), crop coefficient (Kc), and crop stress factor is used to determine consumptive water usage or actual crop evapotranspiration (Ks) as described in equations 1-4. The CROPWAT interface is depicted in Figures 4 and 5, which is used to calculate the watermelon growing cycle, crop water requirements (CWR), effective rainfall (EffRain), and irrigation needs (Irr. Req). Table 2 presents the simulated outputs in the month of August which fell on the initial crop growth stage; CWR and CWU values of 28.8 mm and 23.0 mm were estimated, whereas EffRain and ETo of 128.5 and 103.3 were computed under a rainfed system (no irrigation applied) (Figure 4 and 5). However, the marginal difference of 5.3 between CWR and CWU could be explained by potential water stress that could develop during the water melon's early growth stage. Consequently, the crop was at a developmental stage by the end of September. In this period, the CWR and CWU climbed to 101.4 mm and 91.3 mm, respectively, but during mid-season (flowering and fruit-filling stages as shown in plate 1e), the CWU and CWR significantly reduced to 61.6 mm and 64.8 mm, respectively.

Table 2. Total number of consumptive water use, crop water requirements, irrigation applied, effective rainfall and seasonal evapotranspiration

Month	CWR (mm)	CWU (mm)	IA (mm)	EffRain (mm)	ETo	Ks
August	28.8	23.0	0.0	128.5	103.3	0.800
September	101.4	91.3	0.0	129.7	104.7	0.900
October	64.8	61.6	0.0	75.6	71.8	0.950
Total	**195.0**	**175.9**	**0.0**	**333.8**	**279.8**	

Month	Decade	Stage	Kc coeff	ETc mm/day	ETc mm/dec	Eff rain mm/dec	Irr. Req. mm/dec
Aug	1	Init	0.18	0.65	5.2	35.8	0.0
Aug	2	Init	0.18	0.66	6.6	45.5	0.0
Aug	3	Deve	0.28	1.03	11.4	45.9	0.0
Sep	1	Deve	0.55	1.96	19.6	47.5	0.0
Sep	2	Deve	0.81	2.82	28.2	48.6	0.0
Sep	3	Mid	0.95	3.35	33.5	44.3	0.0
Oct	1	Mid	0.95	3.38	33.8	40.8	0.0
Oct	2	Mid	0.95	3.41	34.1	37.8	0.0
Oct	3	Late	0.91	3.28	36.1	28.4	7.7
Nov	1	Late	0.82	2.98	29.8	16.6	13.2
Nov	2	Late	0.74	2.69	26.9	7.1	19.8
					265.4	398.5	40.7

Figure 6. Simulation of crop water requirements, effective rainfall and irrigation requirement

Throughout the 76-day growing cycle of the watermelon, the simulation result showed a total consumptive water consumption (CWU) of 175.9 mm and 195.0 mm for CWR. According to the simulationresults in Figure 4, the crop will be ready for harvest on November 20, 2022. However, it is anticipated that before it will be fully mature for harvest, the CWR and CWU of 130 mm and 125 mm, respectively, would be needed. It follows that effective rainfall in October and November will need to be supplemented by supplemental irrigation of 23.1 mm and 59.4 mm, as shown by the simulation in Figure 5 and Figure 6. Because of this, if precision irrigation is not used in October and November, crop water stress may grow and the watermelon CWU may subsequently decrease. The results are consistent with a study by [9], which revealed that 343 mm of crop water is needed for watermelon. The results are consistent with those of [10], who found that irrigation relieved water stress and decreased appropriately. Water stress then gradually increased to a maximum value right before the next irrigation application when the soil water in the crop root was depleted.
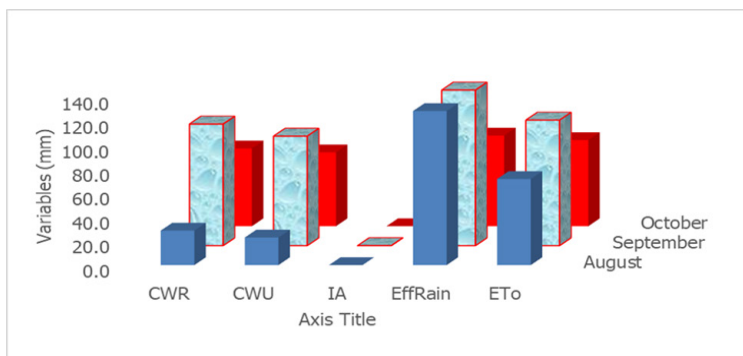
Figure 7. Calibration of consumptive water use (CWU)

3.3. Watermelon Phenological Development

The results are shown in Figure 7 and show how the length of the growing cycle affects the length and width of watermelon leaves. The LL and LW of 3.8 cm and 4.2 cm were measured at 16 DAP (Figure 8). However, as shown in Figure 8, the leaf's length and width rose to 11.2 cm and 6.8 cm at 27 DAP and then abruptly increased to 15.8 cm and 12.2 cm at 61 DAP. The coefficient of determination R^2 values of 0.857 and 0.840 were estimated between the LL and DAP, and LW against DAP. Hence, it showed that the effect of moisture stress was less from the initial to development growth stages. The results were consistent with those of [11], who found that phenological reactions to water shortages can occasionally interfere with reproduction. Water deficiencies may potentially hasten senescence, according to [12], despite reports that they promote progressive leaf fall and obstruct effective N transfer [13].

Table 3. Statistical metrics for experimental treatments

Phenological growth	N	Mean	Std. dev.	Std.Error	P-value
LL	9	9.10	5.26	1.75	0.0004
LW	9	7.53	4.77	1.59	
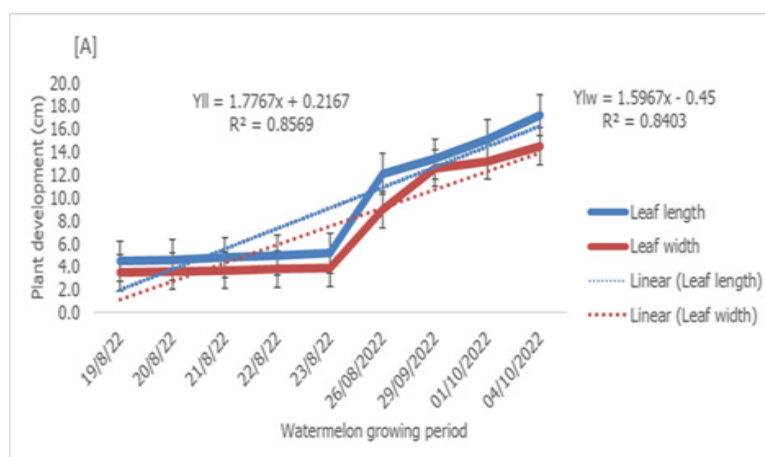
Figure 8. Watermelon phenological development

Figure 9 presents the exhibited relationship among the phenological variables such as plant height (PH), emergency of a new leaf (PLE), and number of plant leaves (PNL) with respect to the growing cycle length. 4.2 cm, 0 and 4 numbers of leaves were recorded at the 16 DAP (19/08/2022). On August 21, 2022 (19 DAP),

one (1) leaf emerged (recorded), corresponding to PH and PNL values of 4.7 cm and 6 leaves (Figure 10 and Figure 11). Hence, the greatest PH of 4.8 cm was measured at 21 DAP and sustained throughout the water melon growth cycle. The watermelon plant height (PH) analysis of variance result showed a high level of significance at $P < 0.005$ as shown in Table 3.
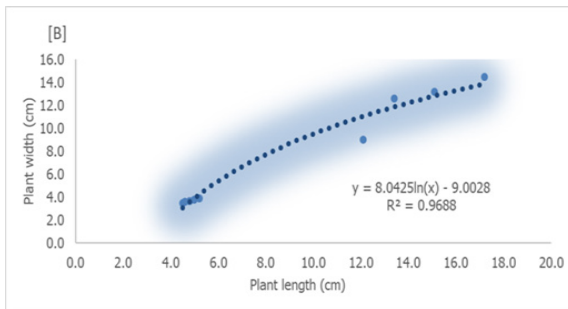
Figure 9. Changes in plant leaf width and plant leaf length
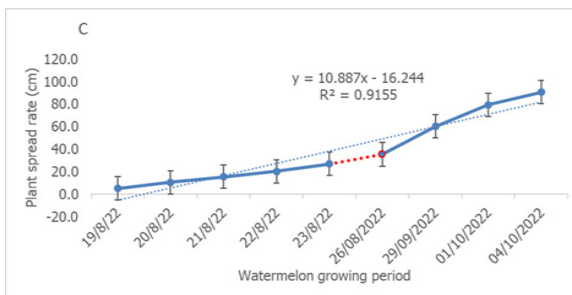
Figure 10. Watermelon spread rate
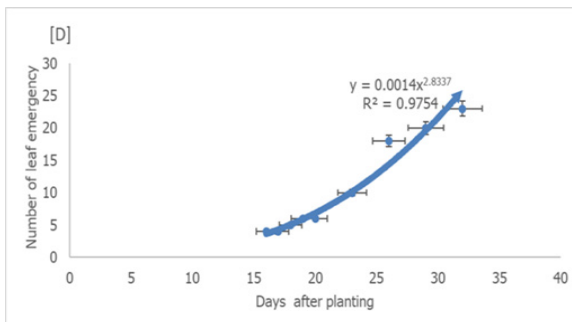
Figure 11. Leaf emergency rate
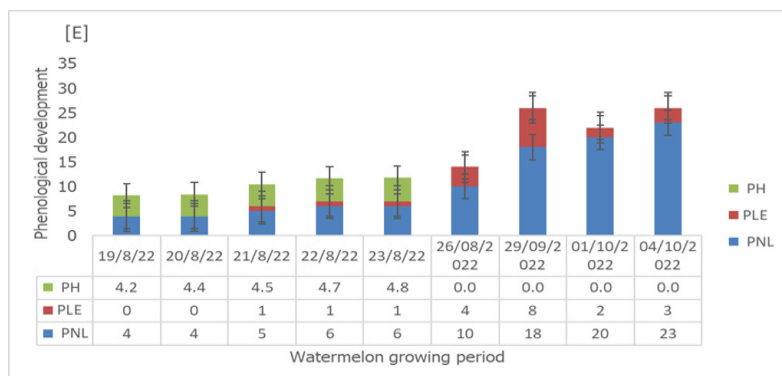
Figure 12. Total watermelon phenological development

4. Conclusions

Using a process-based model (CROPWAT), the study examines the consumptive water use of watermelon using CROPWAT Software version 8.15. The software was also used to calculate crop water requirements (CWR), effective rainfall (EffRain), and irrigation requirements (Irr.req.). The entire simulation revealed seasonal consumptive water use (CWU), CWR, EffRain, and ETo of 175.9 mm, 195.0 mm, 333.8 mm, and 279.8 mm for the growing crop period of 62 days (August, September, and October). However, a total growing period of 110 days was projected from the CROPWAT model, with the harvest day on November 20, 2022. Therefore, a total supplemental water application of 23.1 mm and 59.4 mm will be required to meet the estimated CWR and CWU of 340.2 mm and 310.1 mm by the end of November 2022. Additionally, there was a strong correlation between the growing cycle length and the established association between phenological data. Since the crop requires between 300 mm and 400 mm of crop water requirements during a short maturity period of about 110 days, it is advised that extra water be included in the design whenever farmers intend to go for watermelon production.

Author Contributions: Conceptualization, Y. Olotu, methodology, D.A. Okodugha, writing-review, O.Olarinde, and editing, V.E. Momoh. All authors have read and agreed to the published version of the manuscript.

Conflicts of interest: The authors declare no conflict of interest.

References

1. S.P. Harry, Origin and Emergence of the Sweet Dessert Watermelon, Citrullus lanatus, *Journal of Annals and Botany*, 116(2), 2015, pp.133–148.
2. FAOSTAT, FAO Statistical Database. Agriculture 4th March 2004. http://apps.fao.org/faostat/default.jsp (downloaded on 12.09.2012).
3. G. Anons, *Nasarawa State Agricultural Development Programme, Annual Crop Area and yield Survey (CAYS), Lafia, Nasarawa State*, Unpublished survey report, 2006.
4. FAO, 2001 *Statistics of horticultural crops*. faostat.fao.org/site/365/default.aspx (downloaded on 5.01.2013).
5. M.A. Husaini, A.A. Ramalan, M.K. Othman, Soil Moisture Regime Effect on the Performance of Watermelon under Varying Nitrogen levels in a Semi-Arid region, *Journal of Applied Horticulture*, 6 (2), 2004, pp. 72–75.
6. S. Bekele, K. Tilahun, Regulated deficit irrigation scheduling of onion in semi-arid region of Ethiopia, *Agric Water Manage*, 89, 2007, pp. 148-152.
7. A. Phocaides *Technical Handbook on Pressurized Irrigation Techniques*. FAO, Rome, 2000.
8. A. Kadayifci, G.I. Tuylu, Y. Ucar, B. Carmak, Effects of Mulch and Irrigation Water Amounts on Lettuce's Yield, Evaporation, Transpiration and Soil Evaporation in Isparta Location, Turkey. *Journal of biological sciences*, 4(6), 2004, pp. 751-755.
9. P.Hembram, C. Suibudhi, R. Subudhi, Water and Irrigation Requirement for Watermelon (Citrullus lanatus) Crop of North Central Plateau Zone of Odisha, *South Asian Research Journal of Biology and Applied Biosciences*, 2(4), 2020, pp. 1-6.
10. A.H. Orta, Y. Erdem, T. Erdem, Crop water stress index for watermelon, *Scientia Horticulturae*, 98, 2002, pp. 121–130.
11. T. Poos, E. Varju, Mass Transfer Coefficient for Water Evaporation by Theoretical and Empirical Correlations, *International Journal of Heat and Mass Transfer*, 153, 2020, pp.3-8.
12. J. Aronson, J. Kigel, A. Shmida, J. Klein, Adaptive phenology of desert and mediterranean populations of annual plants grown with and without water-stress, *Oecologia*, 89(7). 1992, pp.17-26.
13. J.M. Delarco, A. Escudero, M.V. Garrido, Effects of site characteristics on nitrogen retranslocation from senescing leaves, *Ecology*, 72(5), 2020, pp. 701-708.

Addresses:

- Yahaya Olotu, Department of Agricultural & Bio-Environmental Engineering, Auchi Polytechnic, Auchi, Edo State, Nigeria.
  realyahaya@yahoo.com
  (*corresponding author*)
- Dauda Aluyah Okodugha, Department of Civil Engineering, Auchi Polytechnic, Auchi, Edo State, Nigeria.
- Olasimbo Olarinde, Federal Ministry of Agriculture, Green House, Akure, Ondo State, Nigeria.
- Vivian Enyopo Momoh, Department of Mechanical Engineering, Delta State Polytechnic, Ogwashiuku, Nigeria.
- Rasheed Ibrahim, Department of Agricultural & Bio-Environmental Engineering, Auchi Polytechnic, Auchi, Edo State, Nigeria.

Robotic Assembly – Mobile Platform for Construction Field

Cosmin Preda* [ID], Robert-Marian Bleotu [ID]

Abstract. *Construction sites often involve the manual transportation of heavy objects, posing risks to workers' safety and efficiency. In this paper, it was proposed a design, development, and evaluation of a service robot specifically created for carrying heavy objects in the construction field. The robot is equipped with robust locomotion capabilities, intelligent perception systems, and efficient control mechanisms to navigate through complex environments and handle various types of loads. It was presented the technical design of the robot, including its hardware components, sensing modalities, and software architecture. Furthermore, it was discussed the experimental validation of the robot's performance in real-world construction scenarios, highlighting its effectiveness in improving productivity, reducing labor costs, and enhancing workplace safety. Through this research, the aim is to demonstrate the potential of service robots as valuable assets in the construction industry, paving the way for future advancements in robotic assistance technologies.*

Keywords: *human-robot collaboration, manipulation, autonomous systems, object transportation, mechanics.*

1. Introduction

The construction industry faces significant challenges with the manual transportation of heavy objects, a task that is both labor-intensive and fraught with risks. Workers frequently encounter physical strain, potential injuries, and inefficiencies while lifting and moving heavy loads, which underscores the need for innovative solutions to enhance safety and productivity [1].

In recent years, the integration of robotics has dramatically transformed various industries, leading to significant improvements in efficiency, productivity, and safety. The construction field, in particular, stands out as an area ripe for innovation through robotics [3]. Advances in robotic technology offer promising solutions to automate labor-intensive tasks, mitigate risks associated with manual handling, and streamline construction processes [2]-[5].

This paper presents a novel contribution to the field by focusing on the development and evolution of robotic platforms specifically designed for construction applications. It addresses in the need for automation in the construction industry by designing and developing a mobile robotic platform optimized for heavy object transportation. The proposed platform is illustrated in Figure 1, showcasing its design and functionality.

Figure 1. Operational robotic platform

Robotic platforms combine different areas of technologies, including autonomous vehicles, drones, mobile robots, and manipulators. These platforms are increasingly recognized for their effectiveness in performing tasks within challenging environments where traditional human intervention may be impractical or hazardous [6][7]. In the context of construction, robotic platforms present unique opportunities to automate repetitive tasks, enhance precision, and improve overall efficiency [8].

This research contributes to this evolving field by advancing the design of mobile robotic platforms for construction. The study not only advances the state of the art in robotic platforms but also provides practical insights into how these technologies can be integrated into existing construction workflows to address current challenges effectively.

In summary, this introduction sets the stage for a detailed integration of the development and application of robotic platforms in the construction industry. The work highlights the potential of these technologies to revolutionize construction practices, offering significant improvements in safety, efficiency, and productivity.

1.1. Importance of heavy object transportation in construction

This section introduce into the significance of heavy object transportation within construction operations. It explores various scenarios where the movement of heavy materials, equipment, and structures is essential for project progress. Examples may include transporting construction materials such as bricks, steel beams, or concrete blocks within the site, as well as moving machinery and tools to different locations, as presented in Figure 2 below.

Figure 2. Common construction materials used for transporting

Heavy objects, such as building materials, equipment, and structural components, form the backbone of construction projects, serving as essential building blocks for infrastructure development [9]. These objects range in size, weight, and complexity, and include items such as steel beams, concrete panels, piping systems, and machinery. The efficient transportation of heavy objects is critical for ensuring the timely and cost-effective completion of construction tasks.

1.2. Role of robotics in construction automation

The focus shifts to the role of robotics as a solution to the challenges outlined before. The section discusses how advancements in robotics, particularly in the field of service robotics, offer opportunities to automate tasks traditionally performed by manual labor, a short presentation is visible in Figure 3 [10][11]. It introduces the concept of a service robot designed specifically for heavy object transportation and sets the research for the upcoming discussion on its design, development, and evaluation.

Figure 3. Robots in construction field

This chapter serves to provide a comprehensive overview of the problem domain, establishing the need for innovative solutions such as service robots in the construction industry.

Automation technologies, including robotics and autonomous systems, offer promising solutions to address the challenges of heavy object transportation in construction [12]. By automating the handling and transportation of heavy objects, construction companies can realize several benefits such as:

Enhanced Safety - automated systems reduce the reliance on manual labor, minimizing the risk of workplace injuries and ensuring a safer working environment for construction workers.

Improved Efficiency - automation streamlines construction workflows, enabling faster, more precise, and more reliable transportation of heavy objects, leading to increased productivity and cost savings.

Optimized Resource Utilization - automated systems optimize the use of resources, including manpower, equipment, and materials, resulting in more efficient construction operations and reduced waste.

2. Research methodology

2.1. Differential kinematics of wheeled robots

Differential kinematics is a fundamental concept in wheeled robotics that describes the relationship between wheel velocities and the motion of the robot's end effector (e.g., its center of mass or a designated point on the chassis). In this topic,

226

we explore the differential kinematics of wheeled robots, focusing on how variations in wheel velocities influence the linear and angular velocities of the robot's end effector.

The end effector velocities represent the translational and rotational motion of the robot in its environment. These velocities are typically expressed in terms of linear velocity V and angular velocity ω, which define the robot's motion along its trajectory and its rate of rotation, respectively. The end effector velocities are determined by the velocities of the robot's wheels and the geometric properties of the robot, such as wheelbase and wheel radii.

The differential kinematics equations relate the velocities of the robot's wheels to its end effector velocities. For a differential drive robot with two independently driven wheels, the kinematic equations are:

$$V = \frac{R}{2}(v_r + v_l) \tag{1}$$

$$\omega = \frac{R}{L}(v_r - v_l) \tag{2}$$

where:

V is the linear velocity of the robot's end effector.

ω is the angular velocity of the robot's end effector.

v_r and v_l are the velocities of the right and left wheels.

R – radius of the wheel

L – distance between the two wheels (wheelbase).

These equations describe how variations in wheel velocities affect the linear and angular motion of the robot. By controlling the velocities of the individual wheels, the robot can achieve different combinations of linear and angular velocities, enabling it to navigate along curved paths, rotate in place, or move straight ahead.

2.1.1. Jacobian Matrix

The Jacobian matrix provides a mathematical framework for analyzing the relationship between the velocities of the robot's wheels and its end effector velocities. It is defined as:

$$J = \begin{bmatrix} \dfrac{\partial x}{\partial v} & \dfrac{\partial x}{\partial v} \\ \dfrac{\partial \theta}{\partial v_r} & \dfrac{\partial \theta}{\partial v_l} \end{bmatrix} \tag{3}$$

where:

x is the position of the robot along the x-axis.

θ is the orientation of the robot (yaw angle).

The elements of the Jacobian matrix represent the partial derivatives of the robot's position and orientation with respect to the velocities of its wheels. By analyzing the Jacobian matrix, roboticists can gain insights into the robot's motion characteristics and design control algorithms to achieve desired motion profiles.

2.1.2. Friction forces in wheeled robots

Friction forces play a crucial role in the dynamic behavior of wheeled robots, influencing both longitudinal and angular motion, presented in Figure 4 and Figure 5. In this subchapter, it was explored the principles of friction forces in wheeled robots and their impact on robot dynamics and control, as Liu Y. et al. in their research.
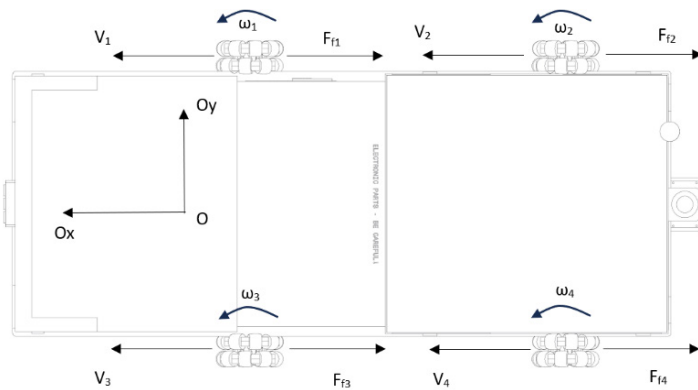
Figure 4. Mobile platform friction forces for longitudinal movement

Longitudinal friction forces occur from the interaction between the wheels of the robot and the ground surface during forward or backward motion. These friction forces affect the robot's acceleration, deceleration, and traction. Key aspects of longitudinal friction forces include:

Static Friction - the maximum friction force that prevents slipping between the wheels and the ground when the robot is at rest or moving at low speeds.

$$F_{static} = \mu_S \cdot N \tag{4}$$

F_{static} - the static friction force.
μ_S - coefficient of static friction.
N – the normal force exerted on the wheels by the ground.

Dynamic Friction - the friction force that opposes the relative motion between the wheels and the ground during acceleration or deceleration.

$$F_{dynamic} = \mu_d \cdot N \qquad (5)$$

$F_{dynamic}$ - dynamic friction force
μ_d - coefficient of dynamic friction

Angular friction forces occur when the robot rotates or turns about its axis, influencing its ability to pivot and change direction. These friction forces are particularly important during maneuvering and navigation tasks. Key aspects of angular friction forces include:

Slip-Induced Friction - the friction force that arises when the wheels skid or slide during turning, affecting the robot's stability and control.

$$F_{slip} = \mu_s \cdot N \qquad (6)$$

F_{slip} - the slip-inducted friction force.
μ_s - coefficient of friction.

Coulomb Friction - the friction force that opposes the rotational motion of the robot, limiting its ability to change direction quickly and accurately.

$$F_{coulomb} = \mu_c \cdot N \qquad (7)$$

$F_{coulomb}$ - the Coulomb friction force.
μ_c - coefficient of Coulomb friction.
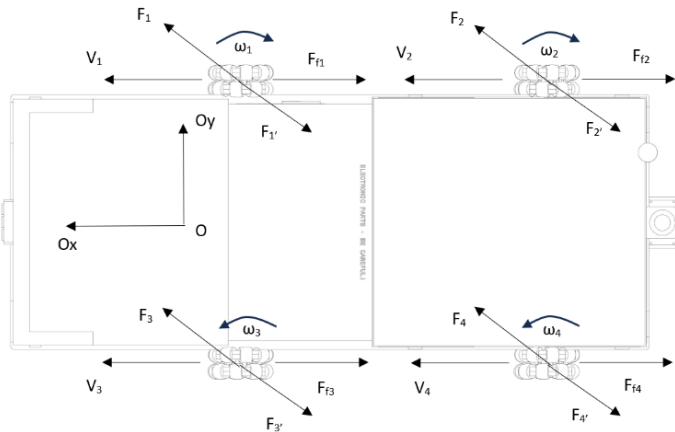
Figure 5. Mobile platform friction forces for angular movement

Friction forces are fundamental aspects of wheeled robot dynamics, influencing both longitudinal and angular motion. By understanding the principles of friction forces and their impact on robot behavior, roboticists can develop effective control strategies and navigation algorithms that optimize the performance and agility of wheeled robots in real-world applications.

3. Mobile platform design: modelling and management tools

This section outlines the specific functional requirements that guided the design of the service robot. It discusses factors such as payload capacity, maneuverability in rugged terrain, compatibility with construction site environments, and safety features to prevent accidents or damage to surroundings and personnel.
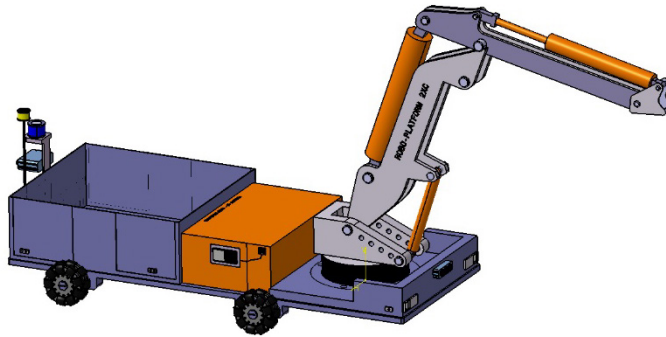
Figure 6. CAD model for the mobile platform

Additionally, it explores design considerations such as scalability, modularity, and ease of maintenance to ensure practicality and adaptability in real-world construction scenarios, the final version of the CAD model can be observed in Figure 6.

3.1. Mechanical structure and locomotion mechanisms

The mechanical design of the service robot is detailed, including its chassis, frame, and locomotion mechanisms. Different locomotion methods, such as wheeled, tracked, or legged systems, are evaluated based on their suitability for navigating construction sites with different terrain and obstacles, based on the research diagram flow presented in Figure 7 below.
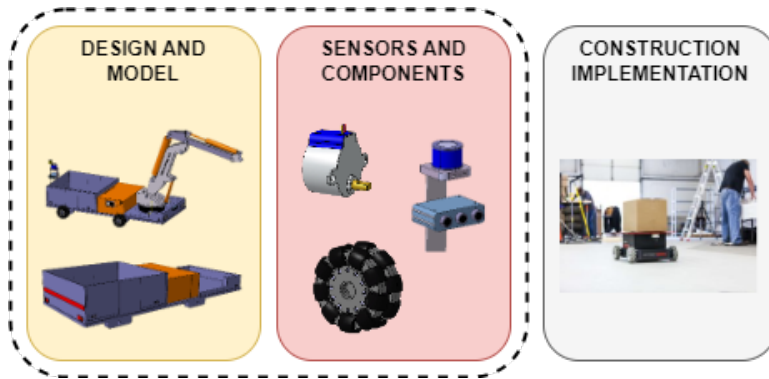
Figure 7. Diagram flow for the mobile-platform structure

The selection of materials and construction techniques to optimize strength, durability, and weight is also discussed, also the main components for the platform, according to Figure 8.
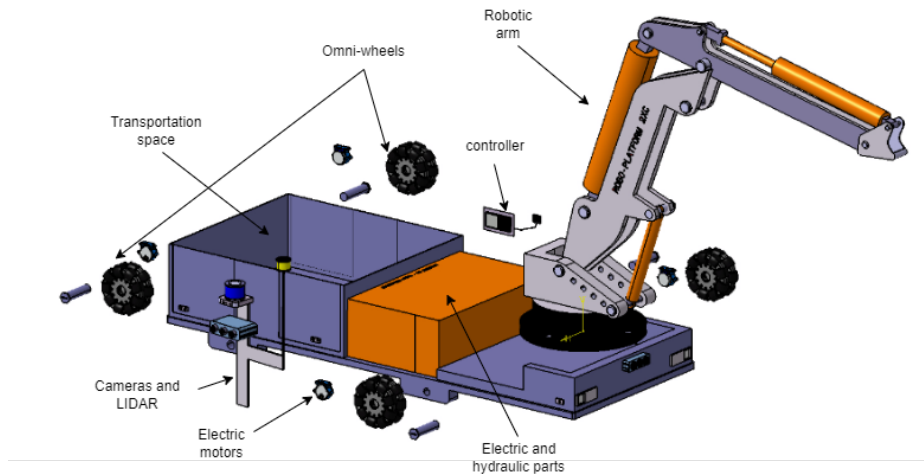
Figure 8. Exploded view with main components

Wheels - wheels are fundamental components of wheeled robots, providing mobility and enabling motion on flat surfaces. The type and configuration of wheels vary depending on the robot's design and intended application.

Omnidirectional Wheels - wheels with rollers or rollers at different angles, allowing for omnidirectional motion. The selected variant is presented in Figure 9.

Figure 9. Omnidirectional wheel used for the platform

Motors - motors are responsible for driving the wheels of the robot, converting electrical energy into mechanical motion. The type and specification of motors depend on factors such as torque requirements, speed, and power efficiency, as the CAD variant from Figure 10.

Stepper Motors - provide precise positioning control and are often used in applications where accuracy is paramount.
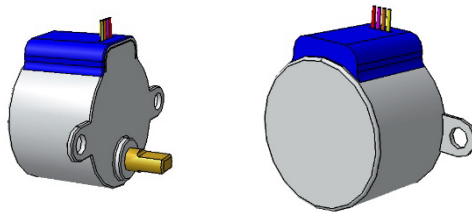
Figure 10. CAD model for stepper motors

Motor controllers regulate the speed and direction of motors, translating control commands from the robot's central processing unit (CPU) into signals that drive the motors. For this research, a stepper motor was used, with the maximum power of 1300W, 25.2 N/m maximum torque Motor controllers vary in complexity and functionality, ranging from simple driver boards to sophisticated motor control units capable of closed-loop feedback control.

Robotic arm - the integration of a hydraulic robot arm into the mobile platform enhances its versatility and functionality, allowing for precise manipulation and handling of heavy objects in construction environments.
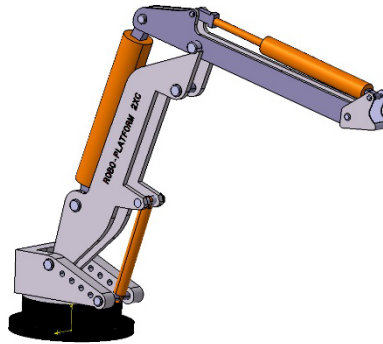
Figure 11. Robotic arm CAD model

While electric robot systems offer certain advantages, such as lower noise levels and greater energy efficiency, hydraulic robot systems excel in applications requiring high power, torque, and ruggedness, the robotic arm is visible in Figure 11 above and mentioned by Chien C.F. et. al in their research. In construction environments, where heavy lifting and robustness are critical, hydraulic systems offer unparalleled performance and reliability.

End tool - the end tool, or end effector, of the robotic arm is a critical component that determines the functionality and versatility of the arm in performing construction activities. In construction settings, various end tools can be attached to the robotic arm to facilitate different tasks, ranging from material handling to precision assembly, as presented in Figure 12.
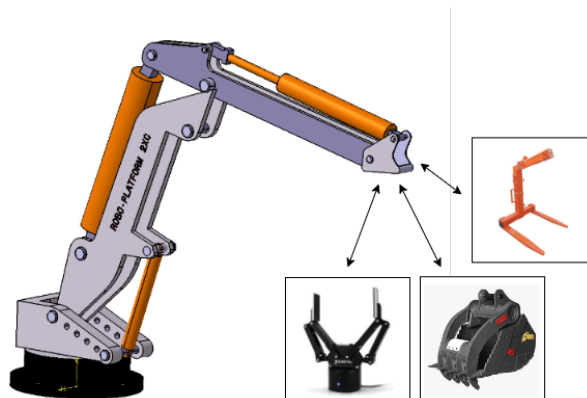
Figure 12. End-tool for robotic arm

Power supply - the power supply provides electrical energy to the robotic platform, powering the motors, sensors, and other electronic components. The power supply system typically consists of:

Batteries - rechargeable batteries are commonly used as the primary power source for mobile robots due to their portability and energy density.

Chassis - the chassis serves as the structural framework of the robotic platform, providing support and housing for the robot's components, from the Figure 13.
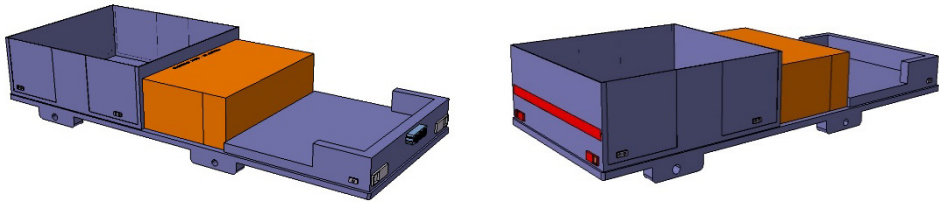
Figure 13. Chassis for the mobile platform

The design and construction of the chassis vary depending on factors such as payload capacity, size constraints, and environmental considerations. Key attributes of the chassis include:

Material - chassis materials range from lightweight metals such as aluminum to durable plastics and composites, balancing strength, weight, and cost considerations. For the following chassis, the material used was aluminium.

Modularity - modular chassis designs allow for easy customization and adaptation to different applications, enabling rapid prototyping and iteration.

3.2. Sensing and perception systems

This section focuses on the sensory capabilities of the service robot, crucial for accurate navigation and object detection in dynamic construction environments. It describes the integration of various sensor modalities, such as cameras, LiDAR, and proximity sensors, to provide comprehensive situational awareness, approached by Boris B. et al. in their work. The choice of sensors, their placement, and data fusion techniques to enhance perception and robustness are explored and presented in Figure 14 and Figure 15.
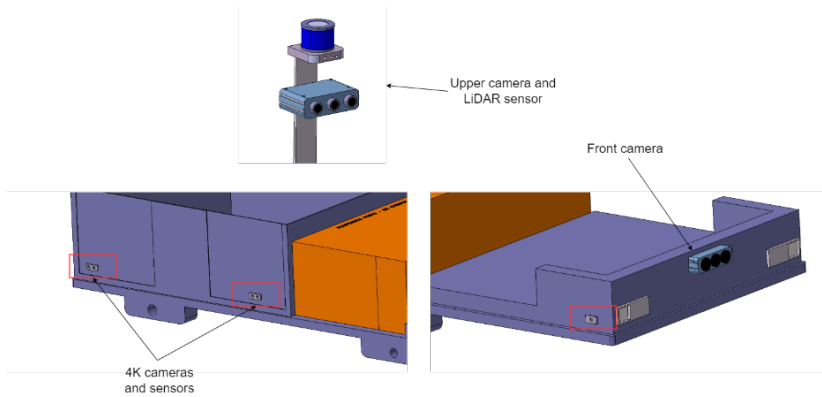
Figure 14. Sensors and cameras on the platform

Vision-Based Object Detection - details the use of cameras and computer vision algorithms to identify and classify objects in the robot's vicinity, enabling it to recognize obstacles, equipment, and materials.

LiDAR for Environment Mapping - discusses the utilization of LiDAR sensors for generating detailed 3D maps of the robot's surroundings, facilitating accurate localization, navigation, and obstacle avoidance.
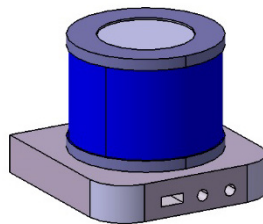
Figure 15. LiDAR sensor

The robotic platform described herein integrates LiDAR (Light Detection and Ranging) sensors and cameras to effectively identify and detect humans in its vicinity. This platform represents a sophisticated solution designed to enhance safety, security, and efficiency in various environments, including industrial settings, construction sites, and public spaces.
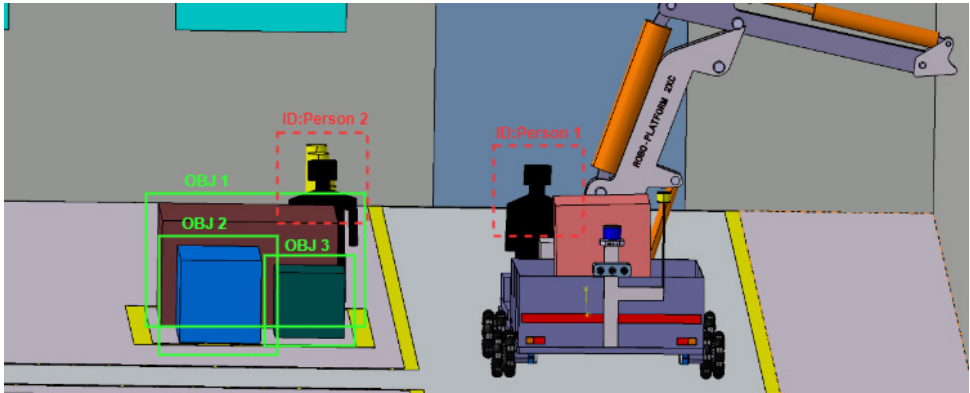
Figure 16. Human identification and avoidance software

This robotic platform is specifically designed to autonomously follow predefined path lines in construction fields, providing efficient and precise navigation capabilities. Equipped with advanced sensors and control systems, the platform seamlessly traverses construction sites, ensuring accurate positioning and adherence to designated routes.
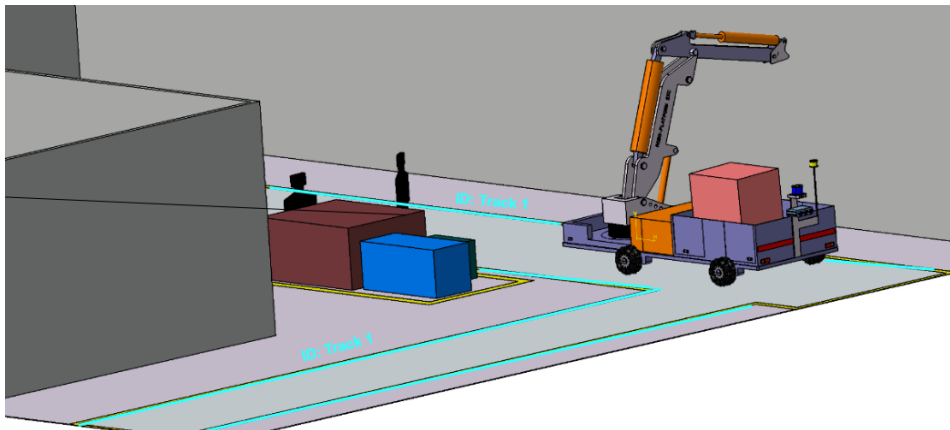
Figure 17. Path follow for the robotic platform in construction field

The robotic platform for path following in construction fields offers a versatile solution for enhancing navigation, efficiency, and safety in construction operations. By autonomously following predefined path lines, the platform streamlines workflows, minimizes human intervention, and maximizes productivity on construction sites, a good working example is presented in Figure 17.

4. Benefits and implications

This section discusses how the deployment of the service robot for heavy object transportation can lead to significant improvements in construction efficiency and productivity. By automating labor-intensive tasks, the robot reduces reliance on manual labor, minimizes downtime, and streamlines workflow processes.
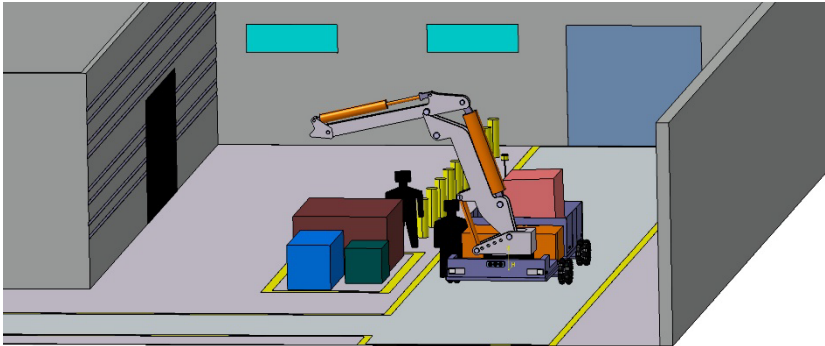
Figure 18. Robot environment functionality

Furthermore, it enables the optimization of resource utilization and project scheduling, ultimately accelerating project completion timelines and reducing overall costs.

The potential relation between the service robot and existing construction equipment and processes are explored and hightlited in Figure 18. The chapter discusses how the robot can seamlessly integrate with other automated systems, such as construction drones, autonomous vehicles, and building information modeling (BIM) software, to create a cohesive ecosystem of robotic assistance. Additionally, it examines opportunities for customization and adaptation of the robot to specific project requirements, enabling tailored solutions for different construction applications and environments.

Through a comprehensive analysis of the benefits and implications of deploying the service robot in construction operations, this chapter highlights its transformative potential in reshaping traditional construction practices.

5. Conclusion

This paper presents the original design, development, and validation of a service robot specifically engineered for the transportation of heavy objects in construction environments. The key contribution of this work is in the creation of an autonomous

robotic platform capable of addressing some of the most significant challenges in construction, such as labor shortages, safety concerns, and the need for improved efficiency in material handling tasks.

Also, this research achieved several key contributions toward the development of a service robot created for use in the construction field, such as:

- Design of the robotic platform: the study presents a comprehensive design of a robust robotic platform created for construction sites. The platform is designed to handle heavy objects. The design includes a selected wheel system to ensure smooth movement across construction environments.
- Development of the robotic arm: the design and integration of a hydraulic robotic arm. The choice of hydraulic actuation over electric motors is one of the study's key innovations, allowing the arm to lift and manipulate heavy loads higher than the capacity of electric systems.
- Motion mechanism and control architecture: a motion control system was developed to enable precise movement of the robot. The control architecture incorporates feedback from integrated sensors (e.g., LiDAR, cameras) to adjust speed, direction, and stability in real time.
- Integration of sensors for navigation and object detection: The sensor suite approach combines data from these to enhance the robot's ability to detect and avoid obstacles, identify humans, and navigate safely through construction sites.

The contribution of this research is the development of a fully autonomous service robot specifically designed for construction labor tasks, with a focus on the transportation of heavy objects. The integration of the mechanical and sensor components allows the robot to perform tasks such as material handling, site inspection, and worker assistance, reducing manual labor.

References

1   Alatise O.M., Ren, Z., Robotics in Construction: A Review of Present Status and Future Trends, *Automation in Construction*, 99, 2019, pp. 324-340.
2   Bryson J., Winfield A.F.T., Standardizing Ethical Design for Artificial Intelligence and Autonomous Systems, *Computer*, 50(5), 2017, pp. 116-119.
3   Cai H., Zhu H., Yu H., Human–robot Collaboration in Construction Industry: A Review, *Automation in Construction*, 119, 103349, 2020.
4   Chien C.F., Liu Y.J.,A Review of Perception and Decision-Making Technologies for UAV Navigation, *Journal of Navigation*, 71(6), 2018, pp. 1361-1377.

5 Kessler J.D., Sreenivasan S.V., Planning and Control of Autonomous Aerial Vehicles: A Review, *Annual Reviews in Control*, 46, 2018, pp. 101-123.

6 Murphy R.R., Tadokoro S., Search and Rescue Robotics. Springer Handbook of Robotics, *2nd Ed. Springer*, 2015, pp. 1613-1635.

7 Shapira A., Shoval S., Chen, Y., Evaluation of Human-Robot Collaboration Performance: A Review, *Journal of Manufacturing Systems*, 53, 2019, pp. 47-64.

8 Thomas B., The future of construction automation: Technological disruption and the upcoming ubiquity of robotics, Automation in Construction, 59, 2015,pp. 113-121.

9 Boris B., Bastian W., Jan S., Tim S., Georgia C., Jan P., Oliver T., Robotic architectural assembly with tactile skills: Simulation and optimization, Automation in Construction, 133, 104206, 2022.

10 Liu Y, Hubo C, Enhanced visualSLAM for construction robots by efficient integration of dynamic object segmentation and scene semantics, Advanced Engineering Informatics, 59, 1002313, 2024.

11 Zemerart A., Michele A., Bram V., Emanuele G., Implementation of a Heterogeneous Multi-Robot System for a Construction Task, IFAC PapersOnline, 56(2), 2023, pp. 3373-3378.

12 Jianqi Z, Xu Y.,Wei W., Jinchao G., Ling D., Vincent C.S.L., Automated guided vehicles and autonomous mobile robots for recognition and tracking in civil engineering, Automation in Construction, 145, 104599, 2022.

13 Nathan M., Justin W., Achim M., On-site autonomous construction robots: Towards unsupervised building, Automation in Construction, 119, 103312, 2020.

Addresses:

- Ph.D. Stud. Eng. Cosmin Preda, Lucian Blaga University of Sibiu, Faculty of Engineering, Strada Emil Cioran 4, 550025, Sibiu, Romania
  cosmin.preda@ulbsibiu.ro
  ([*]corresponding author)
- Ph.D. Stud. Eng. Robert-Marian Bleotu, Lucian Blaga University of Sibiu, Faculty of Engineering, Strada Emil Cioran 4, 550025, Sibiu, Romania
  robert.bleotu@ulbsibiu.ro

Table of content